



**ROTATING SCATTER MASK FOR GAMMA
SOURCE IMAGING**

THESIS

Julie V. Logan

AFIT-ENP-MS-17-M-101

**DEPARTMENT OF THE AIR
FORCE AIR UNIVERSITY**

AIR FORCE INSTITUTE OF TECHNOLOGY

Wright-Patterson Air Force Base, Ohio

DISTRIBUTION STATEMENT A

APPROVED FOR PUBLIC RELEASE; DISTRIBUTION UNLIMITED

The views expressed in this document are those of the author and do not reflect the official policy or position of the United States Air Force, the United States Army, the United States Department of Defense or the United States Government. This material is declared a work of the U.S. Government and is not subject to copyright protection in the United States.

AFIT-ENP-MS-17-M-101

**ROTATING SCATTER MASK FOR GAMMA
SOURCE IMAGING**

THESIS

**Presented to the Faculty Department of Engineering Physics
Graduate School of Engineering and Management Air Force Institute of Technology
Air University
Air Education and Training Command
in Partial Fulfillment of the Requirements for the Degree of Master of Science**

Julie V. Logan, BA, BS

March 2017

DISTRIBUTION STATEMENT A

APPROVED FOR PUBLIC RELEASE; DISTRIBUTION UNLIMITED

AFIT-ENP-MS-17-M-101

**ROTATING SCATTER MASK FOR GAMMA
SOURCE IMAGING**

THESIS

Julie V. Logan, BA, BS

Committee Membership:

LTC Dr. Buckley E. O'Day
Chair

Dr. Larry W. Burggraf
Member

Dr. Justin A. Clinton
Member

Dr. Darren E. Holland
Member

Abstract

Current gamma imaging systems are limited in utility due to their cost, size, narrow field of view, and low image formation efficiency. This effort constitutes a critical step in the development of an imaging system that is limited by none of these factors. This gamma imaging system consists of a routine NaI(Tl) scintillation detector coupled with a rotating scatter mask, the geometry of which is specifically chosen such that the detected signal obtained from one complete mask rotation provides sufficient information to uniquely determine the relative direction of the source position. This mask encases the detector and can be completely encapsulated within a 0.045 m^3 cube (side length of 35.56 cm). A GEANT4 simulation was developed to model the functionality of this system and obtain a library of detector response curves. This simulation was validated via statistical comparisons with experimental and MCNP data. Using the results of the simulation, an algorithm was developed that was shown to predict experimental source direction over a nearly 4π field of view with average errors that were smaller than the resolution in the library of curves employed to image, with an average error in both the azimuthal angle θ and polar angle ϕ of less than 5° .

To Laura and Scott

Acknowledgements

Just as there is a plethora of applications for the RSM Gamma Detection System, the people who I need to thank for their support throughout this effort also abound.

First, I would like to articulate my tremendous appreciation to LTC O'Day for his marvelous guidance. Sir, thank you very much for forming me into the researcher that I have become. Thank you for your patience with my near daily interaction and thank you for always ensuring that I hold on to the remnants of sanity that I had when I started this thesis effort. Thank you for grounding my knowledge of Nuclear Engineering and for encouraging me to aim high.

I would also like to thank the remainder of my committee and collaborators for their guidance and support. Particularly, I would like to thank Dr. Holland. Sir, thank you for keeping up with my disgustingly lengthy email chains and for persisting as we uncovered the mystery of the disappearing particles. I would also like to thank Major Christopher Charles, as his development of the experimental assembly formed the foundation for this effort.

Additionally, I would like to recognize the office of HQAFMC/A9A. Thank you all for not ostracizing me for my physics nerdiness and at least pretending as if you wanted me to go on describing that physics concept. All jest aside, I would like to sincerely thank Dr. Jackson for permitting my AFIT attendance. Without your support, I would not have been able to embark on this endeavor. Thank you for your wisdom and ‘unsolicited’ advice; I

always find it enlightening.

Finally, I would be tremendously remiss if I did not express my thankfulness to my family: Mom, Dad, Nico, and Lily. I love you all so much and would be lost without your acceptance and support. Although you sometimes did not fane interest as well as my coworkers (referenced above), you serve as my foundation. Mom and Dad, I have no idea who I would be without you and I dedicate this effort to you.

Julie V. Logan

Table of Contents

Abstract.....	v
Acknowledgements.....	vii
Table of Contents.....	ix
List of Figures	xi
List of Tables.....	xx
I. Introduction	22
1.1 Background	22
1.2 Motivation.....	3
1.3 Problem.....	5
1.4 Hypothesis	9
1.5 Methods	10
1.6 System Design.....	11
1.7 Research Contributions	14
II. Theory.....	16
2.1 Gamma Interactions with Matter	16
2.2 Neutral Particle Transport Methodologies.....	17
2.3 Photon Detection	18
2.4 Inorganic Scintillation Spectroscopy	20
2.5 Statistical Comparison of Distributions	30
2.6 Literature Review.....	40
III. Simulation	43
3.1 GEANT4 Software.....	43
3.2 Application Developed.....	44
3.3 Simulation Specifications	49
3.4 Variance Reduction.....	51
.....	52
IV. Experiment	53
4.1 Gamma RSM Detection System Setup	53
4.2 Data Acquisition	53
.....	54
V. Results and Analysis	56
5.1 Introduction.....	56
5.2 Energy Spectra MCNP/GEANT Comparisons.....	59
5.3 Detector Response Curve MCNP/GEANT Comparisons	66
5.4 Experiment and Simulation Data Processing.....	76
5.5 Energy Spectra Experiment/GEANT Comparisons	87
5.6 Detector Response Curve Experiment/GEANT Comparisons	89

VI.	Source Position Determination Algorithm.....	102
6.1	Algorithm Development	102
6.2	Algorithm Results	106
VII.	Conclusion	110
7.1	Overview	110
7.2	MCNP/GEANT Comparisons	111
7.3	Experiment/GEANT Comparisons.....	111
7.4	Imaging Algorithm.....	112
7.5	Recommendations for Future Work.....	113
	Appendix A	116
	Appendix B	126
	Appendix C	163
	Appendix D	166
	Appendix E	192
	Appendix F	194
	Appendix G	231
	Appendix H.....	234
	Bibliography	236

List of Figures

Figure 1. Gamma RSM Coordinate System. The mask rotates 360° in the azimuthal angle θ . A source position is defined by a vector indicating a given (θ,ϕ) direction relative to the center of the detector, defined as the origin of the coordinate system [28].	11
Figure 2. Outer radius specification for each cell defined by the cones and planes that form its boundaries. For the smooth CAD design used in the analysis, this table would extend to infinite dimensions [14]. Due to the fact that each column adds to the same sum, the total attenuation of source particles through one complete mask rotation is equal for all source directions. Thus, the amount of signal information that one obtains from the detector is approximately independent of source direction.....	12
Figure 3. Scatter mask geometry. This particular geometry results in a unique detector response for each (θ,ϕ) source position relative to the detector [14].	13
Figure 4. Detector/ scatter mask assembly. The detector is nested within the scatter mask to allow rotation of the mask to impact the detected radiation signal. This image shows the entirety of the RSM imaging assembly. Only the mask, detector volume, and sleeve are modeled within the simulations considered here [14].	14
Figure 5. Contributions of different interaction mechanism to the mass attenuation coefficient of gamma rays within a scintillating NaI detector, as a function of gamma ray energy [21]....	23
Figure 6. Contributions of different interaction mechanism to the mass attenuation coefficient of gamma rays within the experimental polymethacrylate RSM material, as a function of gamma ray energy [21].....	24
Figure 7. Comparison between the ideal energy spectrum of a detector and realized energy spectrum from a realistic detector with imperfect energy resolution resulting in Gaussian broadening to the measured energy detected [19].	25
Figure 8. Angle of gamma deflection in a Compton scattering event as a function of initial energy. This chart demonstrates that, photons undergoing large angle Compton scatters ($> 120^\circ$) all have approximately the same energy, despite differences in initial energy [19]....	28
Figure 9. Decay scheme of ^{137}Cs through which the 662 keV gamma ray in this effort is produced [23].....	29
Figure 10: GEANT visualization of variance reduction employed via a conical source distribution. This cone is seen to encompass the entire RSM system and, thus, approximates an isotopic source. Photon tracks are visualized in blue with incident gammas and scattered gammas being readily apparent in this early stage of the simulation.	52
Figure 11. Components utilized in the experimental data acquisition. The settings for the voltage source, delay line amplifier, and multichannel analyzer are shown.	54
Figure 12. Experimental data acquisition setup of the RSM imaging system. The source is positioned via mechanically controlled crossbars.	55
Figure 13. Visualization of convergence of energy spectrum as number of incident particles	

increases from 200,000 to 30,000,000 incident gamma quanta. This source position, ($\theta = 0^\circ, \varphi = 90^\circ$), was particularly chosen to be one with especially complex mask geometry, thus causing it to converge particularly slowly relative to other more representative source positions.....	59
Figure 14. GEANT and MCNP energy spectra for source positions $\theta, \varphi = 90^\circ, 90^\circ, 90^\circ, 45^\circ, 45^\circ, 90^\circ$, and $45^\circ, 45^\circ$. All values are the unnormalized count of the number of incident source particles that result in energy deposition within the detector volume that falls within the given 1 keV wide energy bin. Each spectrum represents a total of 10,000,000 incident 662 keV gamma particles.	61
Figure 15. Normalized GEANT and MCNP energy spectra for source positions $\theta, \varphi = 90^\circ, 90^\circ, 90^\circ, 45^\circ, 45^\circ, 90^\circ$, and $45^\circ, 45^\circ$ with the 90% confidence interval calculated for each position. Each spectrum represents a total of 10,000,000 incident 662 keV gamma particles.	64
Figure 16. 90% FEP confidence intervals for normalized GEANT and MCNP energy spectra for source positions $\theta, \varphi = 90^\circ, 90^\circ, 90^\circ, 45^\circ, 45^\circ, 90^\circ$, and $45^\circ, 45^\circ$. This shows that the MCNP and GEANT FEP confidence intervals overlap for all positions excluding $(\theta, \varphi) = (90^\circ, 90^\circ)$. Each spectrum represents a total of 10,000,000 incident 662 keV gamma particles.....	65
Figure 17. Detector Response curve plots for each 10° increment of phi $\varphi = 5^\circ$ to 175° . Each point is defined by the number of source particles that contribute to the FEP (deposit all of their energy in the detector volume), out of 500,000 incident 662 keV gamma rays per θ, φ position.	68
Figure 18. Detector Response curve plots for each 10° increment of phi $\varphi = 5^\circ$ to 175° . Each point is defined by the number of source particles that contribute to the Compton Integral (deposit up to 480 keV in the detector volume), out of 500,000 incident 662 keV gamma rays per θ, φ position.	69
Figure 19. Count of gross number of incident particles that contribute to the Compton Integral for $\varphi = 45^\circ - 75^\circ$ in increments of 10° with $\theta = 0^\circ - 355^\circ$ in increments of 5° for each increment of φ . These graphs correspond to GEANT and MCNP results with 500,000 source particles for each (θ, φ) position. The 90% confidence interval is plotted for each..	73
Figure 20. Count of gross number of incident particles that contribute to the Full Energy Peak for $\varphi = 45^\circ - 75^\circ$ in increments of 10° with $\theta = 0^\circ - 355^\circ$ in increments of 5° for each increment of φ . These graphs correspond to GEANT and MCNP results with 500,000 source particles for each (θ, φ) position. The 90% confidence interval is plotted for each..	74
Figure 21. Uncalibrated energy spectrum within the NaI(Tl) detector resulting from the multinuclide source described in Table 6. This spectrum includes background and underlying spectral components beneath the FEP for each isotope.	78
Figure 22. Uncalibrated energy spectrum within the NaI(Tl) detector resulting from the multinuclide source described in Table 6. The background and underlying spectral components not part of the FEP are subtracted out via a function fit to the points where each Gaussian peak reaches its boundaries where it approaches zero. This plot is used to determine the voltage bins in which each isotope's FEP is centered. These values are used to fit the function that will become the calibration curve.	78
Figure 23. Graphical comparison of broadened (via convolution) GEANT simulation energy spectra and calibrated experimental spectra. The experimental data was collected over a 24h period with a ^{137}Cs source and the simulation was run with 10,000,000 incident 662 keV	

gamma rays.....	82
Figure 24. Graphical comparison of broadened (via resampling a Gaussian with standard deviation defined by published power law fit) GEANT simulation energy spectra and calibrated experimental spectra. The experimental data was collected over a 24h period with a ^{137}Cs source and the simulation was run with 10,000,000 incident 662 keV gamma rays.	84
Figure 25. Graphical comparison of broadened (via resampling a Gaussian with standard deviation defined by power law derived for detector used in this effort) GEANT simulation energy spectra and calibrated experimental spectra. The experimental data was collected over a 24h period with a ^{137}Cs source and the simulation was run with 10,000,000 incident 662 keV gamma rays.	85
Figure 26. Comparison of Compton Integral detector response curve derived from broadened and unbroadened simulation energy spectra. It is shown that the broadening has little impact on the detector response curve obtained from the energy spectra. Broadening is achieved via convolution of the energy spectra with a Gaussian defined by the FEP standard deviation of the associated experimental energy spectrum.	92
Figure 27. Normalized count (per total count in the detector response curve) that contribute to the Compton Integral (200 keV – 480 keV) for $\varphi = 45^\circ$ with $\theta = 0^\circ - 355^\circ$ in increments of 5° . These values correspond to GEANT results with 500,000 source particles for each (θ, φ) position and experimental results collected over 24h. The 90% confidence interval is plotted.	97
Figure 28. Normalized count (per total count in the detector response curve) that contribute to the FEP for $\varphi = 45^\circ$ with $\theta = 0^\circ - 355^\circ$ in increments of 5° . These values correspond to GEANT results with 500,000 source particles for each (θ, φ) position and experimental results collected over 24h. The 90% confidence interval is plotted. For each (θ, φ) position, the FEP count comes from a broadened energy spectrum (via convolution for GEANT data and inherently for experimental data).	100
Figure 29. Representative error surface for an input experimental source position. The minimum value in this surface indicates the (θ, φ) vector pointing to the predicted source location. Two methods of quantifying the difference between vectors have been applied. The mean squared error and the modal assurance criterion are shown to predict the same source location.	105
Figure 30. Detector response curves associated with the normalized experimental input detector response curve and the library detector response curve associated with the prediction of the source position (associated with the minimum in <i>Figure 28</i>).	106
Figure 31. For true experimental source positions associated with $\theta = 5^\circ$ to 180° in increments of 5° and $\varphi = 5^\circ$ to 175° in increments of 10° , the error in the predicted source position is presented. This source position is predicted utilizing a simulation-derived library of detector response curves.	108
Figure 32. For true experimental source positions associated with $\theta = 185^\circ$ to 360° in increments of 5° and $\varphi = 5^\circ$ to 175° in increments of 10° , the error in the predicted source position is presented. This source position is predicted utilizing a simulation-derived library of detector response curves.	109
Figure 33. Count of gross number of incident particles that contribute to the Compton Integral for $\varphi = 5^\circ - 35^\circ$ in increments of 10° with $\theta = 0^\circ - 355^\circ$ in increments of 5° for each increment of φ . These graphs correspond to GEANT and MCNP results with 500,000 source particles for each (θ, φ) position. The 90% confidence interval is plotted for each.	117

Figure 34. Count of gross number of incident particles that contribute to the Compton Integral for $\varphi = 45^\circ - 75^\circ$ in increments of 10° with $\theta = 0^\circ - 355^\circ$ in increments of 5° for each increment of φ . These graphs correspond to GEANT and MCNP results with 500,000 source particles for each (θ, φ) position. The 90% confidence interval is plotted for each.	118
Figure 35. Count of gross number of incident particles that contribute to the Compton Integral for $\varphi = 85^\circ - 115^\circ$ in increments of 10° with $\theta = 0^\circ - 355^\circ$ in increments of 5° for each increment of φ . These graphs correspond to GEANT and MCNP results with 500,000 source particles for each (θ, φ) position. The 90% confidence interval is plotted for each.	119
Figure 36. Count of gross number of incident particles that contribute to the Compton Integral for $\varphi = 125^\circ - 155^\circ$ in increments of 10° with $\theta = 0^\circ - 355^\circ$ in increments of 5° for each increment of φ . These graphs correspond to GEANT and MCNP results with 500,000 source particles for each (θ, φ) position. The 90% confidence interval is plotted for each.	120
Figure 37. Count of gross number of incident particles that contribute to the Compton Integral for $\varphi = 125^\circ - 155^\circ$ in increments of 10° with $\theta = 0^\circ - 355^\circ$ in increments of 5° for each increment of φ . These graphs correspond to GEANT and MCNP results with 500,000 source particles for each (θ, φ) position. The 90% confidence interval is plotted for each.	120
Figure 38. Count of gross number of incident particles that contribute to the Full Energy Peak for $\varphi = 5^\circ - 35^\circ$ in increments of 10° with $\theta = 0^\circ - 355^\circ$ in increments of 5° for each increment of φ . These graphs correspond to GEANT and MCNP results with 500,000 source particles for each (θ, φ) position. The 90% confidence interval is plotted for each.	121
Figure 39. Count of gross number of incident particles that contribute to the Full Energy Peak for $\varphi = 45^\circ - 75^\circ$ in increments of 10° with $\theta = 0^\circ - 355^\circ$ in increments of 5° for each increment of φ . These graphs correspond to GEANT and MCNP results with 500,000 source particles for each (θ, φ) position. The 90% confidence interval is plotted for each.	122
Figure 40. Count of gross number of incident particles that contribute to the Full Energy Peak for $\varphi = 85^\circ - 115^\circ$ in increments of 10° with $\theta = 0^\circ - 355^\circ$ in increments of 5° for each increment of φ . These graphs correspond to GEANT and MCNP results with 500,000 source particles for each (θ, φ) position. The 90% confidence interval is plotted for each.	123
Figure 41. Count of gross number of incident particles that contribute to the Full Energy Peak for $\varphi = 125^\circ - 155^\circ$ in increments of 10° with $\theta = 0^\circ - 355^\circ$ in increments of 5° for each increment of φ . These graphs correspond to GEANT and MCNP results with 500,000 source particles for each (θ, φ) position. The 90% confidence interval is plotted for each.	124
Figure 42. Figure 30: Count of gross number of incident particles that contribute to the Full Energy Peak for $\varphi = 165^\circ - 175^\circ$ in increments of 10° with $\theta = 0^\circ - 355^\circ$ in increments of 5° for each increment of φ . These graphs correspond to GEANT and MCNP results with 500,000 source particles for each (θ, φ) position. The 90% confidence interval is plotted for each.	124
Figure 43. Normalized count (per total count in the detector response curve) that contribute to the Compton Integral (200 keV – 480 keV) for $\varphi = 5^\circ$ with $\theta = 0^\circ - 355^\circ$ in increments of 5° . These values correspond to GEANT results with 500,000 source particles for each (θ, φ) position and experimental results collected over 24h. The 90% confidence interval is plotted.	127
Figure 44. Normalized count (per total count in the detector response curve) that contribute to the Compton Integral (200 keV – 480 keV) for $\varphi = 15^\circ$ with $\theta = 0^\circ - 355^\circ$ in increments of 5° . These values correspond to GEANT results with 500,000 source particles for each (θ, φ) position and experimental results collected over 24h. The 90% confidence interval is plotted.	

.....	128
Figure 45. Normalized count (per total count in the detector response curve) that contribute to the Compton Integral (200 keV – 480 keV) for $\varphi = 25^\circ$ with $\theta = 0^\circ - 355^\circ$ in increments of 5° . These values correspond to GEANT results with 500,000 source particles for each (θ, φ) position and experimental results collected over 24h. The 90% confidence interval is plotted. 129
.....	130
Figure 46. Normalized count (per total count in the detector response curve) that contribute to the Compton Integral (200 keV – 480 keV) for $\varphi = 35^\circ$ with $\theta = 0^\circ - 355^\circ$ in increments of 5° . These values correspond to GEANT results with 500,000 source particles for each (θ, φ) position and experimental results collected over 24h. The 90% confidence interval is plotted. 131
.....	132
Figure 47. Normalized count (per total count in the detector response curve) that contribute to the Compton Integral (200 keV – 480 keV) for $\varphi = 45^\circ$ with $\theta = 0^\circ - 355^\circ$ in increments of 5° . These values correspond to GEANT results with 500,000 source particles for each (θ, φ) position and experimental results collected over 24h. The 90% confidence interval is plotted. 133
.....	134
Figure 48. Normalized count (per total count in the detector response curve) that contribute to the Compton Integral (200 keV – 480 keV) for $\varphi = 55^\circ$ with $\theta = 0^\circ - 355^\circ$ in increments of 5° . These values correspond to GEANT results with 500,000 source particles for each (θ, φ) position and experimental results collected over 24h. The 90% confidence interval is plotted. 135
.....	136
Figure 49. Normalized count (per total count in the detector response curve) that contribute to the Compton Integral (200 keV – 480 keV) for $\varphi = 65^\circ$ with $\theta = 0^\circ - 355^\circ$ in increments of 5° . These values correspond to GEANT results with 500,000 source particles for each (θ, φ) position and experimental results collected over 24h. The 90% confidence interval is plotted. 137
.....	138
Figure 50. Normalized count (per total count in the detector response curve) that contribute to the Compton Integral (200 keV – 480 keV) for $\varphi = 75^\circ$ with $\theta = 0^\circ - 355^\circ$ in increments of 5° . These values correspond to GEANT results with 500,000 source particles for each (θ, φ) position and experimental results collected over 24h. The 90% confidence interval is plotted. 139
.....	140
Figure 51. Normalized count (per total count in the detector response curve) that contribute to the Compton Integral (200 keV – 480 keV) for $\varphi = 85^\circ$ with $\theta = 0^\circ - 355^\circ$ in increments of 5° . These values correspond to GEANT results with 500,000 source particles for each (θ, φ) position and experimental results collected over 24h. The 90% confidence interval is plotted. 141
.....	142
Figure 52. Normalized count (per total count in the detector response curve) that contribute to the Compton Integral (200 keV – 480 keV) for $\varphi = 95^\circ$ with $\theta = 0^\circ - 355^\circ$ in increments of 5° . These values correspond to GEANT results with 500,000 source particles for each (θ, φ) position and experimental results collected over 24h. The 90% confidence interval is plotted. 143
.....	144
Figure 53. Normalized count (per total count in the detector response curve) that contribute to the Compton Integral (200 keV – 480 keV) for $\varphi = 105^\circ$ with $\theta = 0^\circ - 355^\circ$ in increments of 5° . These values correspond to GEANT results with 500,000 source particles for each (θ, φ) position and experimental results collected over 24h. The 90% confidence interval is plotted. 145

Figure 54. Normalized count (per total count in the detector response curve) that contribute to the Compton Integral (200 keV – 480 keV) for $\varphi = 115^\circ$ with $\theta = 0^\circ - 355^\circ$ in increments of 5° . These values correspond to GEANT results with 500,000 source particles for each (θ, φ) position and experimental results collected over 24h. The 90% confidence interval is plotted. 138
Figure 55. Normalized count (per total count in the detector response curve) that contribute to the Compton Integral (200 keV – 480 keV) for $\varphi = 125^\circ$ with $\theta = 0^\circ - 355^\circ$ in increments of 5° . These values correspond to GEANT results with 500,000 source particles for each (θ, φ) position and experimental results collected over 24h. The 90% confidence interval is plotted. 139
Figure 56. Normalized count (per total count in the detector response curve) that contribute to the Compton Integral (200 keV – 480 keV) for $\varphi = 135^\circ$ with $\theta = 0^\circ - 355^\circ$ in increments of 5° . These values correspond to GEANT results with 500,000 source particles for each (θ, φ) position and experimental results collected over 24h. The 90% confidence interval is plotted. 140
Figure 57. Normalized count (per total count in the detector response curve) that contribute to the Compton Integral (200 keV – 480 keV) for $\varphi = 145^\circ$ with $\theta = 0^\circ - 355^\circ$ in increments of 5° . These values correspond to GEANT results with 500,000 source particles for each (θ, φ) position and experimental results collected over 24h. The 90% confidence interval is plotted. 141
Figure 58. Normalized count (per total count in the detector response curve) that contribute to the Compton Integral (200 keV – 480 keV) for $\varphi = 155^\circ$ with $\theta = 0^\circ - 355^\circ$ in increments of 5° . These values correspond to GEANT results with 500,000 source particles for each (θ, φ) position and experimental results collected over 24h. The 90% confidence interval is plotted. 142
Figure 59. Normalized count (per total count in the detector response curve) that contribute to the Compton Integral (200 keV – 480 keV) for $\varphi = 165^\circ$ with $\theta = 0^\circ - 355^\circ$ in increments of 5° . These values correspond to GEANT results with 500,000 source particles for each (θ, φ) position and experimental results collected over 24h. The 90% confidence interval is plotted. 143
Figure 60. Normalized count (per total count in the detector response curve) that contribute to the Compton Integral (200 keV – 480 keV) for $\varphi = 175^\circ$ with $\theta = 0^\circ - 355^\circ$ in increments of 5° . These values correspond to GEANT results with 500,000 source particles for each (θ, φ) position and experimental results collected over 24h. The 90% confidence interval is plotted. 144
Figure 61. Normalized count (per total count in the detector response curve) that contribute to the FEP for $\varphi = 5^\circ$ with $\theta = 0^\circ - 355^\circ$ in increments of 5° . These values correspond to GEANT results with 500,000 source particles for each (θ, φ) position and experimental results collected over 24h. The 90% confidence interval is plotted. For each (θ, φ) position, the FEP count comes from a broadened energy spectrum (via convolution for GEANT data and inherently for experimental data). 145
Figure 62. Normalized count (per total count in the detector response curve) that contribute to the FEP for $\varphi = 5^\circ$ with $\theta = 0^\circ - 355^\circ$ in increments of 15° . These values correspond to GEANT results with 500,000 source particles for each (θ, φ) position and experimental results collected over 24h. The 90% confidence interval is plotted. For each (θ, φ) position, the FEP count comes from a broadened energy spectrum (via convolution for GEANT data	

and inherently for experimental data).....	146
Figure 63. Normalized count (per total count in the detector response curve) that contribute to the FEP for $\varphi = 5^\circ$ with $\theta = 0^\circ - 355^\circ$ in increments of 25° . These values correspond to GEANT results with 500,000 source particles for each (θ, φ) position and experimental results collected over 24h. The 90% confidence interval is plotted. For each (θ, φ) position, the FEP count comes from a broadened energy spectrum (via convolution for GEANT data and inherently for experimental data).....	147
Figure 64. Normalized count (per total count in the detector response curve) that contribute to the FEP for $\varphi = 5^\circ$ with $\theta = 0^\circ - 355^\circ$ in increments of 35° . These values correspond to GEANT results with 500,000 source particles for each (θ, φ) position and experimental results collected over 24h. The 90% confidence interval is plotted. For each (θ, φ) position, the FEP count comes from a broadened energy spectrum (via convolution for GEANT data and inherently for experimental data).....	148
Figure 65. Normalized count (per total count in the detector response curve) that contribute to the FEP for $\varphi = 5^\circ$ with $\theta = 0^\circ - 355^\circ$ in increments of 45° . These values correspond to GEANT results with 500,000 source particles for each (θ, φ) position and experimental results collected over 24h. The 90% confidence interval is plotted. For each (θ, φ) position, the FEP count comes from a broadened energy spectrum (via convolution for GEANT data and inherently for experimental data).....	149
Figure 66. Normalized count (per total count in the detector response curve) that contribute to the FEP for $\varphi = 5^\circ$ with $\theta = 0^\circ - 355^\circ$ in increments of 55° . These values correspond to GEANT results with 500,000 source particles for each (θ, φ) position and experimental results collected over 24h. The 90% confidence interval is plotted. For each (θ, φ) position, the FEP count comes from a broadened energy spectrum (via convolution for GEANT data and inherently for experimental data).....	150
Figure 67. Normalized count (per total count in the detector response curve) that contribute to the FEP for $\varphi = 5^\circ$ with $\theta = 0^\circ - 355^\circ$ in increments of 65° . These values correspond to GEANT results with 500,000 source particles for each (θ, φ) position and experimental results collected over 24h. The 90% confidence interval is plotted. For each (θ, φ) position, the FEP count comes from a broadened energy spectrum (via convolution for GEANT data and inherently for experimental data).....	151
Figure 68. Normalized count (per total count in the detector response curve) that contribute to the FEP for $\varphi = 5^\circ$ with $\theta = 0^\circ - 355^\circ$ in increments of 75° . These values correspond to GEANT results with 500,000 source particles for each (θ, φ) position and experimental results collected over 24h. The 90% confidence interval is plotted. For each (θ, φ) position, the FEP count comes from a broadened energy spectrum (via convolution for GEANT data and inherently for experimental data).....	152
Figure 69. Normalized count (per total count in the detector response curve) that contribute to the FEP for $\varphi = 5^\circ$ with $\theta = 0^\circ - 355^\circ$ in increments of 85° . These values correspond to GEANT results with 500,000 source particles for each (θ, φ) position and experimental results collected over 24h. The 90% confidence interval is plotted. For each (θ, φ) position, the FEP count comes from a broadened energy spectrum (via convolution for GEANT data and inherently for experimental data).....	153
Figure 70. Normalized count (per total count in the detector response curve) that contribute to the FEP for $\varphi = 5^\circ$ with $\theta = 0^\circ - 355^\circ$ in increments of 95° . These values correspond to GEANT results with 500,000 source particles for each (θ, φ) position and experimental	

- results collected over 24h. The 90% confidence interval is plotted. For each (θ, φ) position, the FEP count comes from a broadened energy spectrum (via convolution for GEANT data and inherently for experimental data)..... 154
- Figure 71. Normalized count (per total count in the detector response curve) that contribute to the FEP for $\varphi = 5^\circ$ with $\theta = 0^\circ - 355^\circ$ in increments of 105° . These values correspond to GEANT results with 500,000 source particles for each (θ, φ) position and experimental results collected over 24h. The 90% confidence interval is plotted. For each (θ, φ) position, the FEP count comes from a broadened energy spectrum (via convolution for GEANT data and inherently for experimental data)..... 155
- Figure 72. Normalized count (per total count in the detector response curve) that contribute to the FEP for $\varphi = 5^\circ$ with $\theta = 0^\circ - 355^\circ$ in increments of 115° . These values correspond to GEANT results with 500,000 source particles for each (θ, φ) position and experimental results collected over 24h. The 90% confidence interval is plotted. For each (θ, φ) position, the FEP count comes from a broadened energy spectrum (via convolution for GEANT data and inherently for experimental data)..... 156
- Figure 73. Normalized count (per total count in the detector response curve) that contribute to the FEP for $\varphi = 5^\circ$ with $\theta = 0^\circ - 355^\circ$ in increments of 125° . These values correspond to GEANT results with 500,000 source particles for each (θ, φ) position and experimental results collected over 24h. The 90% confidence interval is plotted. For each (θ, φ) position, the FEP count comes from a broadened energy spectrum (via convolution for GEANT data and inherently for experimental data)..... 157
- Figure 74. Normalized count (per total count in the detector response curve) that contribute to the FEP for $\varphi = 5^\circ$ with $\theta = 0^\circ - 355^\circ$ in increments of 135° . These values correspond to GEANT results with 500,000 source particles for each (θ, φ) position and experimental results collected over 24h. The 90% confidence interval is plotted. For each (θ, φ) position, the FEP count comes from a broadened energy spectrum (via convolution for GEANT data and inherently for experimental data)..... 158
- Figure 75. Normalized count (per total count in the detector response curve) that contribute to the FEP for $\varphi = 5^\circ$ with $\theta = 0^\circ - 355^\circ$ in increments of 145° . These values correspond to GEANT results with 500,000 source particles for each (θ, φ) position and experimental results collected over 24h. The 90% confidence interval is plotted. For each (θ, φ) position, the FEP count comes from a broadened energy spectrum (via convolution for GEANT data and inherently for experimental data)..... 159
- Figure 76. Normalized count (per total count in the detector response curve) that contribute to the FEP for $\varphi = 5^\circ$ with $\theta = 0^\circ - 355^\circ$ in increments of 155° . These values correspond to GEANT results with 500,000 source particles for each (θ, φ) position and experimental results collected over 24h. The 90% confidence interval is plotted. For each (θ, φ) position, the FEP count comes from a broadened energy spectrum (via convolution for GEANT data and inherently for experimental data)..... 160
- Figure 77. Normalized count (per total count in the detector response curve) that contribute to the FEP for $\varphi = 5^\circ$ with $\theta = 0^\circ - 355^\circ$ in increments of 165° . These values correspond to GEANT results with 500,000 source particles for each (θ, φ) position and experimental results collected over 24h. The 90% confidence interval is plotted. For each (θ, φ) position, the FEP count comes from a broadened energy spectrum (via convolution for GEANT data and inherently for experimental data)..... 161
- Figure 78. Normalized count (per total count in the detector response curve) that contribute to the

FEP for $\varphi = 5^\circ$ with $\theta = 0^\circ - 355^\circ$ in increments of 175° . These values correspond to GEANT results with 500,000 source particles for each (θ, φ) position and experimental results collected over 24h. The 90% confidence interval is plotted. For each (θ, φ) position, the FEP count comes from a broadened energy spectrum (via convolution for GEANT data and inherently for experimental data).....	162
Figure 79. Error in (θ, φ) predicted direction of the source for each experimental input direction $\theta = 5^\circ - 180^\circ$ and $\varphi = 5^\circ - 175^\circ$	164
Figure 80. Error in (θ, φ) predicted direction of the source for each experimental input $\theta = 185^\circ - 360^\circ$ and $\varphi = 5^\circ - 175^\circ$	165

List of Tables

Table 1. Statistical comparison results of GEANT and MCNP energy spectra for source positions $\theta, \varphi = 90^\circ, 90^\circ, 90^\circ, 45^\circ, 45^\circ, 90^\circ$, and $45^\circ, 45^\circ$. Both non-parametric statistical tests confirm that the energy spectra for each position resulting from the two simulations are statistically indistinguishable. Each spectrum represents a total of 10,000,000 incident 662 keV gamma particles.	62
Table 2. Percentage of energy bin count 90% confidence intervals that overlap for normalized GEANT and MCNP energy spectra for source positions $\theta, \varphi = 90^\circ, 90^\circ, 90^\circ, 45^\circ, 45^\circ, 90^\circ$, and $45^\circ, 45^\circ$. Each spectrum represents a total of 10,000,000 incident 662 keV gamma particles.	64
Table 3. Non-parametric statistical comparison test results for each 10° increment of phi $\varphi = 5^\circ$ to 175° . Each point in each spectrum compared is defined by the number of source particles that contribute to the Full Energy Peak (deposit all of their energy in the detector volume), out of 500,000 incident 662 keV gamma rays per θ, φ position. All p-values resulting from both the application of the Anderson–Darling Test and the Kolmogorov–Smirnov Test, excluding the extreme $\varphi = 175^\circ$ source angle (bold), show that the two codes produce resulting detector response curves that are statistically indistinguishable.	70
Table 4. Non-parametric statistical comparison test results for each 10° increment of phi $\varphi = 5^\circ$ to 175° . Each point in each spectrum compared is defined by the number of source particles that contribute to the Compton Integral (deposit up to 480 keV in the detector volume), out of 500,000 incident 662 keV gamma rays per θ, φ position. All p-values resulting from both the application of the Anderson–Darling Test and the Kolmogorov–Smirnov Test, excluding the extreme $\varphi = 5^\circ$ and $\varphi = 175^\circ$ angles (bold), show that the two codes produce resulting detector response curves that are statistically indistinguishable.	71
Table 5. Percentage of the 72 θ positions ($0^\circ – 355^\circ$ in increments of 5°) for each φ for which the MCNP and GEANT 90% confidence intervals around the normalized (per source particle) counts within the Compton Integral and FEP overlap. These values correspond to GEANT and MCNP results with 500,000 source particles for each (θ, φ) position.....	75
Table 6. Composition of the multinuclide source used in experimental calibration. This source is 413 days old at the time of use and the final activity is calculated for each isotope in the source. It is clear that Cr-51 should not be visible in the resulting spectrum because it has almost entirely decayed away.....	77
Table 7. Isotopes with their associated FEP true energies (keV) and uncalibrated voltage bins associated with these values. These are the points used in the derivation of the calibration curve via a polynomial fit of degree 2.....	79
Table 8. Parameters of the calibrated experimental data describing the FEP for four static mask positions. This information is used to broaden the simulated energy spectra.	80
Table 9. χ^2 statistic calculated to compare the entire experimental energy spectrum and the entire broadened simulated energy spectrum for each of the (θ, φ) source positions. Three different	

broadening methodologies are employed and the Gaussian re-sampling with derived power law standard deviation is shown to be superior. The experimental data was collected over a 24h period with a ^{137}Cs source and the simulation was run with 10,000,000 incident 662 keV gamma rays.....	86
Table 10. χ^2 statistic calculated to compare the 200 keV-1098 keV experimental energy spectrum and the 200 keV-1098 keV broadened simulated energy spectrum for each of the (θ, φ) source positions. Three different broadening methodologies are employed and the convolution of a Gaussian defined by the experimental ^{137}Cs FEP standard deviation with the simulated data is shown to minimize the error. The experimental data was collected over a 24h period with a ^{137}Cs source and the simulation was run with 10,000,000 incident 662 keV gamma rays.	86
Table 11. Non-parametric statistical comparison test results for each of the 4 static mask source positions considered. The data used in each test represents the count within energy bins 200 keV-1098 keV for calibrated experimental data and GEANT data broadened via convolution with a Gaussian function defined by the ^{137}Cs FEP standard deviation. All p-values resulting from both the application of the Anderson–Darling Test and the Kolmogorov–Smirnov Test show that the two codes produce resulting detector response curves that are statistically distinguishable. Thus, the results of experiment and simulation could not have been drawn from the same distribution. The experimental data was collected over a 24h period with a ^{137}Cs source and the simulation was run with 10,000,000 incident 662 keV gamma rays. ..	88
Table 12. Non-parametric statistical comparison test results for each 10° increment of phi $\varphi = 5^\circ - 175^\circ$. Each point in each spectrum compared is defined by the number of source particles that contribute to the unbroadened FEP (deposit exactly 662 keV in the detector volume), out of 500,000 simulated particles per (θ, φ) position and experimental results collected over 24h. At a 0.05 significance level, the bolded p-values indicate that the simulated and experimental results are unlikely to be drawn from the same distribution. Thus, the degree of agreement between the simulated and experimental FEP detector response curves is insufficient and the broadened simulation spectra is required.	93
Table 13. Non-parametric statistical comparison test results for each 10° increment of phi $\varphi = 5^\circ - 175^\circ$. Each point in each spectrum compared is defined by the number of source particles that contribute to the Compton Integral (deposit 200 - 480 keV in the detector volume), out of 500,000 simulated particles per (θ, φ) position and experimental results collected over 24h. At a 0.01 significance level, the majority (bolded) of the detector response curves fail to indicate statistical and experimental agreement. Thus, the detector response curve based on Compton Integral is not useful for source position determination. This is clearly demonstrated in the subsequent graphical comparisons (Appendix B). Agreement only occurs when the GEANT curve also fails to be differentiated in θ	96
Table 14. Non-parametric statistical comparison test results for each 10° increment of phi $\varphi = 5^\circ - 175^\circ$. Each point in each spectrum compared is defined by the number of source particles that contribute to integral beneath a Gaussian curve fitted to the broadened simulation FEP (via convolution using the standard deviation calculated via the derived equation 18), out of 500,000 simulated particles per (θ, φ) position and experimental results collected over 24h. At a 0.01 significance level, the bolded p-values indicate that the simulated and experimental results are unlikely to be drawn from the same distribution. φ of 115° should be discounted due to an experimental error at this angle. Thus, all curves are shown to agree via the Kolmogorov–Smirnov Test.	99

ROTATING SCATTER MASK FOR GAMMA SOURCE IMAGING

I. Introduction

1.1 Background

There is a plethora of applications, from medicine to national security to manufacturing, in which the detection and imaging of a radioactive source are of critical importance. The detection and localization of radioactive material or an orphan radioactive source in a complex environment are challenging for a variety of reasons. The ubiquity of radioactive isotopes creates a background source of radiation that varies with location. Furthermore, environmental conditions can also degrade the ability to detect the signatures of radioactive material. The level of imaging difficulty varies with the particular radiation that a given source emits. Due to their extremely short range in matter—order of tens of microns in solids—the detection of heavy charged particles (HCPs) is not feasible. Light charged particles (LCPs), despite their slightly larger range—order of centimeters or less in solids—are similarly difficult to detect. A relatively small amount of material between source and detector will prevent direct detection of both HCPs and LCPs. Neutral particles, including photons and neutrons, are generally more penetrating than HCPs and LCPs and, thus, the imaging of sources emitting these is feasible. While the range of these neutral particles depends on both the particle energy and the material that they are passing through, energetic gammas (several hundred keV or more) and neutrons may penetrate solids as deeply as tens of centimeters or more. Given their significantly increased penetrating power, neutral particles provide the best opportunity to detect and locate radioactive materials or

radioactive sources.

All radioactive materials emit characteristic particles. The efficacy of an imaging system design depends on its ability to distinguish the signal emanating from the radioactive source from the background. This will depend on the type and strength of the source, interaction of the radiation particles with materials between the source and the detector, the background radiation present, and the characteristics of the detection system.

Many detectors are available to detect neutral particles and some of these detectors have been integrated into systems to provide directional information. Unfortunately, these systems are often bulky, expensive, or both [6]. Further, these systems are often severely limited in their field of view. Additionally, many design schemes have extremely poor imaging efficiency, in that they collimate the signal, reducing the amount of radiation actually detected within a given period of time [6].

An ideal imaging system would be reasonably transportable; inexpensive; and provide omnidirectional, accurate, and rapid IMAGING ability. Such a system might focus on the detection of gamma rays using NaI(Tl) scintillation detectors, which have good intrinsic efficiency, good resolution, and are relatively inexpensive [19]. This effort aims to use a 3" x 3" NaI(Tl) crystal detector with a specially designed, inexpensive rotating polymethacrylate shield, which ultimately allows one to determine directionality of a source. This novel shielding methodology was developed by Jack Fitzgerald in 2015 [14]. The system serves as a gamma imaging detect-and-locate device. This Rotating Scatter Mask (RSM) gamma imaging system could potentially provide an improved ability to detect smuggled nuclear weapons, improvised nuclear devices, dirty bombs, special nuclear material, and orphaned industrial and medical sources. This RSM gamma detection system directly addresses one of the most significant

security problems the United States (US) faces and one of the Secretary of Defense's top Science and Technology priorities, the detection of weapons of mass destruction.

1.2 Motivation

The enhancement of radiation detectors to make them position sensitive could greatly improve their utility and expand their applicability to radiation detection problems. The Department of Defense would have definite and immediate use for the relatively compact, inexpensive RSM gamma imaging device. The small size and meager energy requirements of this system allow it to easily be mounted on terrestrial and air vehicles. Additionally, the low cost would allow for widespread deployment. The mounting of the RSM system could provide gamma imaging functionality to an unmanned aerial vehicle (UAV), rotary wing aircraft, wheeled vehicle, tracked vehicle, or sea-borne surface vessel and allow them to support consequence management, non-proliferation, and counter-proliferation operations. For example, the vehicles could be employed in mapping the edge of a radioactive field in the event of detonation of an improvised nuclear device, searching for a smuggled dirty bomb, or locating stolen or lost industrial and medical imaging sources. The RSM system could aid in the zero-knowledge problem of identifying the presence of nuclear material in a warhead or carrier vehicle without disclosing design information. It could also be used to monitor nuclear material placed in long term storage.

The RSM system would provide similar and additional capabilities to other governmental organizations and civilian organizations. For example, commercial sea-borne vessels carrying cargo containers could be equipped with multiple RSM systems to identify the presence of suspect containers requiring a thorough secondary inspection. Port facilities could mount two

small, robust RSM systems on their equipment used to move containers off the ships to further screen cargo. Customs and Border Protection could use RSM systems to pre-screen tractor trailers and other large vehicles at border crossings to identify vehicles needing a secondary inspection. Placement of RSM systems at truck weigh stations along the interstates could aid in the identification of inadvertently or deliberately trafficked radioactive material. The steel and paper industries could use the RSM system to identify materials set for recycling that should be disposed of. Multiple RSM systems could be employed to monitor the buildup of radioactive materials in a flowing system, such as the heat transfer system for a nuclear reactor or piping for a gaseous diffusion or centrifuge enrichment system.

One specific application that warrants further discussion is the localization of an orphan source. An orphan source is defined as a quantity of material that is actively emitting radiation which has been removed from its proper place via mismanagement or intentional smuggling. Organizations focused on homeland security and environmental protection will find a solution to the orphan source problem to be a game-changing technology as they work to protect the public. The 1983 Juarez, Mexico event provides a harmful and costly example of the hazards posed by an orphaned radioactive source. When a medical therapy machine was sold for scrap, some parts were disposed into a junk yard and other parts, including 6000 75 mCi pellets of ^{60}Co , were reprocessed at a foundry to produce steel. The radioactive hazard was not discovered until two months later when a truck carrying contaminated steel stopped at Los Alamos National Laboratory to ask for directions and set off the radiation detection system. The delay in the discovery of this orphan source resulted in more than 50 people accumulating a dose over 390 rem. The incident also caused tremendous economic loss. The radioactive steel had been used in at least 834 buildings which had to be partially or completely destroyed to remove

contaminated materials [2]. The possibility of a dirty bomb attack in the United States is also receiving increased attention. A 2003 Monterey Institute of International Studies document entitled “Commercial Radioactive Sources: Surveying the Security Risk” outlines the potential terrorist use of radioactive sources and conventional explosives to create a radiological dispersal device (RDD) [3]. RDDs could incorporate commercially available sources as well as orphaned industrial or medical sources. In response to this threat, the US Department of Homeland Security (DHS) has established the “Stand-Off Radiation Detection Systems (SORDS)” project which uses autonomous detectors to locate an unshielded 1mCi gamma source at distances up to 100 meters [2]. The work conducted in this effort contributes research in order to support DHS’s goal without the inherent limitations of the current system in operation.

1.3 Problem

Current techniques of detecting positional information of a gamma radioactive source are impractical, limited, or prohibitively expensive. For example, a user surveying an area with a non-directional (i.e. a “dumb”) hand-held detector may have real time access to energy information from isotope identification software and dose rates but positional information is limited. The surveyor must move around the area and, by monitoring relative changes in count rates, determine where the source is located. It has been shown [5] that the search process can be made significantly more efficient if the detector is made directionally sensitive. There are alternative methods of obtaining this directional information—most of which require much larger and more expensive systems—but each is inherently restricted in the situations it is useful. For example, the SORDS system previously addressed is limited to areas where the large IMAGING vehicle can move.

An ideal gamma imaging system would provide good angular resolution (the ability to identify the precise source direction) and imaging efficiency (an ability to utilize a large portion of incident quanta of energy to produce an image). There are alternative methodologies to conduct gamma imaging, each of which has its inherent limitations. The most basic method is simple proximity imaging, where heightened detector count indicates increased proximity to the source. This methodology has poor angular resolution ($> 30^\circ$) and poor imaging efficiency [6]. Collimator-based imaging systems operate via the placement of a highly absorbing material, with either a single pinhole or an array of parallel holes, in front of the detector. Any system dependent upon collimation has poor field of view ($< 60^\circ$) and poor imaging efficiency [6]. Coded aperture methodologies employ many pinholes in the shielding material to produce a shadow image of the aperture, which can subsequently identify source position via deconvolution or correlation calculations. These improve the pinhole detector efficiency as $\sqrt{\# \text{ of pinholes}}$ and improve the angular resolution to $< 5^\circ$, but have a field of view of $< 60^\circ$ [7]. Examples of the employment of this technique include the Large-Angle Coded-Aperture, Gamma-Ray Imager, which employs a set of 57 10 cm x 10 cm x 10 cm NaI(Tl) detectors positioned behind a coded-aperture mask, consisting of 4 cm x 100 cm x 10 cm rectangular lead blocks [8]. This coded aperture provides imaging capabilities because there is a unique projected pattern on the detector plane for each source location. This pattern allows reconstruction of the image. In a similar manner, the SuperMISTI (Mobile Imaging and Spectroscopic Threat Identification) system pairs an array of 78 NaI detectors with a coded aperture composed of 162 lead blocks in order to image a source. It pairs this with an array of 24 HPGe detectors in order to take advantage of their high-resolution spectroscopic ability to identify the radioisotope being detected [1]. Rotation modulation technologies employ two widely spaced, rotating grids in front

of the detector, and do not require a detector that can determine position of radiation interaction with the detector. They provide these benefits at the expense of a poor field of view [9]. An example of such a system has been constructed of 2 lead masks with slits and slats of 4 mm width and 8 mm pitch. This design achieves 0.5° angular resolution at the expense of a narrow 9° field of view [2]. Finally, Compton Camera techniques employ the ability of a system to detect the position and energy deposition of the initial Compton scatter and subsequent photoelectric absorption of an incident gamma. This information is utilized in order to limit the source position to within a cone via the Klein-Nishina relationship between photon change in energy and scatter angle in a Compton scattering event [10] [11]. This imaging system requires detectors that are able to both ensure scatter and measure the energy and position of the scatter as a separate event from the subsequent absorption. A common implementation technique employs a large flat crystal of NaI with an array of photomultiplier tubes arranged behind it. To gain positional information, the conventional method is to place a collimator in front of the detection crystal. The major downfall of this method is that more than 99% of the incident gammas are attenuated thereby greatly reducing the associated statistics. Thus, one cannot image a weak gamma source. A major benefit of this technique is that it results in good angular resolution and a 360° (2π) field of view [6]. Examples of implementations of the Compton Camera technique include the Cadmium-Zinc-Telluride (CZT) Polaris [12] and GPGE GeGI [13]. Both systems employ expensive arrays of 3-dimensional position sensitive semiconductor radiation detectors. Additionally, both systems require supplementation with other imaging techniques for lower energy incident photons that are less likely to undergo a Compton scatter prior to photoelectric absorption.

The rotating scattering mask developed for and used in this research directly addresses

many of the limitations of extant imaging systems. The gamma RSM design uses a ubiquitous, inexpensive, “dumb” NaI(Tl) detector surrounded by a polymethacrylate mask mounted on a small motor that causes rotation of the mask. The rotation of the RSM about the NaI detector provides a unique response curve—based on the time varying energy spectrum detected—which allows identification of the source direction relative to the detector location. Comparison of the detected output (Full Energy Peak (FEP) counts as a function of RSM rotational angle) against a library of theoretical results (obtained from simulation for different source locations) provides positional information. The “best fit” curve identifies the most probable direction of the source. Since this research serves as proof-of-principle for the gamma RSM detection method, a limited, discrete library was developed which consists of detector response curves associated with source positions corresponding to 5° RSM rotational increments around the long axis of the NaI detector and 10° degree azimuthal angles relative to the long axis of the NaI detector. Future research will involve creation of a higher resolution response surface to augment this library of response curves and will allow matching of the experimental response curve against the response surface to provide higher-fidelity directional information.

This gamma RSM detection system directly addresses many of the limitations found in extant directional detection systems. Specifically, this detector provides:

- 1) An increased detector field of view (nearly 4π in extent)
- 2) An ability to gain information from more events (to include Compton, Photoelectric, and Pair Production interactions) – thus improving the imaging efficiency and requiring less time to obtain the same counting statistics
- 3) A significant reduction of cost due to employment of only a single “dumb” detector

- 4) Increased system portability due to reduced system infrastructure, bulkiness, and weight

In contrast, extant imaging systems are each limited in one or more of the following ways: (1) the imaging system significantly reduces the inherent detector field of view and efficiency, (2) the imaging system is limited to the energy regime where Compton scatter is dominant, or (3) the imaging system requires a large array of expensive detectors. Stationary coded aperture based imagers are subject to the first and third limitations. Rotation modulation technologies are subject to the first limitation. Applications dependent on Compton camera techniques are limited by the second. The imaging system in this effort is not subject to these limitations.

In summary, the output of the RSM system (the detector response curve) is unique to each source direction because the mask geometry presented to the source changes uniquely for each source direction. As an incident photon traverses each unit distance in the mask, there is a small probability that the photon will Compton scatter. If it does so, the photon will change direction by a certain angle, which uniquely determines its change in energy (**Equation 1**). This change in energy and angle determines the amount of energy (if any) deposited within the detector. As such, the distribution in amount of energy deposited in the detector will depend heavily upon the mask geometry presented to the source. Because this geometry changes uniquely for each source angle, the RSM assembly response is unique to each source vector. This provides the RSM assembly with IMAGING capabilities.

1.4 Hypothesis

The experimental response curve associated with the energy spectra obtained via the

gamma RSM detection system can be matched against a library of response curves obtained using Monte-Carlo simulation programs to accurately determine the direction of the radioactive source relative to the Gamma RSM detection system position. Simulation validation is an integral step in this process. As such, this research seeks to demonstrate that the two Monte-Carlo simulation codes, GEANT and MCNP, will produce energy spectra and detector response curves which are statistically indistinguishable from each other and experimental results.

1.5 Methods

This research consists of both experimental work and simulation development. The experimental work consists of data acquisition from the RSM and detector assembly in the presence of a source; each run being differentiated by the source radioisotope, activity, and position relative to the detector (defined by the (θ, φ) direction vector). The experimental work provides proof of concept for the gamma RSM detection system.

The simulation development utilizes the Monte-Carlo radiation transport code, GEANT4. Within the application developed, the source specifications; geometrical specifications; physical processes; and desired output are specified. An external collaborator (Cedarville University), Dr. Darren Holland, developed a similar simulation within an alternative radiation transport code, MCNP. The comparison of the MCNP and GEANT results as well as the GEANT and experimental results is accomplished via three main methods: two non-parametric statistical tests, comparison of confidence intervals, and visual comparison. This simulation work provides a benchmark to validate and verify the experimental results, and provides a starting point for future development and optimization of subsequent neutral particle RSM detection systems.

1.6 System Design

The RSM design is the critical piece of the detection system that transforms a “dumb” detector into a directional detector. The RSM design ensures the energy deposition spectrum is unique to each source position (θ, φ) direction relative to the center of the detector. This coordinate system is demonstrated in *Figure 1* where θ is the azimuthal angle and φ is the polar angle, with the z-axis constituting the central axis of the cylindrical detector. The mask rotates 360° in the azimuthal angle θ and a vector defines a source position via its (θ, φ) components.

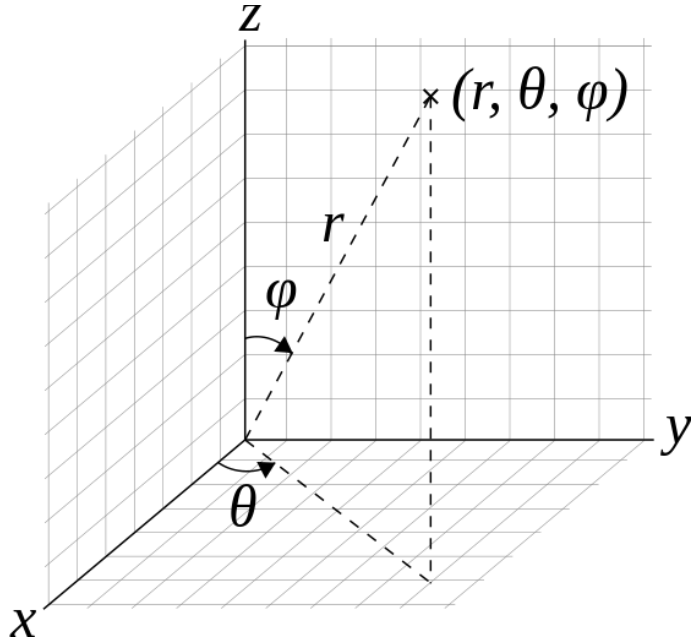


Figure 1. Gamma RSM Coordinate System. The mask rotates 360° in the azimuthal angle θ . A source position is defined by a vector indicating a given (θ, φ) direction relative to the center of the detector, defined as the origin of the coordinate system [28].

Another key element of the RSM design is that, over a rotation of the mask in 360°, the average thickness of mask material between source and detector is approximately the same for all defined source positions. This is a useful characteristic due to the fact that it helps to ensure

that the amount of information the detector obtains in a single rotation is the same regardless of source position vector relative to the center of the detector. These constraints imply the development of the matrix found in **Figure 2**, which defines the outer radius of each cell if the smooth mask is approximated by a series of discrete cells [14].

		Plane Number																																																										
		1	2	3	4	5	6	7	8	9	10	11	12	13	14	15	16	17	18	19	20	21	22	23	24	25	26	27	28	29	30	31																												
Cone Number	1	1	2	3	4	5	6	7	8	9	10	11	12	13	14	15	16	17	18	19	20	21	22	23	24	25	26	27	28	29	30	31																												
	2	2	3	4	5	6	7	8	9	10	11	12	13	14	15	16	2	1	31	30	29	28	27	26	25	24	23	22	21	20	19	18	17																											
	3	3	4	5	6	7	8	9	10	11	12	13	14	15	16	17	3	2	1	31	30	29	28	27	26	25	24	23	22	21	20	19	18																											
	4	4	5	6	7	8	9	10	11	12	13	14	15	16	17	18	4	3	2	1	31	30	29	28	27	26	25	24	23	22	21	20	19	18																										
	5	5	6	7	8	9	10	11	12	13	14	15	16	17	18	19	5	4	3	2	1	31	30	29	28	27	26	25	24	23	22	21	20	19	18																									
	6	6	7	8	9	10	11	12	13	14	15	16	17	18	19	20	6	5	4	3	2	1	31	30	29	28	27	26	25	24	23	22	21	20	19	18																								
	7	7	8	9	10	11	12	13	14	15	16	17	18	19	20	21	7	6	5	4	3	2	1	31	30	29	28	27	26	25	24	23	22	21	20	19	18																							
	8	8	9	10	11	12	13	14	15	16	17	18	19	20	21	22	8	7	6	5	4	3	2	1	31	30	29	28	27	26	25	24	23	22	21	20	19	18																						
	9	9	10	11	12	13	14	15	16	17	18	19	20	21	22	23	9	8	7	6	5	4	3	2	1	31	30	29	28	27	26	25	24	23	22	21	20	19	18																					
	10	10	11	12	13	14	15	16	17	18	19	20	21	22	23	24	10	9	8	7	6	5	4	3	2	1	31	30	29	28	27	26	25	24	23	22	21	20	19	18																				
	11	11	12	13	14	15	16	17	18	19	20	21	22	23	24	25	11	10	9	8	7	6	5	4	3	2	1	31	30	29	28	27	26	25	24	23	22	21	20	19	18																			
	12	12	13	14	15	16	17	18	19	20	21	22	23	24	25	26	12	11	10	9	8	7	6	5	4	3	2	1	31	30	29	28	27	26	25	24	23	22	21	20	19	18																		
	13	13	14	15	16	17	18	19	20	21	22	23	24	25	26	27	13	12	11	10	9	8	7	6	5	4	3	2	1	31	30	29	28	27	26	25	24	23	22	21	20	19	18																	
	14	14	15	16	17	18	19	20	21	22	23	24	25	26	27	28	14	13	12	11	10	9	8	7	6	5	4	3	2	1	31	30	29	28	27	26	25	24	23	22	21	20	19	18																
	15	15	16	17	18	19	20	21	22	23	24	25	26	27	28	29	15	14	13	12	11	10	9	8	7	6	5	4	3	2	1	31	30	29	28	27	26	25	24	23	22	21	20	19	18															
	16	16	17	18	19	20	21	22	23	24	25	26	27	28	29	30	16	15	14	13	12	11	10	9	8	7	6	5	4	3	2	1	31	30	29	28	27	26	25	24	23	22	21	20	19	18														
	17	17	18	19	20	21	22	23	24	25	26	27	28	29	30	31	17	16	15	14	13	12	11	10	9	8	7	6	5	4	3	2	1	31	30	29	28	27	26	25	24	23	22	21	20	19	18													
	18	18	19	20	21	22	23	24	25	26	27	28	29	30	31	1	18	17	16	15	14	13	12	11	10	9	8	7	6	5	4	3	2	1	31	30	29	28	27	26	25	24	23	22	21	20	19	18												
	19	19	20	21	22	23	24	25	26	27	28	29	30	31	1	2	19	18	17	16	15	14	13	12	11	10	9	8	7	6	5	4	3	2	1	31	30	29	28	27	26	25	24	23	22	21	20	19	18											
	20	20	21	22	23	24	25	26	27	28	29	30	31	1	2	3	20	19	18	17	16	15	14	13	12	11	10	9	8	7	6	5	4	3	2	1	31	30	29	28	27	26	25	24	23	22	21	20	19	18										
	21	21	22	23	24	25	26	27	28	29	30	31	1	2	3	4	21	20	19	18	17	16	15	14	13	12	11	10	9	8	7	6	5	4	3	2	1	31	30	29	28	27	26	25	24	23	22	21	20	19	18									
	22	22	23	24	25	26	27	28	29	30	31	1	2	3	4	5	22	21	20	19	18	17	16	15	14	13	12	11	10	9	8	7	6	5	4	3	2	1	31	30	29	28	27	26	25	24	23	22	21	20	19	18								
	23	23	24	25	26	27	28	29	30	31	1	2	3	4	5	6	23	22	21	20	19	18	17	16	15	14	13	12	11	10	9	8	7	6	5	4	3	2	1	31	30	29	28	27	26	25	24	23	22	21	20	19	18							
	24	24	25	26	27	28	29	30	31	1	2	3	4	5	6	7	24	23	22	21	20	19	18	17	16	15	14	13	12	11	10	9	8	7	6	5	4	3	2	1	31	30	29	28	27	26	25	24	23	22	21	20	19	18						
	25	25	26	27	28	29	30	31	1	2	3	4	5	6	7	8	25	24	23	22	21	20	19	18	17	16	15	14	13	12	11	10	9	8	7	6	5	4	3	2	1	31	30	29	28	27	26	25	24	23	22	21	20	19	18					
	26	26	27	28	29	30	31	1	2	3	4	5	6	7	8	9	26	25	24	23	22	21	20	19	18	17	16	15	14	13	12	11	10	9	8	7	6	5	4	3	2	1	31	30	29	28	27	26	25	24	23	22	21	20	19	18				
	27	27	28	29	30	31	1	2	3	4	5	6	7	8	9	10	27	26	25	24	23	22	21	20	19	18	17	16	15	14	13	12	11	10	9	8	7	6	5	4	3	2	1	31	30	29	28	27	26	25	24	23	22	21	20	19	18			
	28	28	29	30	31	1	2	3	4	5	6	7	8	9	10	11	28	27	26	25	24	23	22	21	20	19	18	17	16	15	14	13	12	11	10	9	8	7	6	5	4	3	2	1	31	30	29	28	27	26	25	24	23	22	21	20	19	18		
	29	29	30	31	1	2	3	4	5	6	7	8	9	10	11	12	29	28	27	26	25	24	23	22	21	20	19	18	17	16	15	14	13	12	11	10	9	8	7	6	5	4	3	2	1	31	30	29	28	27	26	25	24	23	22	21	20	19	18	
	30	30	31	1	2	3	4	5	6	7	8	9	10	11	12	13	30	29	28	27	26	25	24	23	22	21	20	19	18	17	16	15	14	13	12	11	10	9	8	7	6	5	4	3	2	1	31	30	29	28	27	26	25	24	23	22	21	20	19	18
	31	31	1	2	3	4	5	6	7	8	9	10	11	12	13	14	31	30	29	28	27	26	25	24	23	22	21	20	19	18	17	16	15	14	13	12	11	10	9	8	7	6	5	4	3	2	1	31	30	29	28	27	26	25	24	23	22	21	20	19

The geometry of the scatter mask is defined by a series of surfaces. Namely, there are a

set of equidistant planes containing the z-axis. The geometry can be approximated by a set of discrete cells, with four of the boundaries of each cell defined by a pair of adjacent planes and a pair of adjacent cones. The innermost cylinder (the detector volume) and the cylinder with radius specified by *Figure 2* form the final two faces required to close each cell. *Figure 3* shows the RSM mask geometry.

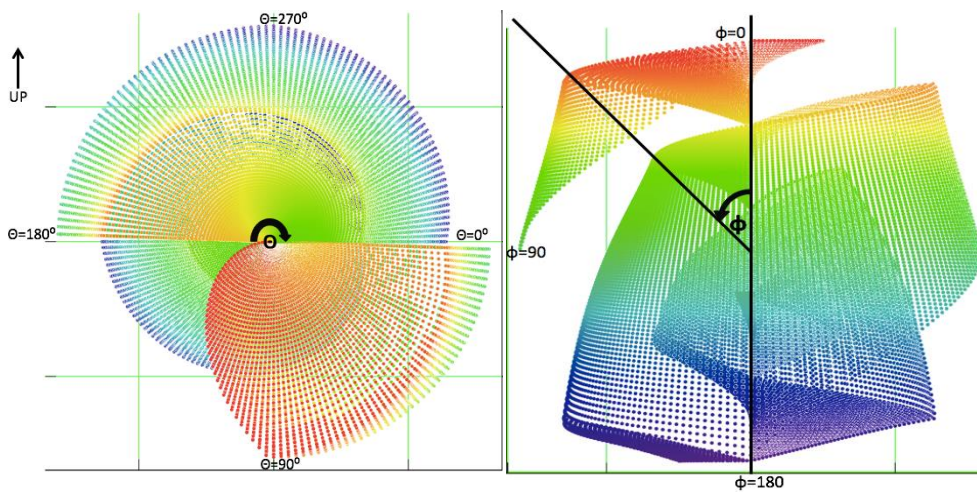


Figure 3. Scatter mask geometry. This particular geometry results in a unique detector response for each (θ, ϕ) source position relative to the detector [14].

The detector is nested within this scattering mask as shown in *Figure 4*. Thus, the radiation that reaches the detector must pass through the rotating mask material to reach the detector volume. This image also shows additional requisite components within the RSM imaging assembly. These include the base and the motor to allow mask rotation of 360° in the azimuthal angle θ about the detector.

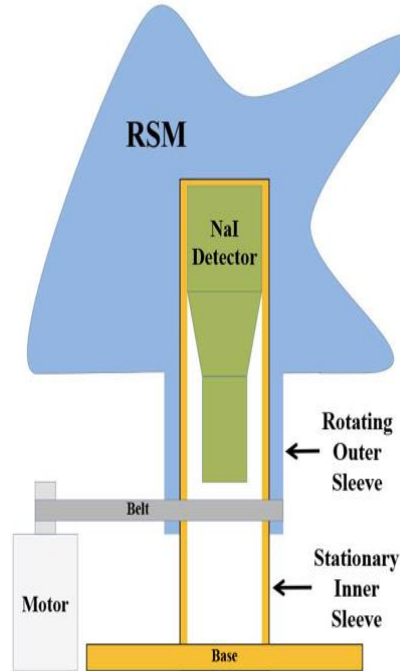


Figure 4. Detector/ scatter mask assembly. The detector is nested within the scatter mask to allow rotation of the mask to impact the detected radiation signal. This image shows the entirety of the RSM imaging assembly. Only the mask, detector volume, and sleeve are modeled within the simulations considered here [14].

1.7 Research Contributions

This proof-of-principle for the Gamma RSM Detection System is a result of unique, original work from the author, system design origination by Jack FitzGerald [14], contributions from a collaborator (Dr. Darren Holland), and initial experimental work by a previous researcher (Maj Christopher Charles). This design had its origin in the work of FitzGerald. Holland conducted MCNP6 simulations of the Gamma RSM Detection System for comparison against GEANT4 simulations. Charles is responsible for the design and construction of the polymethacrylate RSM used in this experiment. Some of Charles' data sets are used in this research. The primary researcher's contributions to the development of the gamma RSM

detection system include:

- Significant expansion of the number of experimental data sets
- Modeling and simulation of the gamma RSM detection system in GEANT4
- Comparison of the GEANT4 simulation results with Holland's MCNP6 simulation
- Synthesis and analysis of the data, and comparison of experimental and simulated data to provide a proof-of-principle algorithm that accomplishes the goal of the gamma RSM detection system as an imaging device

II. Theory

2.1 Gamma Interactions with Matter

Photons interact with matter via three primary mechanisms: the Photoelectric Effect, Compton Scatter, and Pair Production. The reaction cross sections for each interaction mechanism depend on the photon energy and material characteristics. This cross section can be represented by a microscopic or macroscopic cross section, both of which quantify the probability of interaction [19].

The microscopic cross section is in units of length squared and represents the likelihood of interaction of a photon of stated energy with the particular atom. This is composed of the sum of each of the cross sections for each of the particular types of interaction mechanism detailed previously. Generally, low energy photons with energies up to several hundred keV predominantly interact via photoelectric absorption, intermediate energy photons via Compton scatter, and high energy photons, above 5-10 MeV, via pair production (which technically has a threshold and non-zero probability for only photons above 1.02 MeV). Photon interactions also demonstrate a dependence on the atomic number of the material. For a given photon energy, the photoelectric absorption increases proportionally to $\sim Z^{7/2}$, scatter increases proportionally to Z , and pair production increases as Z^2 . Thus, if one seeks to maximize absorption, one would choose a low energy photon source and high Z material and if one seeks to maximize scatter, one would choose a mid-energy photon source and low Z material [19].

The macroscopic cross section is in units of inverse length and quantifies the probability

of interaction per unit distance that the photon traverses through the material. It is equal to the product of the microscopic cross section and the number density of the material. The inverse of this quantity is the mean free path and is defined as the average distance in a material that a photon will navigate before interacting in the material [19].

2.2 Neutral Particle Transport Methodologies

There are two primary methods to predict the transport of neutral particles through a material, both of which incorporate the concept of a macroscopic cross section discussed in the previous section. One method is deterministic and the other is stochastic. A brief review of each is given below but the stochastic approach is used in this project.

The deterministic approach involves the numerical solution to the Boltzmann balance transport equation. This equation involves all potential sources and sinks of neutral particles and, due to its complexity, requires a discretization of time, energy (multigroup), angular direction (S_h), and spatial variables to become tractable. The complexity of this method requires a simplified geometrical design and approximation of the radiation cross-sections via the use of Legendre polynomials and averaging. Even with these simplifications, the solution to this equation requires large computer power and memory. The advantage of this method is that the calculation of particle fluxes and associated reaction rates takes place throughout the geometry rather than at specified boundaries [20].

The alternative to the deterministic approach is a stochastic, or Monte-Carlo approach, which takes advantage of the probabilistic nature of particle transport, as quantified in the cross section for each particular type of interaction. For an isotropic particle source with some distribution of initial energies, a Monte-Carlo algorithm will begin by randomly selecting a

direction of travel and original energy (taking into account the likelihood of each initial energy, as defined by the probability density function (PDF)) of the incident particle. From there, the particle continues transport in this direction until the algorithm, taking into account the cross section for each type of reaction, randomly determines which reaction occurs and at what location. If this is a scattering reaction, a new particle energy and direction are randomly sampled and particle transport proceeds. This process repeats until the particle passes beneath a threshold for transport, is purposefully killed by the code developer, or passes out of the world defined for the problem. Secondary particles formed through any of the reactions that the initial particle undergoes are tracked in the same manner. This technique is very dependent on the underlying physics models used, which describe particle properties, potential interactions, and the associated cross sections [20].

2.3 Photon Detection

Photon detection requires that the photon interact with a material to produce a measureable result. As described previously, the three main mechanisms by which photons do this are Photoelectric Absorption, Compton Scatter, and Pair Production. The first two mechanisms involve the incident photon transmitting all (Photoelectric Effect) or part (Compton scatter) of its energy to an electron in the absorbing material. These electrons will subsequently lose energy through interactions with the surrounding material via ionizations and excitations and, to a much lesser extent, bremsstrahlung emission.

A photon incident on a detector may deposit all, none, or some fraction of its energy within the detector volume. Regardless of the interaction mechanisms, if all of the incident photon energy deposits in the detector, the result is a contribution to the full energy peak (FEP).

If many identical gammas deposit all of their energy in a detector, they will not necessarily produce identical signals from the detector. The stochastic nature of energy deposition and characteristics of the detector will result in some spread or variance in the produced signal. Further, some fraction of the initial photon's energy may escape the detector, which greatly depends on the composition and geometry of the detector. Any escape of energy results in a pulse that falls beneath the FEP in the energy spectrum collected.

If the detector is insufficiently large and some gamma-ray photons escape, retaining some of their energy, the detector response will consist of the Compton continuum and the FEP. This Compton continuum exists since the sharing of energy between the scattered photon and the recoil electron is a statistical process. If the scattered photon escapes, only the electron deposits its energy in the detector and the Compton continuum results. The full-energy peak (FEP), also known as a photopeak, occurs when the incident photon transfers all of its energy to an electron. A photoelectric absorption leads to full energy deposition because there is no scattered gamma-ray photon free to escape and reduce the energy deposition. One measure of the detector quality is the photofraction, defined as the ratio of the energy under the full-energy peak to the area under the entire response function. Thus, it is equal to the likelihood, given that a gamma ray has deposited some energy within the detector, that it deposits all of its energy in the detector [19].

A 3" x 3" Sodium Iodide Thallium-Activated, NaI(Tl), scintillation detector was selected for the Gamma RSM Detection System because it is well suited for the desired application. First, the large atomic number of Iodine ($Z = 53$) increases the probability of photoelectric absorption relative to the other interaction mechanisms of gamma-ray photons. Secondly, the material is relatively dense (3.67 g/cc) which leads to larger macroscopic cross sections and, as a result, larger intrinsic efficiency. This allows use of detectors of smaller dimensions. Third, this

scintillating material has adequate energy resolution over a broad range of energies of interest. Fourth, NaI(Tl) has a large light output, producing a strong signal. Finally, NaI detectors are inexpensive. Overall, NaI's large intrinsic efficiency, sufficient resolution, large photo-fraction, and low cost make it an ideal selection for the detector employed in this proof-of-principle imaging system [19].

It should be noted that, within the context of the RSM system, incident photons may forward scatter in the mask and deposit their remaining energy within the detector. As such, these photons could contribute to any facet of the energy spectrum due to the moderate resolution of the detector. Namely, these scattered photons could contribute to the FEP, the energy gap between the FEP and the Compton edge, or the Compton continuum.

2.4 Inorganic Scintillation Spectroscopy

A NaI scintillation detector operates in the following manner. First, the incident radiation deposits energy within the scintillating NaI(Tl) crystal, which produces visible light photons. These photons then strike a photocathode, resulting in the emission of electrons via the photoelectric effect. These electrons then pass through a photomultiplier tube, in which repeated accelerations and bombardment of dynodes causes them to multiply in number via secondary electron emission. This amplified electrical signal is subsequently detected [19].

The operation of this detection scheme is dependent upon the electronic band structure of the NaI(Tl) crystal; consisting of a valance band, band gap, and conduction band. This structure is present due to the delocalized molecular bonding of the crystal, in which the sodium and iodine electron orbitals combine to form the valance and conduction bands. These bands are

analogous to the covalent bonding and antibonding orbitals, respectively. Additionally, there are electronic levels in the forbidden band gap at the Tl impurity activation sites. Particularly, there is an activator excited state beneath the conduction band and an activator ground state above the valence band. As highlighted previously, when an incident gamma ray interacts in a material via the photoelectric and Compton interactions, high energy electrons are produced. These electrons (delta rays) go on to excite and ionize many atoms, create many lower energy electrons. Most of these will dissipate their energy as heat, but some will have the correct amount of energy to be excited into the conduction band, leaving a hole behind in the valence band. Through this process, a single incident gamma ray will produce a large number of electron-hole pairs in the crystal. The electrons in the conduction band can traverse the crystal, but cannot immediately de-excite to the valence band due to the forbidden (quantum mechanically very unlikely) nature of this transition. Instead, they will find the lowest energy state that is available to them, the activation site excited state. This transition releases thermal energy. The hole part of the electron-hole pair quickly transitions to an impurity activation site. Here, an electron from the ground state of the activator atom will fill this hole in the lower-energy valence band of the bulk crystal, releasing thermal energy as it does so. This leaves the impurity atom in an excited state, with a hole in its ground state. These two processes have produced an activator atom with an electron in its excited state and a hole in its ground state. The electron then de-excites in this transition that is not quantum mechanically forbidden, emitting a scintillation photon of energy equal to the difference between the activator energy levels [33].

As the impetus for this process, the incident gamma photon can interact via the photoelectric effect, through which it transfers its entire energy (less ionization potential) to an atomic electron it frees from the atom, or through Compton scatter. Compton scattering results in

electrons and scattered gamma rays, each with a spectrum of energies, given by **Equation 1**, where E_{e_-} and E_γ are the energies of the scattered quantum and electron and E_o is the energy of the incident gamma ray [19].

$$E_{e_-} = E_o - \frac{E_o}{1 + \frac{E_o}{m_{e_-}c^2} * (1 - \cos(\theta))} \quad (1)$$

Thus, as the angle between the direction of the primary and scattered photon θ increases, the electron energy increases as well, reaching a maximum when the gamma ray is perfectly back-scattered at 180°.

The relative contribution of photoelectric and Compton interactions for a given material varies with incident gamma energy. The photoelectric effect generally dominates for energies up to a few 100 keV and is more prevalent for higher Z materials, while Compton scattering and later Pair Production dominate at higher energies. Note that the analysis omits pair production since incident gammas (662 keV) used in this experiment and simulation effort do not meet the energy threshold requirement for pair production [19]. The ratio of the probability of Compton (incoherent) scatter to Photoelectric interaction for the ^{137}Cs gammas of 662 keV used in this effort is 7.6545:1 in the scintillating NaI material and 10,916:1 for the experimental polymethacrylate RSM material. **Figure 5** demonstrates the contributions of different interaction mechanisms to the total mass attenuation coefficient of gammas in NaI as a function of gamma energy. **Figure 6** demonstrates the contributions of different interaction mechanisms to the total mass attenuation coefficient of gammas in polymethacrylate as a function of gamma energy.

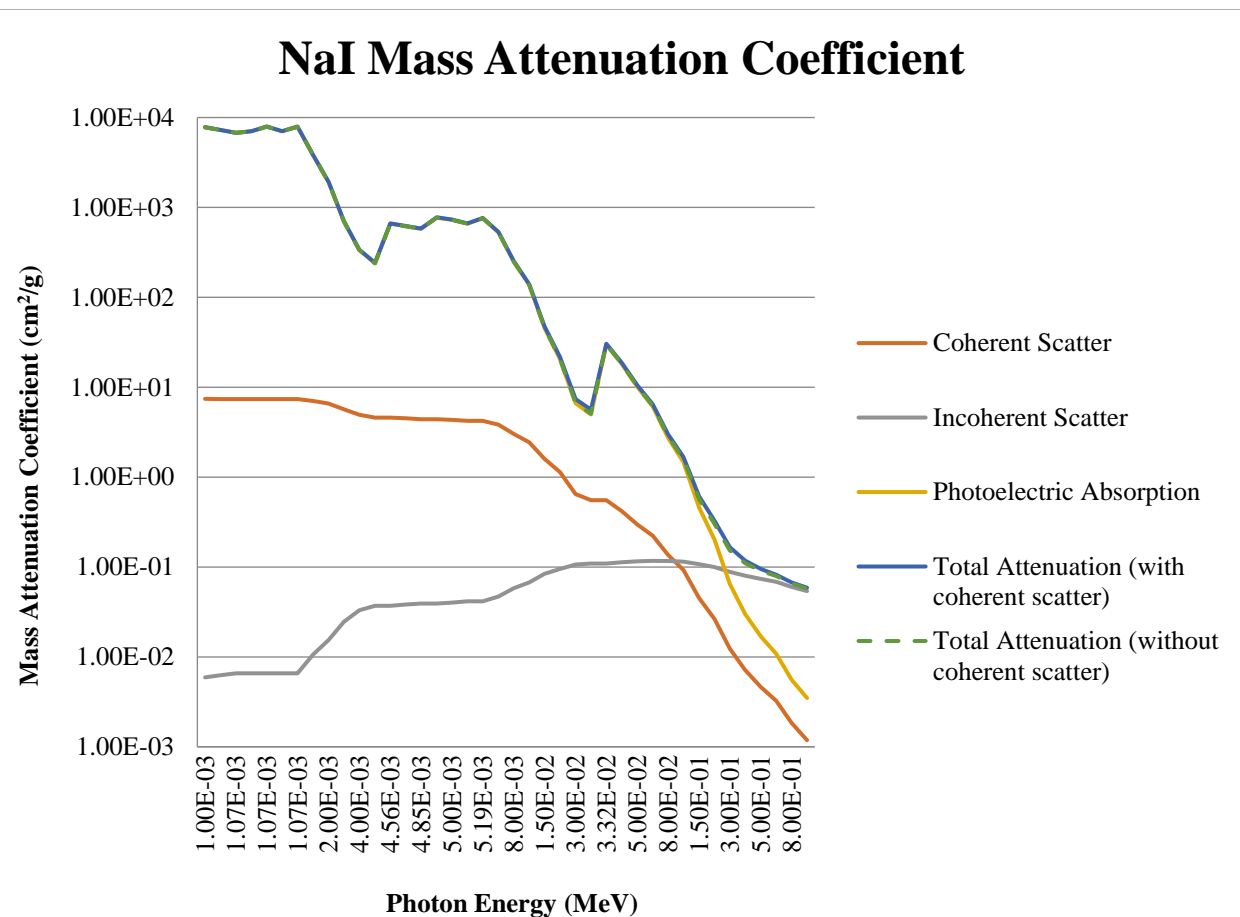


Figure 5. Contributions of different interaction mechanism to the mass attenuation coefficient of gamma rays within a scintillating NaI detector, as a function of gamma ray energy [21].

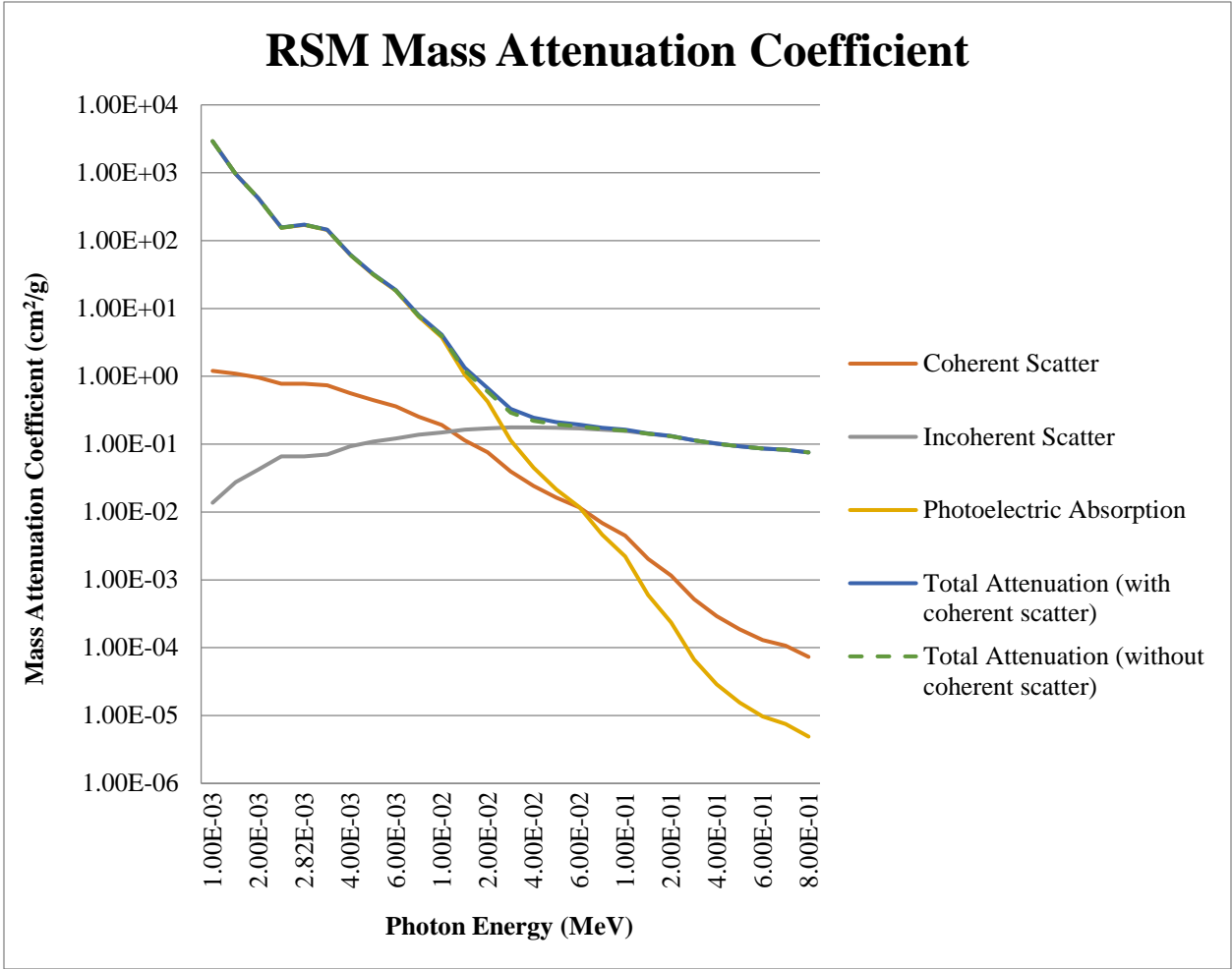


Figure 6. Contributions of different interaction mechanism to the mass attenuation coefficient of gamma rays within the experimental polymethacrylate RSM material, as a function of gamma ray energy [21].

Given the above discussion on interactions, it is now possible to predict the spectral features present for 662 keV photons incident on a NaI detector. Analysis of the energy deposited within the NaI detector for a monoenergetic source of gamma rays, including only the first interaction of the gamma ray in the energy deposited, would result in a single spike in the energy spectrum at the full incident energy (FEP) associated with a photoelectric interaction and a continuum at lower energies associated with Compton scatter interactions. As shown in *Figure 7*, this ideal spectrum is broadened in a Gaussian manner due to fluctuations of light output in the

phosphor and the statistical nature of processes occurring in the electron multiplication, which constitutes the output signal of the detector [19].

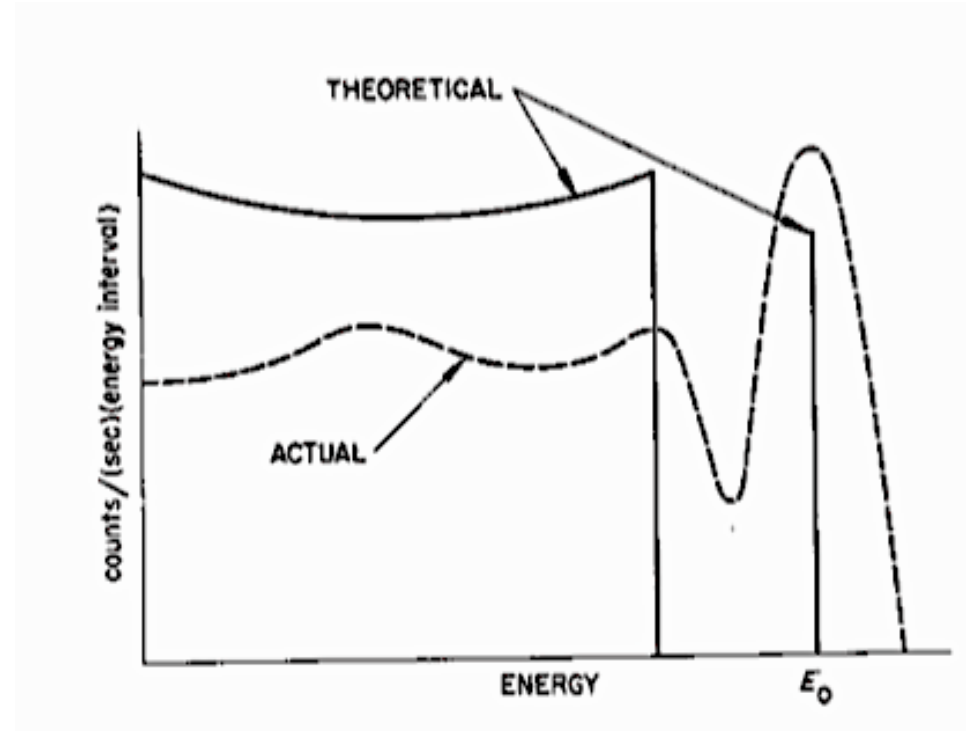


Figure 7. Comparison between the ideal energy spectrum of a detector and realized energy spectrum from a realistic detector with imperfect energy resolution resulting in Gaussian broadening to the measured energy detected [19].

Particularly, there exists statistical uncertainty, and thus random fluctuations, in the following basic steps in the scintillation process.

1. Efficiency of the conversion of the kinetic energy of primary electrons created through a photoelectric interaction into light
2. Efficiency of photons arriving to the photocathode
3. Efficiency of conversion of photons to photoelectrons at the photocathode

4. Efficiency of directing these photoelectrons to the first secondary-emitting dynode

5. Degree of electron multiplication in the dynode series [19]

There is also statistical uncertainty related to instrumental variables including the finite width of the pulse-height channels in the pulse analyzer, noise modulation, variation in the zero voltage reference in the analyzer, gain in the electronic pulse amplifier, or ramp slope in the analogue-to-digital converter of the analyzer [19].

Although probabilistic fluctuations in the conversion of incident gamma energy to an indicative output signal broaden the FEP, the photopeak associated with total gamma energy lost in the detector serves as a distinguishing characteristic of all energy spectra. The width of this peak is a property of the detector used and is an indicator of the resolution of the detector. A gamma ray could contribute to this full energy peak in two ways. The first is an initial photoelectric interaction followed by interactions of the electron. The second is an initial Compton scatter, followed by subsequent Compton scatters, and ending with a photoelectric interaction, the probability of which increases as the gamma loses energy through Compton scattering events. In both cases, no photons or electrons escape from the scintillating volume [19].

A number of observed spectroscopic phenomena are notable. Imperfect conversion of incident gamma energy to photons, which are then converted to the output signal, lead to these phenomena. These are detailed below:

1. Compton Edge

The Compton edge is the sharp cutoff in the Compton continuum that represents the

maximum energy transferable to an electron in a Compton scatter interaction of a gamma ray. In this process, the gamma possibly backscatters at 180° and escapes the detector without further interaction. Only the energy transferred to the electron deposits in the detector. Using Equation 1 and a ^{137}Cs source, we expect the Compton edge to appear at 478 keV:

$$E_{e-} = 662 \text{ keV} - \frac{662 \text{ keV}}{1 + \frac{662 \text{ keV}}{511 \text{ keV}} * (1 - \cos(180^\circ))} = 478 \text{ keV} \quad (2)$$

2. X-Ray Escape Peak

Following a photoelectric interaction, Auger electrons or characteristic X-rays are emitted from the excited atom. If this interaction occurs near the surface of the detector, the subsequent X-ray emitted when a K-shell electron de-excites in iodine may escape the detector, leading to a peak in the spectrum of energy deposited in the detector at 28 keV less than the FEP of ^{137}Cs [19].

3. Backscatter Peak

This phenomenon in the energy spectrum is a consequence of Compton scattering of gamma rays, in the material surrounding the detector, back into the detector volume. The relationship between the angle of scatter and the subsequent energy of the scattered gamma is shown in **Figure 8**. This relationship was described by Equation 2. It is clear that the final energy of the scattered photon for large scatter angles greater than about 120° is relatively insensitive to both the angle of scatter and the initial energy of the photon. Thus, backscattered photons all have approximately the same energy and contribute to a specific peak in the spectrum of energy deposited within the detector. The larger the photoelectron cross section of gammas in

the surrounding material, the smaller this peak will be due to the reduced likelihood of a Compton scatter in the surroundings resulting in backscatter of the photon back into the detector volume [19]. This phenomenon is of particular note in the RSM design due to the fact that the detector is couched within the RSM, providing polymethacrylate scattering material directly behind the detector.

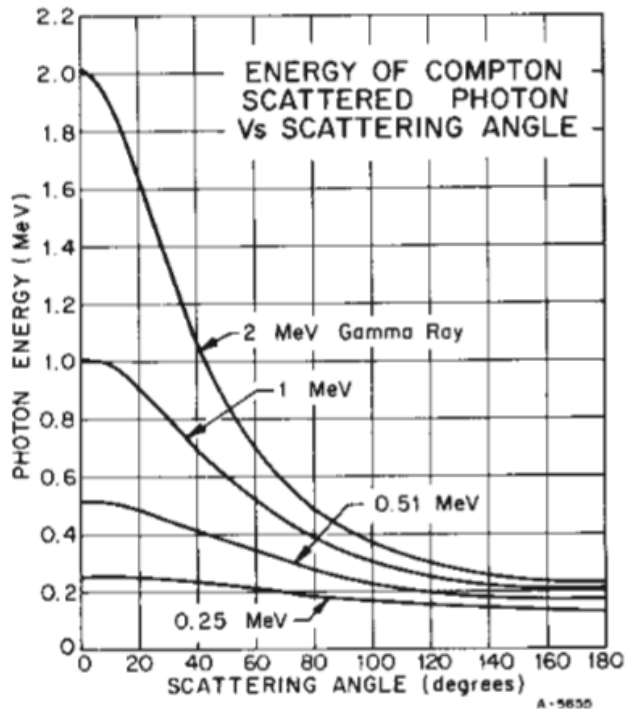


Figure 8. Angle of gamma deflection in a Compton scattering event as a function of initial energy. This chart demonstrates that, photons undergoing large angle Compton scatters ($> 120^\circ$) all have approximately the same energy, despite differences in initial energy [19].

4. X-Ray Production in the Surrounding Material

Just as X-rays emitted from interactions occurring near the surface of the detector can escape the detector and contribute to the X-ray escape peak, X-rays can escape volumes adjacent to the detector following a gamma interaction near the surface of these volumes. This can lead

to a peak in the detector energy spectrum associated with the detection of these X-rays. This X-ray peak associated with the K-shell is 72 keV and 1.5 keV for Pb and Al, respectively [22]. Materials composed of these elements are found in the lab environment surrounding the DRC assembly and are, thus, important.

5. Coincident Gamma Rays

A coincidence occurs when two photons interact in the detector at the same time and deposit energy. In the energy spectrum, the sum of the energy deposited by the two photons will appear as a single event. [19].

The ^{137}Cs decay scheme is shown in **Figure 9**. This isotope has a half-life of 30.08 years and the total Q value of its decay is 1175.62 keV.

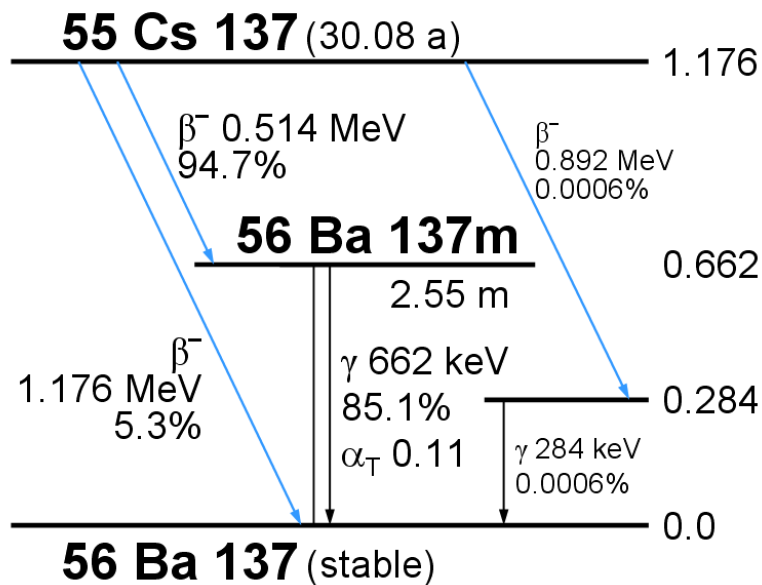


Figure 9. Decay scheme of ^{137}Cs through which the 662 keV gamma ray in this effort is produced [23]

It decays via β^- to the ground state of ^{137}Ba 5.6% of the time and to the excited state

of $^{137m}_{56}Ba$ 94.36% of the time. This β^- reaction is shown below [24].



The gammas of interest throughout the simulation are the 662 keV gammas emitted as the excited $^{137m}_{56}Ba$ relaxes to its stable ground state (*Figure 9*). This relaxation occurs 85.1% of the time. This gamma decay competes with internal conversion, whereby a nuclear deexcitation causes ejection of an electron from an atomic shell, imparting it with a kinetic energy equal to the excited energy of the nucleus less the binding energy of the emitted electron. This decay mode is favored for elements of low Z and for low energy transitions. The K and L-shell electrons are most likely to be involved due to their proximity to the nucleus. Gammas of 662 keV occur for only 85.1% of transformations, so internal conversion must occur for $94.7\% - 85.1\% = 9.6\%$ of transformations. X-rays will also originate from the rearrangement of orbital electrons in $^{137}_{56}Ba$ following an internal conversion nuclear deexcitation [23].

2.5 Statistical Comparison of Distributions

The output from the two simulations and the simulation and experimental data are compared using three statistical methodologies. This comparison delivers the critical model validation, which ensures that the simulation provides a sufficiently accurate portrayal of the system output in a real world environment. All analysis involves the comparison of distributions either as a function of energy or of mask rotation angle. First, the analysis determines whether the confidence intervals overlap for associated values in the two distributions. For this comparison, one requires the standard deviation for each value. The standard deviation is derived

in the first section. A second comparison methodology employed two non-parametric distribution-free statistical tests to assess the similarity of distributions. The theory behind these statistical tests is discussed in the second main section. A final, less rigorous, comparison methodology employed concurrent graphical representation of the data to allow subjective comparison [25].

A. Standard Deviation Derivation

A thorough analysis comparing two datasets takes into careful consideration the statistics involved in the problem. MCNP, by definition, reports the normalized standard deviation of any estimate that it calculates. GEANT4, due to the intent that the simulation tool be highly non-specific and flexible to accommodate a diverse user set, provides no such functionality. As a result, this effort has developed a sound statistical methodology to determine the uncertainty in the tallies calculated via the GEANT simulation. Each simulation run consists of N incident gammas, or events as they are termed within the GEANT lexicon. As with any valid Monte-Carlo simulation, each of the events is independent of any other event. For each incident gamma, the resulting energy deposited in the detector is counted into one of the M one keV wide bins. Thus, in referring to the results of the simulation of N incident particles, the variables in Equation 4 are utilized.

$$j = \text{number of trial} = 1 \dots N$$

$$i = \text{number of energy bin} = 1 \dots M$$

Each of the $\mathbf{j} = 1 \dots N$ independent trials:

$$x_{ij} = \begin{cases} 1 & \text{if the } i^{\text{th}} \text{ bin is hit in the } j^{\text{th}} \text{ trial} \\ 0 & \text{otherwise} \end{cases}$$

Thus, following a simulation, the output will consist of a count of the number of incident gammas that resulted in energy deposition that fell within each bin given by $x_{i1} + x_{i2} + x_{i3} + \dots + x_{iN}$, which equals the number of times that the i^{th} energy bin is hit over the N trials (events).

Due to the fact that both detection simulations are Monte-Carlo in nature and that experimental particle interactions are probabilistic, there is a particular probability that the incident gamma will result in energy deposition corresponding to bin i . This is an unknown value that is approximated via the simulation. This value is also independent of any of the other events (i.e. each incident gamma interacts in a manner that is independent of the interactions of any of the other incident particles). There is a 100% likelihood that an incident gamma will result in energy deposition that falls into one of the energy bins because the energy bins encompass the entire range of potential gamma energies. Thus, these probabilities will sum to 100%. That is,

$p_i = \text{probability the } i^{\text{th}} \text{ bin hit in the } j^{\text{th}} \text{ trial (independent of trial number } j)$

and

$$p_1 + p_2 + p_3 + \dots + p_M = 1 \text{ (completely cover the sample space).}$$

Due to the binary nature of x_{ij} , the sample consists of a set of independent Bernoulli trials, with each equivalent to a random variable defined by the $\text{Binomial}(1, p_i)$ distribution. Since the simulation populates the dataset of x_{ij} values, the value of p_i can be approximated. Given that each trial is $\text{Binomial}(1, p_i)$, it follows that the variance of each is equal to $p_i(1 - p_i)$ where

$$\hat{p}_i = \frac{x_{i1} + x_{i2} + x_{i3} + \dots + x_{iN}}{N}$$

Equation 5 shows this estimator to be an unbiased estimator (a requisite statistical property) of the probability.

$$\begin{aligned}
E[\hat{p}_i] &= E\left[\frac{x_{i1} + x_{i2} + x_{i3} + \dots + x_{iN}}{N}\right] = \frac{1}{N}(E[X_{i1}] + E[X_{i2}] + E[X_{i3}] + \dots + E[X_{iN}]) \\
&= \frac{1}{N}(p_{i1} + p_{i2} + p_{i3} + \dots + p_{iN}) = p_i
\end{aligned} \tag{5}$$

Since each of the trials is independent, the variance of the sum is equal to the sum of the variances. In calculating the variance of a constant (N) multiplied by a random variable, one is permitted to pull out the square of the constant from within the variance calculation, as done in Equation 6.

$$\begin{aligned}
Var(\hat{p}_i) &= Var\left(\frac{x_{i1} + x_{i2} + x_{i3} + \dots + x_{iN}}{N}\right) \\
&= \frac{1}{N^2}(Var[X_{i1}] + Var[X_{i2}] + Var[X_{i3}] + \dots + Var[X_{iN}]) \\
&= \frac{1}{N^2}(p_i(1 - p_i) + p_i(1 - p_i) + p_i(1 - p_i) + \dots + p_i(1 - p_i)) = \frac{1}{N}p_i(1 - p_i)
\end{aligned} \tag{6}$$

$$Stdev(\hat{p}_i) = \sqrt{Var(\hat{p}_i)} = \sqrt{\frac{1}{N}p_i(1 - p_i)}$$

Within this simulation, directional biasing serves as a variance reduction method. Section 3.4 explains the application of this variance reduction method in the GEANT simulation. This

variance reduction allows the simulation to avoid wasting resources in tracking particles that are very unlikely to interact within the detector assembly. In accomplishing this biasing, MCNP applies a weight to each of the incident particles, to approximate the fact that there were many more incident particles that were not tracked due to their small likelihood of interacting with the detector. This weight reflects a constant multiplicative value to each of the x_{ij} because of the directional biasing employed in variance reduction. This constant, C , can be handled statistically as shown in Equation 7, where $p'_i = C * p_i$. Thus, it appears in the standard deviation as a constant multiplicand of the expected value of the likelihood of energy deposition within each bin.

$$\begin{aligned}
Stdev(\widehat{p'_i}) &= \sqrt{Var(\widehat{p'_i})} \\
&= \sqrt{Var(C * p_i)} \\
&= \sqrt{\frac{C^2}{N} * p_i(1 - p_i)} \\
&= \sqrt{\frac{1}{N}(C^2 * p_i - C^2 * p_i^2)} \\
&= \sqrt{\frac{1}{N}(C * p'_i - p'^2_i)}
\end{aligned} \tag{7}$$

With this standard deviation derived in Equation 7, the confidence intervals, rather than the point estimates, that the two simulation software codes produce can be directly compared. Thus, one is permitted to go beyond the pronouncement that the two energy deposition

histograms “look similar” and vigorously compare the histograms in a statistically sound manner.

B. Non-Parametric Statistical Tests for Comparison of Distributions

If one is seeking to compare experimental data collected in two different situations, one needs a standard, numerical way of determining whether the differences in the two datasets are significant enough to conclude that the situations lead to different measured results. By definition, there will be some difference between the two distributions due to the random nature of nature and the way that this randomness is handled in the Monte Carlo simulations. Indeed, if one were to collect data from the identical experimental setup twice, the two datasets would differ to some degree. One would like a test that can determine whether the datasets could have been collected under the same circumstances or if the differences are extreme enough to conclude that the datasets were collected in two situations that differ substantially. One finds such a test in the field of statistics. Many statistical tests make assumptions regarding the underlying distribution of the datasets considered (often assuming an underlying normal distribution). If this assumption is not met, the results of these statistical tests cannot be trusted [26].

In this effort, the energy spectra obtained through the two different Monte-Carlo simulation codes must be compared to determine if the simulation code used impacts the resulting energy spectrum obtained. Additionally, the detector response curves obtained from the two codes and the experimental results must be compared in a way that makes no assumptions about the actual shape of these distributions. As a result, statistical tests that do not make the assumption of normality were chosen. These tests are called non-parametric tests and those chosen for this analysis are intended to discern the compatibility or distinguishability of two

histograms and, hence, the compatibility of flows of events according to the samples collected from them. In the energy spectra comparisons, these two flows of events represent the energy deposited in the detector volume within a MCNP or GEANT simulation or via experiment. In the detector response curve comparison, this flow of events represents the count of the full energy peak or the count within the Compton continuum for each discretized rotation angle of the mask for a given φ angle, obtained via experimentation or via the GEANT simulation.

Due to the fact that the purpose is to measure the compatibility between the two distributions, i.e. could they have been obtained from the same flow of events, the problem is reduced to a hypothesis test. In the tests considered, the null hypothesis (H_0) is that the two distributions are indistinguishable, i.e. whether the distribution is obtained via GEANT or MCNP or whether the distribution is obtained from GEANT or experimentation does not substantially effect the results obtained. The alternative hypothesis (H_1) is that the distributions do differ substantially and the situation in which they were obtained effects the distribution measured (the two flows of events are inherently dissimilar). In such a test, there is always going to be some chance that one concludes that the incorrect hypothesis is correct. The results of these tests come in the form of a value of a test statistic, which is then converted into a P-value. This P-value can be interpreted as the probability that the data would produce a more extreme P-value given that the null hypothesis is correct, the two distributions do come from indistinguishable flows of events (the distributions do not differ substantially, statistically speaking). If one obtains a small P-value, then the test statistic obtained is rare and the assumption of the null hypothesis is similarly unlikely. Thus, a small P-value indicates that one should reject the null hypothesis in favor of the alternative hypothesis, H_1 , and conclude that the two distributions do differ, statistically [26].

The two non-parametric statistical tests employed in the analysis are the Kolmogorov-Smirnow (K-S) test and the Anderson-Darling test. The Anderson-Darling is a variation of the K-S test which gives greater weight to the tails of the distribution and is generally considered to be a more sensitive test (has more power) [26]. For completion, both of these tests were employed in the comparison of distributions in this analysis. The theory behind the Kolmogorov-Smirnow (K-S) test is discussed below [25].

The cumulative distribution function (CDF) of a function is defined as

$$F_x(x) = P(X \leq x)$$

The probability density function (PDF) is defined for a continuous distribution as

$$p_x(x) dx = P(x \leq X \leq x + dx)$$

and for a discrete distribution, the PDF is given by

$$p_x(x) dx = \sum_x P(X = x) \delta(X - x)$$

From these definitions, it follows that the CDF can also be written in terms of the continuous PDF as

$$F_x(x) = \int_{-\infty}^x p_x(s) ds.$$

At the current time, in this problem, it is not feasible to derive an analytical distribution for either the energy spectra or detector response curves under consideration [25]. As such, samples are drawn either from experimentation or from Monte-Carlo simulations (GEANT and MCNP). Both methods of sampling represent independent random samples composed of N sampled points x_1, x_2, \dots, x_N .

Each draw is associated with a given mask rotation angle (θ) and energy deposited within the detector. These intervals, $\theta = 0^\circ \dots 360^\circ$ and $E = 0 \text{ keV} \dots 662 \text{ keV}$, which are

discretized in intervals of 5^o and 1 keV , have a subinterval width defined by the constant W . If one represents each subinterval as I_i , one can define the characteristic function $\chi(x, I_i)$ as shown in Equation 8.

$$\chi(x, I_i) = \begin{cases} 1, & \text{if } x \in I_i \\ 0, & \text{otherwise} \end{cases} \quad (8)$$

With this binning of the data in place, one can define the histogram found in Equation 9, which is an approximation for the PDF $p_x(x) dx$. It represents the number of samples residing in bin I_i , which must be subsequently normalized by the number of incident particles, N , and width of each bin, W , in order for it to have all of the properties inherent to a continuous PDF.

$$h_x(I_i) = \frac{1}{W} * \frac{1}{N} \sum_{j=1}^N \chi(x_j, I_i) \quad (9)$$

Equation 9 can be interpreted as the average density function of the sampled points in interval I_i . When the number of bins approaches infinity, the width of each W reduces to zero. When each interval approaches a point, h_x approaches p_x , the associated continuous probability density function. Due to the fact that the widths used in this problem are sufficiently narrow (the numbers of discretized energy and angle bins are sufficiently large), the approximation of p_x with h_x is valid.

Thus, the approximation to the CDF, the empirical distribution function given in Equation 10 is a valid approximation of $F_x(x)$, where M is the total number of bins utilized in the discretization.

$$F_x(x) = \sum_{i=1}^M h_x(I_i) \quad (10)$$

The validity of this approximation is critical to the comparison methodology, the Kolmogorov distance, utilized in comparing the datasets obtained from the experimental and simulation efforts.

For systems with a bistable distribution, such as the energy spectra and detector response curves concerning which this thesis focuses, it does not make logical sense to compare the means and standard deviations of the distributions. Rather than comparing certain parameters of the distributions, one seeks to compare the entire distribution over its entire range. One methodology for doing so, defined in information theory, is the Kolmogorov distance [26].

For two random variables X and Y , with associated CDFs F_x and F_y the Kolmogorov distance is defined in Equation 11.

$$K(X, Y) = \max_{-\infty < x < \infty} |F_x(x) - F_y(x)| \quad (11)$$

Thus, this distance will compare the entire scope of each distribution over the entire range of each. It is a function distance (comparing the two CDFs) rather than a variable distance. It has the properties of being independent of scale and bounded above by 1 [26].

$$\text{Scaling Property: } K(\lambda X, \lambda Y) = K(X, Y)$$

$$\text{Bound Property: } K(X, Y) \leq 1$$

This Kolmogorov distance is utilized in the Kolmogorov-Smirnov Test. This test is employed to compare two distributions with the null hypothesis being

$$H_0 = U(x) = V(x)$$

which states that two samples of data have indistinguishable empirical distribution functions given by $U(x)$ and $V(x)$. It was shown through the use of Equation 9 that, in the cases considered in this thesis, these two empirical distribution functions are valid approximations to

the associated underlying CDFs. This was the case because the number of discretized bins used in each case, M and N , were sufficiently large. Smirnov proved that, when this property holds true,

$$S_{MN} = \sqrt{\frac{MN}{M + N}} K_{M,N}(X, Y)$$

has a limiting distribution given by

$$\phi(\lambda) = \sum_{k=-\infty}^{+\infty} (-1)^k e^{-2k^2\lambda^2}$$

The value of this statistic is tabulated and, for a given probability tolerance, one can determine whether the obtained S_{MN} is large enough to require the rejection of H_0 . If this is not the case, H_0 is accepted and one may conclude that the two distributions are statistically indistinguishable [26]. One can come to this conclusion in a statistically sound fashion without making any assumptions as to the underlying distributions of the datasets involved in the comparison. The Anderson-Darling test, also employed in this effort, functions in a similar fashion, except that it uses the squared sum of differences in the CDFs, with a special weighting in order to emphasize the tails of the cumulative distribution functions.

2.6 Literature Review

There are two primary methods that can be used to transform a non-position sensitive detector into a high performance imaging system. Both of these mechanisms are referred to as indirect imaging methods since neither measures the image directly, but uses system output data paired with a mapping function in order to identify the source location relative to the detector. Both mechanisms involve the placement of a particular geometric design of material between a

radioactive source and the detector volume. In each case, the material in front of the detector is rotated, resulting in a constantly changing thickness of material that the radiation must pass through before reaching the detector. Obviously, this changes the signal detected as the mask rotates. These two mechanisms are a Rotating Modulation Collimator (RMC) and a Rotating Scatter Mask (RSM).

Kowash [2] employed the Rotating Modulation Collimator concept to solve the gamma emitting orphan source problem described previously. Boyce later employed the Kowash design to image neutron sources [15]. The overarching concept is that the mask consists of an assembly of spaced disks composed of attenuating material, which have a pattern of parallel slits that run the entire length of the mask. This assembly is mechanically coupled so the disks rotate together about a shared axis. When the assembly rotates about this axis, the projection of the front mask onto the rear mask(s) has the effect of orbiting the rear mask with respect to the source. Thus, as the projection changes, the slits appear to open and close, changing the amount of attenuation and, thus, the signal detected in a way that is unique to each source location. The major negative characteristic of employing this methodology for the gamma orphan source problem is that it has a maximum field of view of $\sim 17^\circ$, which can be increased to $\sim 35^\circ$ at the expense of modulation efficiency. This results in a detrimental effect on both the dynamic range and resolution of the RMC. The RSM would not be constrained by this narrow field of view, which increases its utility tremendously. In fact, Fitzgerald showed that the the field of view of the RSM designed to image gamma sources is 360° azimuthally and 54° above and below the horizontal plane. In section 6.2, this effort shows that the field of view is substantially better than this, approaching 4π .

Alternative imaging systems include gamma cameras and Compton cameras. Unlike the

previously highlighted IMAGING techniques, neither of these involve the rotation of a particularly designed material in front of the detector.

Gamma cameras consist of a mechanical collimator and a thallium doped NaI crystal, with an array of photomultiplier tubes (PMTs) arranged in a particular design (typically hexagonal due to its property of reducing the passive area) behind the absorbing crystal [16]. The signal obtained from each PMT allows determination of the direction from which the radiation came if the incident radiation has been collimated prior to its entry into the scintillating crystal volume. The major issue with this is that even highly sensitive collimators allow detection (and thus aid in imaging) of only ~ 0.56 cps/kBq of source activity, with 50% transparency generally considered to be optimal. This collimation constitutes throwing away over 99% of the potential information obtained from the radioactive source. To obtain the requisite data, a lengthy period of detection is required.

Compton cameras are not subject to the same dependence on collimation [17]. They consist of two detectors that act in coincidence. The first detector records the Compton scatter of a photon and the second detector absorbs that same photon. Thus, given knowledge of the location and energy deposition of both interactions, direct computational methods using the deterministic relationship in Equation 1 can calculate a cone from which the gamma ray must have been emitted. When combined, the intersection of these cones allows one to locate the source position [17].

III. Simulation

3.1 GEANT4 Software

GEANT4 is an application of the Monte Carlo particle transport methodology detailed in Section 2.2, through which the numerous discretizations involved in an analytical deterministic, method can be avoided by taking advantage of the probabilistic nature of the cross sections underlying particle transport. This software package, designed by the European Organization for Nuclear Research (CERN), is written in C++ and thus employs the modern object oriented coding paradigm [18]. GEANT4 simulates a physical system through the implementation of code which defines the particle source, the geometry, the physics processes, and the desired output (written data and visualization). Each particle type has a list of processes that apply to it and these processes can be broadly binned into those that occur along the step, at rest, and following the step; where a step is truncated whenever a particle undergoes an interaction or enters a new volume in the geometry. GEANT4 provides the user with tremendous freedom of choice in developing each of the major inputs to a GEANT4 program. The program provides the user with the ability to retrieve all relevant information about the status of all primary and secondary particles at any point in their transit through the geometry. This level of control gives the developer the unique ability to determine precisely what is occurring in the simulation and draw conclusion about real world situations.

An application in GEANT4 is controlled through the implementation of the *RunManager* class, to which one is required to register the initialization classes and the user action classes.

This run manager controls the flow of the program and manages the event loop(s) within a run. These required classes are implemented by the user as concrete classes, which inherit from the associated abstract GEANT4 class. Two of these, the *UserDetectorConstruction* and *UserPhysicsList*, are initialization classes and the third, *UserPrimaryGeneratorAction*, is a user action class. Though these are, strictly speaking, the only required classes, this simulation required additional output information to be obtained, which was quantified and accumulated within implementations of the *EventAction*, *SteppingAction*, and *RunAction* classes. Individual interaction level information was accessed within the *SteppingAction* class and accumulated within the *EventAction* and *RunAction* classes. A step within GEANT4 is an object (as is everything else) and it contains transient information about a given particle. The endpoint of a step is defined by either the next interaction of the particle or its transport across a volume boundary. This step class contains, for both the pre-step point and post-step point, a plethora of information about the particle status and interaction occurring at that point in space. This includes (but is not limited to) the position (and associated volume and material), the momentum (and direction), the energy, and the polarization [18].

3.2 Application Developed

In accordance with the discussion in Section 3.1, a GEANT4 application representing the detector, scattering mask, and source assembly found in the actual lab environment was developed. As stated above, GEANT4 is inherently an objection-oriented application and is written by the user in C++. This means that the user defines all requisite information for the simulation though the development of classes (.cc and the associated .hh files). A class is a template or blueprint that describes the behavior and state that the object created from it can

support. Thus, one creates objects using the class definitions. These objects, instantiated from the defined classes, have associated fields (state variables) and methods (actions which can be performed on the object to change its state).

The first major input implemented in this GEANT simulation consisted of the geometrical definition. In accomplishing this, first the materials composing the assembly (atomic composition and density) were defined. These constitute the air, forming the background for the geometry, the plexiglass (approximation to polymethacrylate) making up the RSM, the aluminum alloy forming the detector sleeve, and the scintillating NaI forming the active volume of the detector. Next, these defined materials were employed in the definition of the volumes representing their relative positions within the lab setting. The construction of the scattering mask, with its extremely complicated geometrical design, proved a nontrivial task to implement within GEANT4. Initially, a geometrical element called a polycone was employed to accomplish this feat. Despite the fact that, by specifying the inner and outer radius at each level along the axis of a conical shape, a geometrical approximation to the geometry could be obtained, all curvature could not be exactly mimicked and a more exact methodology was sought. This was achieved through the utilization of a CAD file, predefined to contain the geometrical description of the scattering mask. This file, represented in the STL (stereolithography) file format, consists of triangles in space defined by a unit normal vector and three points. This required translation into individual tetrahedra which can approximate the volume required, through the use of a meshing algorithm. GEANT4 has a direct CAD model import interface known as CADMesh, but, unfortunately, the meshing algorithms which underlie this importing mechanism were not sophisticated enough to handle the complicated geometry of the scattering mask and, as such, returned degenerate tetrahedra when a meshing attempt was made.

A solution to this problem was found in the program called Attila, which is actually a finite element S_n deterministic solution to particle transport. Its utility to this project lies in the fact that, in its first step, it produces a mesh of tetrahedra from an STL file and its underlying algorithm for doing so is sophisticated enough to correctly mesh the complicated scattering mask geometry. The output generated from this successful meshing consisted of a set of 91,817 tetrahedra, each represented by 4 points in Cartesian coordinate space. This data was then employed to define a geometrical element in GEANT4. Due to the very long computational times associated with treating each tetrahedron as a completely distinct geometrical volume element, the GEANT concept of an assembly volume was employed. This volume acts as a mother volume, to which each tetrahedron is added, which dramatically increases computational efficiency. Due to the C++ implementation of GEANT4, reading in the definition of each tetrahedron was not a difficult task. Through this effort, a generalized algorithm has been developed that is capable of directly reading in any pre-meshed solid geometry to GEANT4. This algorithm could prove useful to other simulation efforts in which GEANT4's established meshing software is insufficient to handle the degree of complexity of the geometry of interest to the simulation effort.

One of the pre-defined GEANT4 physics packages was utilized in this simulation due to the fact that it incorporated all requisite reaction mechanisms for all particles relevant to this problem. This package, "FTFP_BERT_LIV", uses a Bertini-style cascade for hadronic processes and contains all standard electromagnetic processes necessary for gamma detection. The hadronic model is valid for energies less than 5 GeV, a condition which is very easily met in the system being modeled. The package used also employs a high precision transport model for neutrons with energies less than 20 MeV, beneficial if this simulation is to be used for the future

development of a neutron imaging RSM system. "FTFP_BERT_LIV" is the recommended physics package for radiation protection and shielding applications [27].

With the geometry and interaction mechanisms in place, the source was defined. In order to simulate an isotropic source without incurring the substantial increase in computational time resulting from the tracking of particles initially directed away from the detector with negligible probability of scattering back into the detector, directional biasing was employed. In doing so, a conical beam was produced, the center of which is always directed toward the origin (center of the NaI(Tl) crystal) and whose span completely encompasses the mask and detector assembly once it reaches the front of the scattering mask. More information about this variance reduction technique is contained in Section 3.4. The scattering mask has a radius of approximately 17.78 cm. As such, due to the fact that the location of the source is held to be a constant 86.36 cm away from the detector, a conical beam with a half-angle of $\theta = 17.5^\circ$ will entirely encase the detector assembly. This is shown in Section 3.4, which discusses the variance reduction technique in further detail.

The key feature of this detector retrofitting scheme lies in the rotational motion of the scattering mask about the axis parallel to the center line of the detector. The developer has two options in implementing this rotational motion, both of which represent the same relative motion of the detector and the source. The first option is to rotate the scattering mask, as occurs in the real laboratory environment. The second, more computationally efficient option, lies in moving the source in a circle centered around the origin, while maintaining the same straight-line distance to the plane containing the center of the mask and detector assembly (same Z coordinate). The later option was chosen due to its superior computational efficiency. In order to accomplish this rotational motion, one must implement a scheme to automate this rotation as

well as ensure that the conical beam is continuously directed in the proper direction, toward the origin of the coordinate system (center of the detector cylinder). GEANT4 has a native method to handle moving geometrical elements, utilizing the concept of parameterized geometry, but in this effort, the increased amount of control gained by implementing the mobility by hand was considered worth the additional effort.

This movement of the source was accomplished entirely within the *main() method*, inherent to any C++ program. This is the method which is the entry point of a C++ program. Execution begins with this method and control is transferred from the operating system to the GEANT4 application. This *main() method* allows the user to specify command line arguments, detailing certain parameters of how the program should be executed. One of these arguments is utilized to specify whether the source should rotate or remain stationary. It is also within the *main() method* where one must create an instance of the run manager (which controls the flow of the program and manages the event loops within a run). The developer must then pass information about the detector construction, physics processes, and particle sources to the run manager. This is accomplished by using the run manager's set methods to initialize objects representing each of these requisite inputs to the program. As stated above, the rotation of the source was implemented within this method. For each discrete source location, a given number of incident particles were emitted in an isotropic distribution that is cut off to create a conical beam with a 17.5-degree half-angle, as detailed further in Section 3.4. As such, the rotation of the scattering mask has been automated in a GEANT4 run, to efficiently simulate the operation of the detector assembly in the laboratory setting.

3.3 Simulation Specifications

The simulation was developed in such a way as to mimic the laboratory setup as closely as possible. This was done for a twofold purpose. The first reason was that it allows validation of simulated results in comparison to real-world experimental results. This is a critical stage because it is realized that any Monte-Carlo simulation is an approximation. The underlying physics models detailed in the previous section are certainly imperfect. For this reason, substantiating simulated results with physical results is critical. Additionally, the simulation was designed to mimic experimental specifications because this ensured that there are no other unknown constraints that would hinder the implementation of the simulated setup. Due to the fact that the experimental setup is currently functional in the real world, one can be sure that the experimental setup which was simulated is feasible to be implemented within a real-world environment.

The assembly consists of three geometrical elements, which are each assumed to be of uniform elemental composition. A summary of these compositions follows. The scattering mask, which is composed of plexiglass (approximation for polymethacrylate) of density 1.19 g/cc, is constructed according to the CAD file detailing its geometrical specifications. The maximum extent of the mask in the x and y directions is 17.77 cm and 17.78 cm respectively. The maximum and minimum z coordinates are 17.86 cm and -17.7 cm. The NaI detector assembly is nested within the mask. It is composed of, approximately, 15% sodium and 85% iodine by mass fraction. It constitutes a cylinder with a radius and half-height of 3.81 cm. Surrounding this detector is an aluminum alloy sleeve, which is 0.3175 cm thick and extends behind the detector an additional 46.745 cm. The source position is maintained at a constant straight-line distance from the source to the origin of the coordinate system (which is collocated with the center of the

detector volume) of 86.36 cm. As the source is rotated, it maintains the same straight-line distance to the center of the detector and same distance perpendicular to the z axis. Thus, simple trigonometry is employed to determine the source location through a complete rotation of 360 degrees in theta until the source returns to its initial position. Again, due to the identical relative motion involved, this simulates the rotation of the scattering mask around the Z axis.

The experimental source is a ^{137}Cs isotope (662 keV gamma photons). It should be emphasized that, due to the probabilistic foundation upon which Monte-Carlo simulation is based, a large number of incident particles is required to accurately approximate the true experimental conditions in the real world. As such, a large number of incident particles are required at each position in the rotation. Analysis has been conducted to determine the number of incident particles required for the simulation output to converge to a value that is representative of the true, real-world value. This discussion of GEANT4 simulation solution statistical convergence is found in Section 5.1 and the convergence of a representative simulation energy spectrum is visualized in **Figure 13** as the number of incident particles is increased.

As highlighted in the previous section, GEANT4 allows the developer to have access to all details describing the transit of a particle through the geometry at any time when an interaction takes place or it enters a new geometrical element (the delimiters of a step in GEANT4). One can access information such as position, momentum, type of interaction, energy deposition, distance of travel between interactions, any secondary particles produced via an interaction, and much more. For this analysis, the energy deposited within the NaI detector volume per incident quantum of radiation was of critical interest. This sum could easily be tabulated through the utilization of methods that are predefined within the GEANT4 application and which were highlighted in Section 3.1.

3.4 Variance Reduction

Variance reduction constitutes the effort to reduce needless tracking of unimportant particles in a simulation, thus reducing the computational time necessary to obtain sufficient results. In this effort, direction biasing is employed in that particles initially directed away from the assembly, being unlikely to interact in volumes of interest, are automatically not tracked. To obtain the amount by which the results are biased as a result of this variance reduction technique, the percentage of the surface area of the unit sphere that is encapsulated by a cone whose apex has an angle of 2θ must be determined (θ being the half-angle defining a cone in which source particles are emitted and subsequently tracked within the simulation). The surface area of the portion of the sphere of radius R encapsulated by this cone is given by the integral in Equation 12.

$$\int_0^\theta 2\pi (R \sin\phi) * R d\phi$$

(12)

$$2\pi R^2 \cos(\theta)$$

This surface area is then divided by the entire surface area of the unit sphere, $4\pi R^2$, yielding a directional bias to the results of $\cos(\theta) / 2$. In the case of this analysis, cone half-angle of $\theta = 17.5^\circ$ is sufficient to completely encapsulate the mask/detector assembly. The mask has maximum values in each dimension of approximately 35.56 cm. Thus, the maximum dimension presented to the source could be $\sqrt{35.56^2 + 35.56^2} = 50.2894$ cm. The source is kept at 86.36 cm from the center of the detector at all times. As such, the half-angle defining the conical source must be $86.36 \text{ cm} * \sin(\theta) = \frac{50.2894}{2}$ cm. Thus, θ must be greater than or equal to

16.93° if the conical source is to completely encompass the mask/detector assembly and, thus, properly represent an isotropic source.

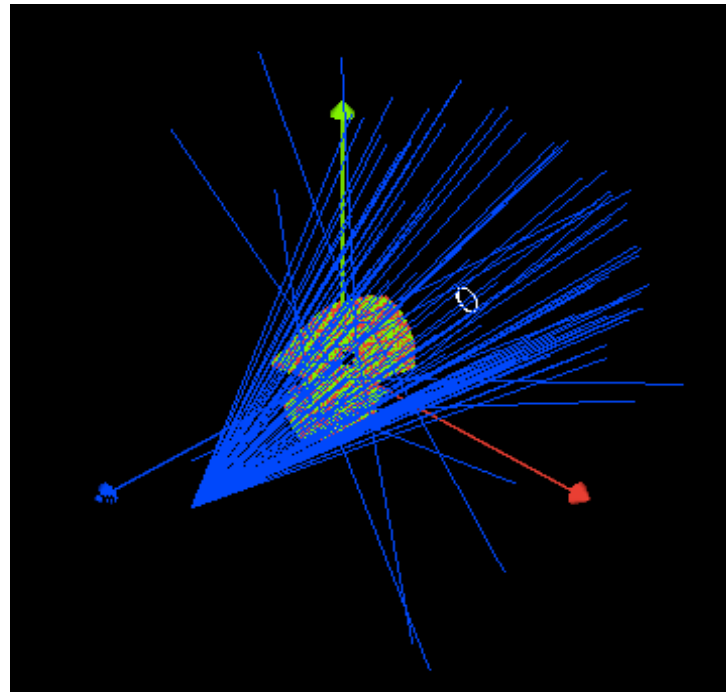


Figure 10: GEANT visualization of variance reduction employed via a conical source distribution. This cone is seen to encompass the entire RSM system and, thus, approximates an isotropic source. Photon tracks are visualized in blue with incident gammas and scattered gammas being readily apparent in this early stage of the simulation.

IV. Experiment

4.1 Gamma RSM Detection System Setup

A fully operational laboratory RSM system was developed by Major Chris Charles. A type 76B76/3M-E1-X-NEG SCIONIX HOLLAND 3" x 3" NaI(Tl) detector (serial number SFQ770) was surrounded by the polymethacrylate RSM with maximum width in each dimension of 35.56 cm. A CAEN Model NIM8304 crate held the ORTEC 556 High Voltage Power Supply, NIMBox NDA8 DAC, ORTEC 460 Delay Line Amplifier, and the ORTEC 926 ADCAM MCB. An ORTEC Pre-Amplifier was placed between the NaI(Tl) detector and the linear amplifier. The configuration is seen in *Figure 11*. Equipment settings are found in Appendix H. A 1.045 mCi ^{137}Cs (T-158) source was positioned at 86.36 cm from the center of the NaI(Tl) detector. This distance was maintained as, for each run, the source was positioned in a direction associated with each 10° increment of phi ($\varphi = 5^\circ$ to 175°). Experimental data was post-processed on a computer using the Maestro software package.

4.2 Data Acquisition

To acquire data for a given source position, the ^{137}Cs source was placed phi degrees off axis from the long axis of the detector. A typical experimental configuration is shown in *Figure 12*. Each experimental run was conducted over an interval of 24h and the results of 18 runs were utilized in this effort (increments of 10° in phi). Runs in theta variants were unnecessary because a different theta angle corresponds to a known rotation of the mask, being demonstrated by a

shift in the final detector response curve.

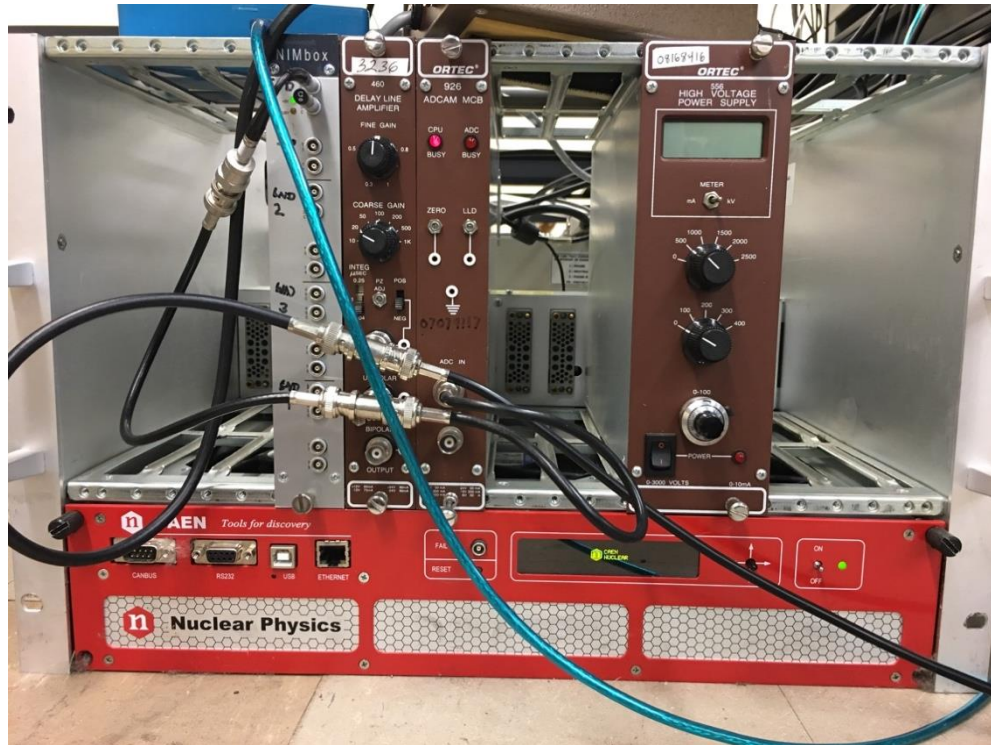


Figure 11. Components utilized in the experimental data acquisition. The settings for the voltage source, delay line amplifier, and multichannel analyzer are shown.

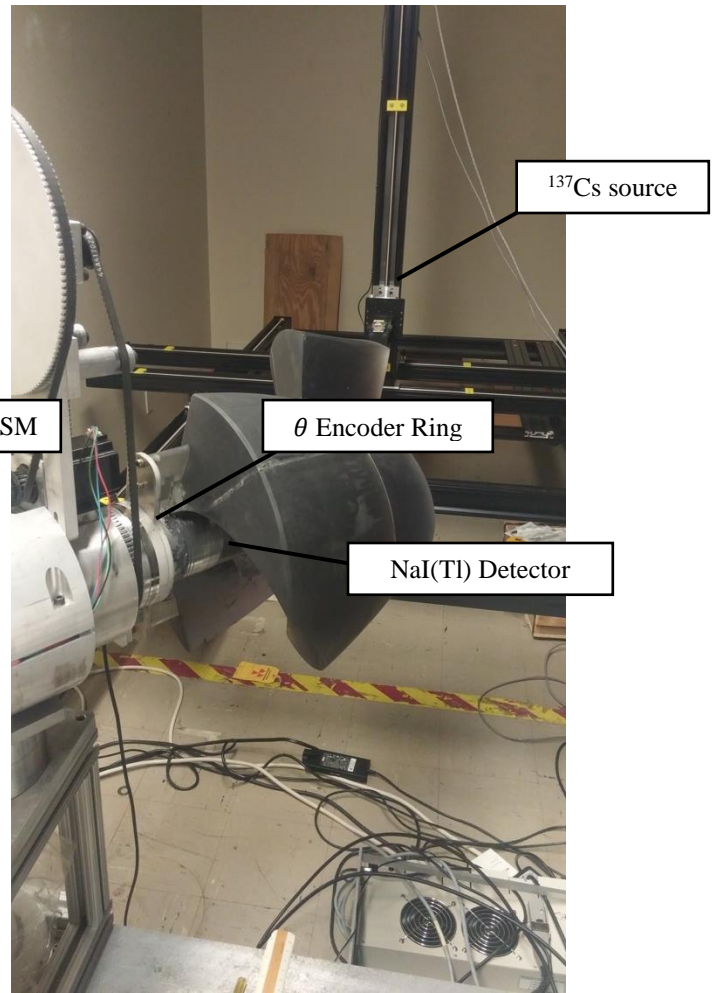
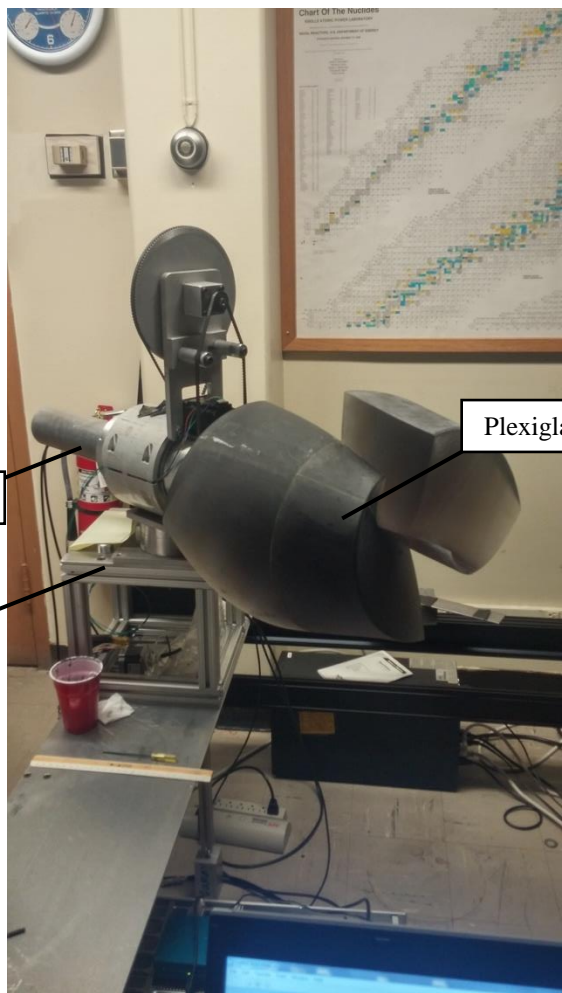


Figure 12. Experimental data acquisition setup of the RSM imaging system. The source is positioned via mechanically controlled crossbars.

V. Results and Analysis

5.1 Introduction

In previous sections, the motivation and methodology for this simulation and experimentation effort have been detailed. In summary, these simulation results are a critical stage in the development of an innovative gamma imaging system. This system consists of an ordinary scintillation detector that is nested within a scattering mask, which rotates 360° in the azimuthal angle θ . Analysis of the data acquired from the detector embedded within the rotating scattering mask provides a detector response curve (resulting from one 360° rotation of the mask in θ) which uniquely identifies the direction of the radioactive source relative to the detector assembly. The detector response curve is unique to each source direction because the geometry of the mask relative to the source changes uniquely for each source direction. As an incident photon traverses each differential unit distance in the mask, there is a probability that the photon will Compton scatter. If it does so, the photon will change direction by a certain angle, which uniquely determines its change in energy (**Equation 1**). This change in energy and angle determines the amount of energy (if any) deposited within the detector. The distribution in amount of energy deposited in the detector will depend heavily upon the mask geometry presented to the source. This provides the RSM assembly IMAGING capability. To determine the direction of the source, the experimental detector response curve must be matched against the detector response curves unique to each direction. While a surface may eventually be developed to provide all possible directions, for purposes of this proof of principle response curves are

developed for increments of theta and phi. Thus, to determine the direction of the source, the experimental detector response curve is compared against a library of response curves that describe all possible directions. This algorithm is described in detail in Section 6.1.

Since resource constraints make development of a library for all possible source energies over all possible directions impractical, simulation is employed. The simulation model must be verified and the results must be validated to ensure they are an accurate portrayal of real-world results. Sections 5.2-5.6 represent two levels of this validation effort.

To verify that the model is working properly, results from GEANT and MCNP Monte-Carlo simulations of the detector/scatter mask assembly are compared. First, a comparison of the entire spectrum of energy deposited within the detector resulting from 4 individual, representative (θ, φ) positions of the source was conducted. The comparison methodology is described in Section 2.5. Both confidence intervals and non-parametric statistical tests were used in the comparison of these spectra for each source position. Next, the comparison focused on the detector response curves resulting from the count of the full energy peak deposited within the detector resulting from single φ source positions through one complete mask rotation of 360° in θ . In addition to the detector response curve resulting from consideration of the FEP, analogous curves resulting from consideration of the integral under the Compton continuum were also considered. Statistical comparison techniques will be employed in the comparison of the detector response curves resulting from GEANT and MCNP for full mask rotations for 18 polar angle φ increments.

Secondly, to verify that the simulation results accurately describe the performance of the Gamma RSM Detection System, experimental results were compared to simulated results. This constitutes the final necessary validation of the results obtained via Monte-Carlo simulation.

GEANT4 is chosen as the simulation code for comparison due to the fact that it was capable of accurately portraying the thickness of the detector sleeve seen experimentally. MCNP experienced geometrical overlap of the volumes, so adjustment to the GEANT code was required for the comparison of the two Monte-Carlo codes.

To review the parameters of simulation described in Section 3.2, a conical beam of monoenergetic 662 keV gamma rays is defined to completely encapsulate the mask/detector assembly. This utilization of variance reduction techniques mimics spherical divergence of a point source located 34" from the center of the NaI detector. 10,000,000 source particles were used for each simulated position as this number of particles was sufficient for simulation convergence.

Prior to giving credence to the output gained from any Monte-Carlo transport code, convergence must be achieved, entailing that variation due to the random nature of the simulation has been reduced to an inconsequential level. It was determined that this equated to 5,000,000 particles, which achieved a 0.76% error in FEP value, when compared to the case of 30,000,000 incident particles (*Figure 13*). The source position selected for the convergence analysis was chosen to be one with especially complex mask geometry since this position would take the largest number of particles to converge. As such, the use of 10,000,000 particles for less complicated mask positions considered in Sections 5.2 and 5.5 represents adequate simulation convergence throughout the energy spectrum. This is the number of particles utilized for the MCNP/GEANT and GEANT/experimental spectral comparisons at 4 representative source positions.

For subsequent comparison of the detector response curves, only the FEP or the area under the Compton continuum are used to construct these curves. As such, convergence of each

individual energy bin is not required and a smaller number of particles is necessary for sufficient convergence. Due to this reason and due to limited computational resources, 500,000 source particles were used per source position (θ, φ) relative to the center of the detector for detector response curve simulations.

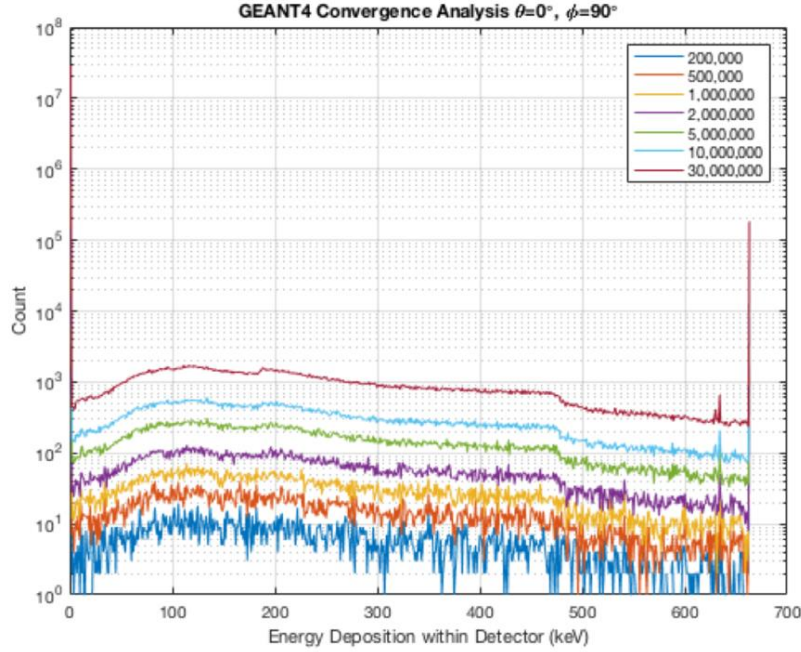


Figure 13. Visualization of convergence of energy spectrum as number of incident particles increases from 200,000 to 30,000,000 incident gamma quanta. This source position, ($\theta = 0^\circ, \phi = 90^\circ$), was particularly chosen to be one with especially complex mask geometry, thus causing it to converge particularly slowly relative to other more representative source positions.

5.2 Energy Spectra MCNP/GEANT Comparisons

The statistical comparison of the MCNP and GEANT convergent energy spectra resulting from four representative source positions is now considered. The purpose of this comparison is to test, statistically, the compatibility or distinguishability of the two histograms obtained. This problem can be simplified to testing the validity of the null hypothesis that the “histograms were obtained in the processing of independent samples taken from one and the same flow of events.”

The two statistical tests used in this comparison are the Anderson-Darling k-sample test and the Kolmogorov-Smirnov test, as detailed in Section 2.5. Each of these tests is valid if one is seeking to compare the similarity of datasets and neither requires any assumptions about the underlying distributions of the datasets (making the tests non-parametric and distribution free). The null hypothesis, H_0 , in each case is that the two datasets do not differ significantly and could have come from a random sampling of the same underlying distribution. It has been shown that the Anderson-Darling test has more power, but both tests were conducted in this analysis for completeness as both tests are useful in the comparison conducted in this effort [26]. The simulation energy spectra for the four representative source positions under consideration are visualized in ***Figure 14***.

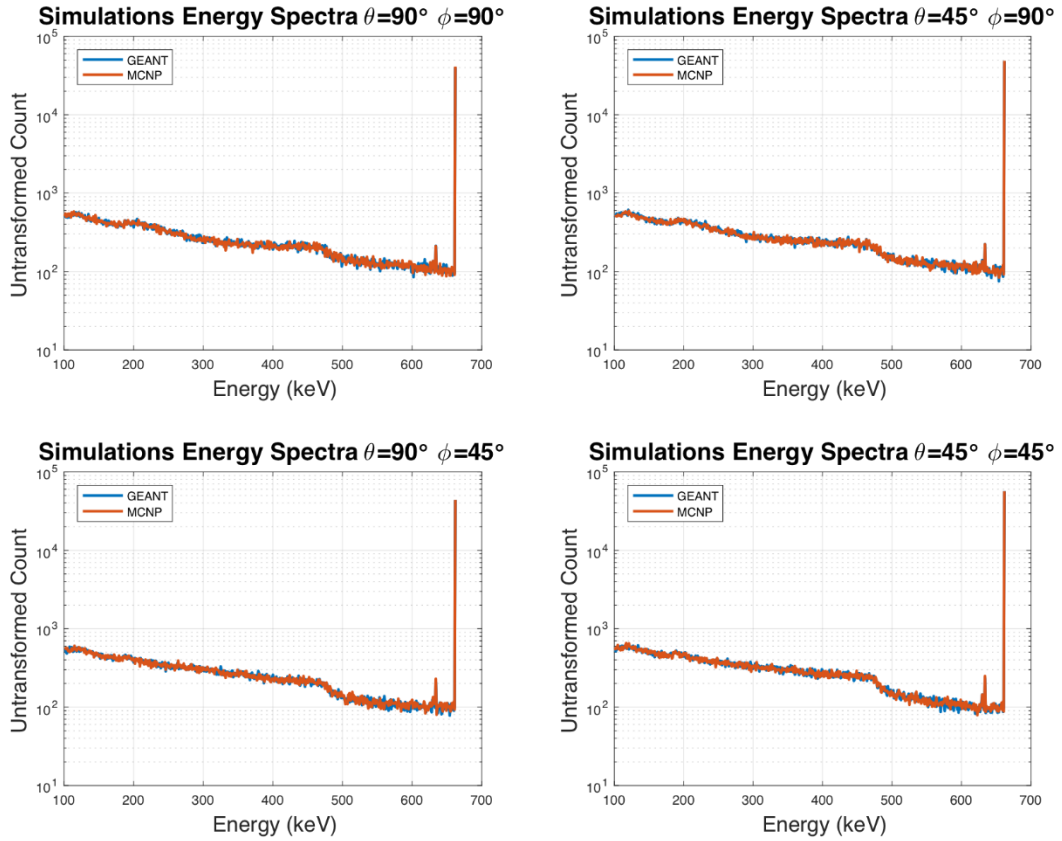


Figure 14. GEANT and MCNP energy spectra for source positions $(\theta, \phi) = (90^\circ, 90^\circ)$, $(90^\circ, 45^\circ)$, $(45^\circ, 90^\circ)$, and $(45^\circ, 45^\circ)$. All values are the unnormalized count of the number of incident source particles that result in energy deposition within the detector volume that falls within the given 1 keV wide energy bin. Each spectrum represents a total of 10,000,000 incident 662 keV gamma particles.

The results of the application of the statistical tests (the p-values) presented in *Table 1* can be interpreted as the likelihood of obtaining a histogram at most as different as the realized histogram if the null hypothesis is true, i.e. the two histograms could have come from the same dataset. The very high p-values in each case indicate that it is very likely that the null hypothesis is true. Thus, the “histograms were obtained in the processing of independent samples taken from one and the same flow of events.” These two flows of events are the MCNP and GEANT simulations and they are shown to be indistinguishable, statistically, even at the very large

significance level of 0.2.

Test (p-value)	(90°,90°)	(90°,45°)	(45°,90°)	(45°,45°)
Anderson-Darling k-sample test p-value	0.9477	0.8869	0.9989	0.8588
Two-sample Kolmogorov-Smirnov test p-value	0.8276	0.905	0.9999	0.9354
FEP % Difference	3.29%.	0.41%	0.54%,	0.39%

Table 1. Statistical comparison results of GEANT and MCNP energy spectra for source positions $(\theta, \varphi) = (90^\circ, 90^\circ)$, $(90^\circ, 45^\circ)$, $(45^\circ, 90^\circ)$, and $(45^\circ, 45^\circ)$. Both non-parametric statistical tests confirm that the energy spectra for each position resulting from the two simulations are statistically indistinguishable. Each spectrum represents a total of 10,000,000 incident 662 keV gamma particles.

An alternative statistical perspective is to consider the confidence intervals around each data point (energy bin count). The derivation of a methodology for determining the standard deviation of the values obtained was presented in Section 2.5. With this measure of the variability of the count per source particle obtained from simulation, a 90% confidence interval can be formed. This is done by adding and subtracting the standard deviation multiplied by $Z_{\alpha/2}$ with $\alpha = 0.1$ in the case of a 90% confidence interval. $Z_{\alpha/2}$ is the value of the standard normal distribution such that $\frac{\alpha}{2}$ percent of the time the calculated value of the standard normal random variable will be more extreme than said value. Thus, the 90% confidence interval is defined such that if one recalculates this confidence interval with many samples, it would be found that 90% of the time, the true value of the count would fall within the confidence interval obtained. The associated formula is shown in equation 13. This is calculated individually for each energy bin and \hat{p}_i is defined as the count in energy bin i divided by the number of source particles (probability of contributing to energy bin i), accounting for the variance reduction technique employed. Namely, one must account for the fact that particles are emitted from the source in a conical manner rather than isotropically, which scales \hat{p}_i . Thus, to get a true measure of

count per source particle, one must divide by the solid angle represented by the cone of incidence. This value, C, is equal to 0.02314 because the cone is defined with a half-angle of 17.5°. This variance reduction technique is further detailed in Section 3.4.

$$90\% \text{ Confidence Interval} = \hat{p}_i \pm Z_{\alpha/2} * \sigma_{p_i} \quad (13)$$

$$90\% \text{ Confidence Interval} = \frac{\hat{p}_i}{C} \pm 1.645 * \sqrt{\frac{1}{N} (C * p'_i - p'^2_i)}$$

The results of the application of this 90% confidence interval in Equation 13 for each energy bin count in each energy spectrum are found in *Figure 15*. It should be noted that the standard deviation comparison employs normalization due to the format of the MNCP output while the previous application of the non-parametric tests utilized the unnormalized, gross output from each simulation.

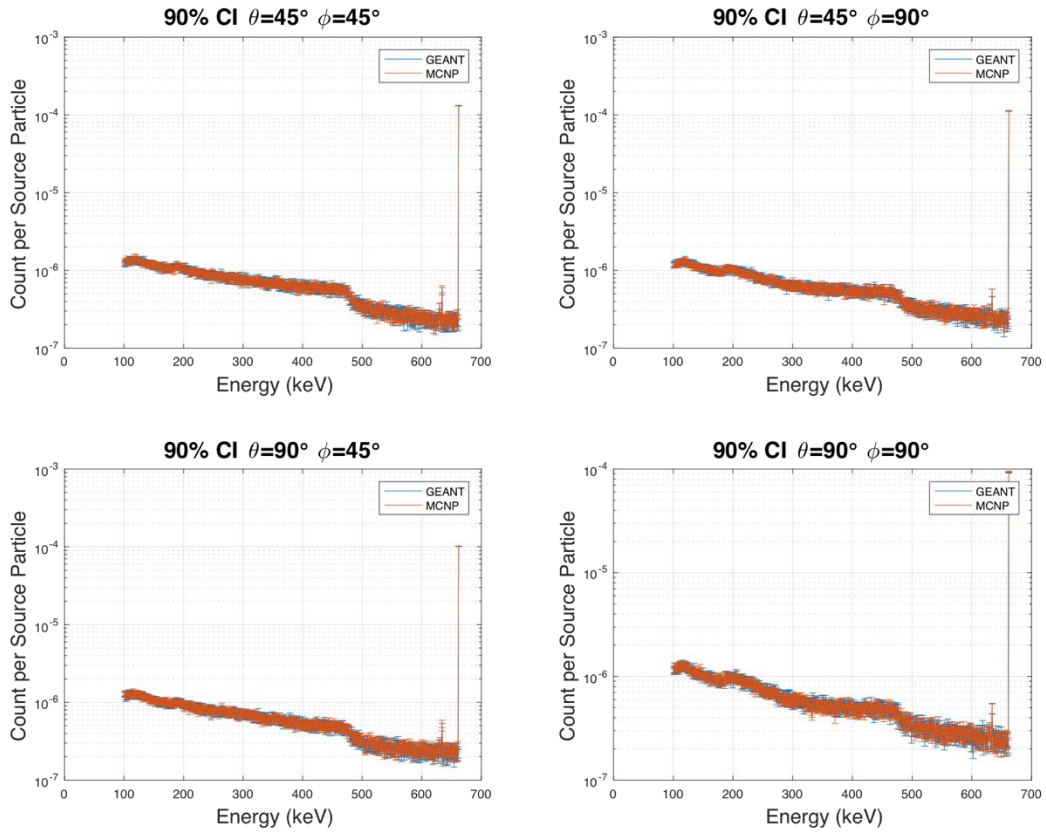


Figure 15. Normalized GEANT and MCNP energy spectra for source positions $(\theta, \varphi) = (90^\circ, 90^\circ)$, $(90^\circ, 45^\circ)$, $(45^\circ, 90^\circ)$, and $(45^\circ, 45^\circ)$ with the 90% confidence interval calculated for each position. Each spectrum represents a total of 10,000,000 incident 662 keV gamma particles.

Overall, for each of the 552 energy bins considered in the plots above (MCNP did not track below 100 keV), the percentage of the 90% confidence intervals that overlap are found in

Table 2.

Angle	$(90^\circ, 90^\circ)$	$(90^\circ, 45^\circ)$	$(45^\circ, 90^\circ)$	$(45^\circ, 45^\circ)$
% of Energy Bins with Overlapping Confidence Intervals	45.0%	51.1%	47.2%	45.6%

Table 2. Percentage of energy bin count 90% confidence intervals that overlap for normalized GEANT and MCNP energy spectra for source positions $(\theta, \varphi) = (90^\circ, 90^\circ)$,

(90°, 45°), (45°, 90°), and (45°, 45°). Each spectrum represents a total of 10,000,000 incident 662 keV gamma particles.

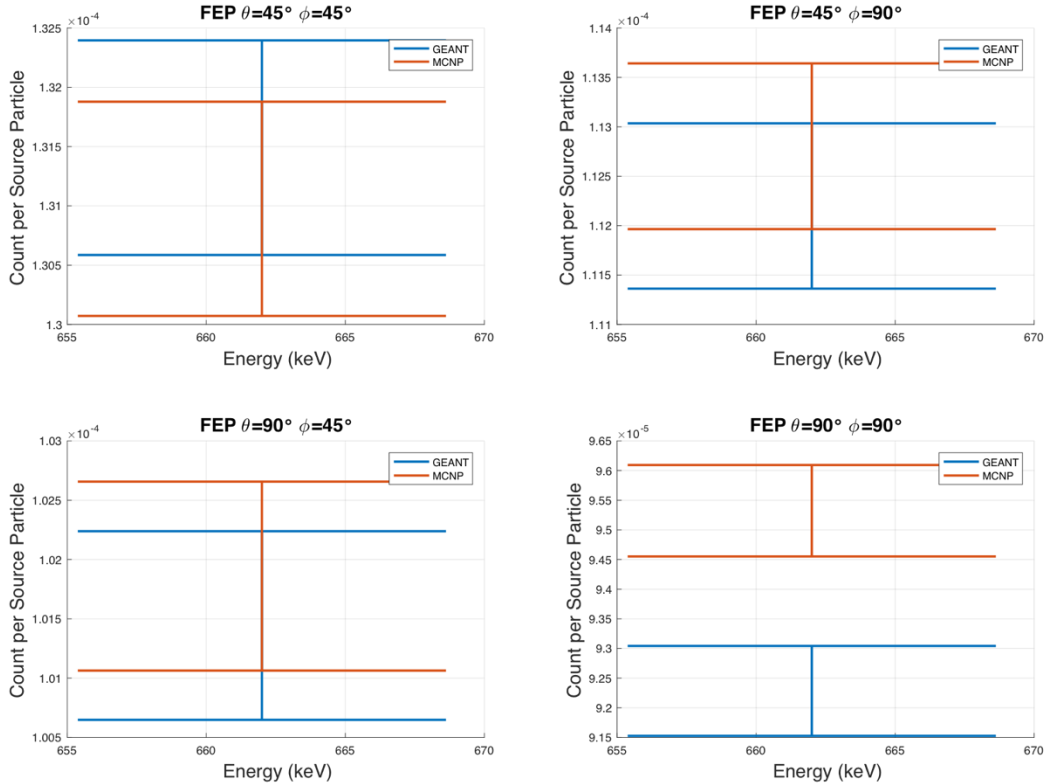


Figure 16. 90% FEP confidence intervals for normalized GEANT and MCNP energy spectra for source positions $(\theta, \varphi) = (90^\circ, 90^\circ)$, $(90^\circ, 45^\circ)$, $(45^\circ, 90^\circ)$, and $(45^\circ, 45^\circ)$. This shows that the MCNP and GEANT FEP confidence intervals overlap for all positions excluding $(\theta, \varphi) = (90^\circ, 90^\circ)$. Each spectrum represents a total of 10,000,000 incident 662 keV gamma particles.

Figure 16 shows that three of the four 90% FEP confidence intervals overlap, indicating statistical indistinguishability. The failure of the confidence intervals to overlap for position $(\theta, \varphi) = (90^\circ, 90^\circ)$ is due to the particularly complicated geometry and thickness of mask found at this position. Gamma rays emitted from this source position must pass through a larger amount

of material than for any of the other three source positions considered. Due to the fact that MCNP and GEANT treat interactions differently, this leads to the increase in divergence when more interactions take place, as is the case for $(\theta, \varphi) = (90^\circ, 90^\circ)$.

In conclusion, despite some variation in the FEP count, the MCNP and GEANT energy spectra are found to be statistically indistinguishable via non-parametric statistical tests and the confidence intervals are found to agree well.

5.3 Detector Response Curve MCNP/GEANT Comparisons

The detector response curve is defined as the curve obtained as the plot of the magnitude of a certain variable (i.e. FEP counts) of the energy spectrum through one rotation the mask in the azimuthal angle θ . Thus, the mask is no longer stationary and we focus only on a single facet of the energy spectrum, rather than the entire distribution of energy deposited in the detector. This results in a distinct curve for each source position relative to the detector due to the geometry of the mask defined in Section 1.6. The position of each discontinuity is clearly seen in the detector response curve. Each detector response curve contains the requisite information to be able to determine both the θ and φ defining the vector from the center of the detector to the source location.

There are two prime candidates that could serve as the facet of the spectrum that is used to derive the detector response curve, the FEP and the counts within the Compton continuum. Use of the FEP equates to counting all of the gamma rays that pass through the mask and deposit their entire initial energy within the detector. Integration of all or a fraction of the Compton continuum may also be used to create a detector response curve. There are two different situations that could cause a gamma photon to be counted within this integral. Firstly, it could

lose a substantial amount of energy by undergoing a Compton scatter within the mask and then deposit all or a large portion of its remaining energy in the detector. Alternatively, a gamma ray could contribute to this integral if it passed through the mask with its entire energy and then only deposited part of its energy in the detector due to the fact that it escaped the detector following a Compton scatter.

As thickness of the mask between source and detector increases, the FEP counts decrease while the area under the Compton integral increases. This is the case because increasing the material the gammas must pass through decreases the number that make it to the detector with their full energy. Concurrently, this increasing amount of material increases the number of gammas that lose some energy in the mask, thus causing them to contribute to the Compton integral if they go on to deposit energy within the detector. This interpretation is complicated to some degree due to the fact that Compton scatter can occur within both the mask and the detector. A Compton scatter in the mask could result in energy deposition in the detector that lies between the Compton edge and the FEP. Integrating under the entire Compton continuum will obscure individual effect from the Compton scatters within the two different volumes.

Thus, each of these candidates for the value used in the detector response curve potentially contains information sufficient to image the source. The number of counts in the Compton integral is generally greater than that in the FEP, so the resulting statistics are superior and decreased counting time is required for source position determination. Alternatively, the presence of a source emitting with multiple energies would decrease the ability to distinguish individual Compton integrals, while the FEPs may still be distinguishable. As such, each candidate has merit and the two might be used in concert. Due to this utility, both methods will be validated in the subsequent analysis via simulation comparisons and experimental

comparisons.

The FEP and Compton Integral Detector Response curve plots for each 10° increment of phi ($\varphi = 5^\circ - 175^\circ$) are shown in **Figure 17** and **Figure 18** to demonstrate that either method of defining the detector response curve provides information concerning the position of the source relative to the detector. This is made clear by the patently distinct curves obtained for each source position. It is the distinguishability of these curves that provides the imaging functionality to the detector.

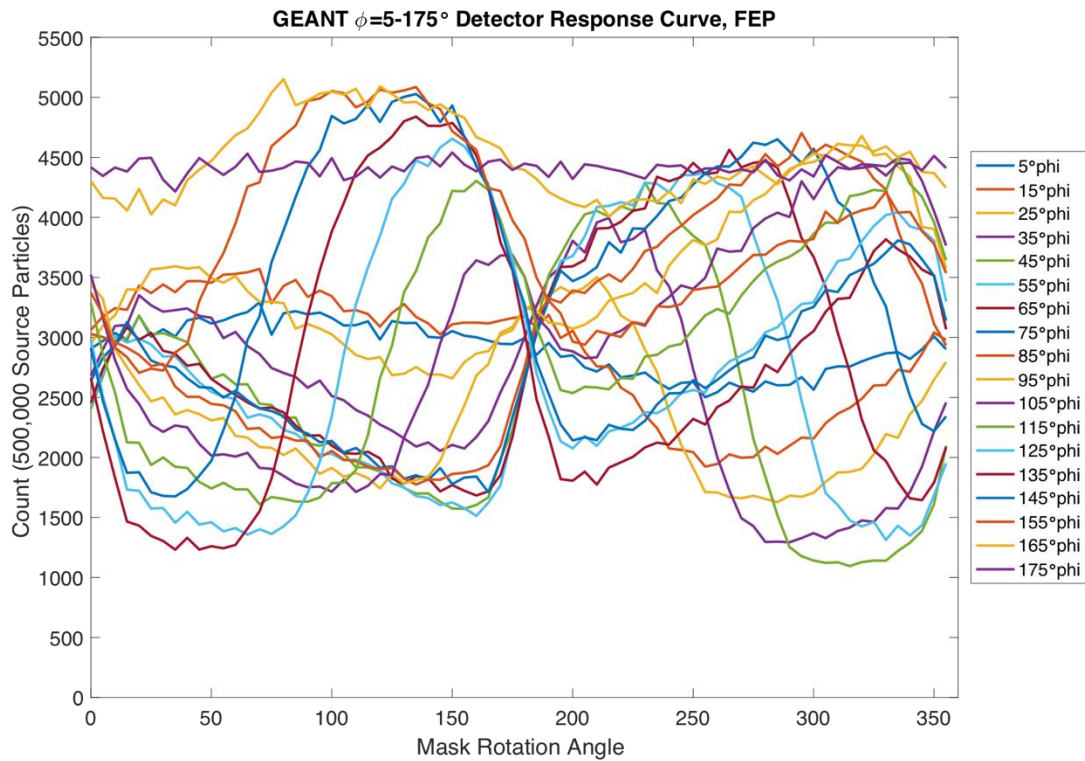


Figure 17. Detector Response curve plots for each 10° increment of phi ($\varphi = 5^\circ$ to 175°). Each point is defined by the number of source particles that contribute to the FEP (deposit all of their energy in the detector volume), out of 500,000 incident 662 keV gamma rays per (θ, φ) position.

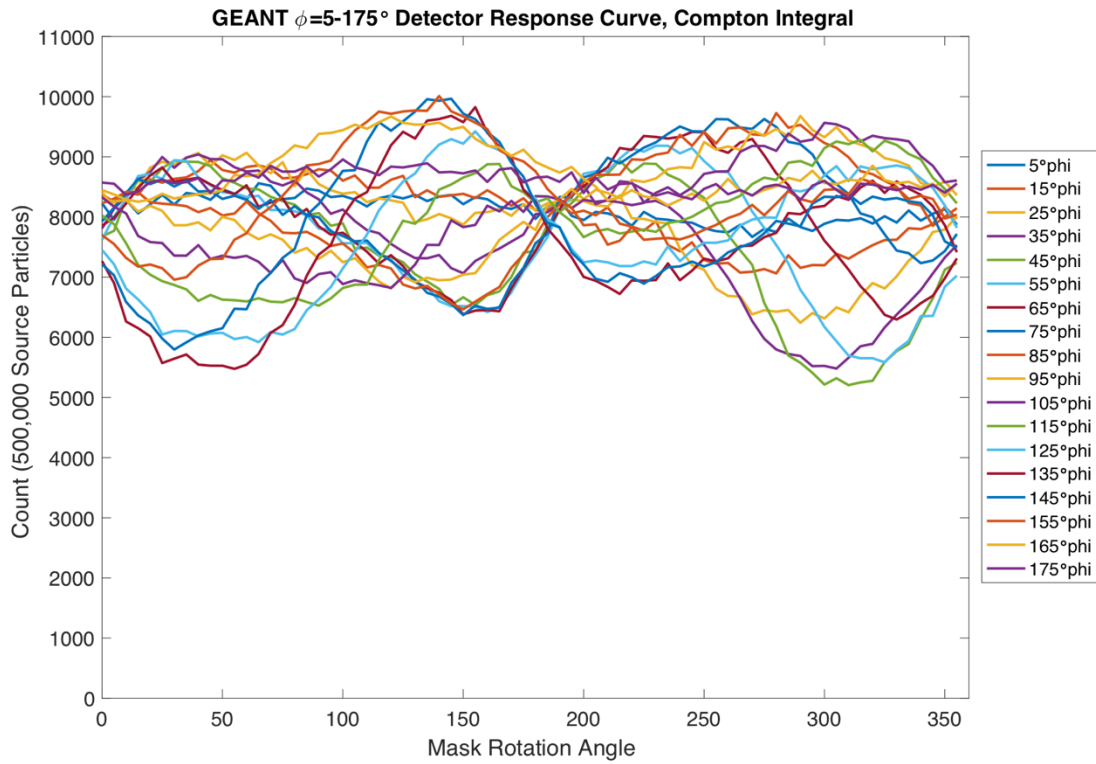


Figure 18. Detector Response curve plots for each 10° increment of phi ($\phi = 5^\circ$ to 175°). Each point is defined by the number of source particles that contribute to the Compton Integral (deposit up to 480 keV in the detector volume), out of 500,000 incident 662 keV gamma rays per (θ, ϕ) position.

Employing an analogous methodology to that utilized in the energy spectra comparisons, the detector response curves are compared. Again, two non-parametric statistical tests, the Kolmogorov-Smirnoff test and the Anderson-Darling test, are applied and the resulting P-Values are found in **Table 4**. To reiterate, a P-Value of above 0.01 can be interpreted as implying that the two distributions could have been statistically drawn from the same random sequence of events. The data used in the comparisons is the unnormalized direct count that results from the simulation runs. For the detector response curve based on the Compton Integral, the MCNP and GEANT results are shown to be statistically indistinguishable for all but $\phi=5^\circ$ and 175° . This is shown to be true with both of the statistical tests utilized in **Table 4**.

For the detector response curve based on the Full Energy Peak, the MCNP and GEANT results are shown to be statistically indistinguishable for all but $\varphi = 175^\circ$. This is shown to be true with both of the statistical tests utilized in *Table 3*.

FEP GEANT/MCNP Comparison		
(θ, φ) Source Position	Anderson–Darling Test P- Value	Kolmogorov–Smirnov Test P- Value
$(0^\circ, 5^\circ)$	0.71507	0.8855519
$(0^\circ, 15^\circ)$	0.9242	0.9639452
$(0^\circ, 25^\circ)$	0.94982	0.9998867
$(0^\circ, 35^\circ)$	0.64533	0.7657632
$(0^\circ, 45^\circ)$	0.68668	0.8855519
$(0^\circ, 55^\circ)$	0.99784	0.9998867
$(0^\circ, 65^\circ)$	1	1
$(0^\circ, 75^\circ)$	0.99975	0.9998867
$(0^\circ, 85^\circ)$	0.99693	0.9998867
$(0^\circ, 95^\circ)$	0.99794	0.9999157
$(0^\circ, 105^\circ)$	0.79638	0.9639452
$(0^\circ, 115^\circ)$	0.93015	0.9639452
$(0^\circ, 125^\circ)$	0.77494	0.8855519
$(0^\circ, 135^\circ)$	0.94295	0.9950665
$(0^\circ, 145^\circ)$	0.99283	0.9998867
$(0^\circ, 155^\circ)$	0.99999	1
$(0^\circ, 165^\circ)$	0.91666	0.9950665
$(0^\circ, 175^\circ)$	0.00014418	0.00128876

Table 3. Non-parametric statistical comparison test results for each 10° increment of phi ($\varphi = 5^\circ$ to 175°). Each point in each spectrum compared is defined by the number of source particles that contribute to the Full Energy Peak (deposit all of their energy in the detector volume), out of 500,000 incident 662 keV gamma rays per (θ, φ) position. All p-values resulting from both the application of the Anderson–Darling Test and the Kolmogorov–Smirnov Test, excluding the extreme $\varphi = 175^\circ$ source angle (bold), show that the two codes produce resulting detector response curves that are statistically indistinguishable.

Compton Integral GEANT/MCNP Comparison		
(θ, φ) Source Position	Anderson–Darling Test P-Value	Kolmogorov–Smirnov Test P-Value
$(0^\circ, 5^\circ)$	0.001661	0.000167297
$(0^\circ, 15^\circ)$	0.20515	0.4909804
$(0^\circ, 25^\circ)$	0.48149	0.2699997
$(0^\circ, 35^\circ)$	0.89769	0.9956171
$(0^\circ, 45^\circ)$	0.71576	0.8855519
$(0^\circ, 55^\circ)$	0.8582	0.9639452
$(0^\circ, 65^\circ)$	0.97824	0.9950665
$(0^\circ, 75^\circ)$	0.61608	0.8855519
$(0^\circ, 85^\circ)$	0.73889	0.8855519
$(0^\circ, 95^\circ)$	0.90054	0.8888351
$(0^\circ, 105^\circ)$	0.31763	0.4909804
$(0^\circ, 115^\circ)$	0.48216	0.8888351
$(0^\circ, 125^\circ)$	0.42132	0.6271671
$(0^\circ, 135^\circ)$	0.9077	0.9639452
$(0^\circ, 145^\circ)$	0.97927	0.9950665
$(0^\circ, 155^\circ)$	0.74985	0.8855519
$(0^\circ, 165^\circ)$	0.49327	0.4909804
$(0^\circ, 175^\circ)$	1.22E-05	8.01E-05

Table 4. Non-parametric statistical comparison test results for each 10° increment of phi ($\varphi = 5^\circ$ to 175°). Each point in each spectrum compared is defined by the number of source particles that contribute to the Compton Integral (deposit up to 480 keV in the detector volume), out of 500,000 incident 662 keV gamma rays per (θ, φ) position. All p-values resulting from both the application of the Anderson–Darling Test and the Kolmogorov–Smirnov Test, excluding the extreme $\varphi = 5^\circ$ and $\varphi = 175^\circ$ angles (bold), show that the two codes produce resulting detector response curves that are statistically indistinguishable.

An alternative methodology for statistical comparison is to examine the standard deviations for the values obtained via the two simulations. If the standard deviations overlap, the differences in the values are likely due to statistical uncertainty and nothing more, assuming that the error is symmetrically distributed. The 90% confidence interval is defined in Equation 14, assuming that the count is a *Binomial*(1, p_i) random variable, as discussed in Section 2.5. This

equation is utilized due to the fact that the untransformed count is being compared.

$$\hat{N} \pm 1.645 * 1/\sqrt{\hat{N}} \quad (14)$$

The application of Equation 14 in the graphical comparison of the Compton Integral detector response curves is found in Appendix A, with representative examples for $\varphi = 45^\circ - 75^\circ$ found in **Figure 19**. An analogous visualization for the complete set of FEP detector response curves is also found in Appendix A, with a similar representative example for $\varphi = 45^\circ - 75^\circ$ visualized in **Figure 20**. These are un-normalized direct counts resulting from the two simulations and excellent agreement is seen. GEANT4 demonstrates larger statistical variation. This is a consequence of the more detailed interaction mechanisms considered in the GEANT particle tracking.

The demonstrated statistical differences between the codes for $\varphi = 5^\circ$ and 175° can be explained with the use of **Figure 17**. This figure shows the lack of differentiation in θ for these more extreme φ source angles. This is the case because the mask thickness presented to the source varies little with mask rotation. Thus, for two essentially flat curves, small variations in the two simulation results will dramatically influence the CDFs used in the statistical tests and cause the test to indicate that the curves differ.

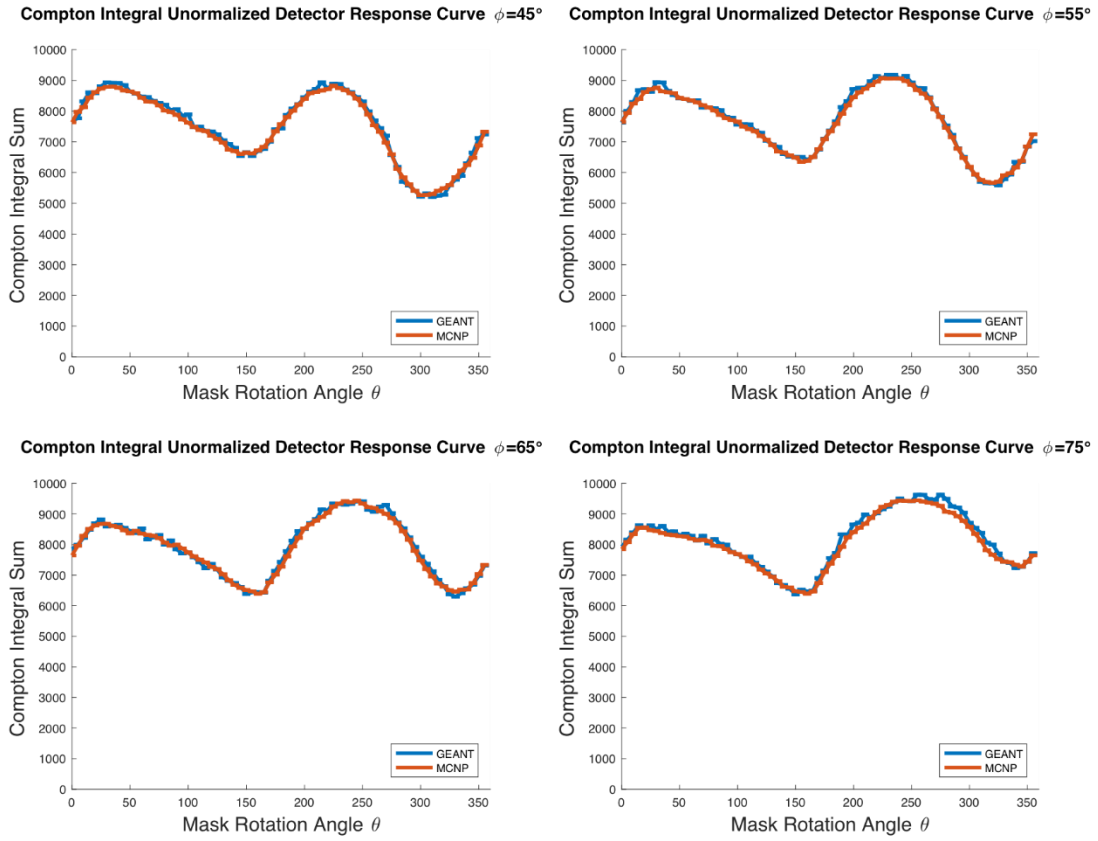


Figure 19. Count of gross number of incident particles that contribute to the Compton Integral for $\varphi = 45^\circ - 75^\circ$ in increments of 10° with $\theta = 0^\circ - 355^\circ$ in increments of 5° for each increment of φ . These graphs correspond to GEANT and MCNP results with 500,000 source particles for each (θ, φ) position. The 90% confidence interval is plotted for each.

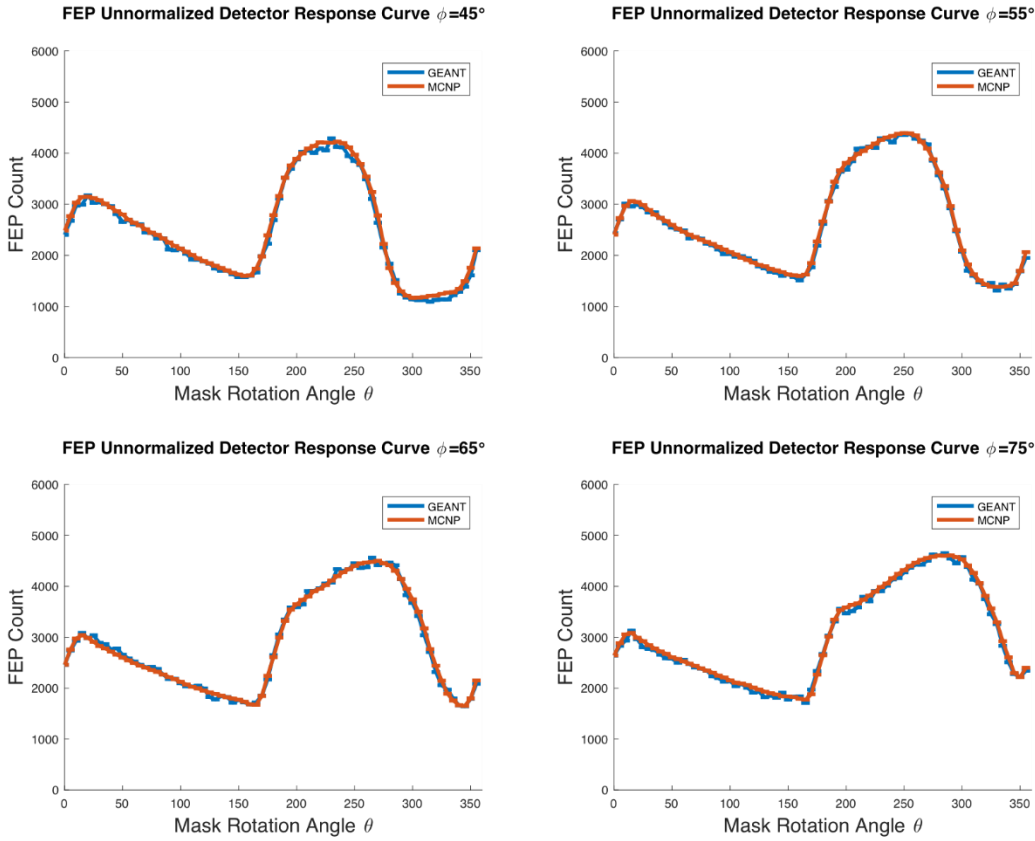


Figure 20. Count of gross number of incident particles that contribute to the Full Energy Peak for $\varphi = 45^\circ - 75^\circ$ in increments of 10° with $\theta = 0^\circ - 355^\circ$ in increments of 5° for each increment of φ . These graphs correspond to GEANT and MCNP results with 500,000 source particles for each (θ, φ) position. The 90% confidence interval is plotted for each.

Table 5 shows the percentage of the confidence intervals that overlap in the simulation detector response curves for each of the phi angles considered. The overlap of confidence intervals indicates statistical indistinguishability and this is found to be true throughout nearly every point in each detector response curve. This agreement is more important than the spectral agreement considered previously in **Table 2** because it is the detector response curves, not the energy spectra, that are directly used to determine source position.

(θ, φ) Source Position	Compton Integral 90% Confidence Interval Percent Overlap	FEP 90% Confidence Interval Percent Overlap
$(0^\circ, 5^\circ)$	97.22%	100.00%
$(0^\circ, 15^\circ)$	100.00%	98.61%
$(0^\circ, 25^\circ)$	97.22%	100.00%
$(0^\circ, 35^\circ)$	100.00%	95.83%
$(0^\circ, 45^\circ)$	100.00%	94.44%
$(0^\circ, 55^\circ)$	100.00%	100.00%
$(0^\circ, 65^\circ)$	100.00%	100.00%
$(0^\circ, 75^\circ)$	94.44%	100.00%
$(0^\circ, 85^\circ)$	95.83%	100.00%
$(0^\circ, 95^\circ)$	98.61%	98.61%
$(0^\circ, 105^\circ)$	97.22%	98.61%
$(0^\circ, 115^\circ)$	97.22%	98.61%
$(0^\circ, 125^\circ)$	95.83%	100.00%
$(0^\circ, 135^\circ)$	94.44%	97.22%
$(0^\circ, 145^\circ)$	100.00%	100.00%
$(0^\circ, 155^\circ)$	98.61%	100.00%
$(0^\circ, 165^\circ)$	100.00%	100.00%
$(0^\circ, 175^\circ)$	95.83%	100.00%

Table 5. Percentage of the 72 θ positions ($0^\circ - 355^\circ$ in increments of 5°) for each φ for which the MCNP and GEANT 90% confidence intervals around the normalized (per source particle) counts within the Compton Integral and FEP overlap. These values correspond to GEANT and MCNP results with 500,000 source particles for each (θ, φ) position.

Thus, the GEANT and MCNP detector response curves resulting from both the use of the Compton Integral and the FEP in their definition were found to be statistically indistinguishable for all but the most extreme source angles relative to the scattering mask. This was shown via application of non-parametric statistical tests as well as analysis of the overlap of count confidence intervals. This difference can be partly attributed to the lack of differentiation in θ for these φ angles. Furthermore, the use of 500,000 incident particles for a given source/detector configuration was shown in the calibration analysis (*Figure 13*) to result in incomplete statistical

convergence for the GEANT data. Thus, simple statistical variability could contribute to this lack of agreement. Additionally, the statistical tests used are dependent upon the accuracy of the derived approximation to the continuous CDF (as a result of data binning with mask rotation angle θ). Any differences resulting from binning could further hinder agreement.

5.4 Experiment and Simulation Data Processing

The setup utilized in the previous simulation results was modeled, as closely as was practical, upon the RSM assembly that was used to collect data to obtain energy histograms and detector response curves (with the slight adjustment previously mentioned in Section 5.1 to allow for agreement with MCNP). As in the simulation, the experimental assembly consists of a ^{137}Cs source located 86.36 cm from the center of the NaI(Tl) detector. This detector is surrounded by an Al-alloy sleeve and mask of identical proportions in both GEANT simulation and in the experimental setup. To reiterate, the sleeve in the MCNP simulations had to be made slightly thinner due to geometry overlaps and subsequent errors. Consequently, comparisons will be made between the GEANT results and experimental data.

Before a comparison can be conducted, the experimental data is calibrated so that the distribution of counts corresponds to radiation energy deposition rather than detector voltage. This was accomplished via the Calibration curve shown in *Figure 21* and *Figure 22*. This calibration is ordinarily very close to linear in form and this was found to be the case in this analysis as well, as the equation of conversion was found to be equal to Equation 15. The makeup of the multinuclide source utilized in the calibration is shown in *Table 6*. This source was 413 days old at the time that this calibration was conducted and this age is taken into account when the activities and ratios are presented in *Table 6*.

Isotope	Gamma Ray (MeV)	Half-Life (Days)	Branching Ratio	Activity (μCi) Initial	Activity (μCi) Final	Ratio to Cs Peak Height (Ideal)
Am-241	0.060	157850.0925	0.36	0.0300	0.0299	0.3039
Cd-109	0.088	462.6	0.0363	0.2987	0.1609	0.1649
Co-57	0.122	271.79	0.856	0.0099	0.0034	0.0831
Te-123m	0.159	119.7	0.84	0.0141	0.0013	0.0307
Cr-51	0.320	27.706	0.0986	0.3355	0.0000	0.0000
Sn-113	0.392	115.09	0.649	0.0497	0.0041	0.0757
Sr-85	0.514	64.849	0.984	0.0642	0.0008	0.0216
Cs-137	0.662	11019.5925	0.851	0.0427	0.0416	1.0000
Y-88	0.898	106.63	0.94	0.1008	0.0069	0.1826
Co-60	1.173	1925.598	0.9986	0.0532	0.0458	1.2917
Co-60	1.333	1925.598	0.9998	0.0532	0.0458	1.2932
Y-88	1.836	106.63	0.994	0.1008	0.0069	0.1931

Table 6. Composition of the multinuclide source used in experimental calibration. This source is 413 days old at the time of use and the final activity is calculated for each isotope in the source. It is clear that Cr-51 should not be visible in the resulting spectrum because it has almost entirely decayed away.

The uncalibrated NaI(Tl) response to this multinuclide source is given in *Figure 21*. The data was acquired over a period of 60 minutes and experimental specifications can be found in Sections 4.1 and 4.2. Additionally, the plot is re-presented with the background removed in *Figure 22*, in an attempt to isolate the FEP for each of the isotopes in the multinuclide source. This removal of all but the Gaussian FEP data was conducted by applying a polynomial fit to the count at the bases of each of the Gaussian peaks and subtracting this polynomial from the energy spectrum. The voltage bin in which each FEP lies, when paired with the known true energy of that FEP, forms the points that are used in the derivation of the calibration curve. This equation can then be used to calibrate the experimental data obtained from the laboratory setup of the RSM assembly.

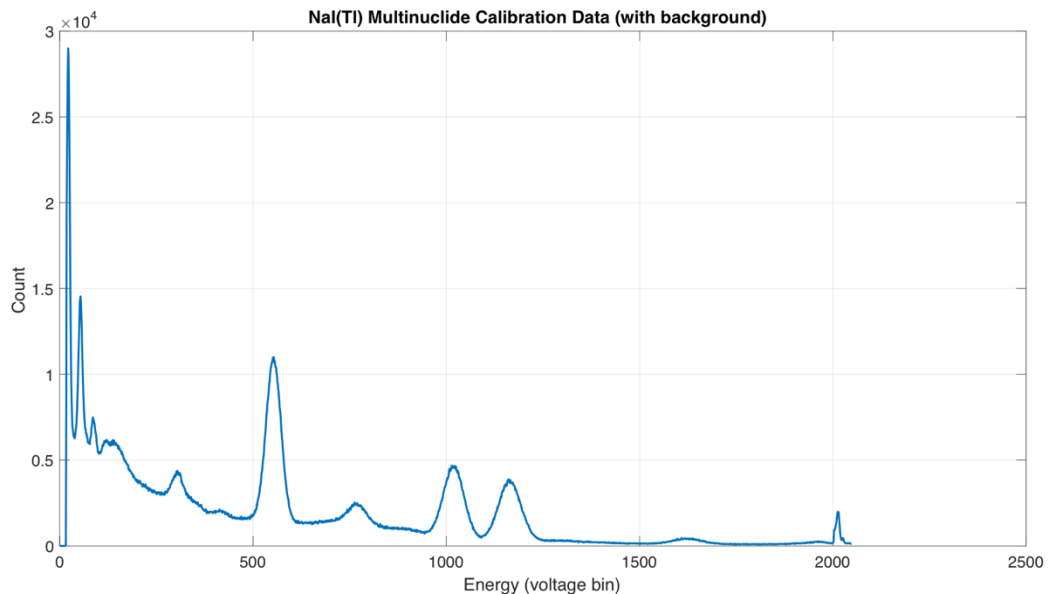


Figure 21. Uncalibrated energy spectrum within the NaI(Tl) detector resulting from the multi-nuclide source described in Table 6. This spectrum includes background and underlying spectral components beneath the FEP for each isotope.

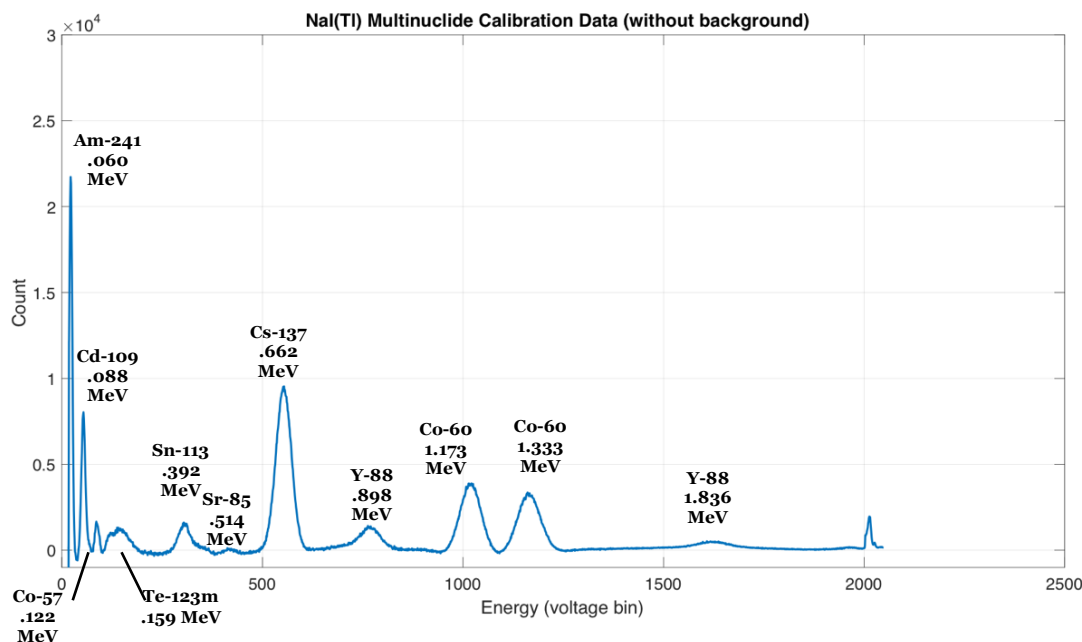


Figure 22. Uncalibrated energy spectrum within the NaI(Tl) detector resulting from the multi-nuclide source described in Table 6. The background and underlying spectral

components not part of the FEP are subtracted out via a function fit to the points where each Gaussian peak reaches its boundaries where it approaches zero. This plot is used to determine the voltage bins in which each isotope's FEP is centered. These values are used to fit the function that will become the calibration curve.

In the development of this calibration curve, the points in **Table 7** were utilized in the application of a polynomial least-squares fit of degree 2 (utilizing the built-in MATLAB function polyfit). ⁵¹Cr is not used because it has almost entirely decayed away before the date that the calibration information was collected, as shown in **Table 6**. Additionally, ⁸⁸Y was not used because its Gaussian was spread to such an extent that precise determination of the true FEP voltage value was not feasible.

Isotope	Gamma Ray (MeV)	Detector Voltage Bin
Am-241	0.06	22
Cd-109	0.088	54
Co-57	0.122	86
Te-123m	0.159	122
Sn-113	0.392	307
Sr-85	0.514	417
Cs-137	0.662	554
Y-88	0.898	770
Co-60	1.173	1021
Co-60	1.333	1166

Table 7. Isotopes with their associated FEP true energies (keV) and uncalibrated voltage bins associated with these values. These are the points used in the derivation of the calibration curve via a polynomial fit of degree 2.

The results of this fit are presented in the nearly linear Equation 15, which is subsequently used as the calibration curve for the experimental energy spectra. The independent variable here is the voltage from the detector used and the dependent variable is the true energy

in keV that this voltage represents.

$$E(x) = -0.0001x^2 + 1.2072x + 18.6880 \quad (15)$$

This fitted equation, with an R^2 value of 0.9994, adequately captures a very large percentage of the variability in the dataset. As a result, this equation is subsequently used to calibrate the experimental results so that they can be directly compared with the energy spectra resulting from simulation. Following the application of this calibration, the parameters of the FEP for each of the primary, representative source position energy spectra considered were calculated. In **Table 8**, the full width of the FEP at half maximum, the energy resolution, and the Gaussian standard deviation are presented for each energy spectrum.

Source Position (θ, φ)	FWHM (keV)	Energy Resolution (R)	Gaussian σ (keV)
(45,45)	54	8.16%	32.4
(90,45)	56	8.46%	33.6
(45,95)	60	9.06%	36.0
(90,95)	66	9.97%	39.6

Table 8. Parameters of the calibrated experimental data describing the FEP for four static mask positions. This information is used to broaden the simulated energy spectra.

There are two main reasons why simulated results and experimental results are not identical. First, in the simulation, the detector was treated as a detector with perfect resolution, as the code was written to record exactly the amount of energy deposited by particles into the detector volume. In comparison, the realistic NaI(Tl) detector has an inherent lack of perfect energy resolution. Second, the simulation does not include any of the external lab environment, which consists of background radiation as well as materials from which radiation can scatter into the system of interest. This includes the base and motor associated directly with the assembly

and found in **Figure 4**.

The first of these two primary sources of difference is treated via a broadening of the simulated energy spectra. The uncertainty in a realistic NaI(Tl) detector can be adequately modeled as Gaussian in form due to its random nature [19]. As such, the parameters of the Gaussian for each energy spectrum were derived from the calibrated experimental energy spectra. These values were presented in **Table 8**.

This Gaussian spread to the simulated data was first accomplished via a convolution. A convolution of one function with another is defined mathematically by Equation 16. This can be interpreted as the function that results when one slides the mirror image of one function along the x-axis across the other, computes the product of the function and the mirrored function at each point, and integrates the area under this product. In other words, it is the area represented by the overlap of two functions as one slides over the entirety of the other [29].

$$\mathbf{f}(\mathbf{x}) * \mathbf{g}(\mathbf{x}) = \int \mathbf{f}(\mathbf{u})\mathbf{g}(\mathbf{x} - \mathbf{u})d\mathbf{u} \quad (16)$$

In this analysis, each energy spectrum is convolved with a Gaussian function defined to have a standard deviation given by the experimental FEP standard deviation. Only the central part of the convolution, of range equal to the range of the broadened energy spectrum, is taken as the resulting broadened simulation energy spectrum to be compared with the experimental results. The resulting spectrum is graphed along with its associated calibrated experimental energy spectrum in **Figure 23**. The data is scaled analogously by multiplying the GEANT spectra by the ratio of the Experimental FEP count to the GEANT FEP count, thus aligning the FEP counts. This was required exclusively in simulation and experimentation comparisons because there is no notion of running the simulation and the experimentation with the same

number of incident source particles. The experimental data was collected over a 24-hour period with a ^{137}Cs source and the simulation was run with 10,000,000 incident 662 keV gamma rays.

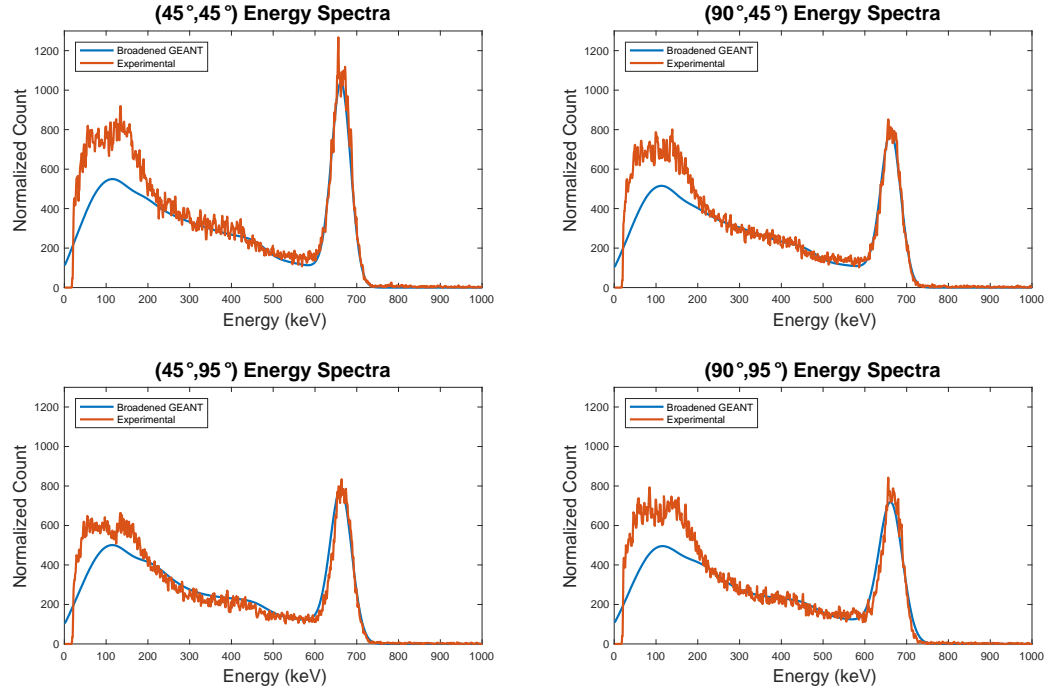


Figure 23. Graphical comparison of broadened (via convolution) GEANT simulation energy spectra and calibrated experimental spectra. The experimental data was collected over a 24h period with a ^{137}Cs source and the simulation was run with 10,000,000 incident 662 keV gamma rays.

It is clear that there is good agreement of the simulated and experimental results down to about 200 keV. At this point, as expected, the results diverge. This results from the lack of uniform Gaussian broadening throughout the detected energy spectrum, interactions occurring within the unsimulated lab environment, and other facets of the detection electronics not accounted for.

In an attempt to correct for this non-constant Gaussian broadening within the NaI(Tl) detector, an alternative methodology for broadening is employed. This methodology employs a

semi-empirical relationship between the calibrated energy bin and the Gaussian standard deviation given by Equation 17. Where E in this formula is the energy bin given in MeV, previous work found that the constants a and b are equal to 0.0302704 and 0.659344 respectively for a 3" \times 3" Heath NaI detector [30].

$$\sigma_T(E) = a * E^b \quad (17)$$

Equation 17 is utilized to apply a Gaussian spread to the simulated data. This is accomplished by taking the energy deposited in the detector by each incident gamma photon, utilizing this and the calculated standard deviation for the detector at this energy to form a Gaussian distribution, sampling from this Gaussian distribution, and replacing the exact energy deposited in the detector with this sampled value. If a negative energy value is sampled, the Gaussian is resampled until a positive energy value is acquired. The data is then rebinned into a histogram. The results of this broadening algorithm (utilizing the published Heath constants) when applied to the simulated data are shown in *Figure 24* alongside the experimental energy spectra.

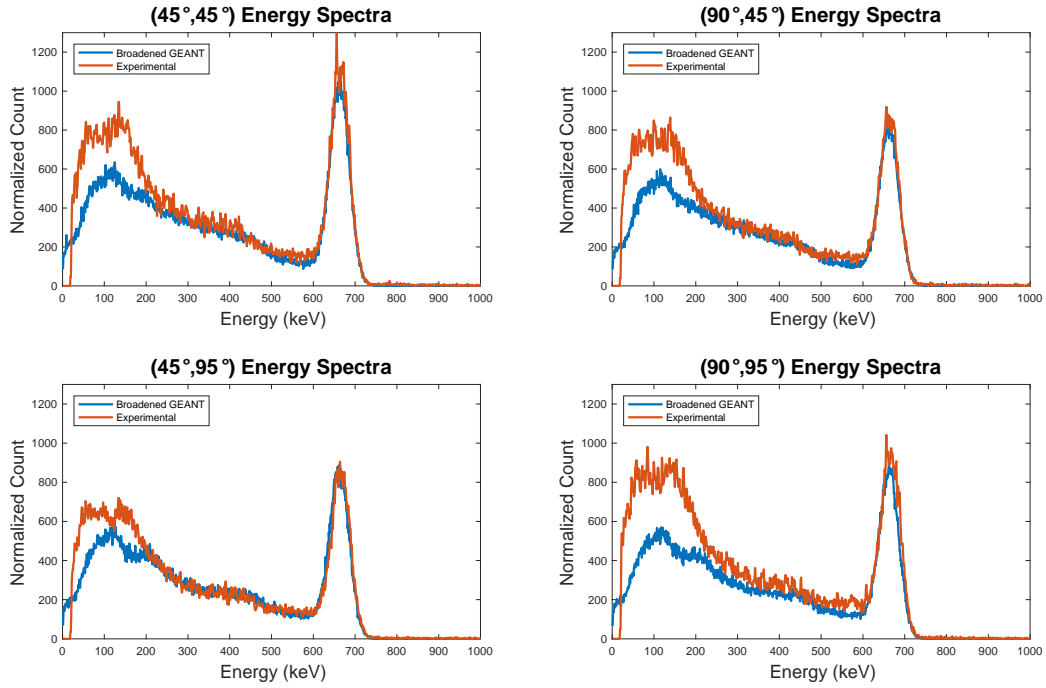


Figure 24. Graphical comparison of broadened (via resampling a Gaussian with standard deviation defined by published power law fit) GEANT simulation energy spectra and calibrated experimental spectra. The experimental data was collected over a 24h period with a ^{137}Cs source and the simulation was run with 10,000,000 incident 662 keV gamma rays.

Additionally, the constants, a and b , in the Equation 17 power law for the standard deviation of the Gaussian broadening formula as a function of energy were calculated for the particular detector utilized in this research. This was accomplished by calculating the standard deviation of each Gaussian FEP in the calibration data with background removed (*Figure 22*) (after calibrating it) and using this and the associated FEP energy value as the input to a least-squares fit to an equation in the form of a power law. Again with energy in MeV, the constants **a** and **b** were found to be 0.0356 and 0.7888 respectively. The results of the broadening algorithm described previously (utilizing the calculated parameters of the power equation) when applied to the simulated data are shown in *Figure 25* alongside the experimental results.

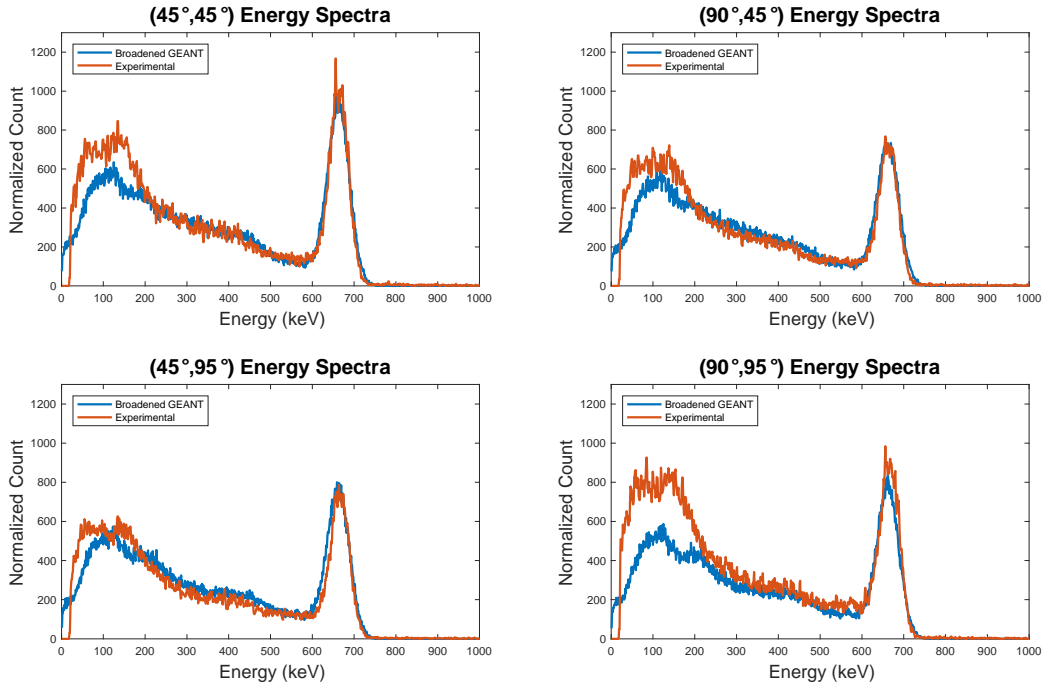


Figure 25. Graphical comparison of broadened (via resampling a Gaussian with standard deviation defined by power law derived for detector used in this effort) GEANT simulation energy spectra and calibrated experimental spectra. The experimental data was collected over a 24h period with a ^{137}Cs source and the simulation was run with 10,000,000 incident 662 keV gamma rays.

These three broadening methodologies are compared in *Table 9*, in terms of their χ^2 statistic. This is defined as the sum of the squared errors divided by the experimental value. It should be noted that this method of comparison is subject to binning errors. This sum is calculated for each methodology and each source position using first the entire energy range and then the energy range from 200 keV and above. It is shown that the Gaussian resampling with derived power law standard deviation is superior when the entire energy spectrum is employed. Contrarily, *Table 10* shows that the convolution of a Gaussian defined by the experimental ^{137}Cs FEP standard deviation with the simulated data is superior when only energy bins 200 keV-1098 keV are considered. This result is not surprising as there is likely some variation in the standard deviation that is not captured in the power law fit. Thus, using the actual standard deviation at

energies around the ^{137}Cs FEP to broaden the data leads to a better fit. But, if one seeks to minimize the accumulated error when all energies are considered, the power law fit produces the superior result.

Broadening Methodology	(45°,45°)	(90°,45°)	(45°,95°)	(90°,95°)
Gaussian Convolution with ^{137}Cs FEP Standard Deviation	39673.85	34938.26	32149.62	38590.50
Gaussian Re-sampling with Published Power Law Standard Deviation	45412.11	42950.78	34100.89	52408.26
Gaussian Re-sampling with Derived Power Law Standard Deviation	38057.36	38612.60	39519.21	45867.12

Table 9. χ^2 statistic calculated to compare the entire experimental energy spectrum and the entire broadened simulated energy spectrum for each of the (θ, φ) source positions. Three different broadening methodologies are employed and the Gaussian re-sampling with derived power law standard deviation is shown to be superior. The experimental data was collected over a 24h period with a ^{137}Cs source and the simulation was run with 10,000,000 incident 662 keV gamma rays.

Broadening Methodology	(45°,45°)	(90°,45°)	(45°,95°)	(90°,95°)
Gaussian Convolution with ^{137}Cs FEP Standard Deviation	4174.87	2821.95	4857.30	6229.57
Gaussian Re-sampling with Published Power Law Standard Deviation	5358.53	4411.26	3684.25	9045.32
Gaussian Re-sampling with Derived Power Law Standard Deviation	5176.28	5788.53	7597.97	6888.56

Table 10. χ^2 statistic calculated to compare the 200 keV-1098 keV experimental energy spectrum and the 200 keV-1098 keV broadened simulated energy spectrum for each of the (θ, φ) source positions. Three different broadening methodologies are employed and the convolution of a Gaussian defined by the experimental ^{137}Cs FEP standard deviation with the simulated data is shown to minimize the error. The experimental data was collected over a 24h period with a ^{137}Cs source and the simulation was run with 10,000,000 incident 662 keV gamma rays.

Thus, the experimental energy spectra have been calibrated to allow for experimental and simulation comparisons in the subsequent sections. Additionally, different methodologies for

broadening of the simulated results have been employed. This, as well, will allow the comparison of the experimental and simulated energy spectra and detector response curves in Section 5.5 and Section 5.6.

5.5 Energy Spectra Experiment/GEANT Comparisons

Firstly, it should be noted that there is an issue with the experimental data obtained for positions corresponding to a phi direction of 115°. This became obvious as the data was analyzed and will be pointed out in subsequent comparisons.

In Section 5.4, it was found that broadening the simulated spectrum via convolution with a Gaussian function defined by the experimental ^{137}Cs FEP standard deviation, produced superior agreement over the range where simulated and experimental data did not diverge (200 keV – 1098 keV). This broadening was required because one is seeking to compare the energy spectra resulting from a simulated detector with perfect energy resolution and an experimental detector with inherently imperfect energy resolution. These energy distributions are depicted in *Figure 23* and will be compared statistically in this section via the statistical methodology discussed in Section 2.5.

As with the comparisons of the two simulation results, a rigorous statistical comparison is sought. As such, the two nonparametric statistical tests, the Anderson-Darling k-sample test and the Kolmogorov-Smirnov test, will again be employed on the energy spectra from 200 keV – 1098 keV (above the range where the distributions tend to diverge). The χ^2 statistic in *Table 10* showed that the ‘Gaussian Convolution with ^{137}Cs FEP Standard Deviation’ broadening methodology produces superior agreement between the simulated and experimental results over this energy range. Despite taking this into account, *Table 11* shows that both statistical tests

clearly demonstrate that the two distributions could not have statistically been drawn from the same energy distribution. Thus, the experimental and simulated energy spectra are not statistically indistinguishable even over this subset of the spectrum where the agreement is generally the closest.

Energy Spectra GEANT/Experimental Comparison		
(θ, φ) Source Position	Anderson–Darling Test P-Value	Kolmogorov–Smirnov Test P-Value
(45°,45°)	1.2558e-15	0
(90°,45°)	3.0068e-14	0
(45°,95°)	1.1531e-12	0
(90°,95°)	1.3693e-09	0

Table 11. Non-parametric statistical comparison test results for each of the 4 static mask source positions considered. The data used in each test represents the count within energy bins 200 keV-1098 keV for calibrated experimental data and GEANT data broadened via convolution with a Gaussian function defined by the ^{137}Cs FEP standard deviation. All p-values resulting from both the application of the Anderson–Darling Test and the Kolmogorov–Smirnov Test show that the two codes produce resulting detector response curves that are statistically distinguishable. Thus, the results of experiment and simulation could not have been drawn from the same distribution. The experimental data was collected over a 24h period with a ^{137}Cs source and the simulation was run with 10,000,000 incident 662 keV gamma rays.

Thus, it has been shown that the experimental and simulated energy spectra are not statistically indistinguishable, even when one considers the portion of the spectrum above 200 keV where the distributions tend to converge. There are a variety of potential causes for these differences, but they are mainly related to the experimental data acquisition and post-processing. The experimental calibration and background data had to be retaken and, due to differences in the lab radiation environment, the retaken data could not be used for background determination. The external background sources of radiation certainly account for part of the differences observed. Additionally, an imperfect job was done in calibrating the experimental data as the calibration information had to be recollected. Also, the differences in detector efficiency with

energy could not be accurately recollected. It is expected that there would also be some variability in detector efficiency and degree of Gaussian broadening with the source position relative to the detector assembly due to the geometry of the mask and detector. These differences were not accounted for within the simulation or experimental data post-processing and account for some of the spectral differences observed.

Fortunately, the imaging system is not dependent on perfect agreement throughout the energy spectra. The detector response curves consist of a specific facet of the spectrum acquired as the scatter mask rotates. This facet is either the count of the particles contributing to the FEP or the integral beneath the Compton Continuum. The comparison of these curves, which is much more critical to source imaging, is considered in Section 5.6.

5.6 Detector Response Curve Experiment/GEANT Comparisons

The GEANT and Experimental detector response curves will now be compared in a manner analogous to the way that the GEANT and MCNP detector response curves were compared in Section 5.3. Again, two non-parametric statistical tests, the Kolmogorov-Smirnov test and the Anderson-Darling test, are applied and the resulting P-Values are found in **Table 12** and **Table 13**. The detector response curves calculated from both the FEP count and the integral beneath the Compton continuum are both considered. As in the simulations to compare with MCNP, a simulation is run for each 10° increment of phi ($\varphi = 5^{\circ} - 175^{\circ}$). Each point in each detector response curve is associated with a (θ, φ) position of the source relative to the detector, for which 500,000 incident 662 keV gamma rays were simulated. Each experimental detector response curve was collected over a 24h period.

Unlike in the comparison between GEANT and MCNP, one cannot simply run the simulation and experiment with the same number of incident particles. This inability would also occur if one were to employ this system for source detection in the field. As such, some normalization is required prior to comparison. A normalization by the integral underneath each detector response curve is utilized. This is equivalent to the sum of the total number of particles that contribute to the FEP or the Compton Integral through the complete rotation of the mask for one phi angle. Alternative normalization schemes, including normalizing by the ratio of the maximum and minimum count for a θ position, were found to provide inferior agreement between the experimental and GEANT results. Thus, this simple normalization technique is employed.

The derivation of the FEP and Compton Integral detector response curves for the experimental comparisons is somewhat more involved than for the simulation cases. This is due to the fact that the experimental data requires energy calibration and due to the fact that the experimental data has an inherent Gaussian broadening due to imperfect energy resolution in the detector. This, in turn, impacts the way that these values should be derived from the simulated energy spectra. Discussion of the derivation of each of these values is found below.

1. Experimental Detector Response Curve Derivation

The energy calibration is achieved in the manner described in Section 5.4.

- a. Compton Integral – This is defined as the sum of counts within bins representing energy deposition of 200-480 keV within the NaI(Tl) detector. This range was used because Section 5.4 demonstrated that the energy spectra diverged below 200 keV.

b. FEP – To determine the FEP count for each experimental energy spectrum associated with each (θ, φ) position, a Gaussian is fit to the FEP (following background removal), the area under this Gaussian is approximated by integrating the Gaussian from -2σ to 2σ , and this integral is divided by the percentage of the Gaussian found within this range, 0.9545. This indirect integral calculation is required because the Gaussian fit extends to infinity in either direction.

2. Simulated Detector Response Curve Derivation

In the derivation of the simulated detector response curves, one must now consider the broadened nature of the experimental data to which one is comparing. In Section 5.4, three methodologies for broadening the data were employed and it was determined that a convolution of the simulated data with a Gaussian function defined by the standard deviation at the FEP provided the best agreement between the experimental data and the simulated data for energies in excess of 200 keV. In this broadening, the standard deviation given by Equation 17, with the detector derived parameters of 0.0356 and 0.7888, is utilized. As such, the simulated data was broadened in this manner and this broadened data represents the simulated data used to derive the simulated detector response curves which are then compared to the inherently broadened experimental data. This broadening is shown in **Figure 26** to have little impact on the simulation Compton Integral detector response curves as the gross counts differ by less than 3% in each binned angle, but it is shown to have an important impact on the simulation FEP detector response curves in that it substantially improves agreement with the experimental results.

a. Compton Integral - In a manner analogous to that employed to derive the experimental Compton Integral, the simulated Compton integral was obtained by summing the resulting count in bins from 200 keV to 480 keV within the

broadened, via convolution, simulated energy spectra. The difference between the detector response curve derived from the convolved simulated spectra and the unconvoluted is minimal. An example of this difference for a representative phi position is shown in **Figure 26**.

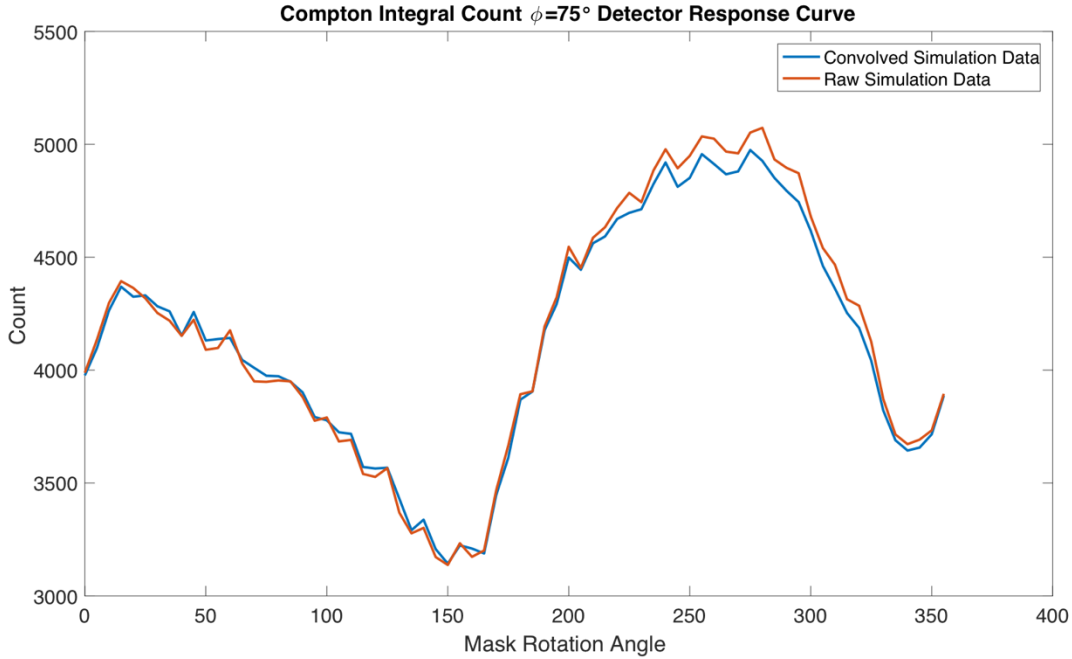


Figure 26. Comparison of Compton Integral detector response curve derived from broadened and unbroadened simulation energy spectra. It is shown that the broadening has little impact on the detector response curve obtained from the energy spectra. Broadening is achieved via convolution of the energy spectra with a Gaussian defined by the FEP standard deviation of the associated experimental energy spectrum.

- b. FEP - In a manner analogous to that employed to derive the experimental FEP values for each (θ, φ) point in the detector response curve, the simulated FEP is obtained via a Gaussian fit to the FEP contained within the convoluted simulation energy spectra. The integral under this Gaussian is approximated by integrating the Gaussian from -2σ to 2σ and dividing by the percentage of the Gaussian found within this range (95.45%). Initially, the simulation of a detector with

perfect energy resolution was taken advantage of and the FEP was taken to be simply the count of incident particles that deposit all of their energy, 662 keV, directly into the detector volume. This is shown in Table 12 to result in lack of agreement between the experimental and simulated detector response curves, as it fails to account for broadening phenomena experienced in the experimental situation.

FEP GEANT/Experimental Comparison – Derived from Unbroadened Simulated Data		
(θ, φ) Source Position	Anderson–Darling Test P- Value	Kolmogorov–Smirnov Test P- Value
(0°,5°)	0.05269	0.27000
(0°,15°)	0.10676	0.19181
(0°,25°)	0.04305	0.27000
(0°,35°)	0.05727	0.19110
(0°,45°)	0.04206	0.19110
(0°,55°)	0.00351	0.03578
(0°,65°)	0.00150	0.01329
(0°,75°)	0.00051	0.00227
(0°,85°)	0.00054	0.00241
(0°,95°)	0.00096	0.00418
(0°,105°)	0.00290	0.00773
(0°,115°)	0.00015	0.00030
(0°,125°)	0.00530	0.05713
(0°,135°)	0.01339	0.13142
(0°,145°)	0.18214	0.37220
(0°,155°)	0.04985	0.08787
(0°,165°)	0.00410	0.02222
(0°,175°)	0.00818	0.02222

Table 12. Non-parametric statistical comparison test results for each 10° increment of phi ($\varphi = 5^\circ - 175^\circ$). Each point in each spectrum compared is defined by the number of source particles that contribute to the unbroadened FEP (deposit exactly 662 keV in the detector volume), out of 500,000 simulated particles per (θ, φ) position and experimental results collected over 24h. At a 0.05 significance level, the bolded p-values indicate that the

simulated and experimental results are unlikely to be drawn from the same distribution. Thus, the degree of agreement between the simulated and experimental FEP detector response curves is insufficient and the broadened simulation spectra is required.

This is the case because the number of photons depositing energy in the experimental detector between the Compton cutoff and the FEP differs as a function of rotation angle, just as the true FEP count does. These are intentionally not included within the FEP count calculated via the Gaussian fit to the experimental data because background is removed prior to fitting. When these are removed, however, some true FEP counts are also removed due to the inherent broadening in the experimental spectrum. Thus, the number of these excluded FEP counts varies with rotational angle of the mask, which distorts the FEP count calculated via the Gaussian fit and subsequent integral. This effect is not taken into account if one simply sums the number of gammas that deposit precisely 662 keV into the simulated detector with no energy broadening. As such, the simulated FEP is derived from the convoluted simulated energy spectra in the same manner as the experimental FEP is derived from the inherently broadened experimental energy spectra. Namely, as stated above, a Gaussian function is fit to the FEP energy data range and the integral beneath this fitted curve is approximated.

Now that the Compton Integral and FEP detector response curves have been obtained in the same manner for both the simulated and experimental datasets, statistical comparisons may be conducted. The Compton Integral detector response curves are considered first. The results of this comparison via the Anderson-Darling and Kolmogorov-Smirnov tests are shown in **Table 13**. It is clear from this chart and the subsequent graphs that there is a statistically significant difference between these curves. The set of experimental Compton Integral detector response curves does not show sufficient differentiation in θ differently for each φ angle and, thus, does

not contain the requisite information to derive the source direction and serve as a library for source imaging. On the other hand, the simulated data was shown to be sufficiently differentiated for all but the extreme phi angles. Agreement only occurs when the GEANT curve also fails to be differentiated in θ , as was the case for the more extreme phi angles. A conservative confidence level of 99% (significant level of 0.01) is utilized because the functioning of the imaging system does not require an exact match, but only that the curves associated with a given (θ, φ) source position match better than any of the alternative curves in the library. This is equivalent to saying that the probability of rejecting the null hypothesis when it is true is 1%. Thus, if we repeat the test many times with two curves that could have been drawn from the same distribution, we will only say that they are not identical 1% of the time. Despite the use of this confidence level, the Compton Integral detector response curves from experiment and simulation clearly do not agree, as shown in *Table 13*.

Compton Integral GEANT/Experimental Comparison		
(θ, φ) Source Position	Anderson–Darling Test P- Value	Kolmogorov–Smirnov Test P- Value
$(0^\circ, 5^\circ)$	0.61283	0.49098
$(0^\circ, 15^\circ)$	0.00004	0.00061
$(0^\circ, 25^\circ)$	0.00004	0.00008
$(0^\circ, 35^\circ)$	0.00005	0.00003
$(0^\circ, 45^\circ)$	0.00006	0.00007
$(0^\circ, 55^\circ)$	0.00002	0.00007
$(0^\circ, 65^\circ)$	0.00001	0.00061
$(0^\circ, 75^\circ)$	0.00000	0.00034
$(0^\circ, 85^\circ)$	0.00000	0.00004
$(0^\circ, 95^\circ)$	0.00000	0.00000
$(0^\circ, 105^\circ)$	0.00001	0.00014
$(0^\circ, 115^\circ)$	0.00000	0.00001
$(0^\circ, 125^\circ)$	0.00000	0.00004
$(0^\circ, 135^\circ)$	0.00000	0.00000

(0°,145°)	0.00003	0.00003
(0°,155°)	0.00008	0.00002
(0°,165°)	0.14896	0.49098
(0°,175°)	0.01082	0.00437

Table 13. Non-parametric statistical comparison test results for each 10° increment of phi ($\varphi = 5^\circ - 175^\circ$). Each point in each spectrum compared is defined by the number of source particles that contribute to the Compton Integral (deposit 200 - 480 keV in the detector volume), out of 500,000 simulated particles per (θ, φ) position and experimental results collected over 24h. At a 0.01 significance level, the majority (bolded) of the detector response curves fail to indicate statistical and experimental agreement. Thus, the detector response curve based on Compton Integral is not useful for source position determination. This is clearly demonstrated in the subsequent graphical comparisons (Appendix B). Agreement only occurs when the GEANT curve also fails to be differentiated in θ .

An additional statistical comparison methodology is again employed, which consists of the comparison of the confidence intervals around each count for each (θ, φ) position. Due to the normalization by a constant value, the GEANT and Experimental 90% confidence intervals for each point are given by Equation 18, where \hat{p}_l is the likelihood that a count falls within a given (θ, φ) position and N (a constant value) is the integral underneath the detector response curve for that methodology (experimental or GEANT) and phi angle. This equation was derived in Section 2.5.

$$\text{Stdev}(\hat{p}_l) = \sqrt{\text{Var}(\hat{p}_l)} = \sqrt{\frac{1}{N} p_i (1 - p_i)} \quad (18)$$

Thus, the 90% confidence interval is given by

$$\hat{p}_l \pm 1.645 * \text{Stdev}(\hat{p}_l).$$

The resulting graphs displaying these detector response curves and 90% confidence intervals for the Compton Integrals are found in Appendix B, with a representative curve for $\varphi = 45^\circ$ found in **Figure 27**. The lack of agreement is made abundantly clear and validates the results

found in **Table 13**. This is a consequence of the nearly flat Compton Integral detector response curve derived from the experimental data. In fact, the qualitative trends in these two curves are nearly opposite. This is likely due to the previously mentioned potential for Compton scatter within both the mask and the detector. The concurrent impact of both effects on the Compton integral affects the results.

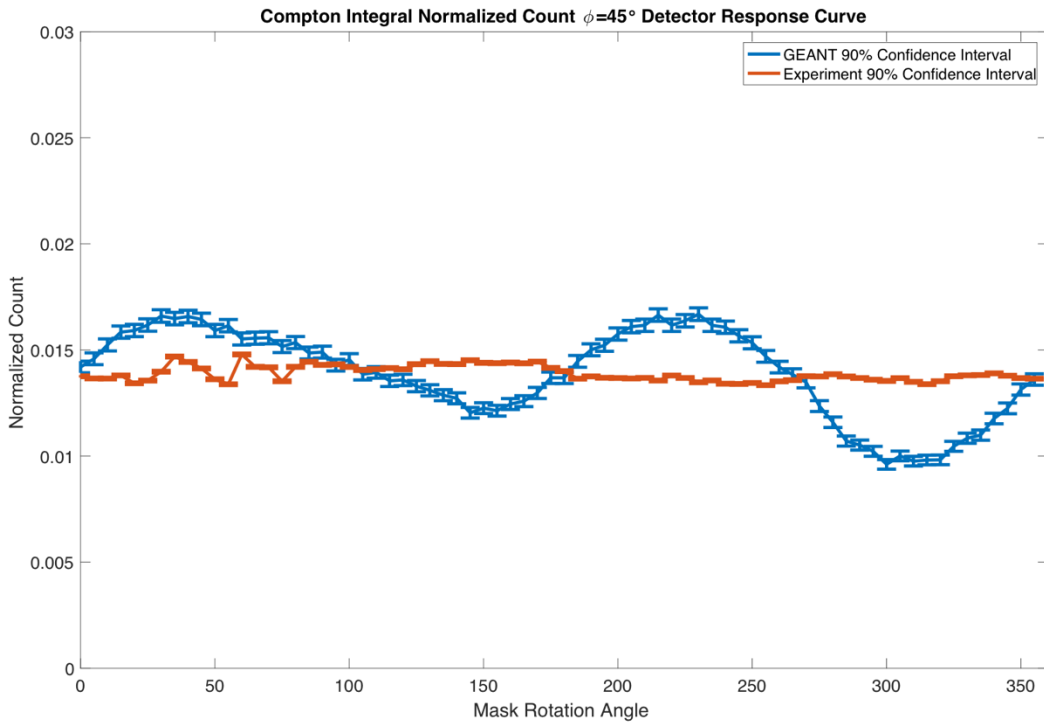


Figure 27. Normalized count (per total count in the detector response curve) that contribute to the Compton Integral (200 keV – 480 keV) for $\varphi = 45^\circ$ with $\theta = 0^\circ - 355^\circ$ in increments of 5° . These values correspond to GEANT results with 500,000 source particles for each (θ, φ) position and experimental results collected over 24h. The 90% confidence interval is plotted.

The statistical comparison of the FEP detector response curves is now considered. Again, the results of the application of the Anderson-Darling and Kolmogorov-Smirnov tests will be considered followed by a confidence interval and graphical comparison. The p-values resulting from the non-parametric statistical tests are shown in **Table 14**. For the same reasons as cited

previously for the comparison of the Compton Integral detector response curves, a conservative confidence level of 99% (significant level of 0.01) is again employed to judge the degree of similarity between the FEP detector response curves. As stated when the theory was discussed, the Anderson-Darling is the more powerful of the two tests employed and this is clearly seen in that this test concludes that the two distributions could not be drawn from the same distribution for $\varphi = 5^\circ, 85^\circ, 115^\circ, 165^\circ$. Two of these are for extreme values of phi where the system is not expected to operate well due to small variation in the thickness of mask material presented to the source as the mask rotates. As stated previously, there was probably an error in the experimental run at 115° so this disagreement should not be considered. Finally, for $\varphi = 85^\circ$, the p-value is nearly large enough to allow acceptance of the null hypothesis that the two curves are identically distributed, given the P-value chosen. If one considers the less powerful Kolmogorov–Smirnov test, the agreement is predicted to be even better in that the only curves that fail to agree are those for $\varphi = 115^\circ$, for which there was a recognized error in the experimental data acquisition. Thus, there is sufficient agreement between the GEANT and experimental data to conclude that the simulation has been validated against experiment and that it can be utilized to generate a library of curves capable of forming the basis of a radioactive source imaging algorithm.

FEP GEANT/Experimental Comparison – Derived from Broadened (via Convolution) Simulated Data		
(θ, φ) Source Position	Anderson–Darling Test P- Value	Kolmogorov–Smirnov Test P- Value
$(0^\circ, 5^\circ)$	0.0033463	0.02186591
$(0^\circ, 15^\circ)$	0.37549	0.3721987
$(0^\circ, 25^\circ)$	0.41592	0.769547
$(0^\circ, 35^\circ)$	0.36133	0.769547

(0°,45°)	0.18449	0.4938319
(0°,55°)	0.060512	0.1316586
(0°,65°)	0.023857	0.1316586
(0°,75°)	0.015072	0.08778698
(0°,85°)	0.0088668	0.02186591
(0°,95°)	0.016873	0.03578049
(0°,105°)	0.053276	0.1316586
(0°,115°)	0.00048322	0.000609175
(0°,125°)	0.022341	0.05686472
(0°,135°)	0.098328	0.2713245
(0°,145°)	0.92734	0.9956171
(0°,155°)	0.17919	0.3721987
(0°,165°)	0.0054124	0.03578049
(0°,175°)	0.27495	0.1316586

Table 14. Non-parametric statistical comparison test results for each 10° increment of phi ($\varphi = 5^\circ - 175^\circ$). Each point in each spectrum compared is defined by the number of source particles that contribute to integral beneath a Gaussian curve fitted to the broadened simulation FEP (via convolution using the standard deviation calculated via the derived equation 18), out of 500,000 simulated particles per (θ, φ) position and experimental results collected over 24h. At a 0.01 significance level, the bolded p-values indicate that the simulated and experimental results are unlikely to be drawn from the same distribution. φ of 115° should be discounted due to an experimental error at this angle. Thus, all curves are shown to agree via the Kolmogorov–Smirnov Test.

It is clear from the detector response curves in Appendix B that it is nonsensical to compare the percentage of confidence intervals that overlap between the GEANT and experimental results, as was done for the GEANT and MCNP results. This is the case because very few of the confidence intervals overlap. Despite this, it is clear from the plots and the statistical analysis presented in *Table 14* that the FEP curves agree to a sufficient extent to allow source determination via comparison. This is not the case for the Compton Integral detector response curves. The simulation results indicated that the use of this part of the energy spectra contained information to allow imaging, but experimental results do not show adequate differentiation of count for each (θ, φ) position. The experimental confidence intervals are

narrower than the GEANT confidence intervals due to the larger counts per (θ, φ) position. To reiterate, each experimental detector response curve was collected over a period of 24 hours and the simulation consisted of 500,000 incident source gammas per (θ, φ) position. The FEP detector response curves, with their 90% confidence intervals, are visualized in Appendix B, with a representative example for $\varphi = 45^\circ$ shown in **Figure 28**.

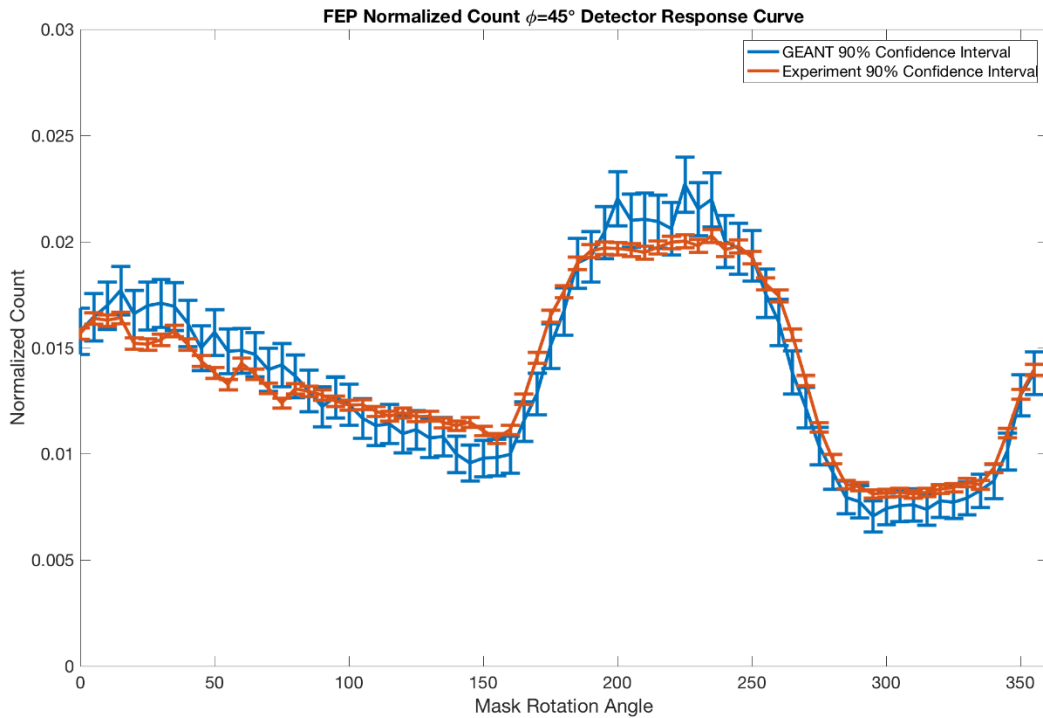


Figure 28. Normalized count (per total count in the detector response curve) that contribute to the FEP for $\varphi = 45^\circ$ with $\theta = 0^\circ - 355^\circ$ in increments of 5° . These values correspond to GEANT results with 500,000 source particles for each (θ, φ) position and experimental results collected over 24h. The 90% confidence interval is plotted. For each (θ, φ) position, the FEP count comes from a broadened energy spectrum (via convolution for GEANT data and inherently for experimental data).

Thus, the detector response curves, derived using the FEP and the Compton Integral, from experiment and GEANT simulation have been compared. The detector response curve

associated with the Compton Integral from simulation was shown to be differentiated in θ differently for each φ angle, and thus contained source position information useful in an imaging algorithm. Experimental results failed to contain this requisite differentiation and would not be useful for source position determination. Furthermore, simulation and experimental results were shown to differ in a statistically significant manner. On the other hand, the detector response curve based on the FEP was shown to be differentiated in θ differently for each φ angle for both the experimental and simulated data. Additionally, it has been shown that the two curves for identical source positions could have been drawn randomly from the same distribution for the vast majority of cases. Thus, the GEANT simulation has been shown to provide a sufficiently accurate proxy for the experimental RSM assembly. As a result, the simulation developed can be utilized as an efficient methodology for developing a library of detector response curves. This library allows the development of an algorithm to predict the (θ, φ) source vector from an unknown detector response curve (and source position). This algorithm is described in the subsequent section.

VI. Source Position Determination Algorithm

6.1 Algorithm Development

The validated simulation allows development of a detector response curve library that can be used to determine source direction. This section describes the algorithm used to image experimental detector response curves employing the validated GEANT simulation detector response curve library.

The experimentally obtained FEP detector response curve acquired as the RSM/detector assembly is exposed to a radioactive source at an unknown position relative to the detector serves as the algorithm input. To normalize the detector response curve, the FEP count at each point in the experimental curve is divided by the total number of counts in all of the FEP peaks forming the detector response curve. This scales the curve and also makes the normalized detector response curve time-independent. This normalization is discussed further in Section 5.6. The algorithm output consists of a predicted (θ, φ) vector pointing in the direction of the radioactive source relative to the center of the radiation detector. To produce this output, the algorithm compares the normalized experimental detector response curve against the library of broadened, normalized FEP detector response curves obtained from GEANT simulations as discussed in Section 5.6. Normalization of the simulated detector response curves is conducted in the same manner as the experimental results. The broadening technique of convolution

previously applied to the GEANT simulation energy spectra library allows the simulated detector response curve library to be viewed as a static input to the algorithm. This library consists of GEANT FEP detector response curves for each potential (θ, φ) combination with $\theta = 5^\circ - 360^\circ$ in increments of 5° and $\varphi = 5^\circ$ to 175° in increments of 10° . Each detector response curve consists of a normalized FEP count for each of the 72 discretized rotation angles of the mask, $\theta = 5^\circ$ to 360° in increments of 5° . Thus, this library takes the form of a matrix with the following dimensions: (72,18,72) associated with dimensions $(\theta, \varphi, shifted \theta)$.

The algorithm compares the experimental detector response curve against the entire library of simulated detector response curves, accumulating the simple mean squared error in each comparison. The mean squared error for an experimental input curve with the library curve associated with (θ_i, φ_j) is given in Equation 19 and forms the entry at (i, j) within the error matrix associated with the input experimental detector response curve.

$$\text{ErrorMatrix}(i, j) = \quad (19)$$

$$\sum_{rotationAngle=1}^{72} \frac{[SimLibrary(i, j, rotationAngle) - ExprCurve(rotationAngle)]^2}{72}$$

A plot of this error matrix as a function comparing an experimental detector response curve with each of the simulated library detector response curves for each of the 72 possible theta and 18 possible phi values allows creation of a 3D surface. **Figure 29** shows a representative example of such a surface. The location of minimum in this surface denotes the predicted source direction. The curve in the library with the minimum squared error indicates the FEP detector response curve that most closely matches the experimental curve and, thus,

denotes the (θ, φ) direction of the position of the mystery experimental source.

Also in **Figure 29**, the application of an alternative method of quantifying the difference between two detector response curves, the modal assurance criterion (MAC), is shown. This value quantifies the degree of proportion between two vectors, with a value near one indicating a strong linear relationship and a value near zero indicating near linear independence between the vectors. When this criterion, quantified in **Equation 20**, of similarity was applied for each experimental vector with each simulated library vector, the two criterion were found to always agree in their prediction of the experimental source position. In other words, the library curve with the smallest squared error was always found to align with the library curve with the largest MAC value [32].

(20)

$$MAC(\{SimLibrary(i,j)\}, \{ExprCurve\}) = \frac{|\{SimLibrary(i,j)\}^t \cdot \{ExprCurve\}|^2}{(\{SimLibrary(i,j)\}^t \cdot \{SimLibrary(i,j)\})(\{ExprCurve\}^t \cdot \{ExprCurve\})}$$

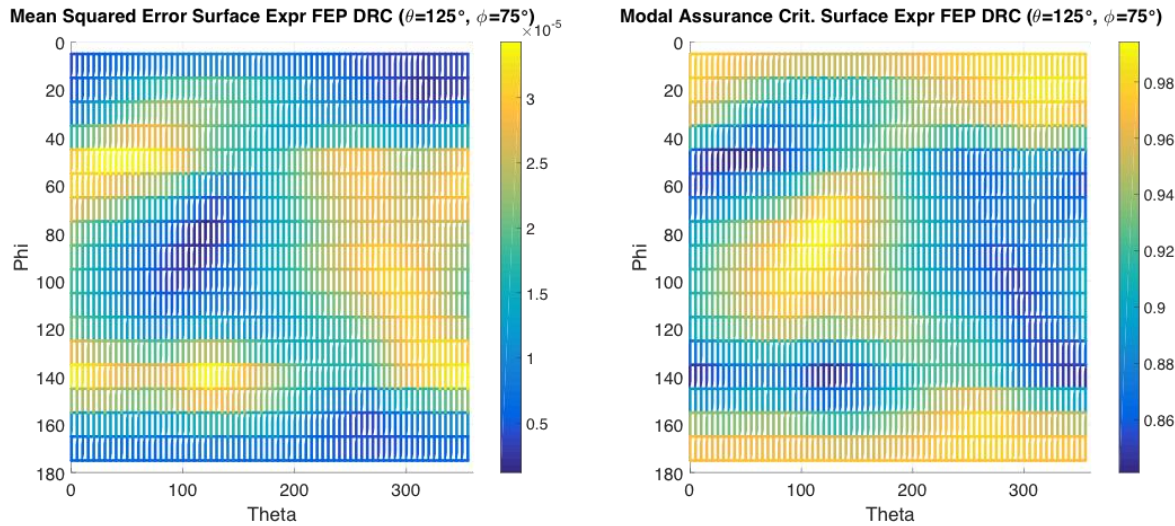


Figure 29. Representative error surface for an input experimental source position. The minimum value in this surface indicates the (θ, φ) vector pointing to the predicted source location. Two methods of quantifying the difference between vectors have been applied. The mean squared error and the modal assurance criterion are shown to predict the same source location.

The true position associated with the experimental input detector response curve inputted to the algorithm and represented by *Figure 29* is $(\theta, \varphi) = (125^\circ, 75^\circ)$. The global minimum in this surface occurs at $(\theta, \varphi) = (125^\circ, 75^\circ)$ and, thus, the algorithm predicts the correct source location. The two detector response curves associated with this matching are shown in

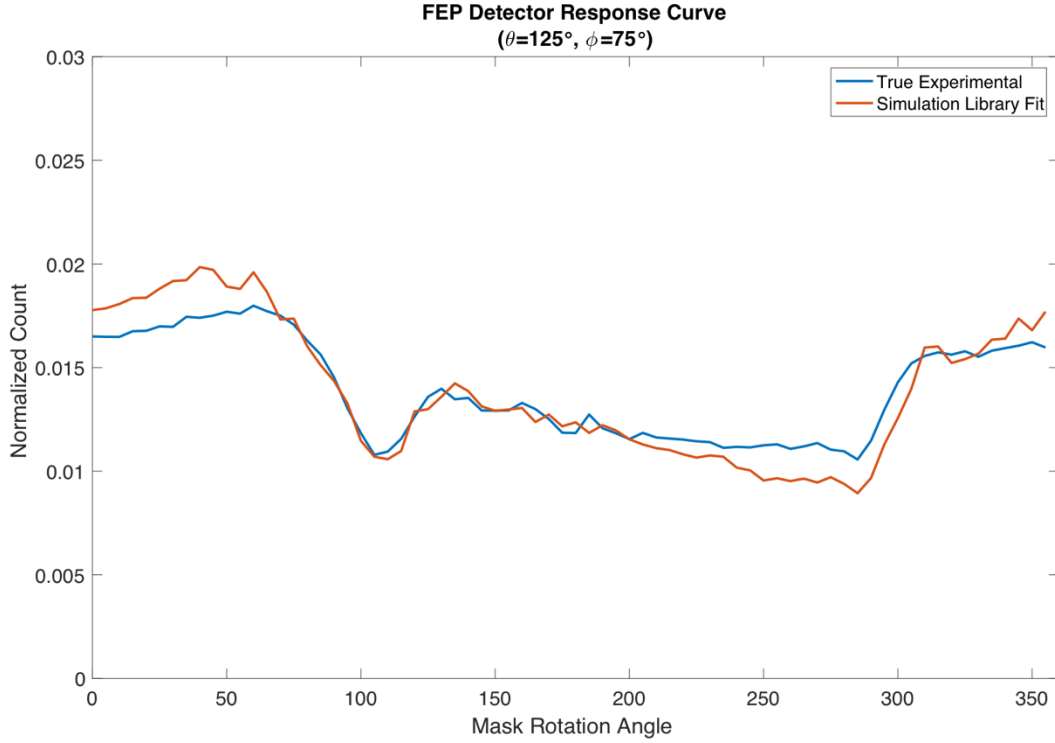


Figure 30. Detector response curves associated with the normalized experimental input detector response curve and the library detector response curve associated with the prediction of the source position (associated with the minimum in *Figure 29*).

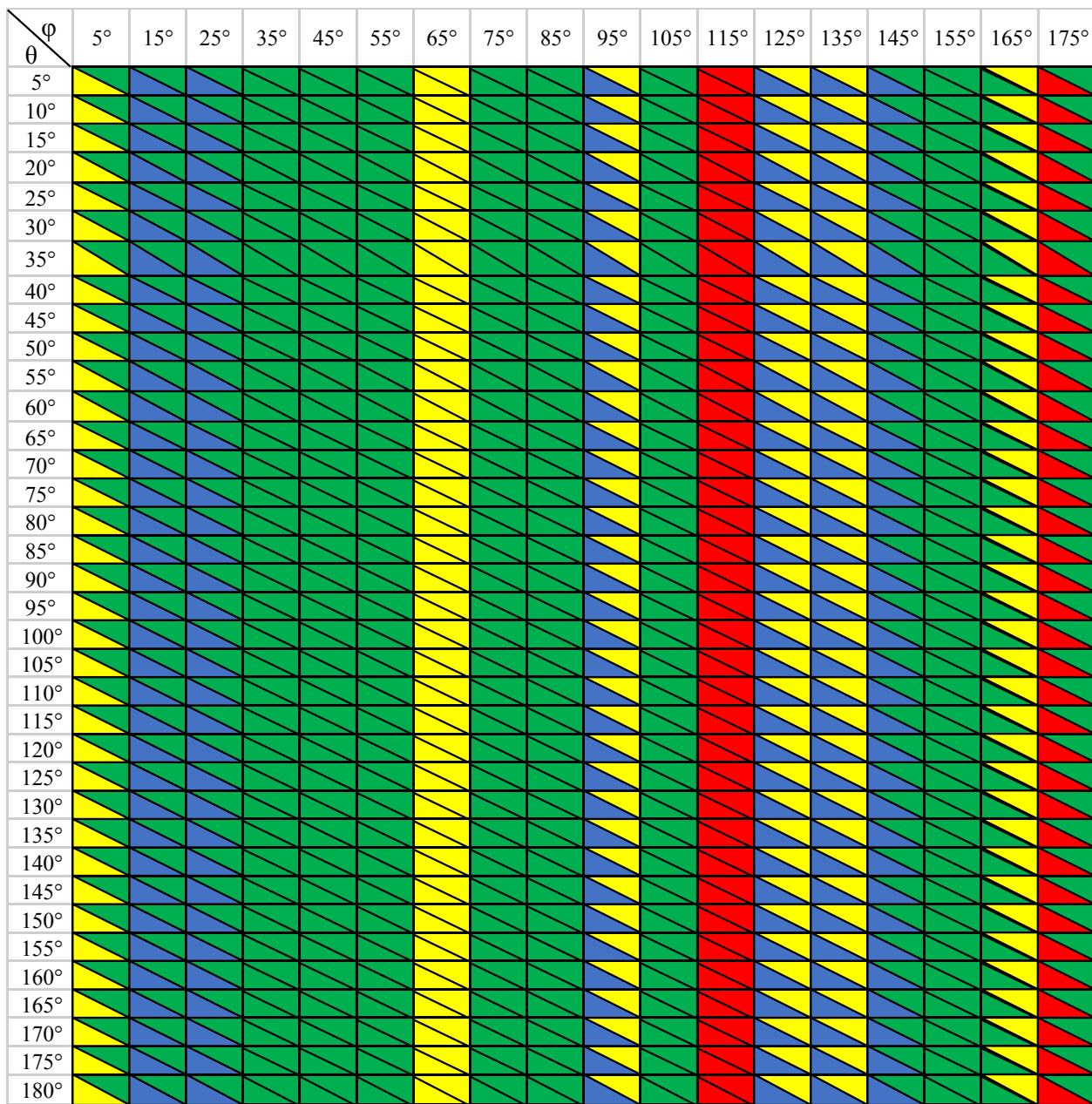
6.2 Algorithm Results

This simple algorithm used works remarkably well. To test its functionality, experimental detector response curves for each potential source position (θ, φ) combination with $\theta = 5^\circ$ to 360° in increments of 5° and $\varphi = 5^\circ$ to 175° in increments of 10° were fed into the algorithm. The algorithm completed this set of 1296 source direction determinations in less than a second, implying the algorithm computational time is of negligible concern. The resulting errors in the predicted (θ, φ) source directions are shown in *Figure 31* and *Figure 32*, for each of the true experimental source positions. The complete set of errors are found in Appendix C.

The colors used in **Figure 31** and **Figure 32** represent the difference between the true, known experimental source vector and the source vector predicted via the algorithm (which used the GEANT FEP detector response curve library). For example, the upper left value represents the error in the predicted source position for a true experimental source located at a position associated with the vector ($\theta = 5^\circ, \varphi = 5^\circ$). The algorithm predicted the correct phi value of $\varphi = 5^\circ$ and a theta value that was off by 10° , in this case predicting that $\varphi = 15^\circ$. Excluding the erroneous experimental run at $\varphi = 115^\circ$, for which the accuracy of the (θ, φ) vector is poor, the average (absolute value) errors of both the azimuthal angle θ and polar angle φ are less than 5° . This is a good result as the resolution in θ is 5° and the resolution in φ is 10° .

It must be noted that the set of input experimental detector response curves consist of 18 unique experiments. The complete set of 1296 input curves can be obtained from these 18 curves because a change in the source position associated with a different θ angle for the same φ angle simply represents a shift of the $(\theta, \varphi) = (0^\circ, \varphi)$ curve by the angle associated with the experimental position in θ . Put in a different way, different source positions with the same φ simply represent different starting points of tracking of the rotation angle of the mask in θ . Thus, the curve shapes are identical, but shifted in their position along the θ axis.

Due to this feature of the experimental input dataset, all input curves which represent positions with the same φ polar angle will have the same detector response curve shape, with the offset indicating the different θ azimuthal angle of the source. Thus, when the algorithm is applied to this set of curves, if the φ angle is predicted correctly, but there is an error in the θ angle predicted, this same error will occur with all φ angle experimental positions. This effect is clear in **Figure 31** and **Figure 32**.



Key: Error in Predicted
Source Vector Component
 increments of 5° and ϕ = 5° to 175° in increments of 10°,
source position is presented. This source position is predicted utilizing a simulation-derived
 library of detector response curves.
 5° error
 10° error
 >10° error

Figure 31. For true experimental source positions associated with $\theta = 5^\circ$ to 180° in increments of 5° and $\phi = 5^\circ$ to 175° in increments of 10°, the error in the predicted source position is presented. This source position is predicted utilizing a simulation-derived library of detector response curves.

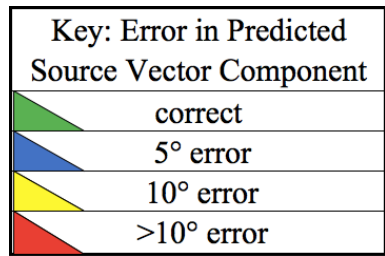
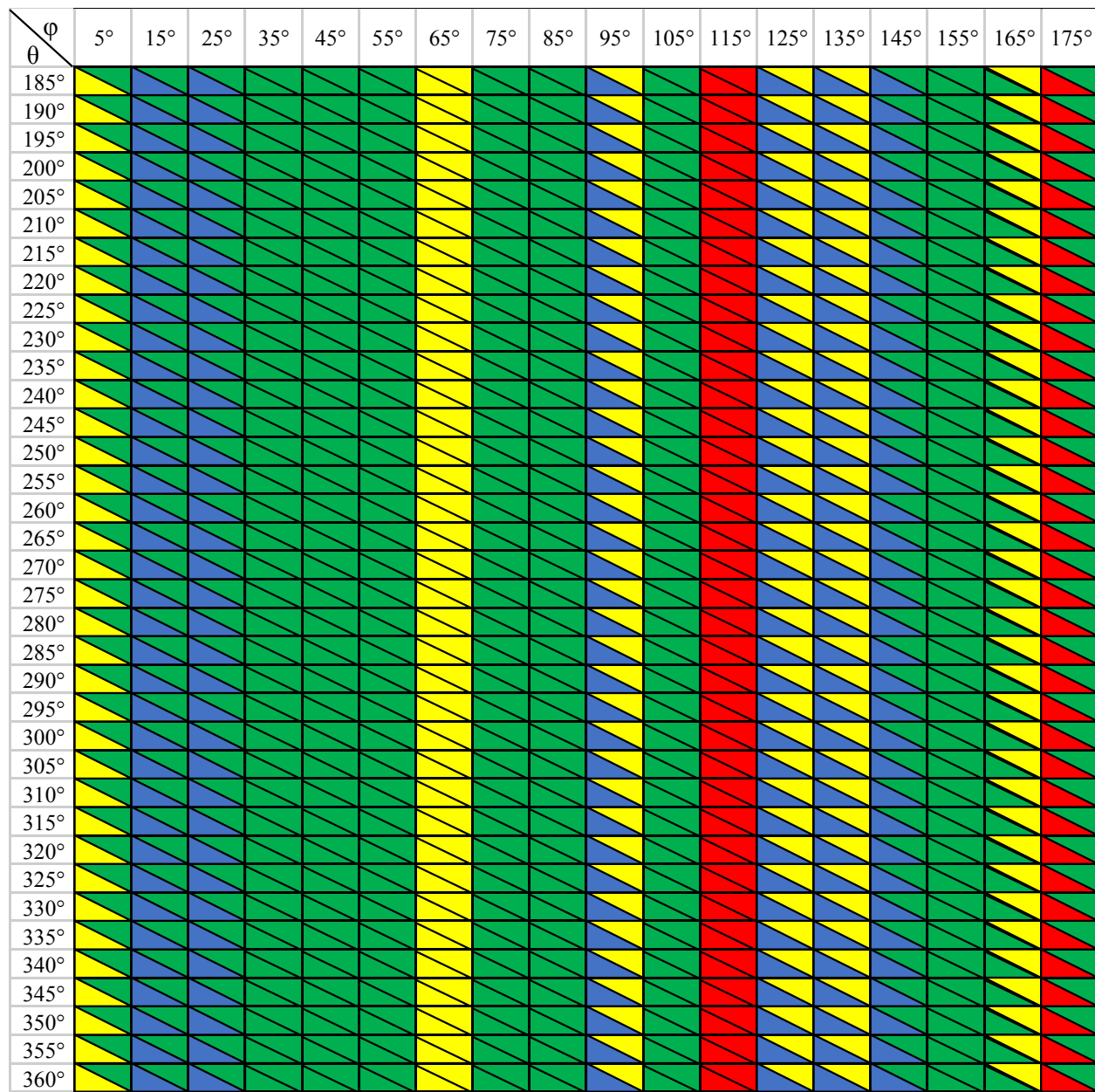


Figure 32. For true experimental source positions associated with $\theta = 185^\circ$ to 360° in increments of 5° and $\varphi = 5^\circ$ to 175° in increments of 10° , the error in the predicted source position is presented. This source position is predicted utilizing a simulation-derived library of detector response curves.

VII. Conclusion

7.1 Overview

This research provides a proof-of-principle for the continuing development of a Gamma Rotating Scatter Mask Detection System. The agreement in the comparison of Geant4 and MCNP6 simulations, and agreement between the Geant4 simulations and experimentally obtained data, demonstrates that both applications developed may be used for future modeling and simulation to support further system development and optimization in the future. The ability to compare experimental and simulated FEP detector response curves in order to predict direction of a radioactive source shows the efficacy of the RSM as an imaging device.

This research demonstrated the effective development of a gamma imaging system via the fitting of a simple scintillation detector with a rotating scatter mask. Analysis of experimental FEP data obtained during the rotation of the scatter mask allows creation of a detector response curve that can be compared against a library of simulated detector response curves to determine radioactive source direction relative to the detector in (θ, φ) . This effort contributes a validated simulation that allows one to efficiently derive this library of curves as well as experiment with alternative mask designs and source specifications.

The key achievements of this research:

- Verification that both the Geant4 and MCNP6 applications developed can be used for future development of a Gamma RSM Detection System
- Development of a Geant4 simulation that can be used to create a library of detector response curves or a detector response surface at other gamma energies of interest

- Proof-of-Principle that a “dumb” detector, retrofitted with a rotating polymethacrylate RSM can be used to determine the direction of a radioactive source relative to the detection system

The conclusions of the MCNP6/Geant4 comparisons, experimental/Geant4 comparisons, imaging algorithm, and recommendations for future work will now be discussed in further detail.

7.2 MCNP/GEANT Comparisons

This research demonstrated that MCNP6 and Geant4 are both effective modeling and simulation tools for development of the Gamma RSM Detection System. Comparison of the simulated energy spectra showed that MCNP and GEANT energy spectra were statistically indistinguishable, in that they could have been randomly drawn from the same distribution. Furthermore, for both MCNP and GEANT, the detector response curves defined by the FEP and the Compton Integral for each θ rotation angle for each φ were shown to be statistically indistinguishable for all but the most extreme source angles relative to the scattering mask. Given the minimal variation of mask geometry with rotation at these extreme angles, this lack of agreement was anticipated. Thus, the first phase of model validation was successful in that the two codes agree to a sufficient degree.

7.3 Experiment/GEANT Comparisons

The second phase of validation consisted of comparison of GEANT simulation results with experimental results. It would be unrealistic to expect perfect agreement due to the effects of imperfect detector energy resolution and the complicated lab environment on the experimental energy spectra and detector response curves. Neither of these effects were included in the

simulation. Keeping this in mind, analogous comparisons were made between experimental and GEANT data as were made between GEANT and MCNP outputs. Energy-calibrated experimental data and broadened simulated data were compared. The assessment of the energy spectra derived experimentally and via simulation showed that the spectra, although graphically quite similar, could not be proven to have been statistically drawn from the same distribution. This was not unexpected since the Geant4 model developed did not account for many aspects of the experimental environment that would have led to increased lower energy counts from scatter within the environment into the RSM assembly. Comparison of the experimental and GEANT Compton Integral detector response curves showed pronounced disagreement due to failure of the experimental data to be adequately differentiated with θ rotation angle for each φ , the count being fairly constant as the mask rotated. This finding does not necessarily eliminate use of information obtained in the Compton continuum from being useful, due to the fact that simulation showed that variation should exist, but further research is needed to determine if and how it may be obtained experimentally.

Fortunately, the imaging system does not rely on agreement throughout the energy spectra. Comparison of the experimental and GEANT FEP detector response curves showed that the curves could have been statistically drawn from identical distributions for all but the most extreme φ angles. Graphical analysis confirms the agreement between the GEANT and experimental FEP detector response curves. This is especially promising since, if an experimental spectrum contains multiple FEPs from multiple sources, each FEP may be used to independently determine the source(s) location(s).

7.4 Imaging Algorithm

A simple algorithm was used to predict the correct experimental source locations employing only the experimentally acquired detector response curves, using a library of GEANT-produced simulated detector response curves. The inputs for the algorithm were a normalized experimental detector response curve and the normalized simulated detector response curve library. Despite the fact that this preliminary library was limited in resolution (θ discretized in 5° increments and ϕ discretized in 10° increments), the application of the algorithm to 1296 experimental detector response curves resulted in an average error in θ of 4° and an average error in ϕ of 3° . Further, the application of this simple algorithm is very unintensive in terms of computational time.

7.5 Recommendations for Future Work

The success of this work provides two main branches of future research efforts. These efforts are broadly categorized into those related to extending the work accomplished on the Gamma RSM Detection System and those related to developing a related neutron source imaging scheme. These will be discussed in turn.

There are numerous additional avenues available to refine and improve on the Gamma RSM Detection System to allow it to better fulfill Department of Defense objectives:

- Optimize, via simulation, the RSM System mask design in terms of density, material, geometry, and dimensions. This will allow the data acquisition time, cost, and/or required size of the assembly to be reduced.
- Conduct an optimization study to determine the ideal size and type of detector for the Gamma RSM Detection System. This will allow the data acquisition time, cost, and/or required size of the assembly to be reduced.

- Expand the detector response curve library or develop a response surface that will increase the resolution of the imaging algorithm. This will improve precision of the IMAGING system.
- Expand the experiment and simulation to cover additional gamma energies of interest, including mixed and distributed sources. This will expand the applicability of the system in terms of the acceptable operating environment.
- Develop a “real-time” interface to successively update projected source location on a screen for the user. This will allow operational use of the system.
- Conduct a study to determine if the imaging potential in the simulated Compton Integral detector response curves can be obtained experimentally. This will allow the data acquisition time, cost, and/or required size of the assembly to be reduced.
- Study the performance of the system in a mixed neutron-gamma source environment. This will expand the applicability of the system for source IMAGING.

While not addressed in this research, initial results using the same RSM setup with a generic neutron detector have shown promise. Recommended avenues for development of a Neutron RSM Detection System include:

- Conduct simulations with the extant shield to determine the feasibility of using a polymethacrylate RSM shield to identify the direction of a neutron source
- Conduct simulations to determine ideal Neutron RSM geometries (design and dimensions) and material (composition and density)
- Analyze the neutron energies for which a Neutron RSM Detection System is feasible
- Determine the ideal neutron detector to be used in this neutron imaging system

- Study the performance of the Neutron RSM Detection System in a mixed neutron-gamma environment

Appendix A

Appendix A contains the complete set of graphical comparisons between the GEANT and MCNP Monte-Carlo simulation detector response curves. This includes the detector response curves obtained by taking each of two different values from the energy spectrum: the count within the FEP and the integral of counts within the Compton Continuum. Graphs are shown for each 10^o increment of phi ($\varphi = 5^o - 175^o$). The 90% confidence interval around each value is plotted. All values represent the unnormalized, gross counts obtained from each simulation. Thus, no scaling was required in order to obtain agreement between the simulation outputs obtained.

The FEP is defined as the simple count within the 662 keV energy bin. The integral of counts within the Compton Continuum is given by the sum of all of the counts from energy bins $0 - 480$ keV.

Compton Continuum Detector Response Curves

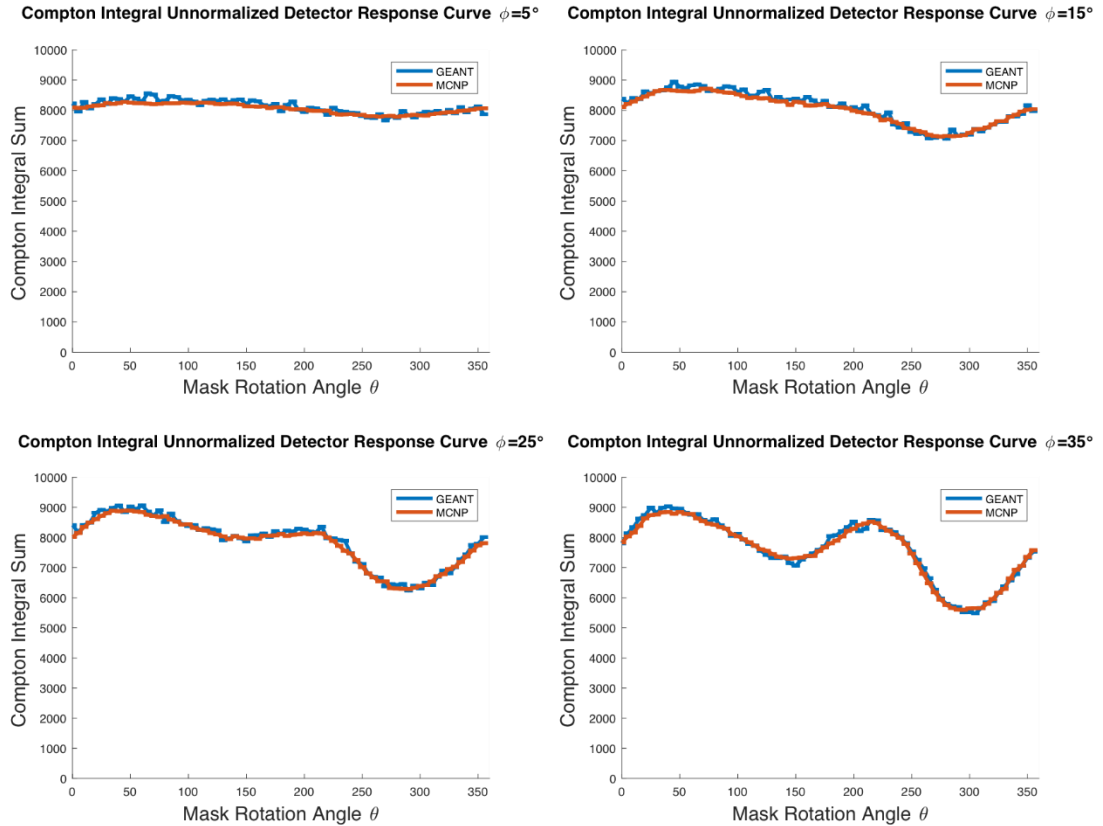


Figure 33. Count of gross number of incident particles that contribute to the Compton Integral for $\varphi = 5^\circ - 35^\circ$ in increments of 10° with $\theta = 0^\circ - 355^\circ$ in increments of 5° for each increment of φ . These graphs correspond to GEANT and MCNP results with 500,000 source particles for each (θ, φ) position. The 90% confidence interval is plotted for each.

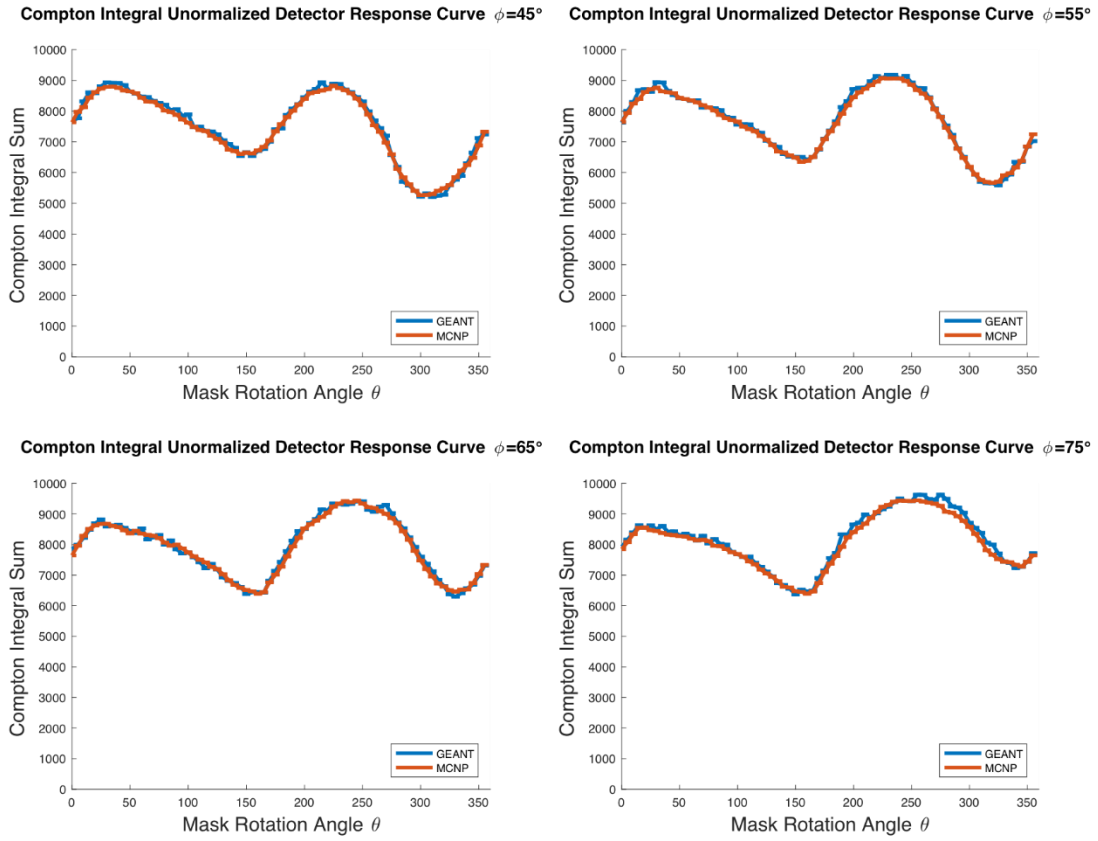


Figure 34. Count of gross number of incident particles that contribute to the Compton Integral for $\phi = 45^\circ - 75^\circ$ in increments of 10° with $\theta = 0^\circ - 355^\circ$ in increments of 5° for each increment of ϕ . These graphs correspond to GEANT and MCNP results with 500,000 source particles for each (θ, ϕ) position. The 90% confidence interval is plotted for each.

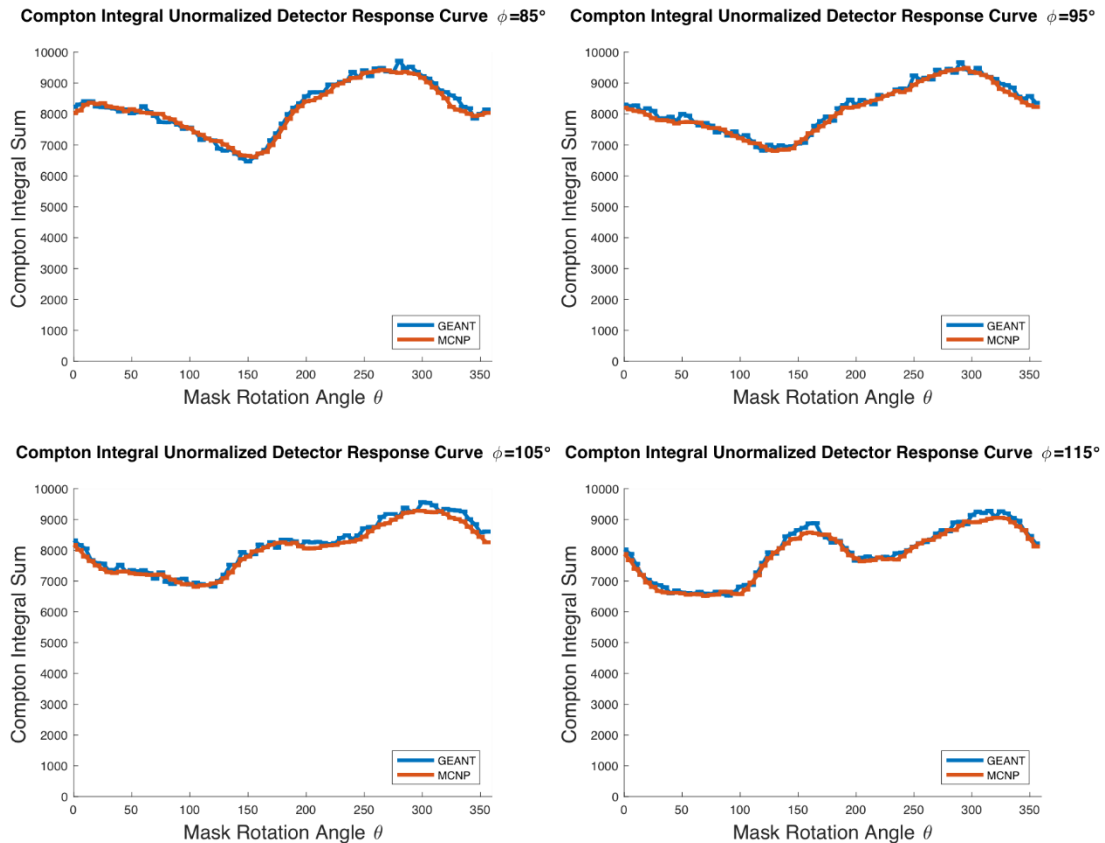


Figure 35. Count of gross number of incident particles that contribute to the Compton Integral for $\phi=85^\circ\text{-}115^\circ$ in increments of 10° with $\theta=0^\circ\text{-}355^\circ$ in increments of 5° for each increment of ϕ . These graphs correspond to GEANT and MCNP results with 500,000 source particles for each (θ,ϕ) position. The 90% confidence interval is plotted for each.

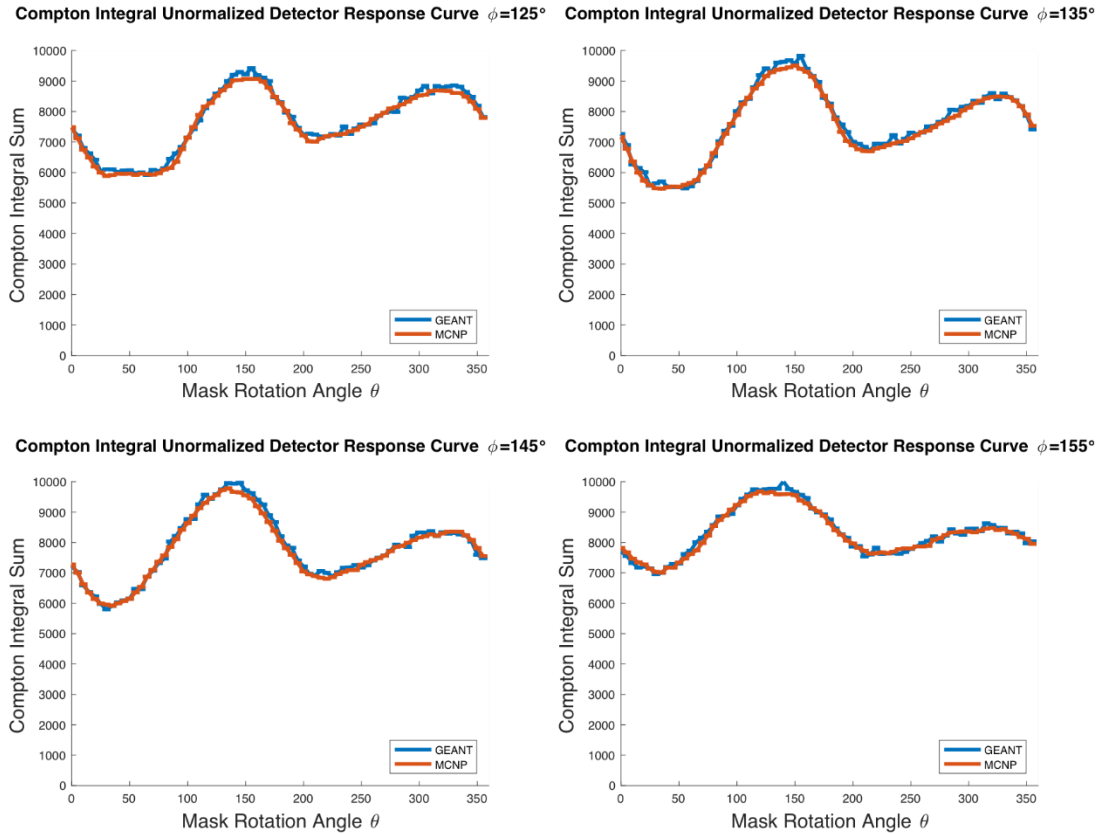


Figure 36. Count of gross number of incident particles that contribute to the Compton Integral for $\phi=125^\circ-155^\circ$ in increments of 10° with $\theta=0^\circ-355^\circ$ in increments of 5° for each increment of ϕ . These graphs correspond to GEANT and MCNP results with 500,000 source particles for each (θ, ϕ) position. The 90% confidence interval is plotted for each.

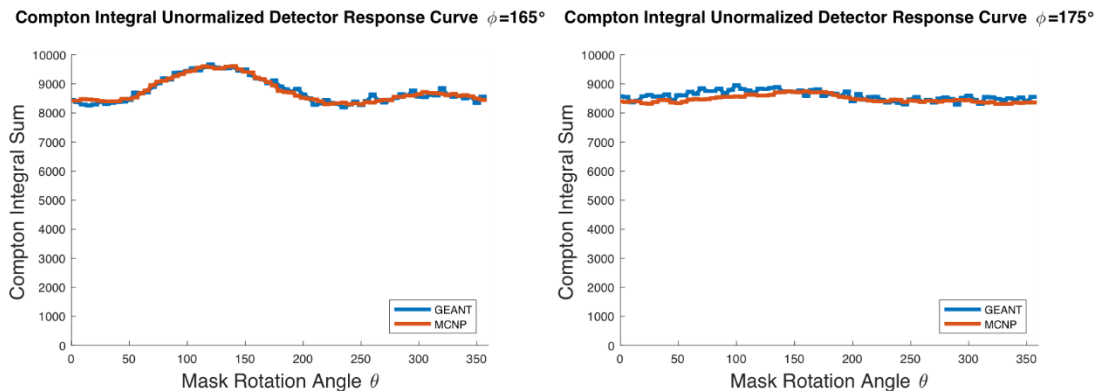


Figure 37. Count of gross number of incident particles that contribute to the Compton Integral for $\phi = 125^\circ - 155^\circ$ in increments of 10° with $\theta = 0^\circ - 355^\circ$ in increments of 5° for each increment of ϕ . These graphs correspond to GEANT and MCNP results with

500,000 source particles for each (θ, φ) position. The 90% confidence interval is plotted for each.

FEP Detector Response Curves

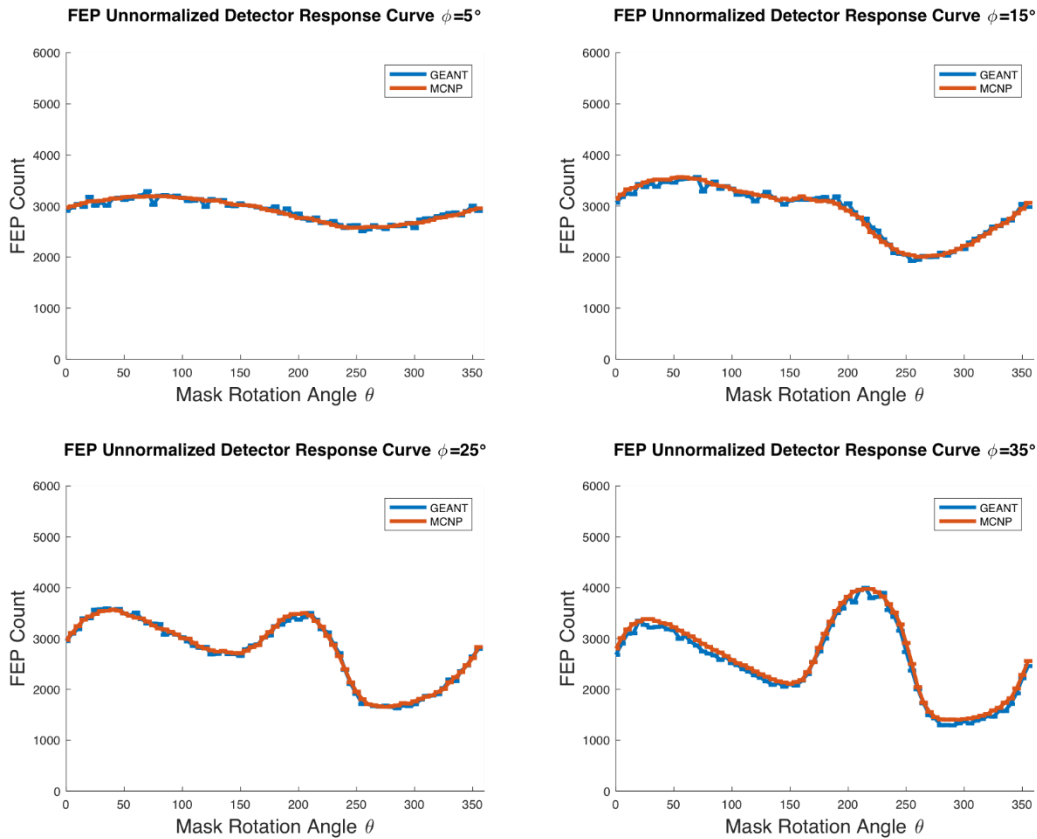


Figure 38. Count of gross number of incident particles that contribute to the Full Energy Peak for $\varphi = 5^\circ - 35^\circ$ in increments of 10° with $\theta = 0^\circ - 355^\circ$ in increments of 5° for each increment of φ . These graphs correspond to GEANT and MCNP results with 500,000 source particles for each (θ, φ) position. The 90% confidence interval is plotted for each.

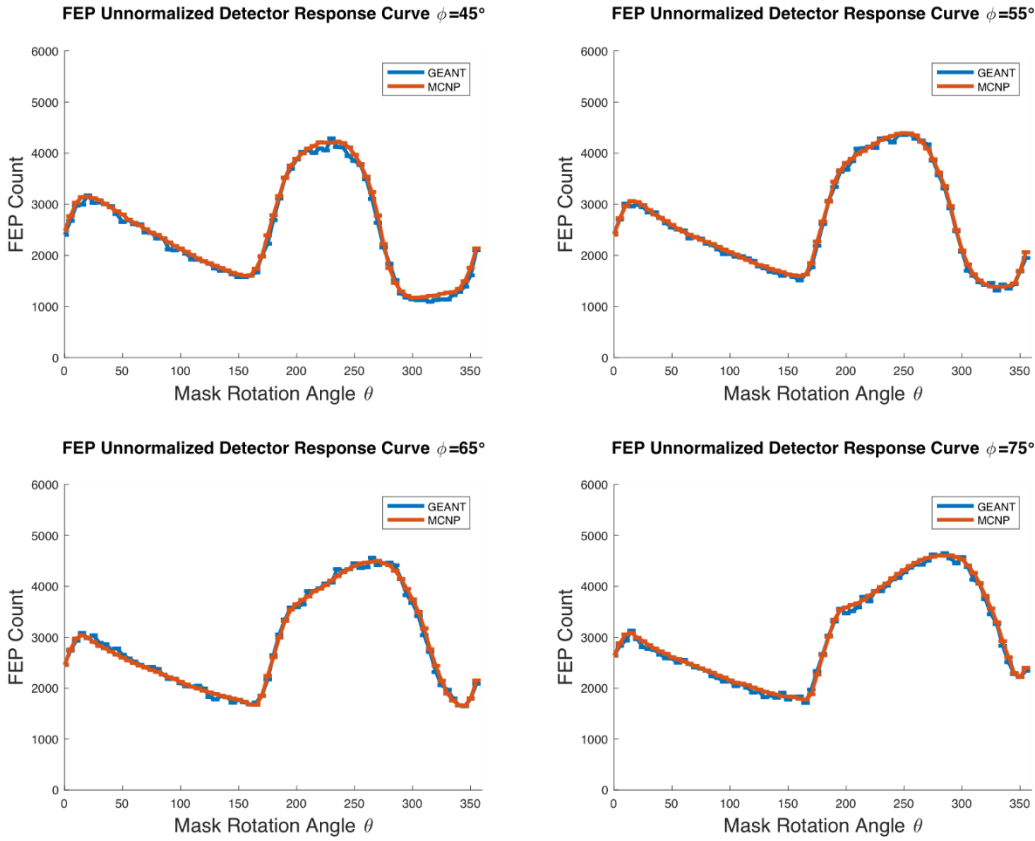


Figure 39. Count of gross number of incident particles that contribute to the Full Energy Peak for $\varphi = 45^\circ - 75^\circ$ in increments of 10° with $\theta = 0^\circ - 355^\circ$ in increments of 5° for each increment of φ . These graphs correspond to GEANT and MCNP results with 500,000 source particles for each (θ, φ) position. The 90% confidence interval is plotted for each.

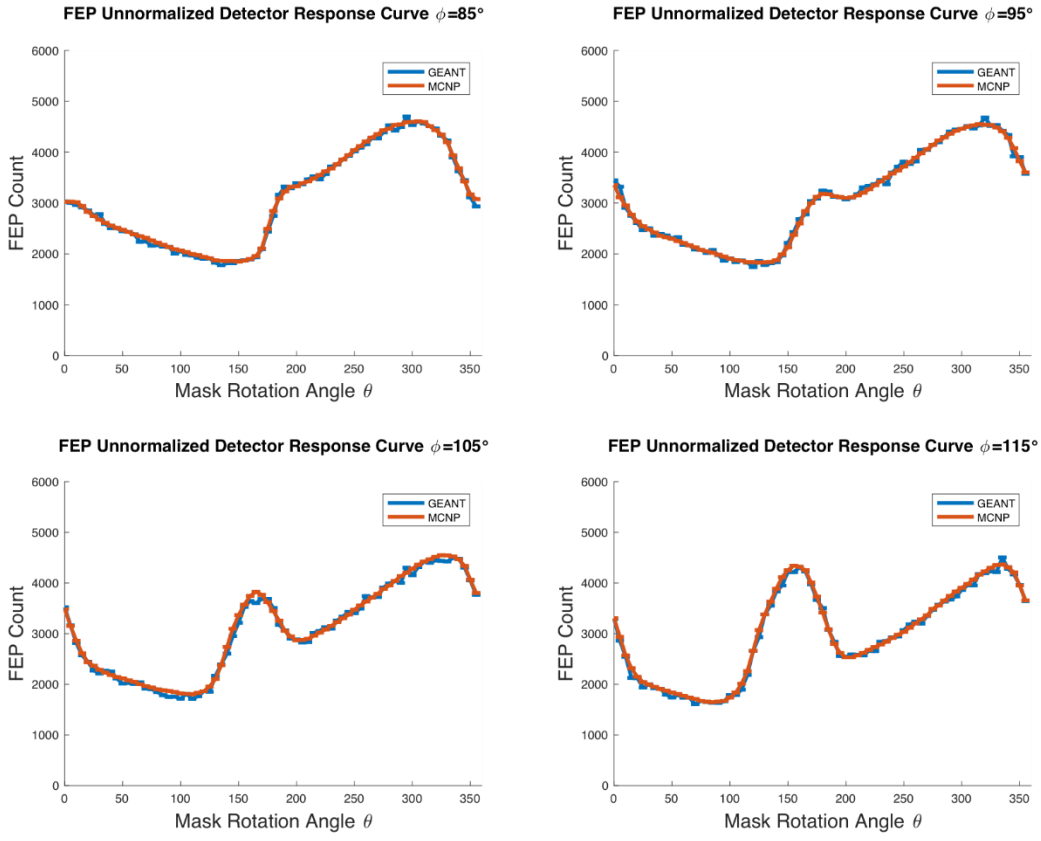


Figure 40. Count of gross number of incident particles that contribute to the Full Energy Peak for $\varphi = 85^\circ - 115^\circ$ in increments of 10° with $\theta = 0^\circ - 355^\circ$ in increments of 5° for each increment of φ . These graphs correspond to GEANT and MCNP results with 500,000 source particles for each (θ, φ) position. The 90% confidence interval is plotted for each.

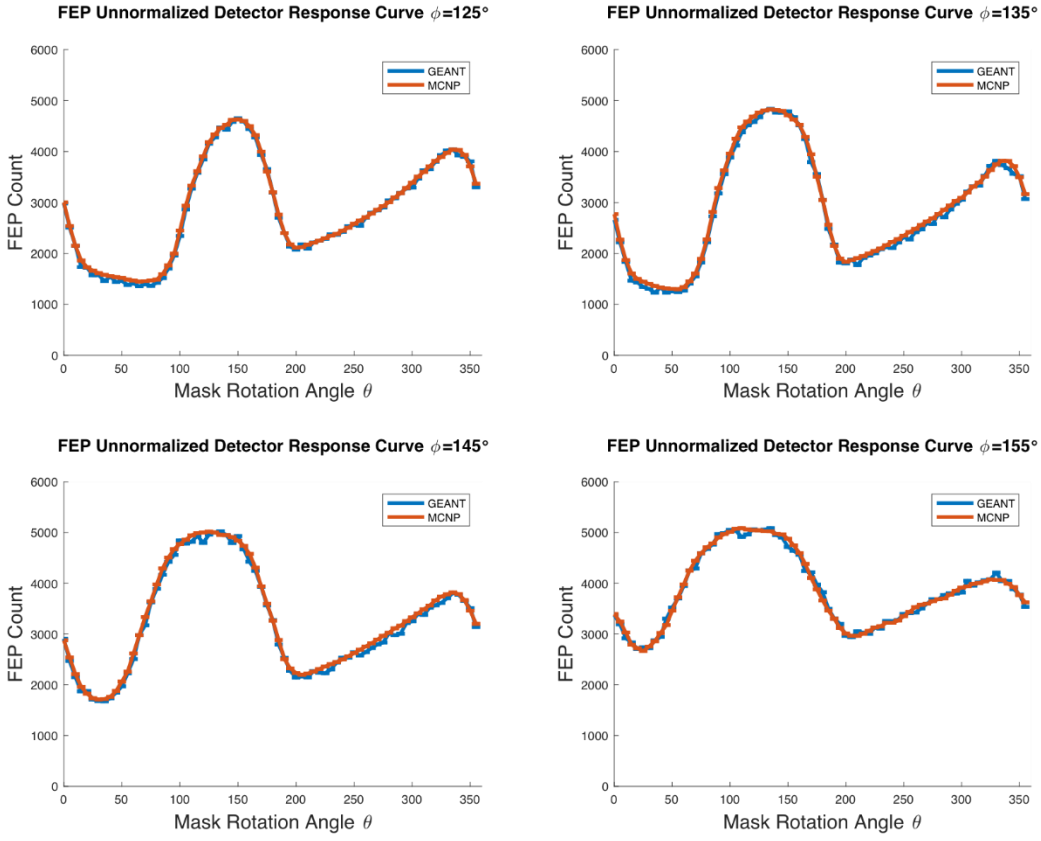


Figure 41. Count of gross number of incident particles that contribute to the Full Energy Peak for $\phi = 125^\circ - 155^\circ$ in increments of 10° with $\theta = 0^\circ - 355^\circ$ in increments of 5° for each increment of ϕ . These graphs correspond to GEANT and MCNP results with 500,000 source particles for each (θ, ϕ) position. The 90% confidence interval is plotted for each.

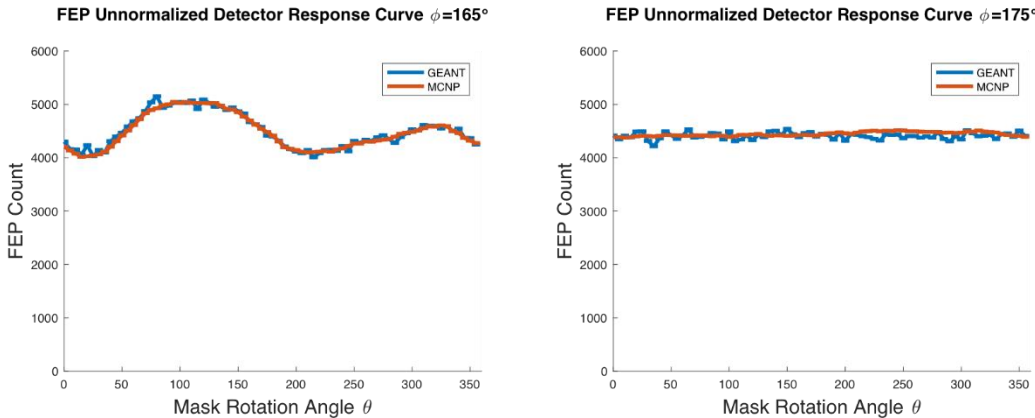


Figure 42. Figure 30: Count of gross number of incident particles that contribute to the Full Energy Peak for $\phi = 165^\circ - 175^\circ$ in increments of 10° with $\theta = 0^\circ - 355^\circ$ in increments of 5° for each increment of ϕ . These graphs correspond to GEANT and MCNP

results with 500,000 source particles for each (θ, φ) position. The 90% confidence interval is plotted for each.

Appendix B

Appendix B contains the complete set of graphical comparisons between the GEANT Monte-Carlo simulation and Experimental detector response curves. This includes the detector response curves obtained by taking each of two different values from the energy spectrum: the count within the FEP and the integral of counts within the Compton Continuum. Graphs are shown for each 10° increment of phi ($\varphi = 5^\circ - 175^\circ$). The 90% confidence interval around each value is plotted. Unlike in the comparison between GEANT and MCNP, calibration is required due to unequal number of source particles. A normalization by the integral underneath each detector response curve is utilized. The experimental data is calibrated and the simulated data is broadened via convolution with a Gaussian function defined by the standard deviation at the FEP calculated via Equation 17.

The Compton Integral is defined as the sum of counts within energy bins 200 keV – 480 keV for both the simulated and experimental data. The FEP is defined as the integral underneath a Gaussian function fit to the broadened simulated data and calibrated experimental data, following the removal of background.

Compton Continuum Detector Response Curves

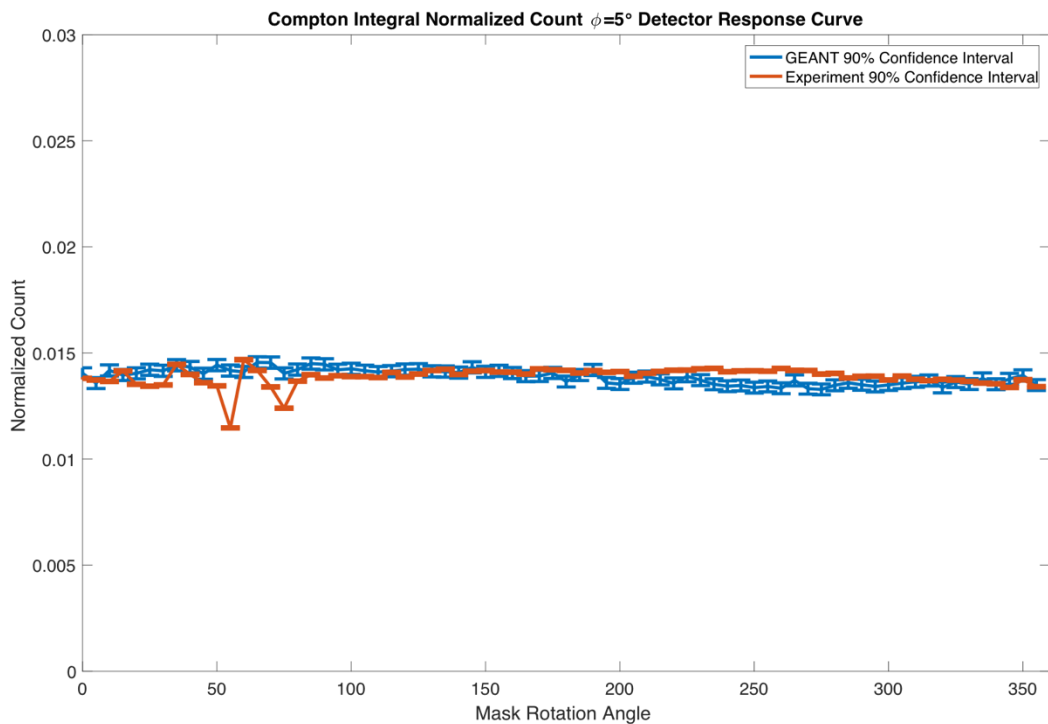


Figure 43. Normalized count (per total count in the detector response curve) that contribute to the Compton Integral (200 keV – 480 keV) for $\varphi = 5^\circ$ with $\theta = 0^\circ - 355^\circ$ in increments of 5° . These values correspond to GEANT results with 500,000 source particles for each (θ, φ) position and experimental results collected over 24h. The 90% confidence interval is plotted.

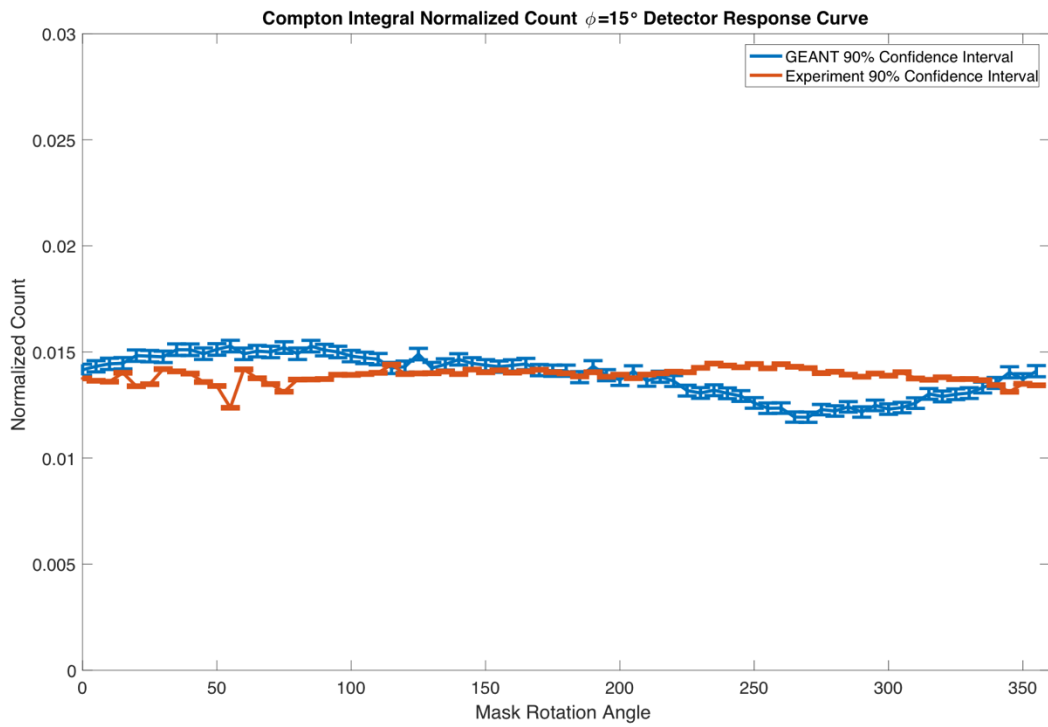


Figure 44. Normalized count (per total count in the detector response curve) that contribute to the Compton Integral (200 keV – 480 keV) for $\varphi = 15^\circ$ with $\theta = 0^\circ - 355^\circ$ in increments of 5° . These values correspond to GEANT results with 500,000 source particles for each (θ, φ) position and experimental results collected over 24h. The 90% confidence interval is plotted.

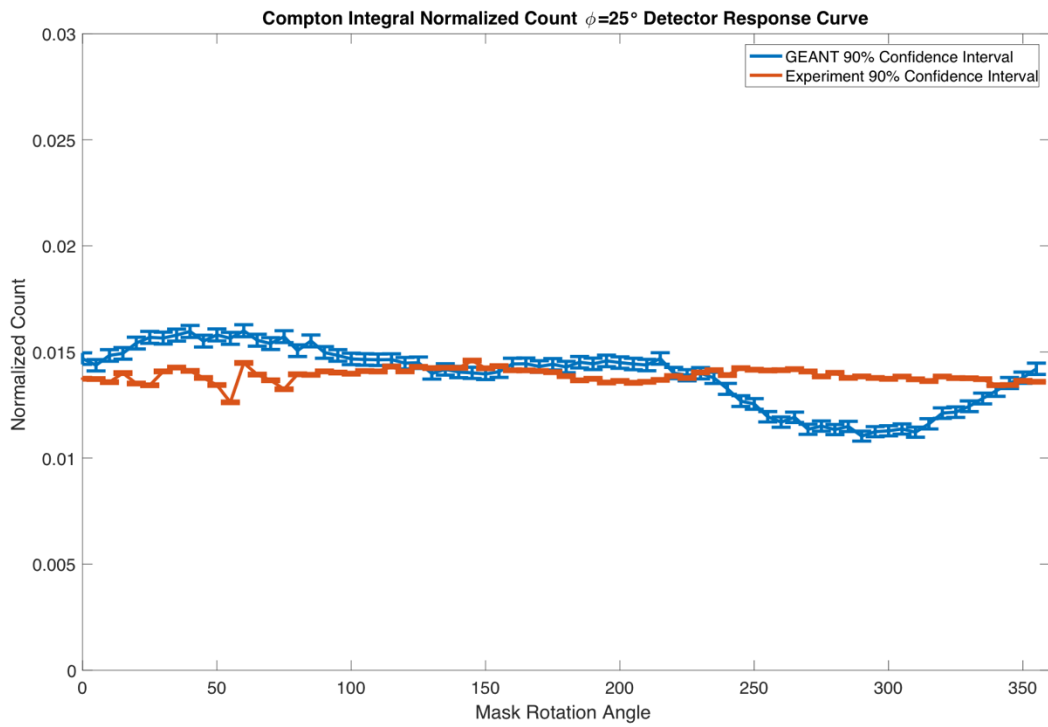


Figure 45. Normalized count (per total count in the detector response curve) that contribute to the Compton Integral (200 keV – 480 keV) for $\varphi = 25^\circ$ with $\theta = 0^\circ - 355^\circ$ in increments of 5° . These values correspond to GEANT results with 500,000 source particles for each (θ, φ) position and experimental results collected over 24h. The 90% confidence interval is plotted.

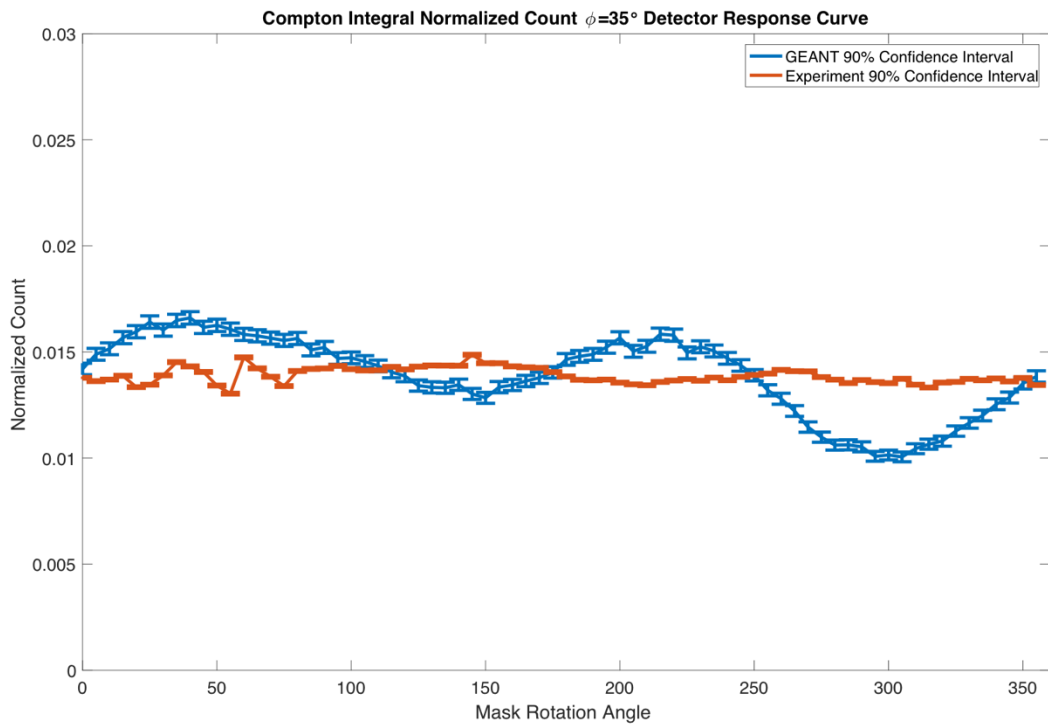


Figure 46. Normalized count (per total count in the detector response curve) that contribute to the Compton Integral (200 keV – 480 keV) for $\varphi = 35^\circ$ with $\theta = 0^\circ - 355^\circ$ in increments of 5° . These values correspond to GEANT results with 500,000 source particles for each (θ, φ) position and experimental results collected over 24h. The 90% confidence interval is plotted.

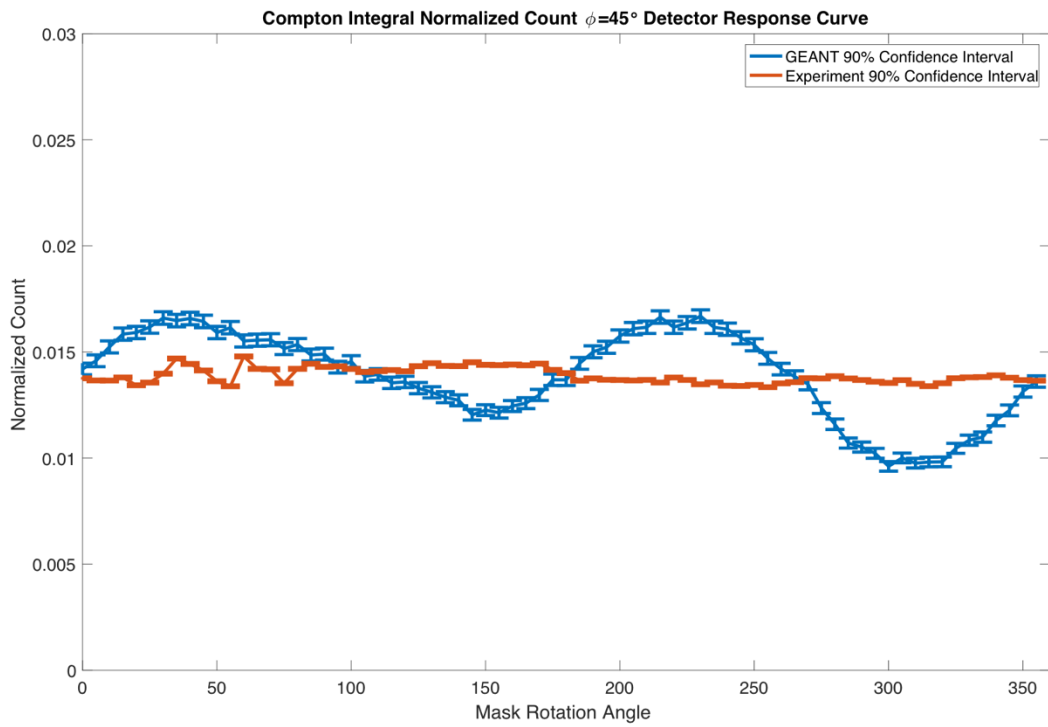


Figure 47. Normalized count (per total count in the detector response curve) that contribute to the Compton Integral (200 keV – 480 keV) for $\varphi = 45^\circ$ with $\theta = 0^\circ - 355^\circ$ in increments of 5° . These values correspond to GEANT results with 500,000 source particles for each (θ, φ) position and experimental results collected over 24h. The 90% confidence interval is plotted.

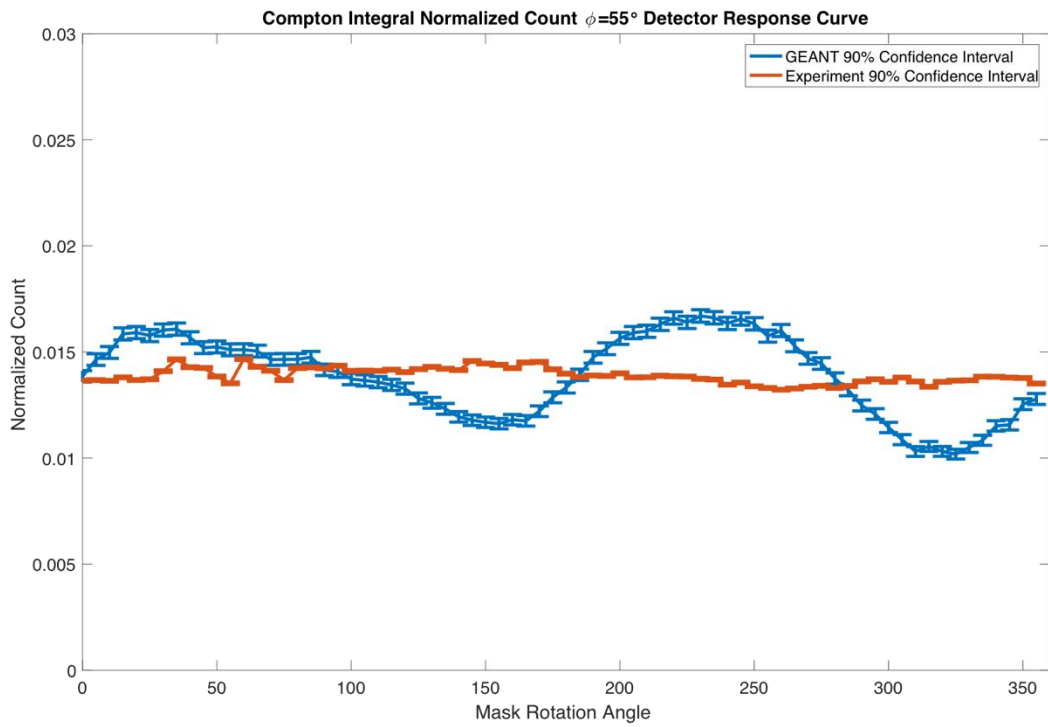


Figure 48. Normalized count (per total count in the detector response curve) that contribute to the Compton Integral (200 keV – 480 keV) for $\varphi = 55^\circ$ with $\theta = 0^\circ - 355^\circ$ in increments of 5° . These values correspond to GEANT results with 500,000 source particles for each (θ, φ) position and experimental results collected over 24h. The 90% confidence interval is plotted.

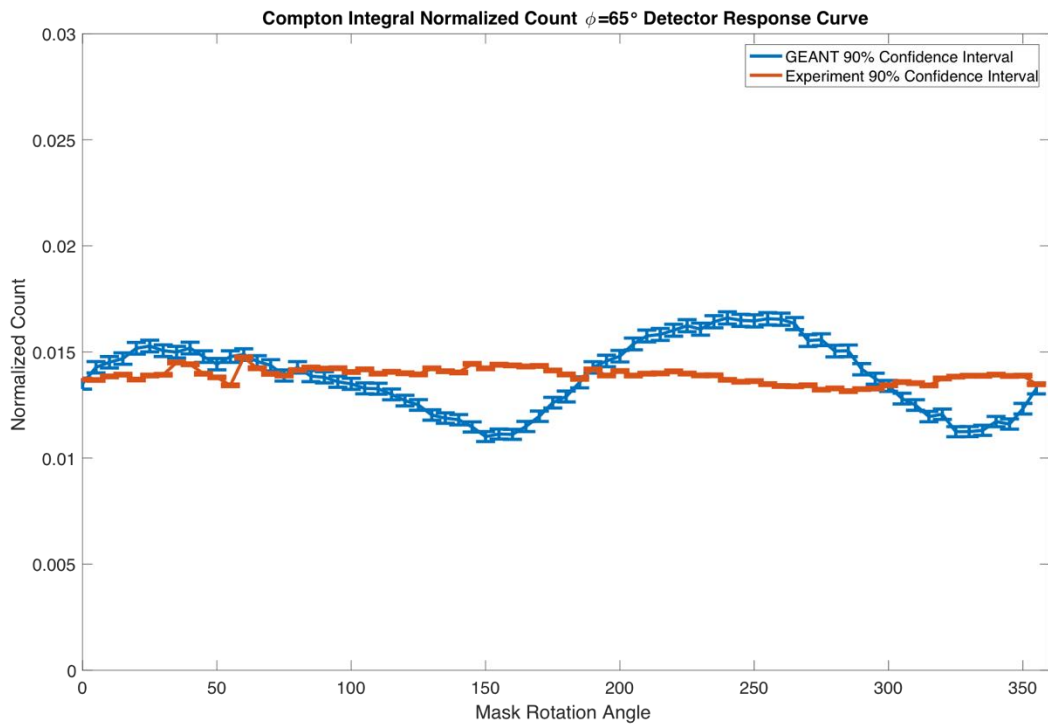


Figure 49. Normalized count (per total count in the detector response curve) that contribute to the Compton Integral (200 keV – 480 keV) for $\varphi = 65^\circ$ with $\theta = 0^\circ - 355^\circ$ in increments of 5° . These values correspond to GEANT results with 500,000 source particles for each (θ, φ) position and experimental results collected over 24h. The 90% confidence interval is plotted.

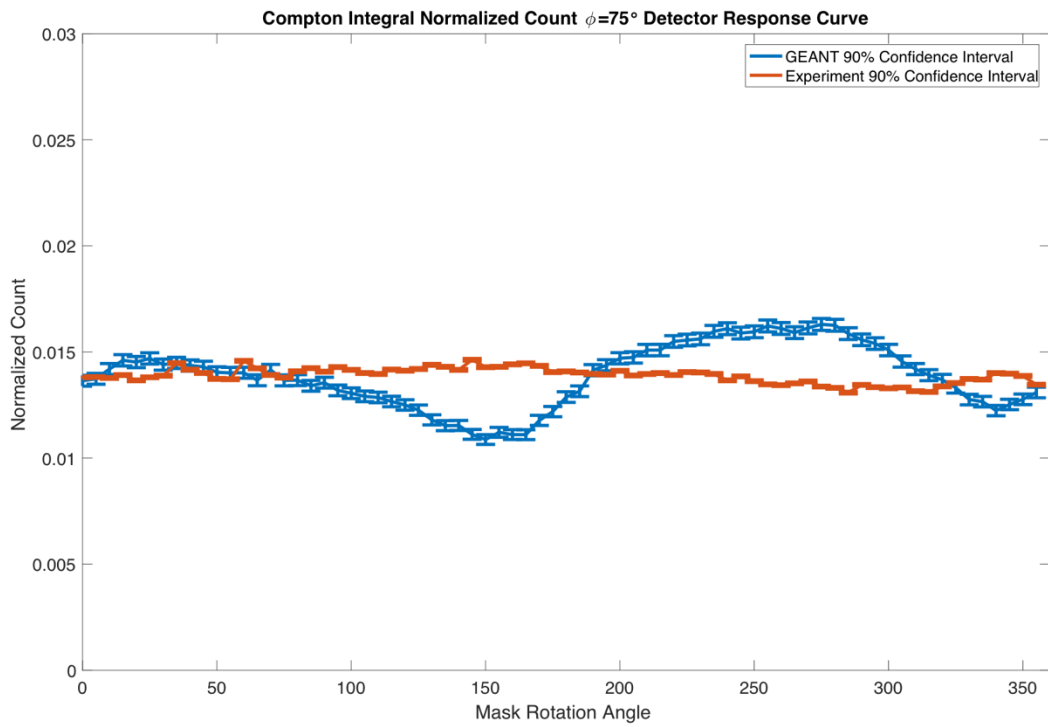


Figure 50. Normalized count (per total count in the detector response curve) that contribute to the Compton Integral (200 keV – 480 keV) for $\varphi = 75^\circ$ with $\theta = 0^\circ - 355^\circ$ in increments of 5° . These values correspond to GEANT results with 500,000 source particles for each (θ, φ) position and experimental results collected over 24h. The 90% confidence interval is plotted.

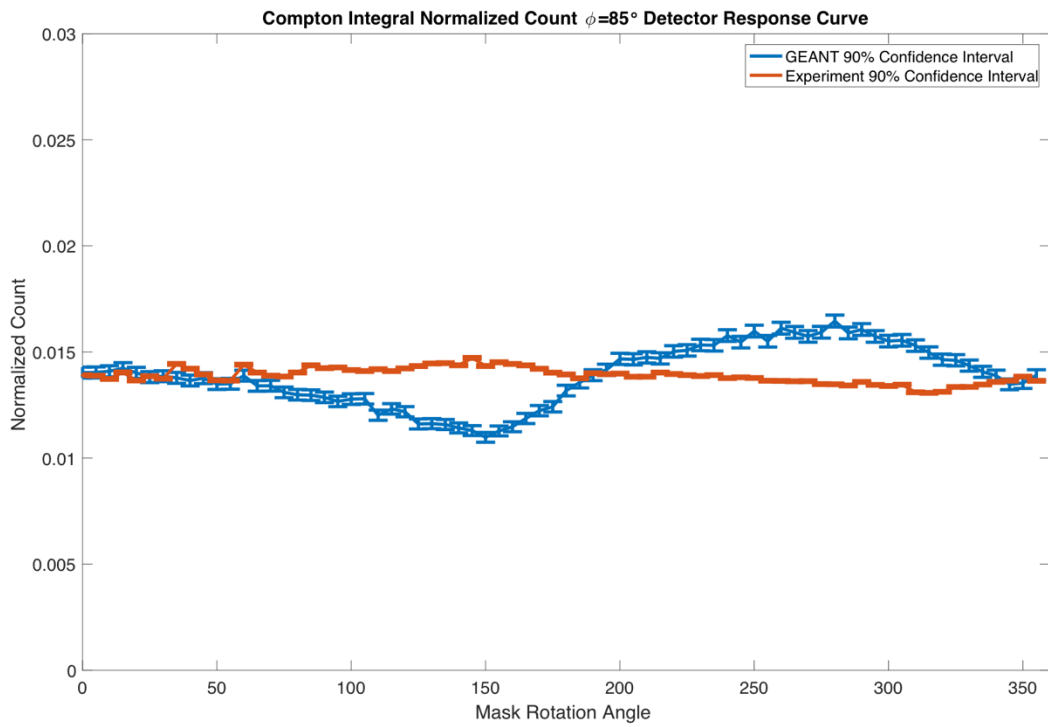


Figure 51. Normalized count (per total count in the detector response curve) that contribute to the Compton Integral (200 keV – 480 keV) for $\varphi = 85^\circ$ with $\theta = 0^\circ - 355^\circ$ in increments of 5° . These values correspond to GEANT results with 500,000 source particles for each (θ, φ) position and experimental results collected over 24h. The 90% confidence interval is plotted.

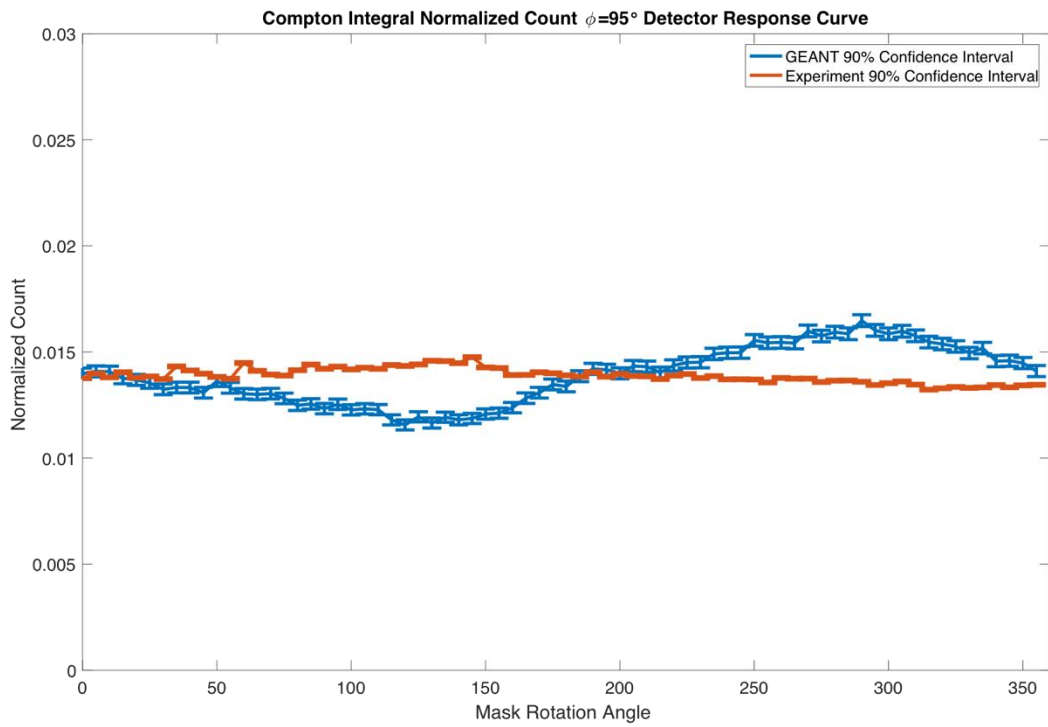


Figure 52. Normalized count (per total count in the detector response curve) that contribute to the Compton Integral (200 keV – 480 keV) for $\varphi = 95^\circ$ with $\theta = 0^\circ - 355^\circ$ in increments of 5° . These values correspond to GEANT results with 500,000 source particles for each (θ, φ) position and experimental results collected over 24h. The 90% confidence interval is plotted.

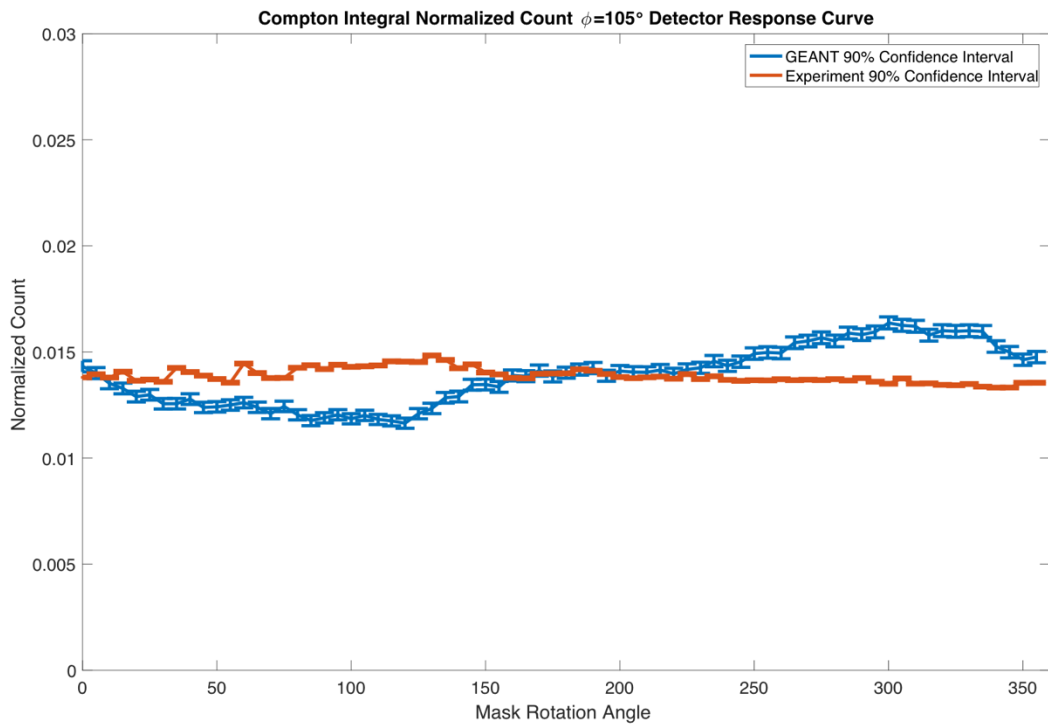


Figure 53. Normalized count (per total count in the detector response curve) that contribute to the Compton Integral (200 keV – 480 keV) for $\varphi = 105^\circ$ with $\theta = 0^\circ - 355^\circ$ in increments of 5° . These values correspond to GEANT results with 500,000 source particles for each (θ, φ) position and experimental results collected over 24h. The 90% confidence interval is plotted.

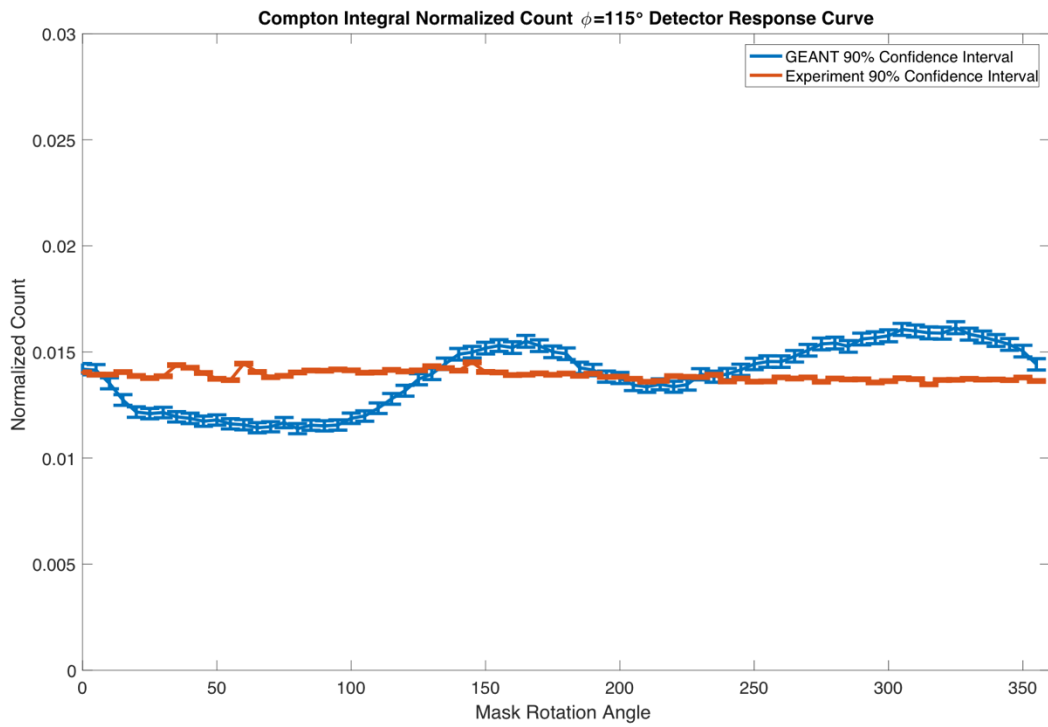


Figure 54. Normalized count (per total count in the detector response curve) that contribute to the Compton Integral (200 keV – 480 keV) for $\varphi = 115^\circ$ with $\theta = 0^\circ - 355^\circ$ in increments of 5° . These values correspond to GEANT results with 500,000 source particles for each (θ, φ) position and experimental results collected over 24h. The 90% confidence interval is plotted.

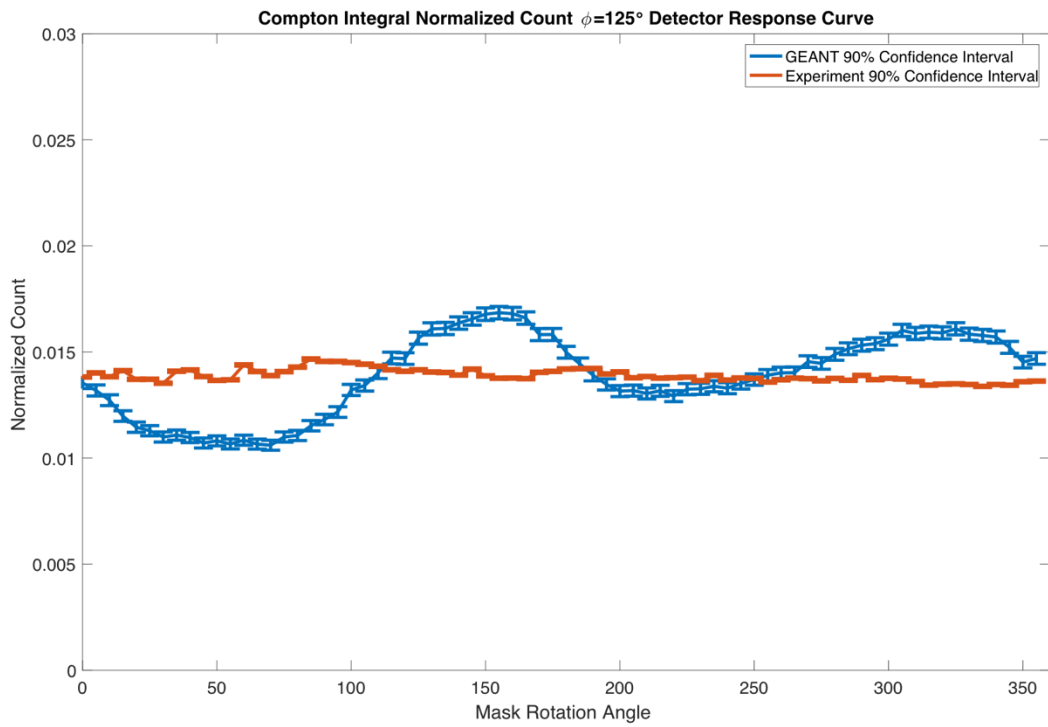


Figure 55. Normalized count (per total count in the detector response curve) that contribute to the Compton Integral (200 keV – 480 keV) for $\varphi = 125^\circ$ with $\theta = 0^\circ - 355^\circ$ in increments of 5° . These values correspond to GEANT results with 500,000 source particles for each (θ, φ) position and experimental results collected over 24h. The 90% confidence interval is plotted.

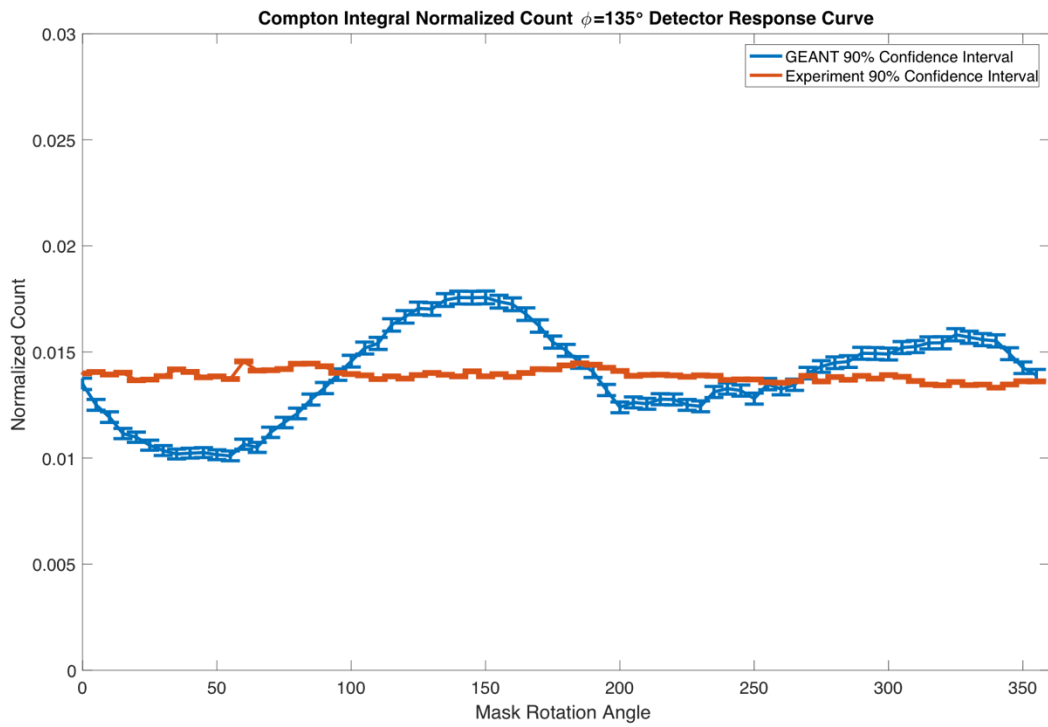


Figure 56. Normalized count (per total count in the detector response curve) that contribute to the Compton Integral (200 keV – 480 keV) for $\varphi = 135^\circ$ with $\theta = 0^\circ - 355^\circ$ in increments of 5° . These values correspond to GEANT results with 500,000 source particles for each (θ, φ) position and experimental results collected over 24h. The 90% confidence interval is plotted.

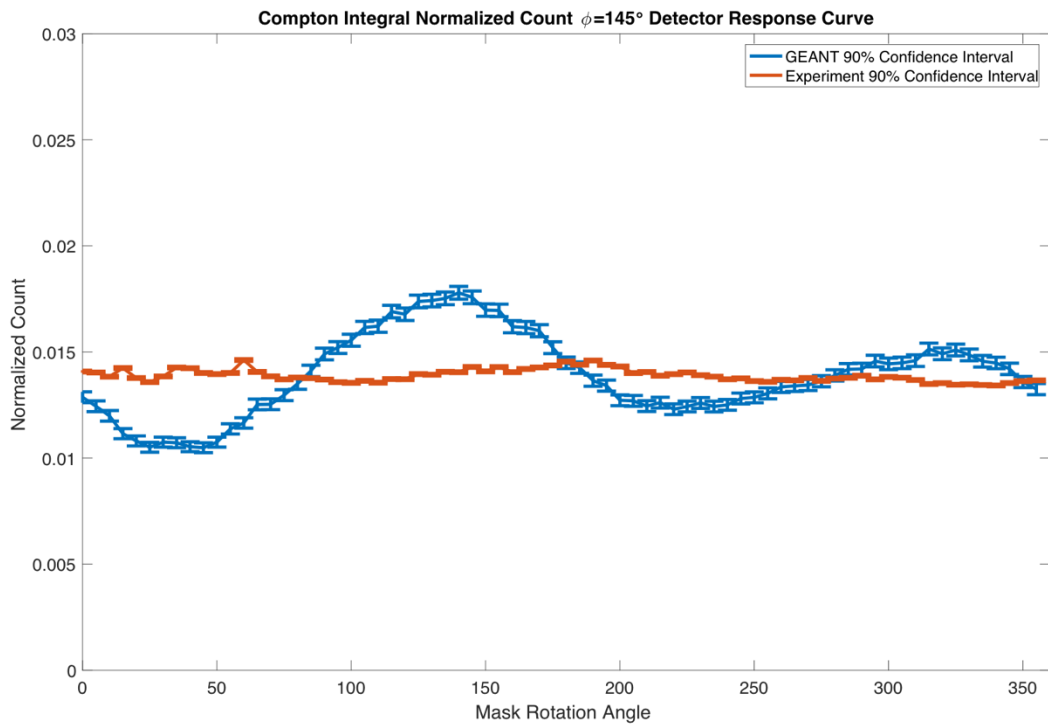


Figure 57. Normalized count (per total count in the detector response curve) that contribute to the Compton Integral (200 keV – 480 keV) for $\varphi = 145^\circ$ with $\theta = 0^\circ - 355^\circ$ in increments of 5° . These values correspond to GEANT results with 500,000 source particles for each (θ, φ) position and experimental results collected over 24h. The 90% confidence interval is plotted.

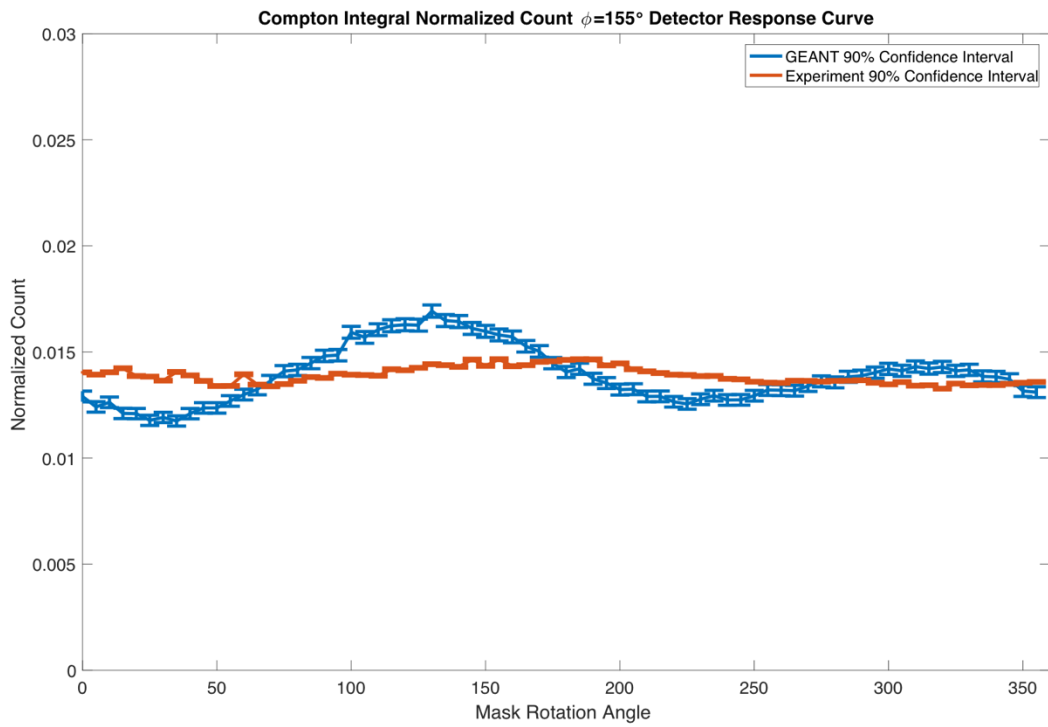


Figure 58. Normalized count (per total count in the detector response curve) that contribute to the Compton Integral (200 keV – 480 keV) for $\varphi = 155^\circ$ with $\theta = 0^\circ - 355^\circ$ in increments of 5° . These values correspond to GEANT results with 500,000 source particles for each (θ, φ) position and experimental results collected over 24h. The 90% confidence interval is plotted.

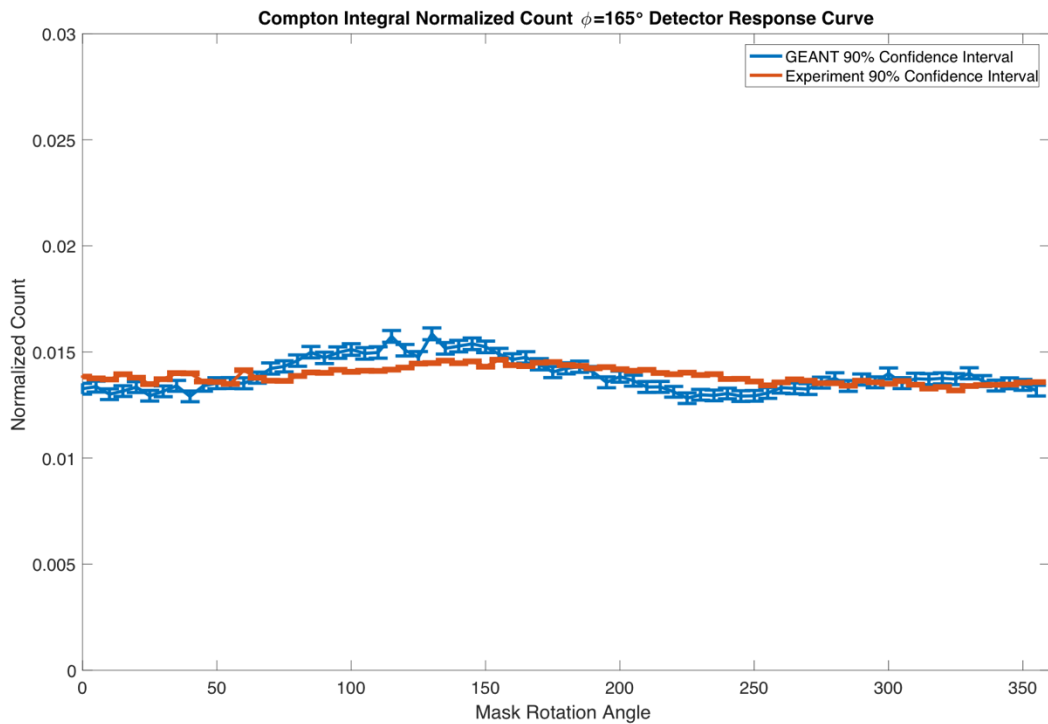


Figure 59. Normalized count (per total count in the detector response curve) that contribute to the Compton Integral (200 keV – 480 keV) for $\varphi = 165^\circ$ with $\theta = 0^\circ - 355^\circ$ in increments of 5° . These values correspond to GEANT results with 500,000 source particles for each (θ, φ) position and experimental results collected over 24h. The 90% confidence interval is plotted.

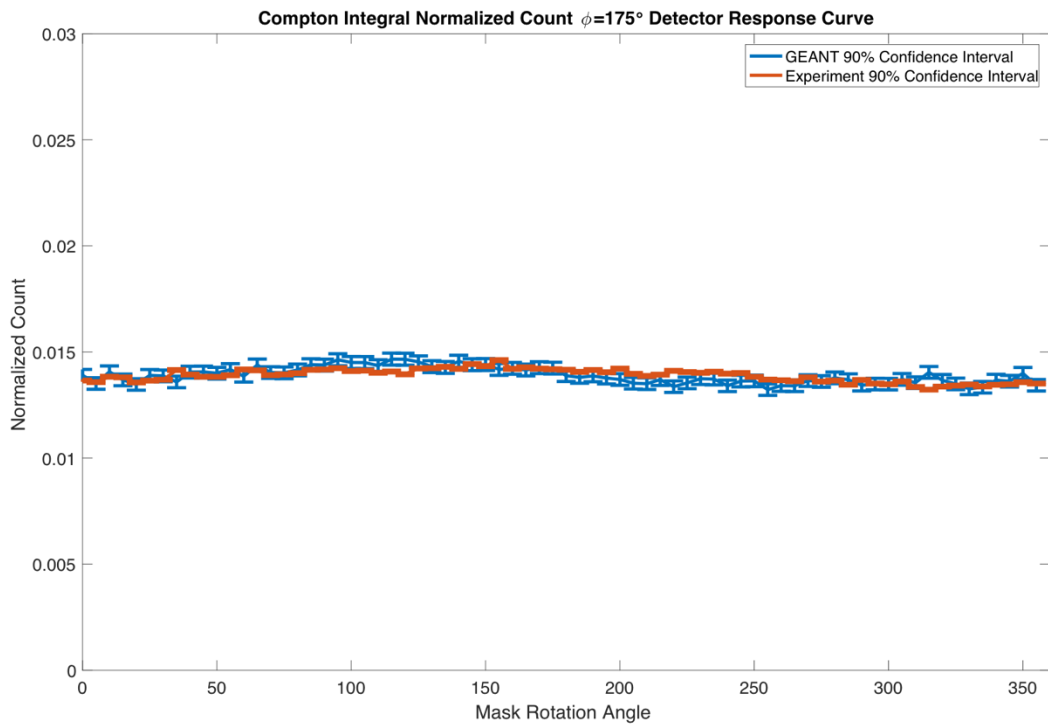


Figure 60. Normalized count (per total count in the detector response curve) that contribute to the Compton Integral (200 keV – 480 keV) for $\varphi = 175^\circ$ with $\theta = 0^\circ - 355^\circ$ in increments of 5° . These values correspond to GEANT results with 500,000 source particles for each (θ, φ) position and experimental results collected over 24h. The 90% confidence interval is plotted.

FEP Detector Response Curves

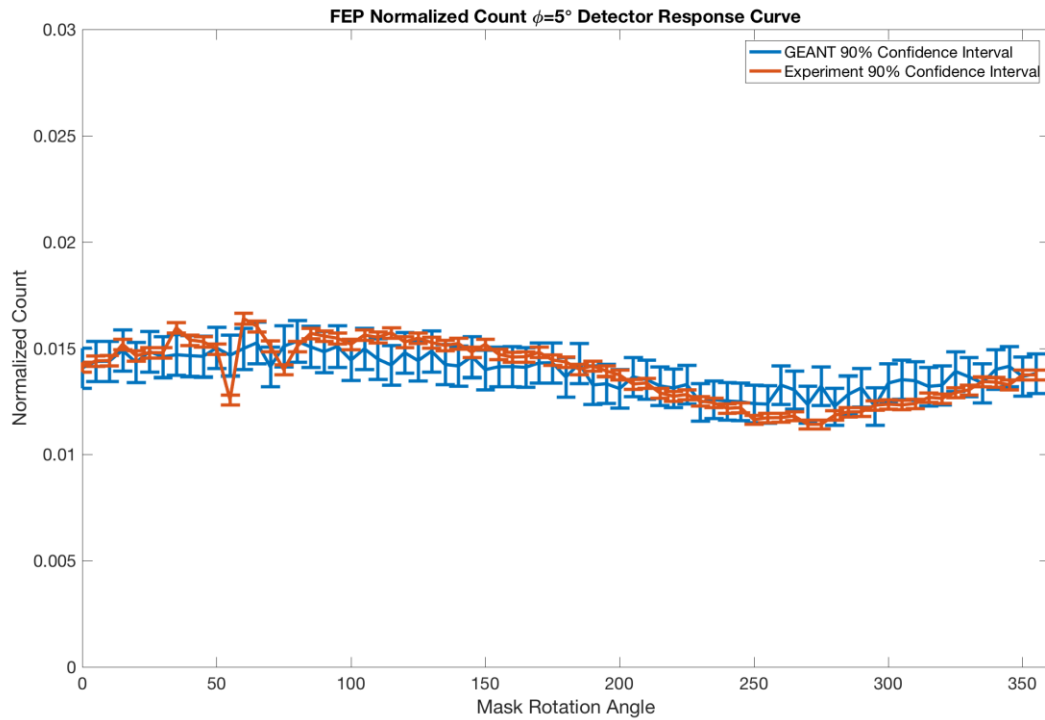


Figure 61. Normalized count (per total count in the detector response curve) that contribute to the FEP for $\varphi = 5^\circ$ with $\theta = 0^\circ - 355^\circ$ in increments of 5° . These values correspond to GEANT results with 500,000 source particles for each (θ, φ) position and experimental results collected over 24h. The 90% confidence interval is plotted. For each (θ, φ) position, the FEP count comes from a broadened energy spectrum (via convolution for GEANT data and inherently for experimental data).

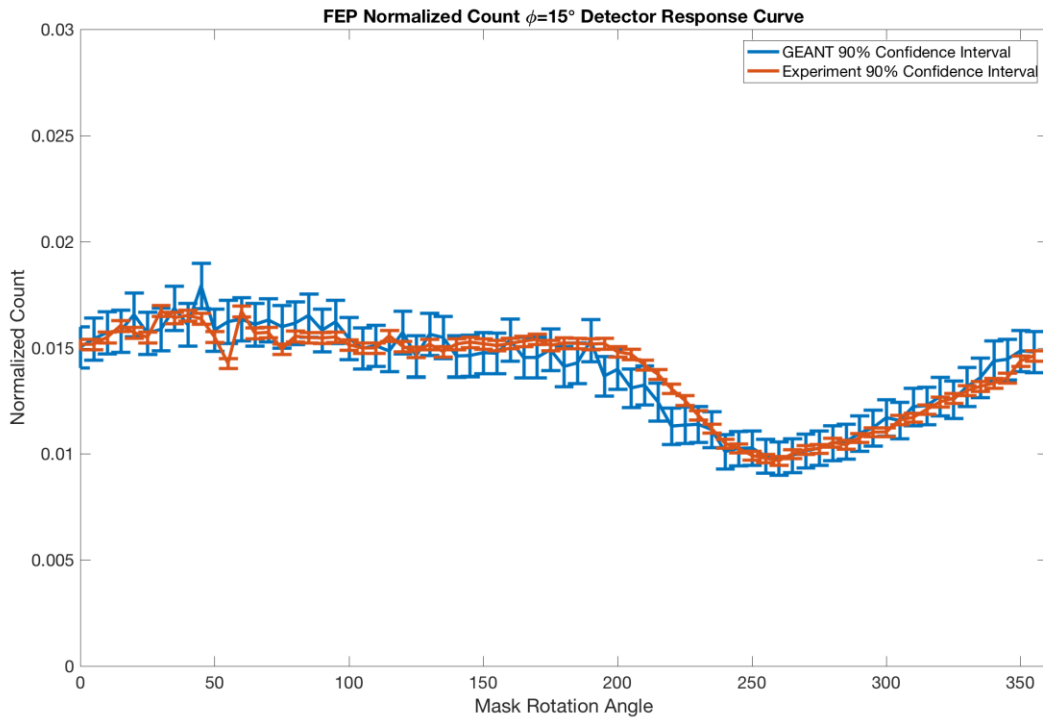


Figure 62. Normalized count (per total count in the detector response curve) that contribute to the FEP for $\varphi = 5^\circ$ with $\theta = 0^\circ - 355^\circ$ in increments of 15° . These values correspond to GEANT results with 500,000 source particles for each (θ, φ) position and experimental results collected over 24h. The 90% confidence interval is plotted. For each (θ, φ) position, the FEP count comes from a broadened energy spectrum (via convolution for GEANT data and inherently for experimental data).

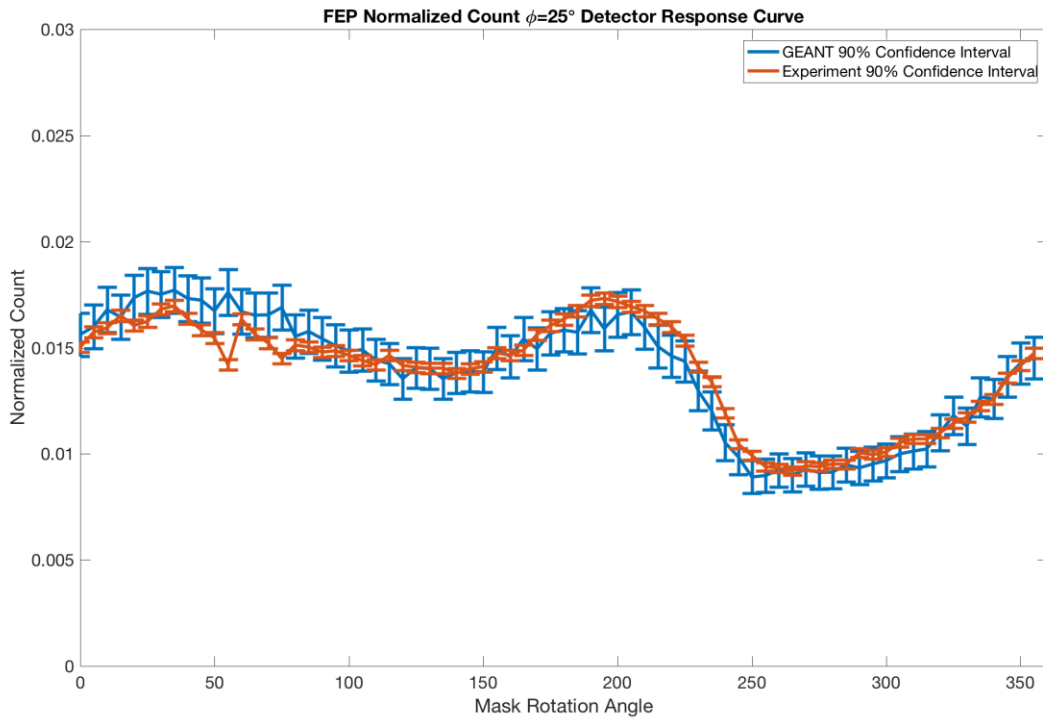


Figure 63. Normalized count (per total count in the detector response curve) that contribute to the FEP for $\varphi = 5^\circ$ with $\theta = 0^\circ - 355^\circ$ in increments of 25° . These values correspond to GEANT results with 500,000 source particles for each (θ, φ) position and experimental results collected over 24h. The 90% confidence interval is plotted. For each (θ, φ) position, the FEP count comes from a broadened energy spectrum (via convolution for GEANT data and inherently for experimental data).

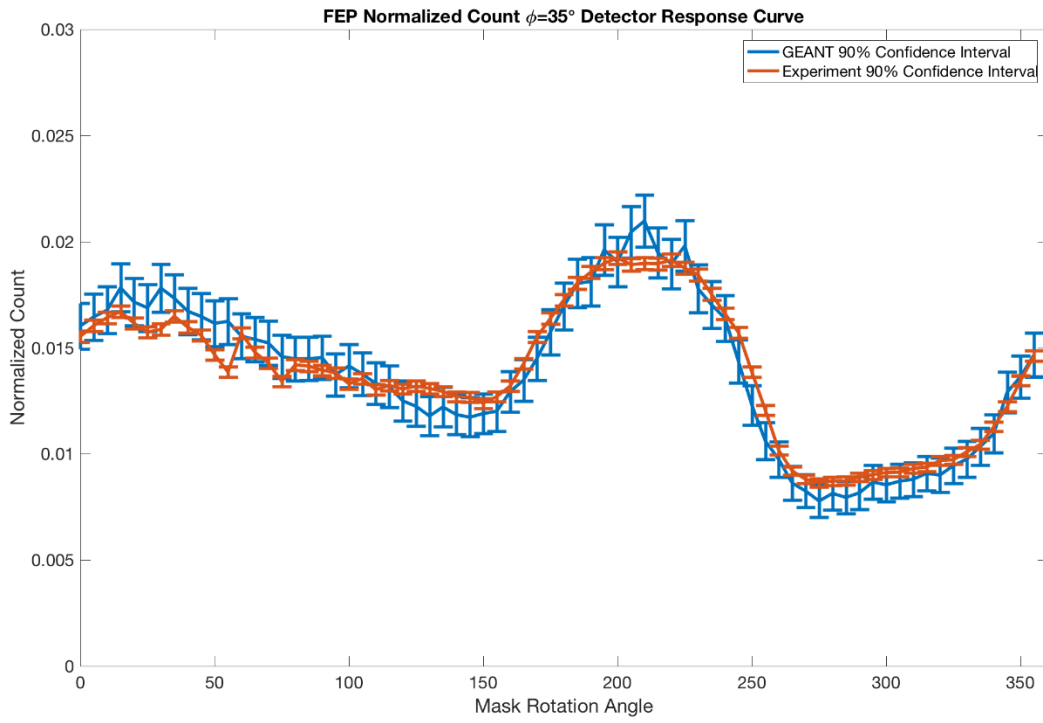


Figure 64. Normalized count (per total count in the detector response curve) that contribute to the FEP for $\varphi = 5^\circ$ with $\theta = 0^\circ - 355^\circ$ in increments of 35° . These values correspond to GEANT results with 500,000 source particles for each (θ, φ) position and experimental results collected over 24h. The 90% confidence interval is plotted. For each (θ, φ) position, the FEP count comes from a broadened energy spectrum (via convolution for GEANT data and inherently for experimental data).

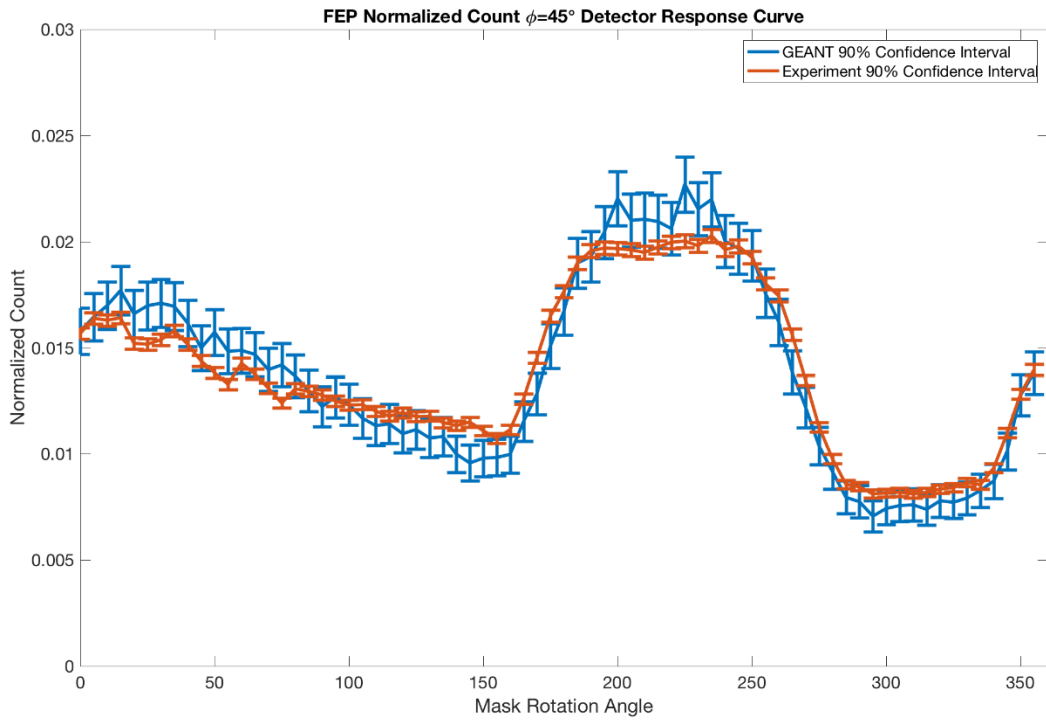


Figure 65. Normalized count (per total count in the detector response curve) that contribute to the FEP for $\varphi = 5^\circ$ with $\theta = 0^\circ - 355^\circ$ in increments of 45° . These values correspond to GEANT results with 500,000 source particles for each (θ, φ) position and experimental results collected over 24h. The 90% confidence interval is plotted. For each (θ, φ) position, the FEP count comes from a broadened energy spectrum (via convolution for GEANT data and inherently for experimental data).

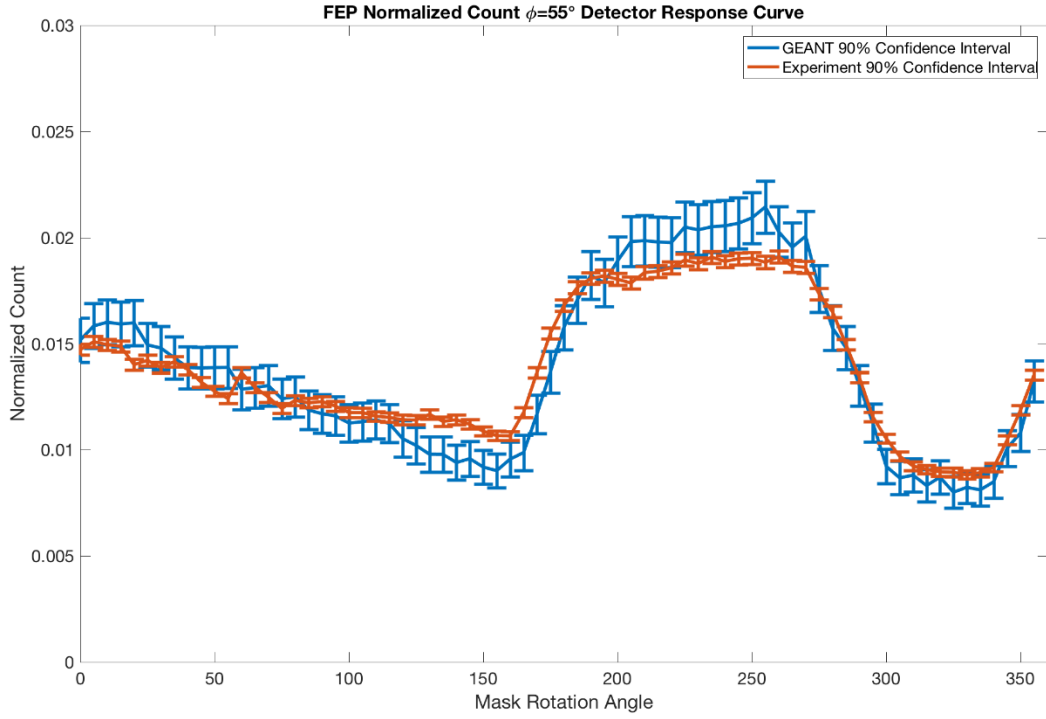


Figure 66. Normalized count (per total count in the detector response curve) that contribute to the FEP for $\varphi = 5^\circ$ with $\theta = 0^\circ - 355^\circ$ in increments of 55° . These values correspond to GEANT results with 500,000 source particles for each (θ, φ) position and experimental results collected over 24h. The 90% confidence interval is plotted. For each (θ, φ) position, the FEP count comes from a broadened energy spectrum (via convolution for GEANT data and inherently for experimental data).

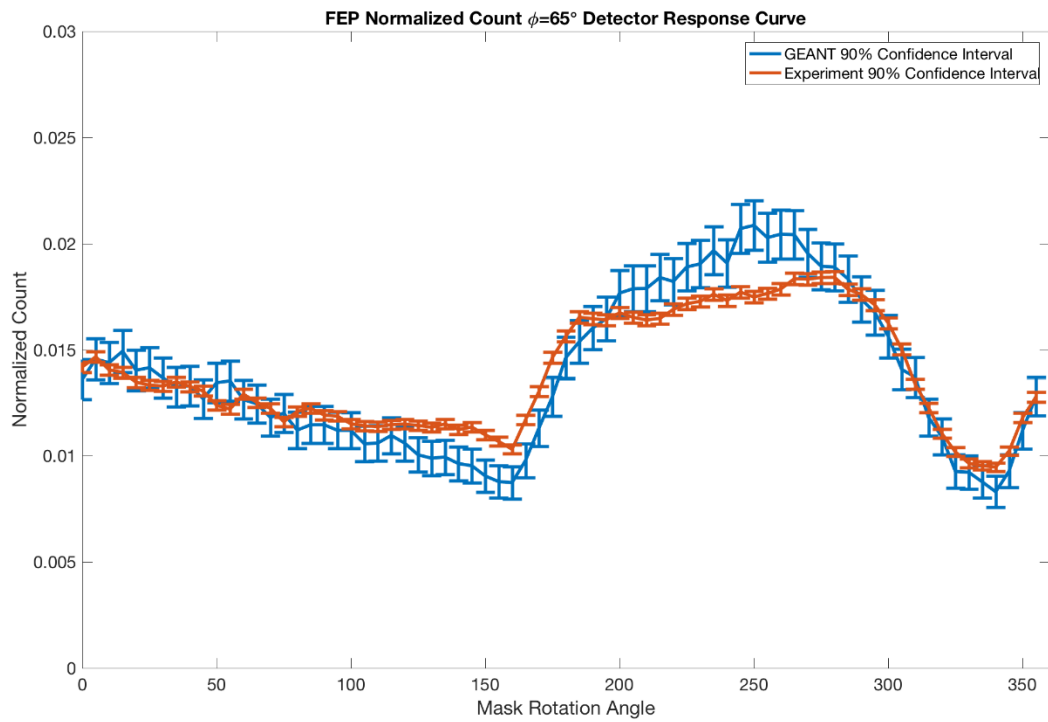


Figure 67. Normalized count (per total count in the detector response curve) that contribute to the FEP for $\varphi = 5^\circ$ with $\theta = 0^\circ - 355^\circ$ in increments of 65° . These values correspond to GEANT results with 500,000 source particles for each (θ, φ) position and experimental results collected over 24h. The 90% confidence interval is plotted. For each (θ, φ) position, the FEP count comes from a broadened energy spectrum (via convolution for GEANT data and inherently for experimental data).

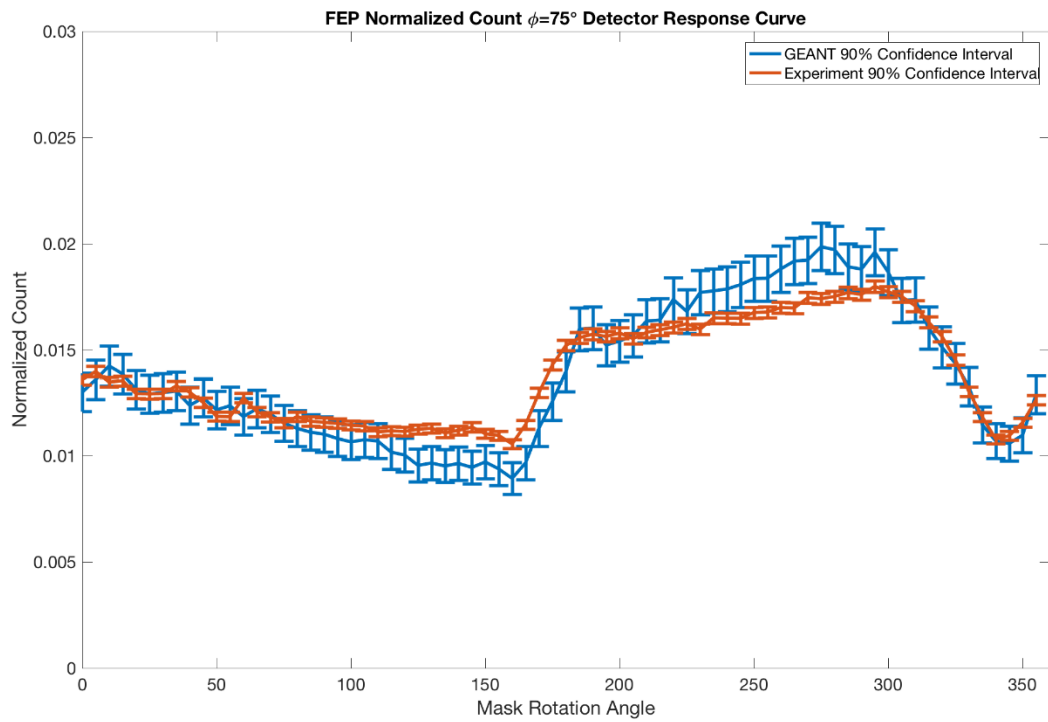


Figure 68. Normalized count (per total count in the detector response curve) that contribute to the FEP for $\varphi = 5^\circ$ with $\theta = 0^\circ - 355^\circ$ in increments of 75° . These values correspond to GEANT results with 500,000 source particles for each (θ, φ) position and experimental results collected over 24h. The 90% confidence interval is plotted. For each (θ, φ) position, the FEP count comes from a broadened energy spectrum (via convolution for GEANT data and inherently for experimental data).

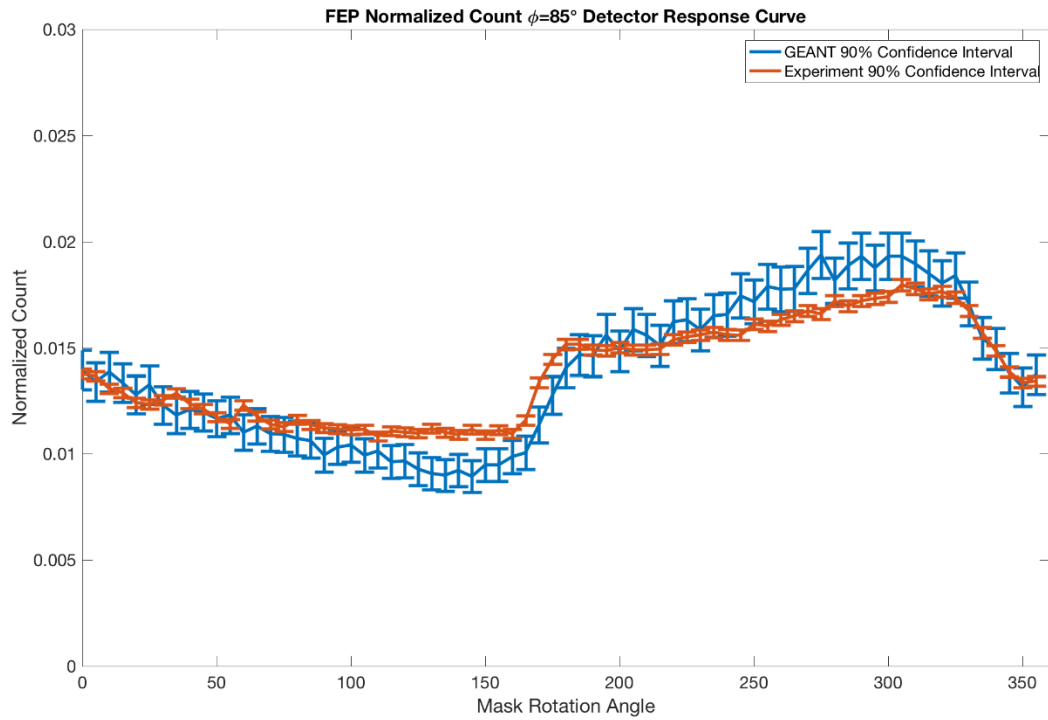


Figure 69. Normalized count (per total count in the detector response curve) that contribute to the FEP for $\varphi = 5^\circ$ with $\theta = 0^\circ - 355^\circ$ in increments of 85° . These values correspond to GEANT results with 500,000 source particles for each (θ, φ) position and experimental results collected over 24h. The 90% confidence interval is plotted. For each (θ, φ) position, the FEP count comes from a broadened energy spectrum (via convolution for GEANT data and inherently for experimental data).

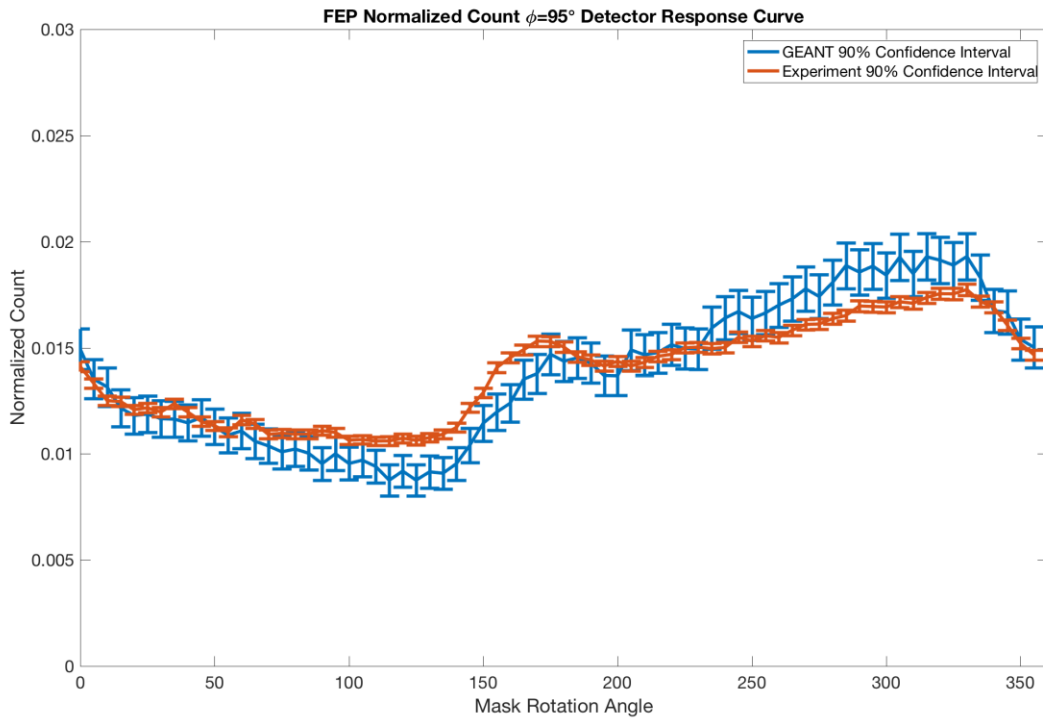


Figure 70. Normalized count (per total count in the detector response curve) that contribute to the FEP for $\varphi = 5^\circ$ with $\theta = 0^\circ - 355^\circ$ in increments of 95° . These values correspond to GEANT results with 500,000 source particles for each (θ, φ) position and experimental results collected over 24h. The 90% confidence interval is plotted. For each (θ, φ) position, the FEP count comes from a broadened energy spectrum (via convolution for GEANT data and inherently for experimental data).

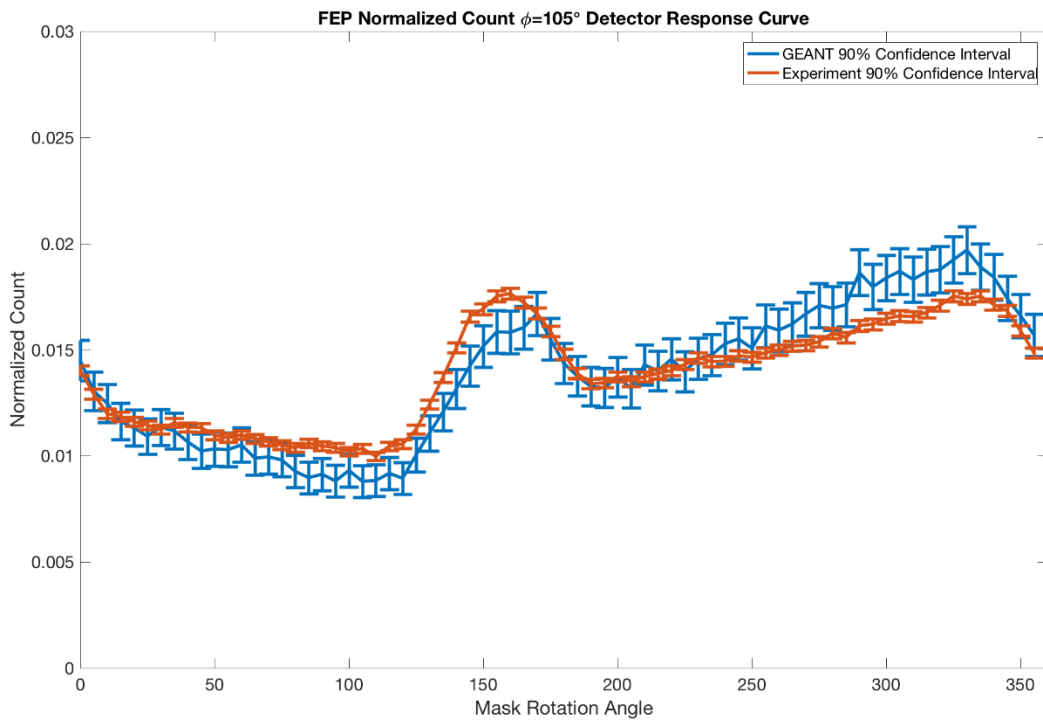


Figure 71. Normalized count (per total count in the detector response curve) that contribute to the FEP for $\varphi = 5^\circ$ with $\theta = 0^\circ - 355^\circ$ in increments of 105° . These values correspond to GEANT results with 500,000 source particles for each (θ, φ) position and experimental results collected over 24h. The 90% confidence interval is plotted. For each (θ, φ) position, the FEP count comes from a broadened energy spectrum (via convolution for GEANT data and inherently for experimental data).

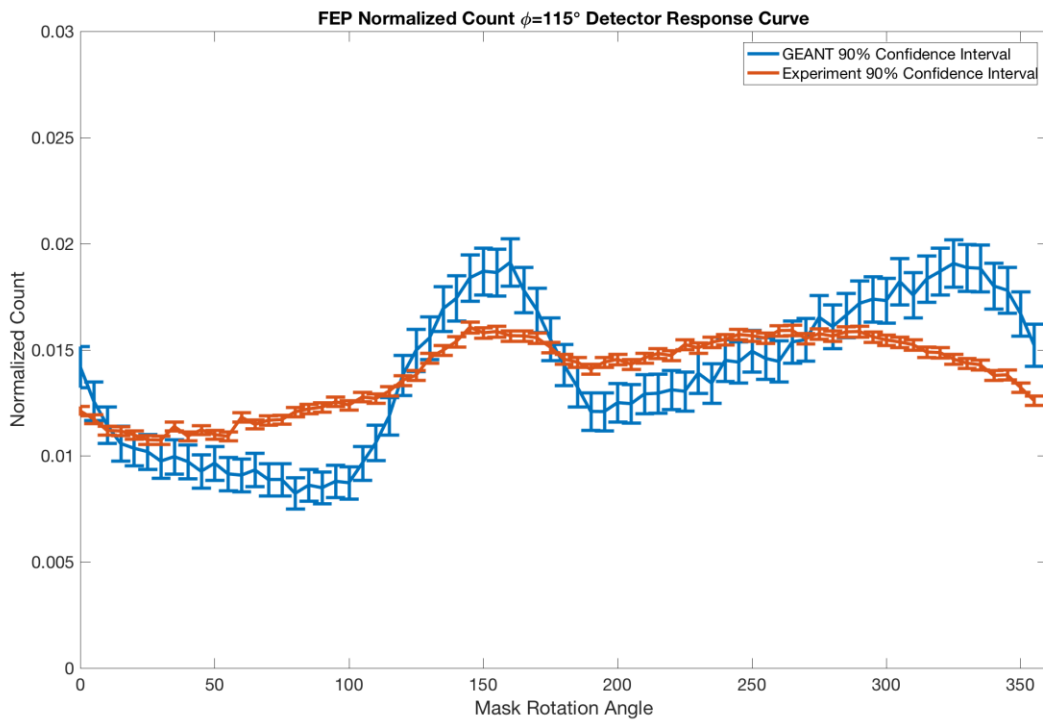


Figure 72. Normalized count (per total count in the detector response curve) that contribute to the FEP for $\varphi = 5^\circ$ with $\theta = 0^\circ - 355^\circ$ in increments of 115° . These values correspond to GEANT results with 500,000 source particles for each (θ, φ) position and experimental results collected over 24h. The 90% confidence interval is plotted. For each (θ, φ) position, the FEP count comes from a broadened energy spectrum (via convolution for GEANT data and inherently for experimental data).

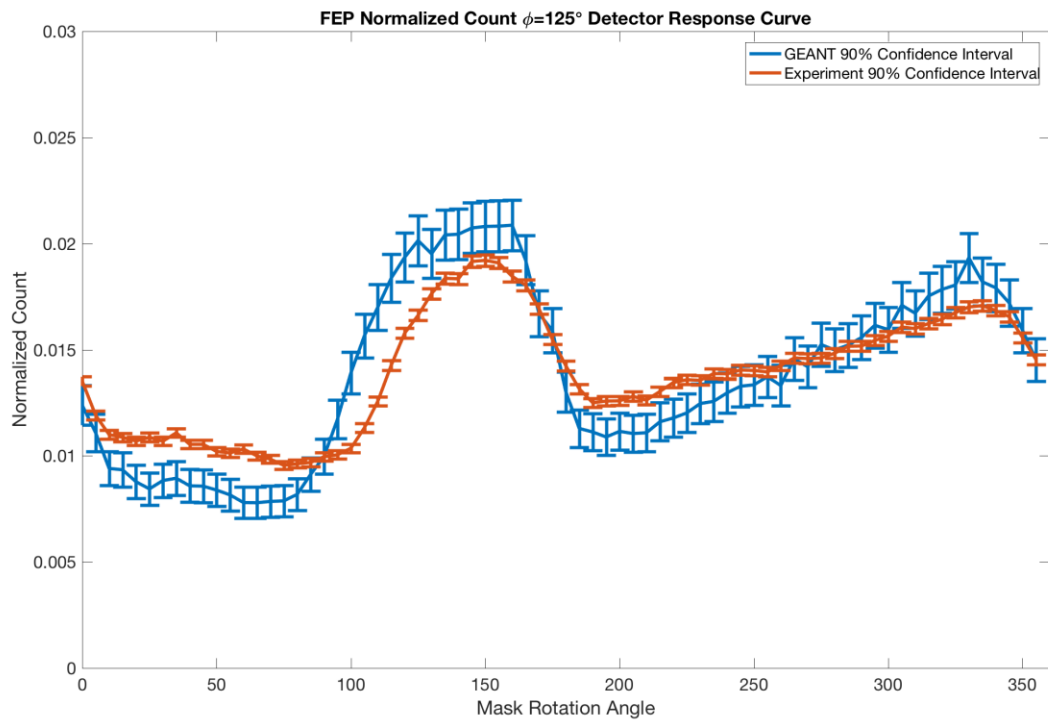


Figure 73. Normalized count (per total count in the detector response curve) that contribute to the FEP for $\varphi = 5^\circ$ with $\theta = 0^\circ - 355^\circ$ in increments of 125° . These values correspond to GEANT results with 500,000 source particles for each (θ, φ) position and experimental results collected over 24h. The 90% confidence interval is plotted. For each (θ, φ) position, the FEP count comes from a broadened energy spectrum (via convolution for GEANT data and inherently for experimental data).

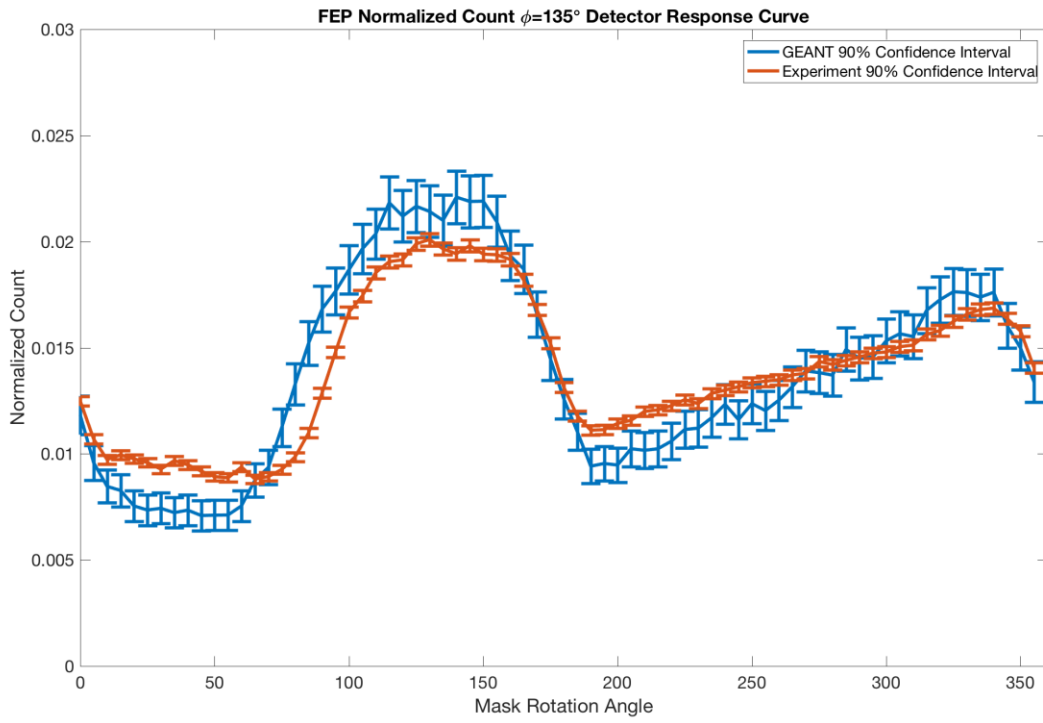


Figure 74. Normalized count (per total count in the detector response curve) that contribute to the FEP for $\varphi = 5^\circ$ with $\theta = 0^\circ - 355^\circ$ in increments of 135° . These values correspond to GEANT results with 500,000 source particles for each (θ, φ) position and experimental results collected over 24h. The 90% confidence interval is plotted. For each (θ, φ) position, the FEP count comes from a broadened energy spectrum (via convolution for GEANT data and inherently for experimental data).

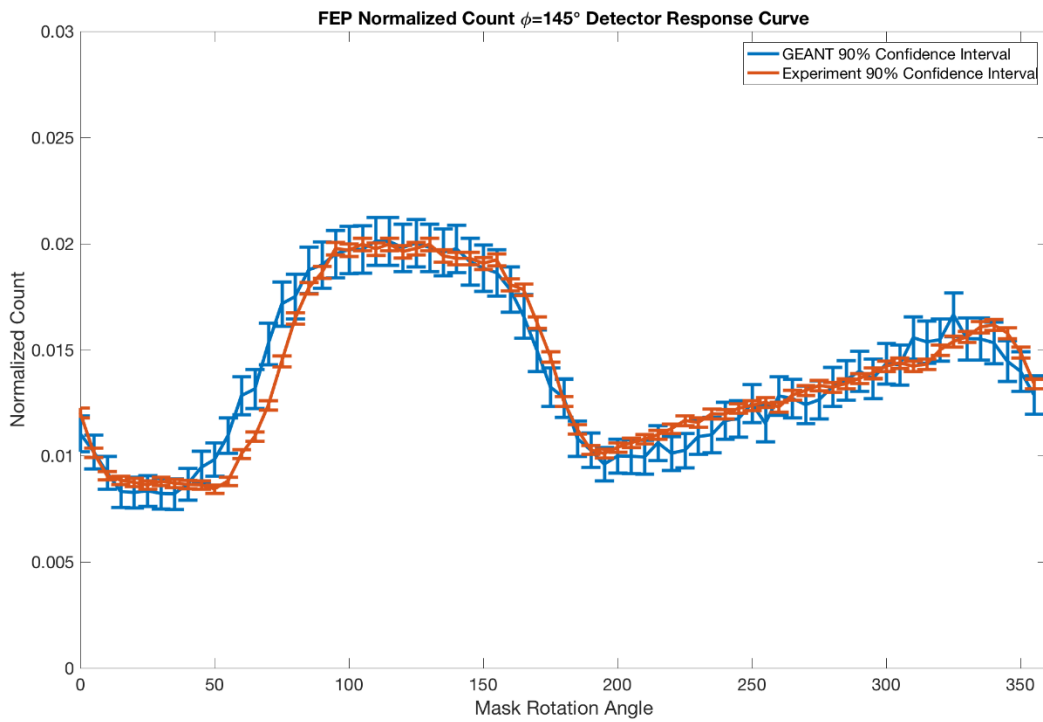


Figure 75. Normalized count (per total count in the detector response curve) that contribute to the FEP for $\varphi = 5^\circ$ with $\theta = 0^\circ - 355^\circ$ in increments of 145° . These values correspond to GEANT results with 500,000 source particles for each (θ, φ) position and experimental results collected over 24h. The 90% confidence interval is plotted. For each (θ, φ) position, the FEP count comes from a broadened energy spectrum (via convolution for GEANT data and inherently for experimental data).

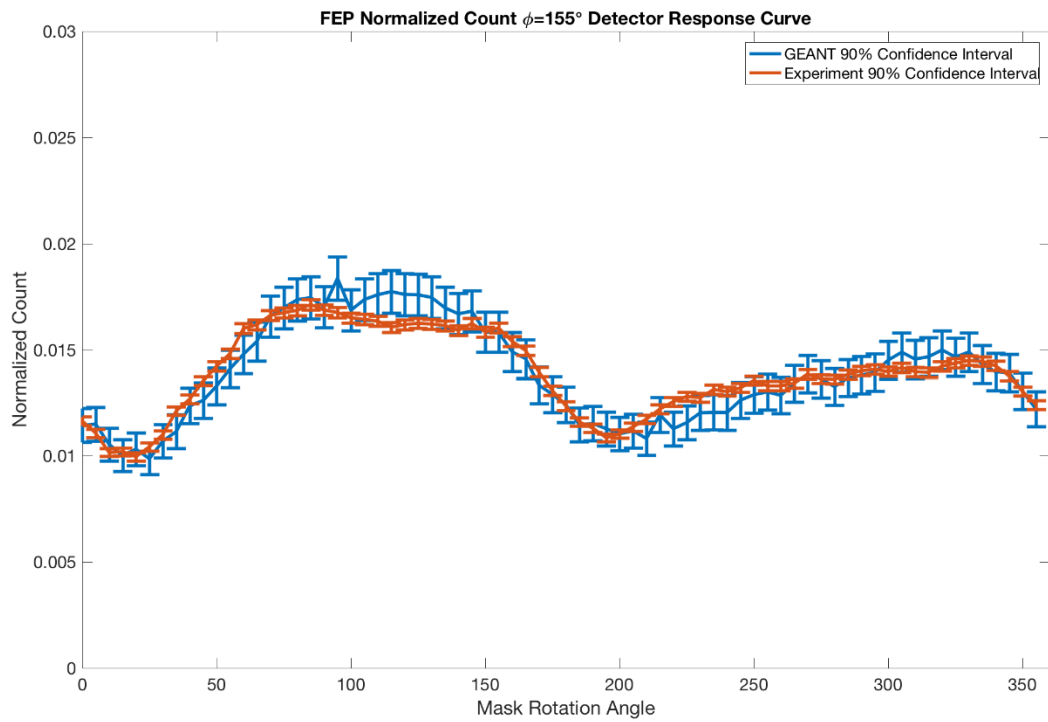


Figure 76. Normalized count (per total count in the detector response curve) that contribute to the FEP for $\varphi = 5^\circ$ with $\theta = 0^\circ - 355^\circ$ in increments of 155° . These values correspond to GEANT results with 500,000 source particles for each (θ, φ) position and experimental results collected over 24h. The 90% confidence interval is plotted. For each (θ, φ) position, the FEP count comes from a broadened energy spectrum (via convolution for GEANT data and inherently for experimental data).

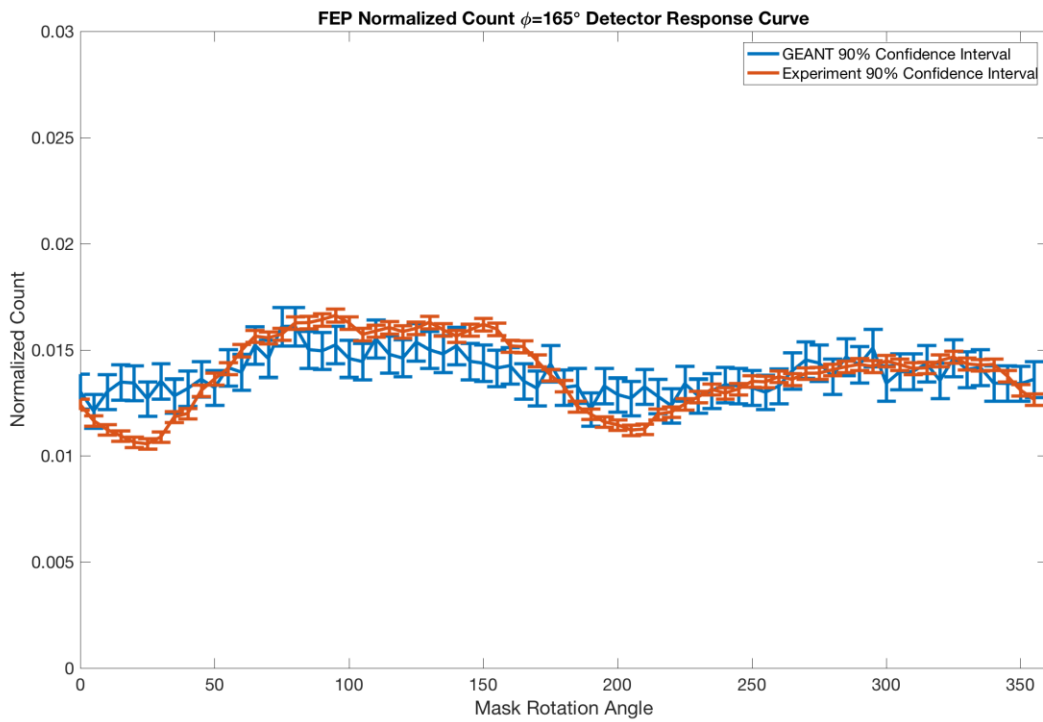


Figure 77. Normalized count (per total count in the detector response curve) that contribute to the FEP for $\varphi = 5^\circ$ with $\theta = 0^\circ - 355^\circ$ in increments of 165° . These values correspond to GEANT results with 500,000 source particles for each (θ, φ) position and experimental results collected over 24h. The 90% confidence interval is plotted. For each (θ, φ) position, the FEP count comes from a broadened energy spectrum (via convolution for GEANT data and inherently for experimental data).

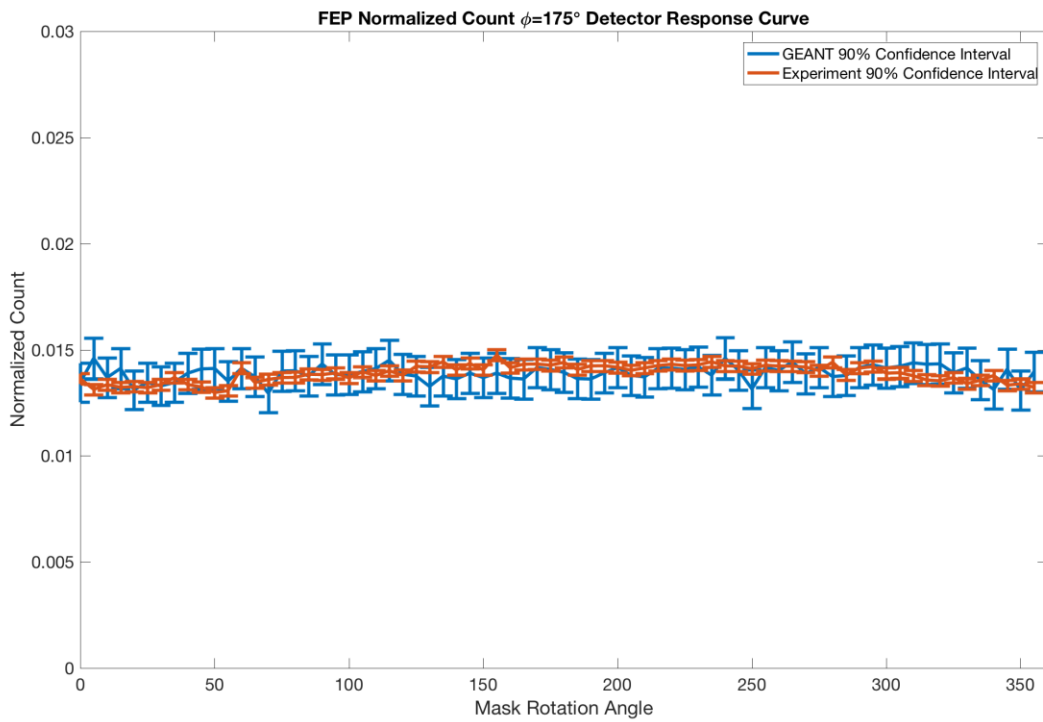


Figure 78. Normalized count (per total count in the detector response curve) that contribute to the FEP for $\varphi = 5^\circ$ with $\theta = 0^\circ - 355^\circ$ in increments of 175° . These values correspond to GEANT results with 500,000 source particles for each (θ, φ) position and experimental results collected over 24h. The 90% confidence interval is plotted. For each (θ, φ) position, the FEP count comes from a broadened energy spectrum (via convolution for GEANT data and inherently for experimental data).

Appendix C

Appendix C contains the complete results of the application of the algorithm developed to a set of experimental data. This includes 1296 experimental detector response curves, one for each potential source position (θ, φ) combination with $\theta = 5^\circ - 360^\circ$ in increments of 5° and $\varphi = 5^\circ - 175^\circ$ in increments of 10° . These experimental curves served as input to the algorithm. The algorithm completed this set of 1296 source direction determinations in less than a second, implying the algorithm computational time is of negligible concern. The resulting errors in the predicted (θ, φ) positions are shown in **Figure 79** and **Figure 80** for each of the true experimental source positions. For example, the upper left value in the table “1o/o” indicates that for a true experimental detector response curve obtained for a source located at a position associated with $(\theta = 5^\circ, \varphi = 5^\circ)$, the algorithm predicted the correct phi value of $\varphi = 5^\circ$ and a theta value that was off by 10° , in this case predicting that $\varphi = 15^\circ$. Excluding the erroneous experimental run at $\varphi = 115^\circ$, for which the accuracy of the (θ, φ) is poor, the average error in θ is 4.12° and the average error in φ is 2.94° . This is a remarkable result as the resolution in θ is 5° and the resolution in φ is 10° .

Figure 79. Error in (θ, φ) predicted direction of the source for each experimental input direction $\theta = 5^\circ - 180^\circ$ and $\varphi = 5^\circ - 175^\circ$

Figure 80. Error in (θ, φ) predicted direction of the source for each experimental input $\theta = 185^\circ - 360^\circ$ and $\varphi = 5^\circ - 175^\circ$

Appendix D

This appendix contains the set of GEANT4 input files used in the simulation. Header files (.hh) and implementation files (.cc) are included for completeness. All .mac interactions with the code have been built into the main() method. To run in this automatic manner, a runtime parameter keyword is used. In this case, the following should be run in order to initiate a run with mask rotation: `. /myMesh -m julieRun` Commented code has been maintained due to its utility in expanding the output obtained from the simulation, if run duration or computational power of the system permits such acquisition.

Action Initialization

B4aActionInitialization.hh

```
#ifndef B4aActionInitialization_h
#define B4aActionInitialization_h 1

#include "G4VUserActionInitialization.hh"

class B4DetectorConstruction;

/// Action initialization class.
///

class B4aActionInitialization : public G4VUserActionInitialization
{
public:
    B4aActionInitialization(B4DetectorConstruction* );
    virtual ~B4aActionInitialization();
    virtual void BuildForMaster() const;
    virtual void Build() const;

private:
    B4DetectorConstruction* fDetConstruction;
};
```

```
#endif
```

B4aActionInitialization.cc

```
#include "B4aActionInitialization.hh"
#include "B4PrimaryGeneratorAction.hh"
#include "B4RunAction.hh"
#include "B4aEventAction.hh"
#include "B4aSteppingAction.hh"
#include "B4DetectorConstruction.hh"

//....oooOOoOOooo.....oooOOoOOooo.....oooOOoOOooo.....oooOOoOOooo.....
```

```
B4aActionInitialization::B4aActionInitialization
    (B4DetectorConstruction* detConstruction)
: G4VUserActionInitialization(),
  fDetConstruction(detConstruction)
{
```

```
//....oooOOoOOooo.....oooOOoOOooo.....oooOOoOOooo.....oooOOoOOooo.....
```

```
B4aActionInitialization::~B4aActionInitialization()
{
```

```
//....oooOOoOOooo.....oooOOoOOooo.....oooOOoOOooo.....oooOOoOOooo.....
```

```
void B4aActionInitialization::BuildForMaster() const
{
  SetUserAction(new B4RunAction);
}
```

```
//....oooOOoOOooo.....oooOOoOOooo.....oooOOoOOooo.....oooOOoOOooo.....
```

```
void B4aActionInitialization::Build() const
{
  SetUserAction(new B4PrimaryGeneratorAction);
  B4RunAction* runAction = new B4RunAction;
  SetUserAction(runAction);
  B4aEventAction* eventAction = new B4aEventAction(runAction);
  SetUserAction(eventAction);
  SetUserAction(new B4aSteppingAction(fDetConstruction,eventAction));
}
```

```
//....oooOOoOOooo.....oooOOoOOooo.....oooOOoOOooo.....oooOOoOOooo.....
```

Detector Construction

B4aActionInitialization.hh

```

#ifndef B4DetectorConstruction_h
#define B4DetectorConstruction_h 1

#include "G4VUserDetectorConstruction.hh"
#include "globals.hh"

class G4VPhysicalVolume;
class G4GlobalMagFieldMessenger;

class B4DetectorConstruction : public G4VUserDetectorConstruction
{
public:
    B4DetectorConstruction();
    virtual ~B4DetectorConstruction();

public:
    virtual G4VPhysicalVolume* Construct();
    virtual void ConstructSDandField();

    // get methods
    //
    //const G4VPhysicalVolume* GetAbsorberPV() const;

private:
    // methods
    //
    void DefineMaterials();
    G4VPhysicalVolume* DefineVolumes();

    // data members
    //
    static G4ThreadLocal G4GlobalMagFieldMessenger* fMagFieldMessenger;
        // magnetic field messenger

    //G4VPhysicalVolume* detectorNaI_Physical; // the absorber physical volume

    G4bool fCheckOverlaps; // option to activate checking of volumes overlaps
};

// inline functions

//inline const G4VPhysicalVolume* B4DetectorConstruction::GetAbsorberPV() const {
//    return detectorNaI_Physical;
//}

//....oooOOoOOooo.....oooOOoOOooo.....oooOOoOOooo.....oooOOoOOooo.....
```

#endif

B4aActionInitialization.cc

```

#include "B4DetectorConstruction.hh"

#include "G4Material.hh"
#include "G4NistManager.hh"

#include "G4Box.hh"
#include "G4LogicalVolume.hh"
#include "G4PVPlacement.hh"
#include "G4PVReplica.hh"
#include "G4GlobalMagFieldMessenger.hh"
#include "G4AutoDelete.hh"
#include "G4Tubs.hh"
#include "G4Orb.hh"
#include "G4SubtractionSolid.hh"

#include "G4GeometryManager.hh"
#include "G4PhysicalVolumeStore.hh"
#include "G4LogicalVolumeStore.hh"
#include "G4SolidStore.hh"

#include "G4VisAttributes.hh"
#include "G4Colour.hh"

#include "G4PhysicalConstants.hh"
#include "G4SystemOfUnits.hh"
#include "G4UnitsTable.hh"
#include <iterator>

// CADMESH //
#include "G4String.hh"
#include "G4ThreeVector.hh"
#include "G4TessellatedSolid.hh"
#include "G4TriangularFacet.hh"
#include "G4Tet.hh"
#include "G4AssemblyVolume.hh"
#include "G4Material.hh"
#include "G4LogicalVolume.hh"
#include "G4SystemOfUnits.hh"
#include "G4UIcommand.hh"

// GEANT4 //
#include "globals.hh"
#include "G4ThreeVector.hh"
#include "G4Transform3D.hh"

#include "G4Box.hh"
#include "G4LogicalVolume.hh"
#include "G4PVPlacement.hh"
#include "G4AssemblyVolume.hh"

```



```

// Vacuum
new G4Material("Galactic", z=1., a=1.01*g/mole,density= universe_mean_density,
kStateGas, 2.73*kelvin, 3.e-18*pascal);

// Print materials
//G4cout << *(G4Material::GetMaterialTable()) << G4endl;
}

//....oooOOoOOooo.....oooOOoOOooo.....oooOOoOOooo.....oooOOoOOooo..... 

G4VPhysicalVolume* B4DetectorConstruction::DefineVolumes()
{
    // Geometry parameters
    G4double worldRadius = 100*cm;

    G4NistManager* nistManager = G4NistManager::Instance();

    // Get materials
    G4Material* water_mat = nistManager->FindOrBuildMaterial("G4_WATER");
    G4Material* air_mat = nistManager->FindOrBuildMaterial("G4_AIR");
    //   G4_POLYETHYLENE (C_2H_4)_N-Polyethylene  0.94      57.4
    //     1  0.143711
    //     6  0.856289
    G4Material* poly_mat = nistManager->FindOrBuildMaterial("G4_POLYETHYLENE");
    //   G4_PLEXIGLASS      1.19      74
    //     1  0.080538
    //     6  0.599848
    //     8  0.319614
    G4Material* plexi_mat = nistManager->FindOrBuildMaterial("G4_PLEXIGLASS");
    G4Material* Bi_mat = nistManager->FindOrBuildMaterial("G4_Bi");
    G4Material* concrete_mat = nistManager->FindOrBuildMaterial("G4_CONCRETE");
    G4Material* wax_mat = nistManager->FindOrBuildMaterial("G4_M3_WAX");
    G4Material* LiFl_mat = nistManager->FindOrBuildMaterial("G4_LITHIUM_FLUORIDE");
    // 2  G4_SODIUM_IODIDE      3.667      452
    //    11  0.153373
    //    53  0.846627
    G4Material* NaI_mat = nistManager->FindOrBuildMaterial("G4_SODIUM_IODIDE");

    // defining BiPb
    G4double z, a, fractionmass, density;
    G4String name, symbol;
    G4int ncomponents;
    a = 208.98*g/mole;
    G4Element* elBi = new G4Element(name="Bismuth",symbol="Bi", z= 83., a);
    a = 207.2*g/mole;
    G4Element* elPb = new G4Element(name="Lead" ,symbol="Pb" , z= 82., a);
    density = 10.5*g/cm3;
    G4Material* BiPb = new G4Material(name="BiPb ",density,ncomponents=2);
    BiPb->AddElement(elBi, fractionmass=45*perCent);
    BiPb->AddElement(elPb, fractionmass=55*perCent);
}

```

```

// defining aluminum alloy

G4Material* G4_Mg = nistManager->FindOrBuildMaterial("G4_Mg");

G4Material* G4_Al = nistManager->FindOrBuildMaterial("G4_Al");

G4Material* G4_Si = nistManager->FindOrBuildMaterial("G4_Si");

G4Material* G4_Ti = nistManager->FindOrBuildMaterial("G4_Ti");

G4Material* G4_Cr = nistManager->FindOrBuildMaterial("G4_Cr");

G4Material* G4_Mn = nistManager->FindOrBuildMaterial("G4_Mn");

G4Material* G4_Fe = nistManager->FindOrBuildMaterial("G4_Fe");

G4Material* G4_Cu = nistManager->FindOrBuildMaterial("G4_Cu");

G4Material* G4_Zn = nistManager->FindOrBuildMaterial("G4_Zn");

G4Material* G4_C = nistManager->FindOrBuildMaterial("G4_C");

G4Material* G4_N = nistManager->FindOrBuildMaterial("G4_N");

G4Material* G4_O = nistManager->FindOrBuildMaterial("G4_O");

G4Material* G4_Ar = nistManager->FindOrBuildMaterial("G4_Ar");

G4Material* G4_H = nistManager->FindOrBuildMaterial("G4_H");

```

//// ?????? MATERIALS FOR CROSS SECTIONS TESTS

```

G4Material* Vaccuum = new G4Material("Galactic", z=1., a=1.01*g/mole,density=
universe_mean_density, kStateGas, 2.73*kelvin, 3.e-18*pascal);

// Scatter Mask Density H,O,C (density = 1.19 g/cc)
G4double densityMask = plexi_mat->GetDensity();
G4Material* H_mask = new G4Material("H_mask",densityMask, ncomponents=1);
H_mask->AddMaterial(G4_H, 1.);
G4Material* O_mask = new G4Material("O_mask",densityMask, ncomponents=1);
O_mask->AddMaterial(G4_O, 1.);
G4Material* C_mask_AND_forSphere = new G4Material("C_mask",densityMask,
ncomponents=1);
C_mask_AND_forSphere->AddMaterial(G4_C, 1.);

G4cout << "Density of the Mask: " << G4BestUnit(H_mask->GetDensity(), "Volumic
Mass");

```

```

// Detector Density H,O,C (density = 3.667 g/cc)
G4double densityDetector = NaI_mat->GetDensity();
G4Material* H_detector = new G4Material("H_detector",densityDetector,
ncomponents=1);
H_detector->AddMaterial(G4_H, 1.);
G4Material* O_detector = new G4Material("O_detector",densityDetector,
ncomponents=1);
O_detector->AddMaterial(G4_O, 1.);
G4Material* C_detector = new G4Material("C_detector",densityDetector, ncomponents=1);
C_detector->AddMaterial(G4_C, 1.);

G4cout << "Density of the Detector: " << G4BestUnit(C_detector->GetDensity(), "Volumic
Mass");

```

//// ??????

```

G4Material* AlAlloy = new G4Material(name="AlAlloy", density= 2.78*g/cm3,
ncomponents=9);

```

```

AlAlloy->AddMaterial(G4_Mg, fractionmass=0.015);
AlAlloy->AddMaterial(G4_Al, fractionmass=0.927);
AlAlloy->AddMaterial(G4_Si, fractionmass=0.00283);
AlAlloy->AddMaterial(G4_Ti, fractionmass=0.00085);
AlAlloy->AddMaterial(G4_Cr, fractionmass=0.00057);
AlAlloy->AddMaterial(G4_Mn, fractionmass=0.006);
AlAlloy->AddMaterial(G4_Fe, fractionmass=0.00283);
AlAlloy->AddMaterial(G4_Cu, fractionmass=0.0435);
AlAlloy->AddMaterial(G4_Zn, fractionmass=0.00142);

```

```

G4Material* Air_mat_mcnp = new G4Material(name="AirMCNP", density=
0.001205*g/cm3, ncomponents=4);

```

```

Air_mat_mcnp->AddMaterial(G4_C, fractionmass=0.000124);
Air_mat_mcnp->AddMaterial(G4_N, fractionmass=0.755268);
Air_mat_mcnp->AddMaterial(G4_O, fractionmass=0.231781);
Air_mat_mcnp->AddMaterial(G4_Ar, fractionmass=0.012827);

```

```

//  

// World  

//
```

```

G4VSolid* worldS
= new G4Orb("World", worldRadius); // its size

```

```

G4LogicalVolume* worldLV
= new G4LogicalVolume(
worldS, // its solid

```

```

Air_mat_mcnp, // its material
"World"); // its name

G4VPhysicalVolume* worldPV
= new G4PVPlacement(
    o, // no rotation
    G4ThreeVector(), // at (o,o,o)
    worldLV, // its logical volume
    "World", // its name
    o, // its mother volume
    false, // no boolean operation
    o, // copy number
    fCheckOverlaps); // checking overlaps

//worldLV->SetVisAttributes(G4VisAttributes::Invisible);

////////*****///////
//READ IN THE NODES TO 3 VECTORS (x,y,z)
ifstream infile;
infile.open("/Users/jvl2xv/Downloads/RSM_Attila_Nodes.txt");
std::vector<double> xVals;
std::vector<double> yVals;
std::vector<double> zVals;
int i = o;
string line;
while(!infile.eof()) // To get you all the lines.
{
    getline(infile,line); // Saves the line in line
    istringstream buf(line);
    istream_iterator<std::string> beg(buf), end;
    vector<std::string> tokens(beg, end);
    // remove the comma
    tokens[0].pop_back();
    tokens[1].pop_back();
    tokens[2].pop_back();

    xVals.push_back(stod(tokens[1].c_str()));
    yVals.push_back(stod(tokens[2].c_str()));
    zVals.push_back(stod(tokens[3].c_str()));
    //cout << i << " " << xVals[i] << " " << yVals[i] << " " << zVals[i] << endl;

    i++;
}

```

```

infile.close();

//READ IN THE ELEMENTS TO 4 VECTORS (1,2,3,4)
ifstream infile2;
infile2.open("/Users/jvl2xv/Downloads/RSM_Attila_Elements.txt");
std::vector<int> onePoint;
std::vector<int> twoPoint;
std::vector<int> threePoint;
std::vector<int> fourPoint;
int j = 0;
while(!infile2.eof()) // To get you all the lines.
{
    getline(infile2,line); // Saves the line in line
    istringstream buf(line);
    istream_iterator<std::string> beg(buf), end;
    vector<std::string> tokens(beg, end);
    //remove the comma
    tokens[0].pop_back();
    tokens[1].pop_back();
    tokens[2].pop_back();
    tokens[3].pop_back();

    onePoint.push_back(stoi(tokens[1].c_str()));
    twoPoint.push_back(stoi(tokens[2].c_str()));
    threePoint.push_back(stoi(tokens[3].c_str()));
    fourPoint.push_back(stoi(tokens[4].c_str()));
    //cout << j << " " << onePoint[j] << " " << twoPoint[j] << " " << threePoint[j] << " "
    << fourPoint[j] << endl;

    j++;
}

infile2.close();

////////*****///////
G4VisAttributes* visAttributes2 = new G4VisAttributes(G4Colour(1.0, 0.0, 0.0)); //red
//visAttributes2->SetVisibility(true);
G4VisAttributes* visAttributes3 = new G4VisAttributes(G4Colour(0.0, 1.0, 0.0)); //green
//visAttributes3->SetVisibility(false);
G4VisAttributes* visAttributes4 = new G4VisAttributes(G4Colour(0.0, 0.0, 1.0)); //blue
//visAttributes4->SetVisibility(false);
G4VisAttributes* visAttributes5 = new G4VisAttributes(G4Colour(0.0, 1.0, 1.0)); //cyan
//visAttributes5->SetVisibility(false);
G4VisAttributes* visAttributes6 = new G4VisAttributes(G4Colour(1.0, 0.0, 1.0)); //magenta
//visAttributes6->SetVisibility(false);

```

```

// this will be the compendium of all of the tetrahedra
G4AssemblyVolume * assembly = new G4AssemblyVolume();

// create tetrahedra according to the read in lists and add to assembly

G4RotationMatrix * element_rotation = new G4RotationMatrix();
G4ThreeVector element_position = G4ThreeVector();
G4Transform3D assembly_transform = G4Translate3D();

int numVis = 0;
double totMass = 0.;

for (int i=0; i<onePoint.size(); i++) {
    // node numbering starts as 1
    G4String file_name = "julieFile";
    G4ThreeVector p1 = G4ThreeVector(xVals[onePoint[i]-1]*cm, yVals[onePoint[i]-1]*cm,
zVals[onePoint[i]-1]*cm);
    G4ThreeVector p2 = G4ThreeVector(xVals[twoPoint[i]-1]*cm, yVals[twoPoint[i]-1]*cm,
zVals[twoPoint[i]-1]*cm);
    G4ThreeVector p3 = G4ThreeVector(xVals[threePoint[i]-1]*cm, yVals[threePoint[i]-1]*cm,
zVals[threePoint[i]-1]*cm);
    G4ThreeVector p4 = G4ThreeVector(xVals[fourPoint[i]-1]*cm, yVals[fourPoint[i]-1]*cm,
zVals[fourPoint[i]-1]*cm);

    G4String tet_name = file_name + G4String("_tet_") +
G4UIcommand::ConvertToString(i);

    G4VSolid * tet_solid = new G4Tet(tet_name + G4String("_solid"), p1, p2, p3, p4, o);
    G4LogicalVolume * tet_logical = new G4LogicalVolume(tet_solid,
plexi_mat,
tet_name + G4String("_logical"), o, o, o);
totMass = totMass + tet_logical->GetMass();
assembly->AddPlacedVolume( tet_logical, assembly_transform);

//G4VisAttributes* simpleBoxVisAtt= new G4VisAttributes(G4Colour(1.0,1.0,1.0));
//simpleBoxVisAtt->SetVisibility(true);
//calorLV->SetVisAttributes(simpleBoxVisAtt);

}

// if ( xVals[onePoint[i]-1] > 5 || yVals[onePoint[i]-1] > 5 || zVals[onePoint[i]-1] > 5 ) {
//   visAttributes2->SetVisibility(true);
//   visAttributes3->SetVisibility(true);
//   visAttributes4->SetVisibility(true);
//   visAttributes5->SetVisibility(true);
//   visAttributes6->SetVisibility(true);
//   numVis++;
// }

```

```

// else {
    visAttributes2->SetVisibility(true);
    visAttributes3->SetVisibility(true);
    visAttributes4->SetVisibility(false);
    visAttributes5->SetVisibility(false);
    visAttributes6->SetVisibility(false);
}

if (i % 5 == 0) {
    tet_logical->SetVisAttributes(visAttributes2); }
if (i % 5 == 1) {
    tet_logical->SetVisAttributes(visAttributes3); }
if (i % 5 == 2) {
    tet_logical->SetVisAttributes(visAttributes4); }
if (i % 5 == 3) {
    tet_logical->SetVisAttributes(visAttributes5); }
if (i % 5 == 4) {
    tet_logical->SetVisAttributes(visAttributes6); }

//cout << "making the " << i << "th tetrahedra" << endl;
//cout << "NUMBER VISUALIZED: " << numVis << endl;
}

assembly->MakeImprint(worldLV, assembly_transform, o, o);

// double orbRadius = 17.78*cm;

// // SPHERE

// G4Orb* solidOrb = new G4Orb("Orb", orbRadius);

// G4LogicalVolume* logicOrb =
//   new G4LogicalVolume(solidOrb, //its solid
//   C_mask_AND_forSphere, //its material
//   "Orb"); //its name

// G4VPhysicalVolume* physicalOrb =
//   new G4PVPlacement(o, //no rotation
//   G4ThreeVector(), //at (o,o,o)
//   logicOrb, //its logical volume
//   "Orb", //its name
//   worldLV, //its mother volume
//   false, //no boolean operation
//   o, fCheckOverlaps); //copy number

// G4VisAttributes* visAttributes2 = new G4VisAttributes(G4Colour(1.0, 0.0, 0.0)); //red
// visAttributes2->SetVisibility(true);
// visAttributes2->SetForceSolid(true);
// logicOrb->SetVisAttributes(visAttributes2);

```

```

// EMPTY CYLINDER

// G4Tubs* emptyCylinder
// = new G4Tubs("EmptyCylinder",           // its name
//              0.*cm,                  // innerR
//              4.4*cm,                // outerR
//              11.09*cm,               // half height want it to go from -17.78 cm to 4.4 cm
// (height = 22.18, half_height = 11.09, middle = -6.69)
//              0.*deg,                // start angle
//              360.*deg);             // end angle

// G4LogicalVolume* logicEmptyCylinder =
//   new G4LogicalVolume(emptyCylinder, //its solid
//   Vacuum, //its material
//   "EmptyCylinder"); //its name

// G4VPhysicalVolume* physicalEmptyCylinder =
//   new G4PVPlacement(0, //no rotation
//   G4ThreeVector(o.*cm,o.*cm,-6.69*cm), //at (o,o,o)
//   logicEmptyCylinder, //its logical volume
//   "EmptyCylinder", //its name
//   logicOrb, //its mother volume
//   false, //no boolean operation
//   o, fCheckOverlaps); //copy number

```

```
G4cout << "***** TO CHECK ***** the mass of the orb was: " << G4BestUnit(totMass,
"Mass") << G4endl;
```

```
// NaI detector with base center at (0,0,-3.81*cm), axis up to (0,0,7.62*cm), and radius of
3.81*cm
```

```
G4Tubs* detectorNaI_Solid
= new G4Tubs("Detector",           // its name
            0.*cm,                  // innerR
            3.81*cm,                // outerR
            3.81*cm,                // half height
            0.*deg,                 // start angle
            360.*deg);             // end angle
```

```
G4LogicalVolume* detectorNaI_Logical
= new G4LogicalVolume(
    detectorNaI_Solid, // its solid
    NaI_mat,          // its material
    "Detector");      // its name
```

```
G4VPhysicalVolume* detectorNaI_Physical
= new G4PVPlacement(
```

```

        o,           // no rotation
        G4ThreeVector(o.*cm,o.*cm,o.*cm), // center
        detectorNaI_Logical, // its logical volume
        "Detector",      // its name
        worldLV,         // its mother volume
        false,           // no boolean operation
        o,               // copy number
        fCheckOverlaps); // checking overlaps

G4VisAttributes* visAttributes9 = new G4VisAttributes(G4Colour(1.0, 1.0, 0.0)); //red
//detectorNaI_Logical->SetVisAttributes(visAttributes9);
//logicCutOutOrb->SetVisAttributes(visAttributes9);

// NaI detector alluminum alloy sleave .3175 0 cm in depth

G4Tubs* detectorNaI_Solid_Sleave
= new G4Tubs("Detector_Sleave",           // its name
            3.81*cm,                // innerR
            (3.81+.3175)*cm,        // 3.9*cm, outerR note 3.81+.3175 is correct but was changed
for MCNP comparisons to 3.9 cm
            (55/2)*cm,              // half height
            0.*deg,                 // start angle
            360.*deg);             // end angle

G4LogicalVolume* detectorNaI_Logical_Sleave
= new G4LogicalVolume(
    detectorNaI_Solid_Sleave, // its solid
    AlAlloy,                // its material
    "Detector_Sleave");     // its name

G4VPhysicalVolume* detectorNaI_Physical_Sleave
= new G4PVPlacement(
        o,           // no rotation
        G4ThreeVector(o.*cm,o.*cm,-23.3725*cm), // center
        detectorNaI_Logical_Sleave, // its logical volume
        "Detector_Sleave",        // its name
        worldLV,                // its mother volume
        false,                  // no boolean operation
        o,                      // copy number
        fCheckOverlaps);        // checking overlaps

G4VisAttributes* visAttributes7 = new G4VisAttributes(G4Colour(1.0, 0.0, 0.0)); //red
detectorNaI_Logical->SetVisAttributes(visAttributes7);

return worldPV;
}

//....oooOOoOOooo.....oooOOoOOooo.....oooOOoOOooo.....oooOOoOOooo.....
```

```

void B4DetectorConstruction::ConstructSDandField()
{
    // Create global magnetic field messenger.
    // Uniform magnetic field is then created automatically if
    // the field value is not zero.
    G4ThreeVector fieldValue = G4ThreeVector();
    fMagFieldMessenger = new G4GlobalMagFieldMessenger(fieldValue);
    fMagFieldMessenger->SetVerboseLevel(1);

    // Register the field messenger for deleting
    G4AutoDelete::Register(fMagFieldMessenger);
}

//....oooOOoOOooo.....oooOOoOOooo.....oooOOoOOooo.....oooOOoOOooo.....
```

Primary Generator Action

B4aActionInitialization.hh

```

#ifndef B4aActionInitialization_h
#define B4aActionInitialization_h 1

#include "G4VUserActionInitialization.hh"
class B4DetectorConstruction;

/// Action initialization class.
class B4aActionInitialization : public G4VUserActionInitialization
{
public:
    B4aActionInitialization(B4DetectorConstruction* );
    virtual ~B4aActionInitialization();

    virtual void BuildForMaster() const;
    virtual void Build() const;

private:
    B4DetectorConstruction* fDetConstruction;
};

#endif
#endif
```

B4aActionInitialization.cc

```

#include "B4aActionInitialization.hh"
#include "B4PrimaryGeneratorAction.hh"
#include "B4RunAction.hh"
#include "B4aEventAction.hh"
#include "B4aSteppingAction.hh"
```

```

#include "B4DetectorConstruction.hh"

//....oooOOoOOooo.....oooOOoOOooo.....oooOOoOOooo.....oooOOoOOooo..... 

B4aActionInitialization::B4aActionInitialization
    (B4DetectorConstruction* detConstruction)
: G4VUserActionInitialization(),
  fDetConstruction(detConstruction)
{}

//....oooOOoOOooo.....oooOOoOOooo.....oooOOoOOooo.....oooOOoOOooo..... 

B4aActionInitialization::~B4aActionInitialization()
{}

//....oooOOoOOooo.....oooOOoOOooo.....oooOOoOOooo.....oooOOoOOooo..... 

void B4aActionInitialization::BuildForMaster() const
{
  SetUserAction(new B4RunAction);
}

//....oooOOoOOooo.....oooOOoOOooo.....oooOOoOOooo.....oooOOoOOooo..... 

void B4aActionInitialization::Build() const
{
  SetUserAction(new B4PrimaryGeneratorAction);
  B4RunAction* runAction = new B4RunAction;
  SetUserAction(runAction);
  B4aEventAction* eventAction = new B4aEventAction(runAction);
  SetUserAction(eventAction);
  SetUserAction(new B4aSteppingAction(fDetConstruction,eventAction));
}

```

Event Action

B4aEventAction.hh

```

#ifndef B4aEventAction_h
#define B4aEventAction_h 1

#include "G4UserEventAction.hh"
#include "globals.hh"

/// Event action class

class B4RunAction;

class B4aEventAction : public G4UserEventAction

```

```

{
public:
    B4aEventAction(B4RunAction* runAction);
    virtual ~B4aEventAction();

    virtual void BeginOfEventAction(const G4Event* event);
    virtual void EndOfEventAction(const G4Event* event);

    void AddEdepDetector(G4double edep) { eventTotEdepDetector += edep; }
    //void AddEdepMask(G4double edep) { eventTotEdepMask += edep; }
    //void AddNumInteract(G4int count) { eventNumInteract += count; }
    //void AddProcess(G4String stepProcess) { if (stepProcess != "CoupledTransportation")
eventProcesses += stepProcess; }

private:
    G4double eventTotEdepDetector;
    //G4double eventTotEdepMask;
    //G4int eventNumInteract;
    //G4String eventProcesses;
};

#endif

```

B4aEventAction.cc

```

#include "B4aEventAction.hh"
#include "B4RunAction.hh"
#include "B4Analysis.hh"

#include "G4RunManager.hh"
#include "G4Event.hh"
#include "G4Run.hh"
#include "G4UnitsTable.hh"
#include "G4SystemOfUnits.hh"

#include "Randomize.hh"
#include <iomanip>
#include <iostream>
#include <fstream>
#include <stdio.h>
#include <math.h>

using namespace std;

//....oooOOoOOooo.....oooOOoOOooo.....oooOOoOOooo.....oooOOoOOooo..... 

B4aEventAction::B4aEventAction(B4RunAction* runAction)
: G4UserEventAction(),
//eventTotEdepMask(o.),
eventTotEdepDetector(o.)

```



```

ascii file
ofile << runNum << "\t" << eventTotEdepDetector << "\n";
ofile.close();
// THIS IS THE GOOD STUFF

// PRINT EVENT INFO FOR ONES IN THE LITTLE SPIKE
//std::ofstream ofile;
//ofile.open ("LittlePeakEventInfo.txt", ios::out | ios::app);
//if (eventTotEdepDetector > .54 && eventTotEdepDetector < .55) {
//  ofile << eventProcesses << "\n";
//}
//ofile.close();

// std::ofstream ofile2;
// ofile2.open ("90theta_45phi_IncidentAngle_cm", ios::out | ios::app); // ascii file
// //ofile2 << direction.x() << "\t" << direction.y() << "\t" << direction.z() << "\t" <<
direction.mag() << "\t" << direction.theta() << "\t" << direction.phi() << "\n";
// ofile2 << direction.x() << "\t" << direction.y() << "\t" << direction.z() << "\t" <<
vtx.x()/centimeter << "\t" << vtx.y()/centimeter << "\t" << vtx.z()/centimeter << "\n";
// ofile2.close();

// std::ofstream ofile2;
// ofile2.open ("90theta_90phi_NumInteract", ios::out | ios::app); // ascii file
// ofile2 << eventNumInteract << "\n";
// ofile2.close();
}

```

Stepping Action

B4aSteppingAction.hh

```

#ifndef B4aSteppingAction_h
#define B4aSteppingAction_h 1

#include "G4UserSteppingAction.hh"

class B4DetectorConstruction;
class B4aEventAction;

/// Stepping action class.
///
/// In UserSteppingAction() there are collected the energy deposit and track
/// lengths of charged particles in Absorber and Gap layers and
/// updated in B4aEventAction.

class B4aSteppingAction : public G4UserSteppingAction

```

```

{
public:
    B4aSteppingAction(const B4DetectorConstruction* detectorConstruction,
                      B4aEventAction* eventAction);
    virtual ~B4aSteppingAction();

    virtual void UserSteppingAction(const G4Step* step);

private:
    const B4DetectorConstruction* fDetConstruction;
    B4aEventAction* fEventAction;
};

//....oooOOoOOooo.....oooOOoOOooo.....oooOOoOOooo.....oooOOoOOooo.....
```

#endif

B4aSteppingAction.cc

```

#include "B4aSteppingAction.hh"
#include "B4aEventAction.hh"
#include "B4DetectorConstruction.hh"
#include "G4UnitsTable.hh"
#include "G4SystemOfUnits.hh"

#include "G4Step.hh"
#include "G4RunManager.hh"

#include "Randomize.hh"
#include <iomanip>
#include <iostream>
#include <fstream>
#include <stdio.h>
#include <math.h>

#include "G4UImanager.hh"
#include "G4UIcommand.hh"

using namespace std;
```

//....oooOOoOOooo.....oooOOoOOooo.....oooOOoOOooo.....oooOOoOOooo.....

```

B4aSteppingAction::B4aSteppingAction(
    const B4DetectorConstruction* detectorConstruction,
    B4aEventAction* eventAction)
: G4UserSteppingAction(),
  fDetConstruction(detectorConstruction),
  fEventAction(eventAction)
{}
```



```

//G4double edepStep = theStep->GetTotalEnergyDeposit();
//fEventAction->AddEdepMask(edepStep);
//}

//fEventAction->AddProcess(theStep->GetPostStepPoint()->GetProcessDefinedStep()->GetProcessName());

//fEventAction->AddProcess(G4UIcommand::ConvertToString(theStep->GetTotalEnergyDeposit()));

//fEventAction->AddProcess(G4String(" "));



/// // G4cout << "Step is limited by "
// // << theStep->GetPostStepPoint()->GetProcessDefinedStep()->GetProcessName()
// // << G4endl;
// //G4cout << "Processes involved to the step" << G4endl;
// G4StepStatus stepStatus = fpSteppingManager->GetfStepStatus();

// if(stepStatus==fAtRestDoItProc)
// {
//   G4ProcessVector* procAtRest = fpSteppingManager->GetfAtRestDoItVector();
//   G4SelectedAtRestDoItVector* selProcAtRest
//     = fpSteppingManager->GetfSelectedAtRestDoItVector();
//   size_t MAXofAtRestLoops = fpSteppingManager->GetMAXofAtRestLoops();
//   for(size_t i1=0;i1<MAXofAtRestLoops;i1++)
//   {
//     //if((*selProcAtRest)[MAXofAtRestLoops-i1-1]==2)
//     // { G4cout << " At rest : " << (*procAtRest)[i1]->GetProcessName() << " (forced)" << G4endl; }
//     // else if((*selProcAtRest)[MAXofAtRestLoops-i1-1]==1)
//     // { G4cout << " At rest : " << (*procAtRest)[i1]->GetProcessName() << G4endl; }
//   }
// }

// if(stepStatus!=fExclusivelyForcedProc && stepStatus!=fAtRestDoItProc)
// {
//   G4ProcessVector* procAlong = fpSteppingManager->GetfAlongStepDoItVector();
//   size_t MAXofAlongStepLoops = fpSteppingManager->GetMAXofAlongStepLoops();
//   for(size_t i2=0;i2<MAXofAlongStepLoops;i2++)
//   {
//     // if((*procAlong)[i2]!=0)
//     // G4cout << " Along step : " << (*procAlong)[i2]->GetProcessName() << G4endl;
//   }
// }

// if(stepStatus!=fAtRestDoItProc)

```

```

// {
//   G4ProcessVector* procPost = fpSteppingManager->GetfPostStepDoItVector();
//   G4SelectedPostStepDoItVector* selProcPost
//   = fpSteppingManager->GetfSelectedPostStepDoItVector();
//   size_t MAXofPostStepLoops = fpSteppingManager->GetMAXofPostStepLoops();
//   for(size_t i3=0;i3<MAXofPostStepLoops;i3++)
//   {
//     // if((*selProcPost)[MAXofPostStepLoops-i3-1]==2)
//     // { G4cout << " Post step : " << (*procPost)[i3]->GetProcessName() << " (forced)" <<
G4endl; }
//     // else if((*selProcPost)[MAXofPostStepLoops-i3-1]==1)
//     // { G4cout << " Post step : " << (*procPost)[i3]->GetProcessName() << G4endl; }
//   }
// }

// G4int nSecAtRest = fpSteppingManager->GetfN2ndariesAtRestDoIt();
// G4int nSecAlong = fpSteppingManager->GetfN2ndariesAlongStepDoIt();
// G4int nSecPost = fpSteppingManager->GetfN2ndariesPostStepDoIt();
// G4int nSecTotal = nSecAtRest+nSecAlong+nSecPost;
// G4TrackVector* secVec = fpSteppingManager->GetfSecondary();

// if(nSecTotal>0)
// {
//   //G4cout << " ----- List of 2ndaries - " << std::setw(3) << nSecTotal
//   //   << " (Rest=" << std::setw(2) << nSecAtRest
//   //   << ",Along=" << std::setw(2) << nSecAlong
//   //   << ",Post=" << std::setw(2) << nSecPost << ")" << G4endl;

//   for(size_t lp1=(*secVec).size()-nSecTotal; lp1<(*secVec).size(); lp1++)
//   {
//     //G4cout << " : "
//     // << G4BestUnit((*secVec)[lp1]->GetPosition(), "Length") << " "
//     // << std::setw( 9) << G4BestUnit((*secVec)[lp1]->GetKineticEnergy(), "Energy") <<
" "
//     // << std::setw(18) << (*secVec)[lp1]->GetDefinition()->GetParticleName()
//     // << " generated by " << (*secVec)[lp1]->GetCreatorProcess()->GetProcessName()
<< G4endl;
//   }
// }

}

//....oooOOoOOooo.....oooOOoOOooo.....oooOOoOOooo.....oooOOoOOooo.....
```

Run Action

B4aRunAction.hh

```
#ifndef B4RunAction_h
#define B4RunAction_h 1
```

```

#include "G4UserRunAction.hh"
#include "globals.hh"
#include "G4Parameter.hh"

class G4Run;

/// Run action class
///
/// It accumulates statistic and computes dispersion of the energy deposit
/// and track lengths of charged particles with use of analysis tools:
/// H1D histograms are created in BeginOfRunAction() for the following
/// physics quantities:
/// - Edep in absorber
/// - Edep in gap
/// - Track length in absorber
/// - Track length in gap
/// The same values are also saved in the ntuple.
/// The histograms and ntuple are saved in the output file in a format
/// according to a selected technology in B4Analysis.hh.
///
/// In EndOfRunAction(), the accumulated statistic and computed
/// dispersion is printed.
///

class B4RunAction : public G4UserRunAction
{
public:
    B4RunAction();
    virtual ~B4RunAction();

    virtual void BeginOfRunAction(const G4Run* run);
    virtual void EndOfRunAction(const G4Run* run);
};

#endif

```

B4aRunAction.cc

```

#include "B4RunAction.hh"
#include "B4Analysis.hh"

#include "G4Run.hh"
#include "G4RunManager.hh"
#include "G4UnitsTable.hh"
#include "G4SystemOfUnits.hh"
#include "B4PrimaryGeneratorAction.hh"

//....oooOOoOOooo.....oooOOoOOooo.....oooOOoOOooo.....oooOOoOOooo.....
```

B4RunAction::B4RunAction()


```
// << G4endl
// << "-----End of Local Run-----";
// }

// G4cout
// << G4endl
// << " The run consists of " << nofEvents << " " << runCondition
// << G4endl
// << "-----"
// << G4endl
// << G4endl;
}
```

Appendix E

This section contains the MCNP input deck that mimics that which is accomplished via the GEANT input detailed in the previous section. This code was not developed by the author of this paper, but by Dr. Darren Holland.

```
sphere using a cs-137 source and nai detector
c Created from file  : Part2Final.inp
c Using data cards file: RSM16master
c Created on      : 6-22-2016 @ 10:13:49
c
c
c PSEUDO CELLS
1 30 -1.19   o u=1    imp:p=1
2 10 -0.001205  o u=1 imp:p=1
c
c LEGACY CELLS
3 o      -99 1003 fill=1 imp:p=1          $ RSM cell
101 o      999:(1000 1001 99) imp:p=0      $ ignore p outside of sphere
102 10 -0.001205 -999 -1000 1001 99 imp:p=1 $ inside of source sphere, outside of
detector sphere
103 10 -0.001205 -1001 99     imp:p=1      $ inside of detector sphere, outside
of acrylic cylinder
104 20 -3.667    -1002     imp:p=1      $ nai detector
105 21 -2.78     -1003 1005   imp:p=1      $ sleeve
107 10 -0.001205 -1005 1002   imp:p=1      $ air around detector and inside of
sleeve

c SURFACES
99 rcc o o -51 o o 71 20          $ Cylinder holding RSM
999 p 1 o o 87
1000 s 100 o o 100                $ sphere around source
1001 so 50                         $ sphere around detector
1002 rcc o o -3.81 o o 7.62 3.81 $ detector
1003 rcc o o -50.8725 o o 55 4.1275 $ 1/8 inch sleeve outside
1005 rcc o o -50.8725 o o 55 3.81  $ 1/8 inch sleeve inside

c DATA CARDS
embed1 meshgeo=abaqus
mgeoin=part2_large_acrylic_shift.abaq
length= 1.00000E+00      $ scale units to cm
background=    2          $ inferred background cell
```

```

matcell= 1 1 $ mcnp-abaqus material linking
c     meeout=Part2Final.eeout
c
c embee4:p embed=1
c embee14:    embed=1
c embee24:    embed=1
c embee34:    embed=1
c embee44:    embed=1
c embee54:    embed=1
c embee64:$ embed=1
c embee74:p embed=1
c embee84:o embed=1
c embee94:s embed=1
c embee104:i embed=1
c embee114:t embed=1
c embee124:r embed=1
c embee134:o embed=1
c embee144:n embed=1
c embee154:o embed=1
c embee164:n embed=1
c embee174:l embed=1
c embee184:y embed=1
c
c imp:p 1    2R o
c imp: 1    2R o
c imp:$ 1   2R o
c imp:p 1   2R o
c imp:o 1   2R o
c imp:s 1   2R o
c imp:i 1   2R o
c imp:t 1   2R o
c imp:r 1   2R o
c imp:o 1   2R o
c imp:n 1   2R o
c imp:o 1   2R o
c imp:n 1   2R o
c imp:l 1   2R o
c imp:y 1   2R o
c
mode p $ positron only
nps 30000000 $ number of histories
c prdmp o o 1 $ partial history output
c print 110 $ display info on first 50 particles
c material
m10 6000 -0.000124
          7000 -0.755268 $ 7014 for neutrons
          8000 -0.231781 $ 8016 for neutrons

```

```

18000 -0.012827
m20 11000 -0.153373          $ nai detector via pnnl - na 11023 for neutrons
      53000 -0.846627          $ 53127 for neutrons
m21 12000 -0.015            $ aluminum sleeve (assume 2024)
      13000 -0.927           $ 13027 for neutrons
      14000 -0.00283
      22000 -0.00085
      24000 -0.00057
      25000 -0.006           $ 25055 for neutrons
      26000 -0.00283
      29000 -0.0435
      30000 -0.00142
m30 1000 -0.080538          $ lucite/acrylic vi pnnl - h 1001 for neutrons
      6000 -0.599848
      8000 -0.319614          $ 8016 for neutrons

c source
sdef erg 0.662 pos 86.36 o o vec -1 o o dir d1
si1 -1 0.9781 1
sp1 o 0.9891 0.0109
sb1 o o 1
cut:p j 0.1                  $ kill photon below 80kev
c tally
c f4:p 103                   $ sphere interface flux
c e4 0.1 600i 0.7
c sf4 1000
c f2:p 1002.1 1002.2 1002.3 $ detector flux
c e2 0.1 600i 0.7
f8:p 104                     $ detector response
e8 o 1e-5 0.1 600i 0.7

```

const distance from source to center of detector = 34 in
alpha = 11 degrees

Appendix F

This appendix contains representative Matlab code that is used to post-process the data obtained from the GEANT and MCNP simulations as well as from experimentation. This includes comparison of the energy spectra and detector response curves. It also includes the different mechanisms employed in the broadening of the simulated data and the calibration of the experimental data.

GEANT/MCNP Energy Spectra

```
% 10,000,000 particles per source position (the txt files are normalized
% per source particle)
N = 10000000
directionBias = 2.314*10^(-2)
% GEANT is column 1 and MCNP is column 2
Dataset_45_45 = dlmread('45_45.txt');
GEANT_MCNP_45_45.GEANT = Dataset_45_45(:,1)
GEANT_MCNP_45_45.MCNP = Dataset_45_45(:,2)
Dataset_45_90 = dlmread('45_90.txt');
GEANT_MCNP_45_90.GEANT = Dataset_45_90(:,1)
GEANT_MCNP_45_90.MCNP = Dataset_45_90(:,2)
Dataset_90_90 = dlmread('90_90.txt');
GEANT_MCNP_90_90.GEANT = Dataset_90_90(:,1)
GEANT_MCNP_90_90.MCNP = Dataset_90_90(:,2)
Dataset_90_45 = dlmread('90_45.txt');
GEANT_MCNP_90_45.GEANT = Dataset_90_45(:,1)
GEANT_MCNP_90_45.MCNP = Dataset_90_45(:,2)

% RAW PLOTS (without FEP)

figure
hold on
plot(transpose(101:661),GEANT_MCNP_90_90.GEANT(1:561)*10^7/(2.314*10^(-2)),'LineWidth',2)
plot(transpose(101:661),GEANT_MCNP_90_90.MCNP(1:561)*10^7/(2.314*10^(-2)),'LineWidth',2)
title('Simulations Energy Spectra \vartheta=90\circ, \varphi=90\circ', 'fontsize',18);
legend('GEANT', 'MCNP')
xlabel('Energy (keV)', 'fontsize',16)
ylabel('Untransformed Count', 'fontsize',16)
grid on

figure
hold on
```

```

plot(transpose(101:661),GEANT_MCNP_45_90.GEANT(1:561)*10^7/(2.314*10^(-2)), 'LineWidth',2)
plot(transpose(101:661),GEANT_MCNP_45_90.MCNP(1:561)*10^7/(2.314*10^(-2)), 'LineWidth',2)
title('Simulations Energy Spectra \theta=45\circ \phi=90\circ', 'fontsize',18);
legend('GEANT', 'MCNP')
xlabel('Energy (keV)', 'fontsize',16)
ylabel('Untransformed Count', 'fontsize',16)
grid on

```

```

figure
hold on
plot(transpose(101:661),GEANT_MCNP_90_45.GEANT(1:561)*10^7/(2.314*10^(-2)), 'LineWidth',2)
plot(transpose(101:661),GEANT_MCNP_90_45.MCNP(1:561)*10^7/(2.314*10^(-2)), 'LineWidth',2)
title('Simulations Energy Spectra \theta=90\circ \phi=45\circ', 'fontsize',18);
legend('GEANT', 'MCNP')
xlabel('Energy (keV)', 'fontsize',16)
ylabel('Untransformed Count', 'fontsize',16)
grid on

```

```

figure
hold on
plot(transpose(101:661),GEANT_MCNP_45_45.GEANT(1:561)*10^7/(2.314*10^(-2)), 'LineWidth',2)
plot(transpose(101:661),GEANT_MCNP_45_45.MCNP(1:561)*10^7/(2.314*10^(-2)), 'LineWidth',2)
title('Simulations Energy Spectra \theta=45\circ \phi=45\circ', 'fontsize',18);
legend('GEANT', 'MCNP')
xlabel('Energy (keV)', 'fontsize',16)
ylabel('Untransformed Count', 'fontsize',16)
grid on

```

% RAW PLOTS (with FEP)

```

figure
plot(transpose(101:662),GEANT_MCNP_90_90.GEANT(1:562)*10^7/(2.314*10^(-2)), 'LineWidth',2)
plot(transpose(101:662),GEANT_MCNP_90_90.MCNP(1:562)*10^7/(2.314*10^(-2)), 'LineWidth',2)
legend('GEANT', 'MCNP','Location','northwest')
xlabel('Including FEP', 'fontsize',60)

```

```

figure
plot(transpose(101:662),GEANT_MCNP_90_45.GEANT(1:562)*10^7/(2.314*10^(-2)), 'LineWidth',2)
plot(transpose(101:662),GEANT_MCNP_90_45.MCNP(1:562)*10^7/(2.314*10^(-2)), 'LineWidth',2)
legend('GEANT', 'MCNP','Location','northwest')
xlabel('Including FEP', 'fontsize',60)

```

```

figure
plot(transpose(101:662),GEANT_MCNP_45_90.GEANT(1:562)*10^7/(2.314*10^(-2)), 'LineWidth',2)
plot(transpose(101:662),GEANT_MCNP_45_90.MCNP(1:562)*10^7/(2.314*10^(-2)), 'LineWidth',2)
legend('GEANT', 'MCNP', 'Location', 'northwest')
xlabel('Including FEP', 'fontsize',60)

figure
plot(transpose(101:662),GEANT_MCNP_45_45.GEANT(1:562)*10^7/(2.314*10^(-2)), 'LineWidth',2)
plot(transpose(101:662),GEANT_MCNP_45_45.MCNP(1:562)*10^7/(2.314*10^(-2)), 'LineWidth',2)
legend('GEANT', 'MCNP', 'Location', 'northwest')
xlabel('Including FEP', 'fontsize',60)
hold off

% LOG PLOTS
figure
subplot(2,2,1)
semilogy(transpose(101:662),GEANT_MCNP_90_90.GEANT(1:562)*10^7/(2.314*10^(-2)), 'LineWidth',2)
hold on
semilogy(transpose(101:662),GEANT_MCNP_90_90.MCNP(1:562)*10^7/(2.314*10^(-2)), 'LineWidth',2)
title('Simulations Energy Spectra \theta=90\circ \phi=90\circ', 'fontsize',18);
legend('GEANT', 'MCNP', 'Location', 'northwest')
xlabel('Energy (keV)', 'fontsize',16)
ylabel('Untransformed Count', 'fontsize',16)
grid on
subplot(2,2,2)

semilogy(transpose(101:662),GEANT_MCNP_45_90.GEANT(1:562)*10^7/(2.314*10^(-2)), 'LineWidth',2)
hold on
semilogy(transpose(101:662),GEANT_MCNP_45_90.MCNP(1:562)*10^7/(2.314*10^(-2)), 'LineWidth',2)
title('Simulations Energy Spectra \theta=45\circ \phi=90\circ', 'fontsize',18);
legend('GEANT', 'MCNP', 'Location', 'northwest')
xlabel('Energy (keV)', 'fontsize',16)
ylabel('Untransformed Count', 'fontsize',16)
grid on
subplot(2,2,3)

semilogy(transpose(101:662),GEANT_MCNP_90_45.GEANT(1:562)*10^7/(2.314*10^(-2)), 'LineWidth',2)
hold on
semilogy(transpose(101:662),GEANT_MCNP_90_45.MCNP(1:562)*10^7/(2.314*10^(-2)), 'LineWidth',2)
title('Simulations Energy Spectra \theta=90\circ \phi=45\circ', 'fontsize',18);

```

```

legend('GEANT', 'MCNP','Location','northwest')
xlabel('Energy (keV)', 'fontsize',16)
ylabel('Untransformed Count', 'fontsize',16)
grid on
subplot(2,2,4)

semilogy(transpose(101:662),GEANT_MCNP_45_45.GEANT(1:562)*10^7/(2.314*10^(-2)),'LineWidth',2)
hold on
semilogy(transpose(101:662),GEANT_MCNP_45_45.MCNP(1:562)*10^7/(2.314*10^(-2)),'LineWidth',2)
title('Simulations Energy Spectra \theta=45\circ \phi=45\circ', 'fontsize',18);
legend('GEANT', 'MCNP','Location','northwest')
xlabel('Energy (keV)', 'fontsize',16)
ylabel('Untransformed Count', 'fontsize',16)
grid on

```

% GRAPH WITH ERROR BARS

```

toPlot.GEANT = GEANT_MCNP_45_45.GEANT
toPlot.MCNP = GEANT_MCNP_45_45.MCNP

normConst = 2.314*10^(-2)
% Using 90% CI
errGEANT = 1.645*sqrt(times(toPlot.GEANT,(normConst-toPlot.GEANT))*(10^(-7)))
errMCNP = 1.645*sqrt(times(toPlot.MCNP,(normConst-toPlot.MCNP))*(10^(-7)))

```

% Log scale

```

subplot(2,2,1)
errorbar(transpose(101:662),toPlot.GEANT(1:562),errGEANT(1:562))
hold on
errorbar(transpose(101:662),toPlot.MCNP(1:562),errMCNP(1:562))
title('90% CI \theta=45\circ \phi=45\circ', 'fontsize',18);
legend('GEANT', 'MCNP')
xlabel('Energy (keV)', 'fontsize',16)
ylabel('Count per Source Particle', 'fontsize',16)
grid on
set(gca,'yscale','log')

```

% Without FEP

```

figure
subplot(2,2,1)
hold on
errorbar(transpose(101:661),toPlot.GEANT(1:561),errGEANT(1:561))
errorbar(transpose(101:661),toPlot.MCNP(1:561),errMCNP(1:561))
title('Simulations Energy Spectra \theta=45\circ \phi=45\circ', 'fontsize',18);
legend('GEANT', 'MCNP')

```

```

xlabel('Energy (keV)', 'fontsize',16)
ylabel('Count per Source Particle', 'fontsize',16)
grid on

% Just FEP Error Bars

toPlot.GEANT = GEANT_MCNP_90_90.GEANT
toPlot.MCNP = GEANT_MCNP_90_90.MCNP

normConst = 2.314*10^(-2)
% Using 90% CI
errGEANT = 1.645*sqrt(times(toPlot.GEANT,(normConst-toPlot.GEANT))*(10^(-7)))
errMCNP = 1.645*sqrt(times(toPlot.MCNP,(normConst-toPlot.MCNP))*(10^(-7)))

subplot(2,2,1)
legend('GEANT', 'MCNP')
hold on
errorbar(transpose(662),toPlot.GEANT(562),errGEANT(562),'LineWidth',2)
errorbar(transpose(662),toPlot.MCNP(562),errMCNP(562),'LineWidth',2)
title('FEP \theta=90\circ \phi=90\circ', 'fontsize',16);
xlabel('Energy (keV)', 'fontsize',16)
ylabel('Count per Source Particle', 'fontsize',16)
grid on

% Count how many error bars overlap

% Repeated here for convenience
toPlot.GEANT = GEANT_MCNP_90_90.GEANT
toPlot.MCNP = GEANT_MCNP_90_90.MCNP

normConst = 2.314*10^(-2)
% Using 90% CI
errGEANT = 1.645*sqrt(times(toPlot.GEANT,(normConst-toPlot.GEANT))*(10^(-7)))
errMCNP = 1.645*sqrt(times(toPlot.MCNP,(normConst-toPlot.MCNP))*(10^(-7)))

overlaps = 0;
for bin = 1:length(toPlot.GEANT)
    upperMCNP = toPlot.MCNP(bin) + errGEANT(bin);
    lowerMCNP = toPlot.MCNP(bin) - errGEANT(bin);
    upperGEANT = toPlot.GEANT(bin) + errGEANT(bin);
    lowerGEANT = toPlot.GEANT(bin) + errGEANT(bin);

    if (lowerMCNP > upperGEANT)
        agree = 0;
    elseif (lowerGEANT > upperMCNP)
        agree = 0;
    else

```

```

    agree = 1;
end

overlaps = overlaps + agree;
end

```

GEANT/Experiment Energy Spectra

```

%00001 = 5 phi
%00002 = 15 phi
%00003 = 25 phi
%00004 = 35 phi
%00005 = 45 phi
%00006 = 55 phi
%00007 = 65 phi
%00008 = 75 phi
%00009 = 85 phi
%00010 = 95 phi
%00011 = 105 phi
%00012 = 115 phi
%00013 = 125 phi
%00014 = 135 phi
%00015 = 145 phi
%00016 = 155 phi
%00017 = 165 phi
%00018 = 175 phi

```

```

% vector containing binned angles
angles = zeros(72,1)
for i = 1:72
    angles(i,1) = (i-1)*5;
end

```

%%% SIMULATED DATA

```

% (theta,phi)
Sim_DataSet_45_45 = dlmread('RSM_45theta_45phi_EDep_10,000,000.txt');
Sim_DataSet_90_45 = dlmread('RSM_90theta_45phi_EDep_10,000,000.txt');

Sim_DataSet_45_95_runNumToo = dlmread('RSM_45theta_95phi_EDep_10,000,000.txt');
Sim_DataSet_90_95_runNumToo = dlmread('RSM_90theta_95phi_EDep_10,000,000.txt');
Sim_DataSet_45_95 = Sim_DataSet_45_95_runNumToo(:,2);
Sim_DataSet_90_95 = Sim_DataSet_45_95_runNumToo(:,2);

Sim_DataSet(:,1) = Sim_DataSet_45_45;
Sim_DataSet(:,2) = Sim_DataSet_90_45;
Sim_DataSet(:,3) = Sim_DataSet_45_95;
Sim_DataSet(:,4) = Sim_DataSet_90_95;

```

```

Hist_Sim_DataSet = zeros(1098,4);
for position=1:4
    for i=1:size(Sim_DataSet_45_45)
        energyBin = floor(1000*Sim_DataSet(i,position));
        Hist_Sim_DataSet(energyBin+1,position) = Hist_Sim_DataSet(energyBin+1,position) + 1;
    end
end

%%% EXPERIMENTAL DATA

Expr_45Phi = dlmread('00005BIN.txt');
Expr_95Phi = dlmread('00010BIN.txt');

% Note had to take minus 10 because had to line up with correct theta
% definition

Expr_DataSet_45_45 = Expr_45Phi(:,(1+45/5+(72-10)))
Expr_DataSet_90_45 = Expr_45Phi(:,(1+90/5-10))

Expr_DataSet_45_95 = Expr_95Phi(:,(1+45/5+(72-10)))
Expr_DataSet_90_95 = Expr_95Phi(:,(1+90/5-10))

Expr_DataSet(:,1) = Expr_DataSet_45_45;
Expr_DataSet(:,2) = Expr_DataSet_90_45;
Expr_DataSet(:,3) = Expr_DataSet_45_95;
Expr_DataSet(:,4) = Expr_DataSet_90_95;

% CALIBRATE THE EXPERIMENTAL DATA

% isotope, energy, voltage bin
% Am-241      0.06   22
% Cd-109      0.088  54
% Co-57       0.122  86
% Te-123m     0.159  122
% Cr-51       0.32    NA/
% Sn-113      0.392  307
% Sr-85       0.514  417
% Cs-137      0.662  554
% Y-88        0.898  770
% Co-60       1.173  1021
% Co-60       1.333  1166
% Y-88        1.836  1628

% ALL OF THE PEAKS
loganPeaks = [22,54,86,122,307,417,554,770,1021,1166,1628]
loganPeaksEnergies = [60,88,122,159,392,514,662,898,1173,1333,1836]
% SUBSET OF THE PEAKS

```

```

loganPeaks = [0,22,54,86,122,307,417,554,770,1021,1166]
loganPeaksEnergies = [0,60,88,122,159,392,514,662,898,1173,1333]

syms x
invLoganFit = polyfit(loganPeaksEnergies, loganPeaks,2)
% input = keV, output = energyBin
invcalib(x) = symfun(invLoganFit(1)*x^2+invLoganFit(2)*x+invLoganFit(3)*x^0,x)
syms x
LoganFit = polyfit(loganPeaks,loganPeaksEnergies,2)
% input = keV, output = energyBin
calib(x) = symfun(LoganFit(1)*x^2+LoganFit(2)*x+LoganFit(3)*x^0,x)
eval(calib(554))
eval(invcalib(662))
eval(invcalib(0))

Expr_DataSet_Calib = zeros(1000,4);
% for each position
for position=1:4
% for each energy value
for keV_Bin=1:1500
    exprCount = 0;
    lowerExprBin = ceil(invcalib(keV_Bin))-1;
    upperExprBin = ceil(invcalib(keV_Bin));
    for exprBin = lowerExprBin:upperExprBin
        if(exprBin > 0 && exprBin < 1099)
            exprCount = exprCount + Expr_DataSet(exprBin,position);
        end
    end
    Expr_DataSet_Calib(keV_Bin,position) = exprCount;
end
position
end

% CALCULATE GAUSSIAN PARAMETERS
% because the left side is broadened by the x-ray escape peak (662-28keV =
% X-ray escape (iodine K shell))

for position = 1:4
%wayUpIndex = 0;
wayDownIndex = 0;
[maxCount, maxIndexVal] = max(Expr_DataSet_Calib(659:665,position))
maxIndex(position,1) = maxIndexVal + 660
maxIndexTrue = 662
halfMax = maxCount/2;

for i=600:800
    %if (Expr_DataSet_Calib(i,t) <= halfMax && (Expr_DataSet_Calib(i+1,t) >= halfMax) &&
    wayUpIndex == 0)

```

```

% wayUpIndex = i;
%end
if ((Expr_DataSet_Calib(i,position) >= halfMax) && (Expr_DataSet_Calib(i+1,position) <=
halfMax))
    wayDownIndex = i;
end
end
FWHM(1,position) = 2*(wayDownIndex-maxIndexTrue)
FWHM_percent(1,position) = FWHM(1,position)/662
gaussWidth(1,position) = FWHM(1,position)/(2*sqrt(log(2)))

.0302704*.662^0.659344

end

% BROADEN THE SIMULATED WITH THE ABOVE GAUSSIAN

y_conv = zeros(1098,4)
for position=1:4
    y = Hist_Sim_DataSet(1:1098,position);
    y(1) = 0
    x = -1098/2:1098/2
    sigma = FWHM(1,position)/(sqrt(8*log(2)));
    gaussFilter = exp(-x.^2 / (2 * sigma.^2));
    gaussFilter = gaussFilter / sum(gaussFilter); % normalize
    y_conv(:,position) = conv(y, gaussFilter, 'same');
end
a = '(45\circ,45\circ)'
b = '(90\circ,45\circ)'
c = '(45\circ,95\circ)'
d = '(90\circ,95\circ)'
positions = [a;b;c;d];
cellpositions = cellstr(positions)
figure
for positionToPlot = 1:4
    subplot(2,2,positionToPlot)
    plot(y_conv(:,positionToPlot),'LineWidth',2)
    title(strcat(cellpositions(positionToPlot), ' Energy Spectra'), 'fontsize',18);
    xlabel('Energy (keV)', 'fontsize',16)
    ylabel('Normalized Count', 'fontsize',16)
    %multExpr =
    y_conv(maxIndex(positionToPlot,1),positionToPlot)/Expr_DataSet_Calib(maxIndex(positionT
oPlot,1),positionToPlot)
    multExpr = max(y_conv(:,positionToPlot))/max(Expr_DataSet_Calib(:,positionToPlot))
    normExpr(:,positionToPlot) = Expr_DataSet_Calib(:,positionToPlot)*multExpr
    xlim([0,1000])
    ylim([0,1300])
    hold on
    plot(Expr_DataSet_Calib(:,positionToPlot)*multExpr,'LineWidth',2)
    legend('Broadened GEANT','Experimental','Location','northwest')
end

```

```

%%% ALTERNATIVE BROADENING TECHNIQUE
y_gaussSample_heathconsts = zeros(1098,4);
for position = 1:4
    orig = Hist_Sim_DataSet(1:1098,position);
    orig(1) = orig(2)
    for eBin = 1:1098
        sigma = 1000*(.0302704*(eBin*10^(-3))^0.659344);
        %sigma = 1000*(0.0356*(eBin*10^(-3))^0.7888);
        for i = 1:orig(eBin)
            sample = ceil(normrnd(eBin,sigma));
            while sample <= 0
                sample = ceil(normrnd(eBin,sigma));
            end
            y_gaussSample_heathconsts(sample,position) =
            y_gaussSample_heathconsts(sample,position) + 1;
        end
        eBin
    end
end

```

```

figure
for positionToPlot = 1:4
    subplot(2,2,positionToPlot)
    plot(y_gaussSample_heathconsts(:,positionToPlot),'LineWidth',2)
    title(strcat(cellpositions(positionToPlot), ' Energy Spectra'), 'fontsize',18);
    xlabel('Energy (keV)', 'fontsize',16)
    ylabel('Normalized Count', 'fontsize',16)
    multExpr =
    y_gaussSample_heathconsts(maxIndex(positionToPlot,1),positionToPlot)/Expr_DataSet_Calib
    (maxIndex(positionToPlot,1),positionToPlot)
    normExpr(:,positionToPlot) = Expr_DataSet_Calib(:,positionToPlot)*multExpr
    xlim([0,1000])
    ylim([0,1300])
    hold on
    plot(Expr_DataSet_Calib(:,positionToPlot)*multExpr,'LineWidth',2)

```

```

legend('Broadened GEANT','Experimental','Location','northwest')
end

% CHI^2 ERROR CALCULATOR
convError = zeros(4,1)
resampleHEATHConstsError = zeros(4,1)
resampleMYConstsError = zeros(4,1)

for position=1:4
    for eBin=1:1098
        % RESAMPLE HEATH CONSTS
        y_gaussSample_heathconsts(eBin,position);
        multExpr =
y_gaussSample_heathconsts(maxIndex(position,1),position)/Expr_DataSet_Calib(maxIndex(p
osition,1),position);
        expr_norm = Expr_DataSet_Calib*multExpr;
        if expr_norm(eBin,position) ~= 0
            err = (y_gaussSample_heathconsts(eBin,position)-
expr_norm(eBin,position))^2/expr_norm(eBin,position);
            resampleHEATHConstsError(position,1) = resampleHEATHConstsError(position,1) +
err;
        end
        % RESAMPLE MY CONSTS
        y_gaussSample_myconsts(eBin,position);
        multExpr =
y_gaussSample_myconsts(maxIndex(position,1),position)/Expr_DataSet_Calib(maxIndex(posi
tion,1),position);
        expr_norm = Expr_DataSet_Calib*multExpr;
        if expr_norm(eBin,position) ~= 0
            err = (y_gaussSample_myconsts(eBin,position)-
expr_norm(eBin,position))^2/expr_norm(eBin,position);
            resampleMYConstsError(position,1) = resampleMYConstsError(position,1) + err;
        end
        % CONVOLUTION
        y_conv(eBin,position);
        multExpr =
y_conv(maxIndex(position,1),position)/Expr_DataSet_Calib(maxIndex(position,1),position);
        expr_norm = Expr_DataSet_Calib*multExpr;
        if expr_norm(eBin,position) ~= 0
            err = (y_conv(eBin,position)-
expr_norm(eBin,position))^2/expr_norm(eBin,position);
            convError(position,1) = convError(position,1) + err;
        end
    end
end

resampleHEATHConstsError
resampleMYConstsError
convError

```

```

%% OPTION 1
% Broaden the simulated spectrum, R = normrnd(mu,sigma)

[simFEP,simIndex] = max(Hist_Sim_DataSet(2:1098,t));
simIndex = simIndex + 1
Hist_Sim_DataSet_Broadened(:,t) = Hist_Sim_DataSet(:,t);
Hist_Sim_DataSet_Broadened(simIndex,t) = o;

for i = 1:simFEP
    gaussianSample = floor(normrnd(662,gaussWidth));
    Hist_Sim_DataSet_Broadened(gaussianSample,t) =
    Hist_Sim_DataSet_Broadened(gaussianSample,t) + 1;
end

end

```

```

%% OPTION 2
% Condense the experimental spectrum

for j = 1:4

    % fit to gaussian and then get the definite integral
    Expr_DataSet_Calib_Condensed(:,j) = Expr_DataSet_Calib(:,j)
    integralValue = o;

    % only look at the gaussian FEP area (not the Compton continuum)
    xVals = zeros(201,1);
    for val=1:200
        xVals(val,1) = val+400;
    end
    % fit to a single gaussian
    f = fit(xVals,Expr_DataSet_Calib(600:800,j),'gauss1');
    %plot(f,xVals,ExprMatrix(450:650,i+1,a));
    %parameters of the gaussian

```

```

%coefficient
a1 = f.a1;
%mean
b1 = f.b1;
%exponent denominator
c1 = f.c1;
stdev = sqrt(c1/2);
% get the integral
syms x;
integralVal = int(a1*exp(-((x-b1)/c1)^2),x,b1-3*stdev,b1+3*stdev);
% divide by the percent of the distribution that we included within 1
% stdev on either side
integralValue = integralVal/.997;

Expr_DataSet_Calib_Condensed(600:800,j) = o;
Expr_DataSet_Calib_Condensed(662,j) = integralValue;

end

Expr_DataSet(:,1) = Expr_DataSet_45_45;
Expr_DataSet(:,2) = Expr_DataSet_90_45;
Expr_DataSet(:,3) = Expr_DataSet_45_95;
Expr_DataSet(:,4) = Expr_DataSet_90_95;

%%%%% PLOTS
% Order
%45_45;
%90_45;
%45_95;
%90_95;

% BROADENED GEANT (normalized)

%Entire spectrum
toPlot = 4
hold on
plot(Hist_Sim_DataSet_Broadened(2:1098,toPlot)/sum(Hist_Sim_DataSet_Broadened(2:1098,toPlot)), 'LineWidth', 2)
plot(Expr_DataSet_Calib(2:1098,toPlot)/sum(Expr_DataSet_Calib(2:1098,toPlot)), 'LineWidth', 2)
title('Simulated and Experimental Spectra for \phi and \theta')
legend('GEANT', 'Experimental')

energies = zeros(998,1);
for i = 1:998
    energies(i,1) = i+100;
end

%100 keV onward
toPlot = 1

```

```

hold on
plot(energies,Hist_Sim_DataSet_Broadened(101:1098,toPlot)/sum(Hist_Sim_DataSet_Broadened(101:1098,toPlot)),'LineWidth',2)
plot(energies,Expr_DataSet_Calib(101:1098,toPlot)/sum(Expr_DataSet_Calib(101:1098,toPlot)),'LineWidth',2)
title({'Simulated and Experimental Spectra for \theta=45\circ and \phi=45\circ'; ''}, 'fontsize',18);
legend('GEANT','Experimental')
xlabel('Energy (keV)', 'fontsize',16)
ylabel('Normalized Count', 'fontsize',16)
set(gca,'FontSize',16)
saveas(gcf,'4545_geant_expr_spectra.png')

```

```
plot(Hist_Sim_DataSet_Broadened(2:1098,:))
title('Simulated Spectra for \phi and \theta')
legend('(45,45)', '(90,45)', '(45,95)', '(90,45)')
```

```
% CONDENSED EXPR
plot(Expr_DataSet_Calib_Condensed)
title('Condensed Experimental Spectra for \phi and \theta')
legend('(45,45)', '(90,45)', '(45,95)', '(90,45)')
```

```

plot(Expr_DataSet_Calib_Condensed(1:661,:))
title('Condensed Experimental Spectra for \phi and \theta')
legend('(45,45)', '(90,45)', '(45,95)', '(90,45)')

```

%%DERIVE CALIBRATION CURVE

% SPECTRA CHARACTERISTICS

%634 = 662-28keV = X-ray escape (iodine K shell) ** SEE IN SIM

%180 keV = Backscatter peak for Al (energy of scattered photon for large angles is pretty indp of initial gamma energy and scatter angle), maybe 1 just beneath from initial scatter first

%72 keV = K X-ray from Pb

%480 keV = Compton edge

%X-rays from Ba produced via internal conversion: K shell = 32.1 KeV, L shell = 4.5 KeV.

```
plot(Expr_DataSet(:,1))  
datacursormode on
```

```
%x = [546,55,360,367,1033];  
%y = [634,72,180,436,662*2];
```

```
%x = [546,55,114,367];  
%y = [634,72,180,436];
```

% (Ba L shell, Ba K shell, Pb K X-ray, Compton edge, I X-ray escape, Al backscatter peak)
 $x = [32, 96, 135, 341, 545, 200];$
 $y = [4.5, 32.1, 72, 480, 634, 180];$

```

% experimental
calibFit = polyfit(x,y,2)
% true
invcalibFit = polyfit(y,x,2)

x = 557

% Calibrate the experimental spectra according to polynomial: a = [0.0003, 0.9568, 41.5277]
syms x
% input = experimental, output = calibrated
calib(x) = symfun(calibFit(1)*x^2+calibFit(2)*x+calibFit(3),x)
% input = calibrated, output = experimental
invcalib(x) = symfun(invcalibFit(1)*x^2+invcalibFit(2)*x+invcalibFit(3),x)

% Used smoothed experimental to get rid of some statistical uncertainty
exprSumSmooth = exprSum;
for i = 1:(size(simSum)-1)
    if (i<=1 | i >= (size(exprSum)-1))
        exprSumSmooth(i) = exprSum(i)
    else
        exprSumSmooth(i) = (exprSum(i-1)+exprSum(i)+exprSum(i+1))/3;
    end
end

```

GEANT/MCNP Detector Response Curves

```

get the indices      ROW NUMBER      RUN NUMBER
115 = run 5 of 15-165 : 1+4*72*N:5*72*N      4*72:5*72-1
125 = run 1 of 125-175 : 1+0*72*N:1*72*N      0*72:1*(72)-1
165 = run 7 of 15-165 : 1+6*72*N:7*72*N      6*72:7*72-1
175 = run 2 of 125-175 : 1+1*72*N:2*72*N      1*72:2*72-1

% vector containing binned angles
angles = zeros(72,1)
for i = 1:72
    angles(i,1) = (i-1)*5;
end

%%%%%% READ IN THE DATA FRAMES %%%%%%
% READ IN Phi = 5-105

N = 500000
thetaN = 72
fileName = 'RSM_phi05_105_EDep_500,000_livphysics_matchMCNP.txt'
blankString = "

```

```

phi = 5;
phiInt = 0;
while (phi <= 105)
    startRow = (phiInt*N*thetaN);
    endRow = ((phiInt+1)*N*thetaN-1);
    eval(['SimMatchSim_Phi' num2str(phi) '= dlmread(fileName, blankString, [startRow o
endRow 1]);']);
    phi = phi+10
    phiInt = phiInt + 1;
end

```

% READ IN Phi = 125 and 175

```

SimMatchSim_125_175 =
dlmread('Rotating_RSM_phi125to175_inc50_EDep_500,000_MatchMCNP.txt');
SimMatchSim_Phi125 = SimMatchSim_125_175(1+0*72*N:1*72*N,:);
SimMatchSim_Phi175 = SimMatchSim_125_175(1+1*72*N:2*72*N,:);

```

% READ IN Phi = 115 and 165

```

N = 500000
thetaN = 72
fileName = 'Rotating_RSM_phi15to165_inc25_EDep_500,000_MatchMCNP.txt'
blankString = "
phi = 15;
phiInt = 0;
while (phi <= 165)
    startRow = (phiInt*N*thetaN);
    endRow = ((phiInt+1)*N*thetaN-1);
    eval(['SimMatchSim_Phi' num2str(phi) '= dlmread(fileName, blankString, [startRow o
endRow 1]);']);
    phi = phi+25
    phiInt = phiInt + 1;
end

```

% READ IN Phi = 135 and 145 and 155

```

N = 500000
thetaN = 72
fileName = 'RSM_phi135_155_EDep_500,000_livphysics_matchMCNP.txt'
blankString = "
phi = 135;
phiInt = 0;
while (phi <= 155)
    startRow = (phiInt*N*thetaN);
    endRow = ((phiInt+1)*N*thetaN-1);
    eval(['SimMatchSim_Phi' num2str(phi) '= dlmread(fileName, blankString, [startRow o
endRow 1]);']);
    phi = phi+10
    phiInt = phiInt + 1;
end

```

```
%%%%%% READ IN THE DATA FRAMES %%%%%%
```

```
% FORM A MATRIX THAT IS BINNED IN ENERGY AND ANGLE
% ROW: energy in 1 keV increments = 1 to 1000
% COLUMN: angle in 5 degree increments = 1 to 72

SimMatrix_500thousand_MatchMCNP = zeros(1000,72,18);
N = 500000;
phi = 5;
phiInt = 1;
while (phi <= 175)
    eval(['phiDataset = SimMatchSim_Phi' num2str(phi) ';']);
    for event = 1:72*N
        theta = floor((event-1)/N) + 1;
        run_eDep = phiDataset(event,2);
        energy_keV = run_eDep*10^3;
        energyBin = ceil(energy_keV)+1;
        SimMatrix_500thousand_MatchMCNP(energyBin,theta,phiInt) =
        SimMatrix_500thousand_MatchMCNP(energyBin,theta,phiInt) + 1;
    end
    phi = phi + 10
    phiInt = phiInt + 1;
end

% Read in MCNP
% Format: ScatthX1phX2p
% X1: theta
% X2: phi
% SimMatrix_500thousand_MCNP:
% D1 = energy bin 1-604 (bin 3 = 1 keV, bin 4 = 100 keV, then 1 keV
% differences in energy)
% D2 = theta 1-72 (inc 5)
% D3 = phi 1-36 (inc 5)

SimMatrix_500thousand_MCNP = zeros(604,72,36);
phiInt = 1
while phiInt <= 36
    % he starts with theta of 5 and I start with theta of 0!!
    thetaInt = 1
    while thetaInt <= 72
        theta = thetaInt*5
        phi = phiInt*5
        load(['Scatth' num2str(theta) 'ph' num2str(phi) 'p.mat'])
        if (thetaInt < 72)
            SimMatrix_500thousand_MCNP(:,thetaInt+1,phiInt) = val{1,1}';
        end
        if (thetaInt == 72)
            SimMatrix_500thousand_MCNP(:,1,phiInt) = val{1,1}';
        end
    end
    phiInt = phiInt + 1;
end
```

```

    end
    thetaInt = thetaInt + 1;
end
phiInt = phiInt + 1;
end

% Row 1: Sum up to the Compton edge (480 keV, which is row 481 in the
% dataset)
% Row 2: Sum of FEP
% Column: Theta
GEANTCount_Compton_FEP_MatchMCNP = zeros(2,72,18);

for phiInt = 1:18
    for theta = 1:72
        for energyBin = 2:480
            GEANTCount_Compton_FEP_MatchMCNP(1,theta,phiInt) =
GEANTCount_Compton_FEP_MatchMCNP(1,theta,phiInt) +
SimMatrix_500thousand_MatchMCNP(energyBin,theta,phiInt);
        end
        GEANTCount_Compton_FEP_MatchMCNP(2,theta,phiInt) =
SimMatrix_500thousand_MatchMCNP(663,theta,phiInt);
    end
end

MCNPCount_Compton_FEP = zeros(2,72,36);

for phiInt = 1:36
    for theta = 1:72
        for energyBin = 3:384
            MCNPCount_Compton_FEP(1,theta,phiInt) =
MCNPCount_Compton_FEP(1,theta,phiInt) +
SimMatrix_500thousand_MCNP(energyBin,theta,phiInt);
        end
        MCNPCount_Compton_FEP(2,theta,phiInt) =
SimMatrix_500thousand_MCNP(565,theta,phiInt);
    end
end

phiToPlot = 45
phiNumGEANT = ((phiToPlot+5)/10);
phiNumMCNP = (phiToPlot/5);

plot(angles,MCNPCount_Compton_FEP(1,:,phiNumMCNP)*N/directionBias)
hold on
plot(angles,GEANTCount_Compton_FEP_MatchMCNP(1,:,phiNumGEANT))
title(['Compton Integral Count \phi=25\circ Detector Response Curve']);
xlabel('Mask Rotation Angle', 'fontsize',16)
ylabel('Count (500,000 source particles per)', 'fontsize',16)
set(gca,'FontSize',16)
legend('MCNP','GEANT')

```

```

% store to put into a csv

MCNP_CI = zeros(72,36);
for i = 1:36
    MCNP_CI(:,i) = MCNPCount_Compton_FEP(1,:,i)*N/directionBias;
end

MCNP_FEP = zeros(72,36);
for i = 1:36
    MCNP_FEP(:,i) = MCNPCount_Compton_FEP(2,:,i)*N/directionBias;
end

GEANT_CI = zeros(72,18);
for i = 1:18
    GEANT_CI(:,i) = GEANTCount_Compton_FEP_MatchMCNP(1,:,i);
end

GEANT_FEP = zeros(72,18);
for i = 1:18
    GEANT_FEP(:,i) = GEANTCount_Compton_FEP_MatchMCNP(2,:,i);
end

%%%%%%% AN ASIDE ON PLOTTING STUFF%%%%%
%%%%%%%AN ASIDE ON PLOTTING STUFF%%%%%
%%%%%%%AN ASIDE ON PLOTTING STUFF%%%%%

% PLOT ALL OF THE FEP
figure
for phiInt = 1:18
    phi = phiInt*10^-5
    plot(angles,GEANTCount_Compton_FEP_MatchMCNP(2,:,phiInt), 'LineWidth',2)
    hold on
    title({'GEANT \phi=5-175\circ Detector Response Curve, FEP'}, 'fontsize',18);
    xlabel('Mask Rotation Angle', 'fontsize',16)
    ylabel('Count (500,000 Source Particles)', 'fontsize',16)
    set(gca,'FontSize',16)
    xlim([0,360])
    ylim([0,5500])
end

legend('5\circ','15\circ','25\circ','35\circ','45\circ','55\circ','65\circ','75\circ',
       '85\circ','95\circ','105\circ','115\circ','125\circ','135\circ','145\circ','
       '155\circ','165\circ','175\circ','Location','EastOutside')

% PLOT ALL OF THE COMPTON INTEGRALS
figure
for phiInt = 1:18
    phi = phiInt*10^-5

```

```

plot(angles,GEANTCount_Compton_FEP_MatchMCNP(1,:,phiInt), 'LineWidth',2)
hold on
title({'['GEANT \phi=5-175\circ Detector Response Curve, Compton Integral']}, 'fontsize',18);
xlabel('Mask Rotation Angle', 'fontsize',16)
ylabel('Count (500,000 Source Particles)', 'fontsize',16)
set(gca,'FontSize',16)
xlim([0,360])
ylim([0,11000])
end

legend('5\circ','15\circ','25\circ','35\circ','45\circ','55\circ','65\circ','75\circ',
'85\circ','95\circ','105\circ','115\circ','125\circ','135\circ','145\circ','155\circ',
'165\circ','175\circ','Location','EastOutside')

% PLOT ALL OF THE FEP / COMPTON INTEGRALS
for phiInt = 1:18
    phi = phiInt*10^-5

    plot(angles,GEANTCount_Compton_FEP_MatchMCNP(2,:,phiInt)./GEANTCount_Compton_
FEP_MatchMCNP(1,:,phiInt), 'LineWidth',2)
    hold on
    title({'['GEANT \phi=5-155\circ Detector Response Curve, FEP/Compton Integral']}, 
'fontsize',18);
    xlabel('Mask Rotation Angle', 'fontsize',16)
    ylabel('Count (500,000 source particles per)', 'fontsize',16)
    set(gca,'FontSize',16)
end

legend('5\phi','15\phi','25\phi','35\phi','45\phi','55\phi','65\phi','75\phi','85\phi','95\phi','105\phi','115\phi','
125\phi','135\phi','145\phi','155\phi','165\phi','175\phi')

% PLOT ALL OF THE COMPTON INTEGRALS/FEP
for phiInt = 1:18
    phi = phiInt*10^-5

    plot(angles,GEANTCount_Compton_FEP_MatchMCNP(1,:,phiInt)./GEANTCount_Compton_
FEP_MatchMCNP(2,:,phiInt), 'LineWidth',2)
    hold on
    title({'['GEANT \phi=5-155\circ Detector Response Curve, Compton Integral/FEP']}, 
'fontsize',18);
    xlabel('Mask Rotation Angle', 'fontsize',16)
    ylabel('Count (500,000 source particles per)', 'fontsize',16)
    set(gca,'FontSize',16)
end

legend('5\phi','15\phi','25\phi','35\phi','45\phi','55\phi','65\phi','75\phi','85\phi','95\phi','105\phi','115\phi','
125\phi','135\phi','145\phi','155\phi','165\phi','175\phi')

% Plot just 1 comparison of FEP and Compton Integral / FEP (normalized to
% area underneath the curve
phiInt = 11

```

```

phi = phiInt*10^-5
curveToPlot = GEANTCount_Compton_FEP_MatchMCNP(2,:,:,phiInt);
normalizeCurve = sum(curveToPlot)
ratioToPlot = GEANTCount_Compton_FEP_MatchMCNP(1,:,:,phiInt);
%ratioToPlot = GEANTCount_Compton_FEP_MatchMCNP(1,:,:,phiInt);
normalizeRatio = sum(ratioToPlot)
plot(angles, curveToPlot/normalizeCurve)
hold on
plot(angles, ratioToPlot/normalizeRatio, 'LineWidth',2)

title({'GEANT \phi=' int2str(phi) '\circ Detector Response Curve (FEP vs CI/FEP)'}, 'FontSize',18);
legend('FEP','CI/FEP')
xlabel('Mask Rotation Angle', 'FontSize',16)
ylabel('Normalized Count', 'FontSize',16)
set(gca,'FontSize',16)
hold off

% Plot just 1 comparison of FEP and Compton Integral (per source
% particle)
phiInt = 10
phi = phiInt*10^-5
curveToPlot = GEANTCount_Compton_FEP_MatchMCNP_perSourceParticle(1,:,:,phiInt)
normalizeCurve = sum(curveToPlot)
curveToPlot2 = GEANTCount_Compton_FEP_MatchMCNP_perSourceParticle(2,:,:,phiInt)
plot(angles, curveToPlot, 'LineWidth',2)
hold on
plot(angles, curveToPlot2, 'LineWidth',2)

title({'GEANT \phi=' int2str(phi) '\circ Detector Response Curve (FEP vs CI)'}, 'FontSize',18);
legend('CI','FEP')
xlabel('Mask Rotation Angle', 'FontSize',16)
ylabel('Count per Source Particle', 'FontSize',16)
set(gca,'FontSize',16)
hold off

```

% GRAPH WITH ERROR BARS

```

directionBias = 2.314*10^(-2)
N = 500000
phi = 165
numOverlap = zeros(18,1)
figure
while (phi < 180)
    phiNumGEANT = ((phi+5)/10)
    phiNumMCNP = (phi/5)

    %curveToPlotGEANT =

```

```

GEANTCount_Compton_FEP_MatchMCNP(2,:phiNumGEANT)/N*directionBias
%curveToPlotMCNP = MCNPCount_Compton_FEP(2,:phiNumMCNP)
curveToPlotGEANT = GEANTCount_Compton_FEP_MatchMCNP(1,:phiNumGEANT)
curveToPlotMCNP = MCNPCount_Compton_FEP(1,:phiNumMCNP)*N/directionBias

curveToPlotGEANT_ERR = 1.645*(1./sqrt(curveToPlotGEANT))
curveToPlotMCNP_ERR = 1.645*(1./sqrt(curveToPlotMCNP))

%curveToPlotGEANT_ERR = 1.645*sqrt(times(curveToPlotGEANT,(directionBias-
curveToPlotGEANT))*(1/(500000)))
%curveToPlotMCNP_ERR = 1.645*sqrt(times(curveToPlotMCNP,(directionBias-
curveToPlotMCNP))*(1/(500000)))

hh=gef;
subplot(1,2,phiNumGEANT-16)
hold on
errorbar(angles,curveToPlotGEANT,curveToPlotGEANT_ERR,'LineWidth',3)
errorbar(angles,curveToPlotMCNP,curveToPlotMCNP_ERR,'LineWidth',3)

%title({'['Compton Integral (CI) Normalized'] ;['Detector Response Curve \phi=' num2str(phi)
'\circ']}, 'fontsize',14);
title({'['Compton Integral Unnormalized Detector Response Curve \phi=' num2str(phi)
'\circ'];"}, 'fontsize',14);

%if phi == 75
    legend('GEANT','MCNP','Location','southeast')
%else
%    legend('GEANT','MCNP','Location','northeast')
%end
xlim([0 360])
ylim([0,10000])
xlabel('Mask Rotation Angle \theta', 'fontsize',16)
ylabel('Compton Integral Sum', 'fontsize',16)

%saveas(gcf,[num2str(phiToGraph) 'phiDetectorResponse.png'])

% COUNT NUMBER THAT OVERLAP

overlaps = 0;
for theta = 1:length(curveToPlotMCNP)
    upperMCNP = curveToPlotMCNP(theta) + curveToPlotMCNP_ERR(theta);
    lowerMCNP = curveToPlotMCNP(theta) - curveToPlotMCNP_ERR(theta);
    upperGEANT = curveToPlotGEANT(theta) + curveToPlotGEANT_ERR(theta);
    lowerGEANT = curveToPlotGEANT(theta) - curveToPlotGEANT_ERR(theta);
    if (lowerMCNP > upperGEANT)
        agree = 0;
    elseif (lowerGEANT > upperMCNP)
        agree = 0;
    else
        agree = 1;
    end
    overlaps = overlaps + agree;
end

```

```

    end
    overlaps = overlaps + agree;
end
numOverlap(phiNumGEANT) = overlaps;

phi = phi + 10
end

percentOverlapCI = numOverlap/72
percentOverlapFEP = numOverlap/72

```

GEANT/Experiment Detector Response Curves

```

%00001 = 5 phi
%00002 = 15 phi
%00003 = 25 phi
%00004 = 35 phi
%00005 = 45 phi
%00006 = 55 phi
%00007 = 65 phi
%00008 = 75 phi
%00009 = 85 phi
%00010 = 95 phi
%00011 = 105 phi
%00012 = 115 phi
%00013 = 125 phi
%00014 = 135 phi
%00015 = 145 phi
%00016 = 155 phi
%00017 = 165 phi
%00018 = 175 phi

% vector containing binned angles
angles = zeros(72,1)
for theta = 1:72
    angles(theta,1) = (theta-1)*5;
end

%% READ IN SIMULATED DATA (run to match experimental sleeve thickness)

N = 500000
thetaN = 72
fileName = 'RSM_15to165phi_EDep_500,000_MatchEXPR.txt'
blankString =
phi = 15;

```

```

phiInt = 1;
while (phi <= 165)
    startRow = (phiInt*N*thetaN);
    endRow = ((phiInt+1)*N*thetaN-1);
    eval(['SimMatchExpr_Phi' num2str(phi) ' = dlmread(fileName, blankString, [startRow o
endRow 1]);']);
    phi = phi+10
    phiInt = phiInt + 1;
end

fileName = 'RSM_phi5_500,000_livphysics_MatchEXPR.txt'
SimMatchExpr_Phi5 = dlmread(fileName);
N
fileName = 'RSM_phi175_500,000_livphysics_MatchEXPR.txt'
SimMatchExpr_Phi175 = dlmread(fileName);
N

% FORM A MATRIX THAT IS BINNED IN ENERGY AND ANGLE
% ROW: energy in 1 keV increments = 1 to 1098
% COLUMN: angle in 5 degree increments = 1 to 72

SimMatrix_500thousand_MatchExpr = zeros(2000,72,18);
N = 500000;
phi = 5;
phiInt = 1;
while (phi <= 175)
    eval(['phiDataset = SimMatchExpr_Phi' num2str(phi) ';'']);
    for event = 1:72*N
        run_eDep = phiDataset(event,2);
        energy_keV = run_eDep*10^3;
        energyBin = ceil(energy_keV)+1;
        theta = mod(phiDataset(event,1), 72) + 1;
        SimMatrix_500thousand_MatchExpr(energyBin,theta,phiInt) =
        SimMatrix_500thousand_MatchExpr(energyBin,theta,phiInt) + 1;
    end
    phi = phi + 10
    phiInt = phiInt + 1;
end

```

%%% EXPERIMENTAL DATA

```

Experimental_5Phi = dlmread('oooo1BIN.txt');
Experimental_15Phi = dlmread('oooo2BIN.txt');
Experimental_25Phi = dlmread('oooo3BIN.txt');
Experimental_35Phi = dlmread('oooo4BIN.txt');
Experimental_45Phi = dlmread('oooo5BIN.txt');
Experimental_55Phi = dlmread('oooo6BIN.txt');
Experimental_65Phi = dlmread('oooo7BIN.txt');
Experimental_75Phi = dlmread('oooo8BIN.txt');

```

```

Experimental_85Phi = dlmread('oooo9BIN.txt');
Experimental_95Phi = dlmread('ooo10BIN.txt');
Experimental_105Phi = dlmread('ooo11BIN.txt');
Experimental_115Phi = dlmread('ooo12BIN.txt');
Experimental_125Phi = dlmread('ooo13BIN.txt');
Experimental_135Phi = dlmread('ooo14BIN.txt');
Experimental_145Phi = dlmread('ooo15BIN.txt');
Experimental_155Phi = dlmread('ooo16BIN.txt');
Experimental_165Phi = dlmread('ooo17BIN.txt');
Experimental_175Phi = dlmread('ooo18BIN.txt');

```

```

ExprMatrix = zeros(1098,72,18);
ExprMatrix(:,:,1) = Experimental_5Phi(:,:,2:73);
ExprMatrix(:,:,2) = Experimental_15Phi(:,:,2:73);
ExprMatrix(:,:,3) = Experimental_25Phi(:,:,2:73);
ExprMatrix(:,:,4) = Experimental_35Phi(:,:,2:73);
ExprMatrix(:,:,5) = Experimental_45Phi(:,:,2:73);
ExprMatrix(:,:,6) = Experimental_55Phi(:,:,2:73);
ExprMatrix(:,:,7) = Experimental_65Phi(:,:,2:73);
ExprMatrix(:,:,8) = Experimental_75Phi(:,:,2:73);
ExprMatrix(:,:,9) = Experimental_85Phi(:,:,2:73);
ExprMatrix(:,:,10) = Experimental_95Phi(:,:,2:73);
ExprMatrix(:,:,11) = Experimental_105Phi(:,:,2:73);
ExprMatrix(:,:,12) = Experimental_115Phi(:,:,2:73);
ExprMatrix(:,:,13) = Experimental_125Phi(:,:,2:73);
ExprMatrix(:,:,14) = Experimental_135Phi(:,:,2:73);
ExprMatrix(:,:,15) = Experimental_145Phi(:,:,2:73);
ExprMatrix(:,:,16) = Experimental_155Phi(:,:,2:73);
ExprMatrix(:,:,17) = Experimental_165Phi(:,:,2:73);
ExprMatrix(:,:,18) = Experimental_175Phi(:,:,2:73);

```

```
% CALIBRATE
```

```
% SUBSET OF THE PEAKS
```

```
loganPeaks = [0,22,54,86,122,307,417,554,770,1021,1166]
loganPeaksEnergies = [0,60,88,122,159,392,514,662,898,1173,1333]
```

```

syms x
invLoganFit = polyfit(loganPeaksEnergies, loganPeaks,2)
invcalib(x) = symfun(invLoganFit(1)*x^2+invLoganFit(2)*x+invLoganFit(3)*x^0,x)
syms x
LoganFit = polyfit(loganPeaks,loganPeaksEnergies,2)
calib(x) = symfun(LoganFit(1)*x^2+LoganFit(2)*x+LoganFit(3)*x^0,x)

```

```
% Energy, theta, phi
```

```
ExprMatrix_Calib = zeros(2000,72,18);
for phi = 1:18
    for theta = 1:72
        % for each energy value
```

```

for keV_Bin=1:2000
    exprCount = 0;
    % speed up
    tempBin = ceil(invLoganFit(1)*keV_Bin^2+invLoganFit(2)*keV_Bin+invLoganFit(3));
    lowerExprBin = tempBin-1;
    upperExprBin = tempBin;
    for exprBin = lowerExprBin:upperExprBin
        if(exprBin > 0 && exprBin < 1099)
            exprCount = exprCount + ExprMatrix(exprBin,theta,phi);
        end
    end
    ExprMatrix_Calib(keV_Bin,theta,phi) = exprCount;
end
theta
end
phi
end

% SHIFT TO ALIGN THE PROPER THETAS
ExprMatrix_Calib_Shifted = zeros(2000,72,18);
for phi = 1:18
    for theta = 1:10
        ExprMatrix_Calib_Shifted(:,theta,phi) = ExprMatrix_Calib(:,theta+(72-10),phi);
    end
    for theta = 11:72
        ExprMatrix_Calib_Shifted(:,theta,phi) = ExprMatrix_Calib(:,theta-10,phi);
    end
end

% BROADEN THE SIMULATED
SimMatrix_500thousand_MatchExpr_Conv = zeros(1999,72,18);
for phi = 1:18
    for theta = 1:72
        wayDownIndex = 0;
        [maxCount, maxIndexVal] = max(ExprMatrix_Calib_Shifted(659:665,theta,phi));
        maxIndex = maxIndexVal + 660;
        maxIndexTrue = 662;
        halfMax = maxCount/2;
        minDiff = 100000;
        for i=670:750
            diff = (ExprMatrix_Calib_Shifted(i,theta,phi)- halfMax);
            if (diff < minDiff)
                wayDownIndex = i;
                minDiff = diff;
            end
        end
    end
    FWHM = 2*(wayDownIndex-maxIndexTrue);
    y = SimMatrix_500thousand_MatchExpr(2:2000,theta,phi);
    y(1) = 0;
    x = -2000/2:2000/2;
    sigma = FWHM/(sqrt(8*log(2)));

```

```

gaussFilter = exp(-x.^2 / (2 * sigma ^ 2));
gaussFilter = gaussFilter / sum (gaussFilter); % normalize
SimMatrix_500thousand_MatchExpr_Conv(:, theta, phi) = conv(y, gaussFilter, 'same');
end
phi
end

%% CALCULATE THE FEP AND COMPTON INTEGRAL DRC FOR BOTH

GEANTCount_Compton_FEP_MatchEXPR = zeros(2,72,18);

for phiInt = 1:18
    for theta = 1:72
        for energyBin = 200:480
            GEANTCount_Compton_FEP_MatchEXPR(1,theta,phiInt) =
GEANTCount_Compton_FEP_MatchEXPR(1,theta,phiInt) +
SimMatrix_500thousand_MatchExpr(energyBin,theta,phiInt);
        end
        GEANTCount_Compton_FEP_MatchEXPR(2,theta,phiInt) =
SimMatrix_500thousand_MatchExpr(663,theta,phiInt);
    end
end

GEANTCount_Compton_FEP_MatchEXPR_Conv = zeros(2,72,18);

for phiInt = 1:18
    for theta = 1:72
        for energyBin = 200:480
            GEANTCount_Compton_FEP_MatchEXPR_Conv(1,theta,phiInt) =
GEANTCount_Compton_FEP_MatchEXPR_Conv(1,theta,phiInt) +
SimMatrix_500thousand_MatchExpr_Conv(energyBin,theta,phiInt);
        end
        GEANTCount_Compton_FEP_MatchEXPR_Conv(2,theta,phiInt) =
SimMatrix_500thousand_MatchExpr(663,theta,phiInt);
    end
end

% See difference between convolved and nonconvolved

phiToPlot = 75
phiNumGEANT = ((phiToPlot+5)/10);
plot(angles,GEANTCount_Compton_FEP_MatchEXPR_Conv(1, :, phiNumGEANT),
'LineWidth',2)
hold on
plot(angles,GEANTCount_Compton_FEP_MatchEXPR(1, :, phiNumGEANT), 'LineWidth',2)
title(['Compton Integral Count \phi=' num2str(phiToPlot) '\circ Detector Response Curve']);
xlabel('Mask Rotation Angle', 'fontsize',16)
ylabel('Count', 'fontsize',16)
set(gca,'FontSize',16)
legend('Convolved Simulation Data','Raw Simulation Data')

```

```

EXPRCount_Compton_FEP = zeros(2,72,36);
% GET THE CI
for phiInt = 1:18
    for theta = 1:72
        for energyBin = 1:480
            EXPRCount_Compton_FEP(1,theta,phiInt) =
EXPRCount_Compton_FEP(1,theta,phiInt) +
ExprMatrix_Calib_Shifted(energyBin,theta,phiInt);
        end
    end
end

% GET THE FEP (integrate under Gaussian) for the EXPR
for phi = 1:18
    phi
    integralValues = zeros(72,1);
    for theta = 1:72
        % only look at the gaussian FEP area 600-800 keV (not the Compton continuum)
        xVals = zeros(201,1);
        for j=1:201
            xVals(j,1) = j+599;
        end
        % fit to a single gaussian
        f = fit(xVals,ExprMatrix_Calib_Shifted(600:800,theta,phi),'gauss1');
        %plot(f,xVals,ExprMatrix(450:650,i+1,a));
        %parameters of the gaussian
        %coefficient
        a1 = f.a1;
        %mean
        b1 = f.b1;
        %exponent denominator
        c1 = f.c1;
        stdev = sqrt(c1/2);
        % get the integral
        syms x;
        integralVal = int(a1*exp(-((x-b1)/c1)^2),x,b1-2*stdev,b1+2*stdev);
        % divide by the percent of the distribution that we included within 1
        % stdev on either side
        integralValues(theta,1) = integralVal/.9545;
    end
    EXPRCount_Compton_FEP(2,:,phi) = integralValues(:,1)';
end

% GET THE FEP (integrate under Gaussian) for the SIMULATED
for phi = 1:18

```

```

phi
integralValues = zeros(72,1);
for theta = 1:72
    % only look at the gaussian FEP area 600-800 keV (not the Compton continuum)
    xVals = zeros(201,1);
    for j=1:201
        xVals(j,1) = j+599;
    end
    % fit to a single gaussian
    f = fit(xVals,SimMatrix_500thousand_MatchExpr_Conv(600:800,theta,phi),'gauss1');
    %plot(f,xVals,ExprMatrix(450:650,i+1,a));
    %parameters of the gaussian
    %coefficient
    a1 = f.a1;
    %mean
    b1 = f.b1;
    %exponent denominator
    c1 = f.c1;
    stdev = sqrt(c1/2);
    % get the integral
    syms x;
    integralVal = int(a1*exp(-((x-b1)/c1)^2),x,b1-2*stdev,b1+2*stdev);
    % divide by the percent of the distribution that we included within 1
    % stdev on either side
    integralValues(theta,1) = integralVal/.9545;
end
GEANTCount_Compton_FEP_MatchEXPR_Conv(2,:,:phi) = integralValues(:,1)';
end

%% FOR STAT COMPARE AND THESIS GRAPHS
phiToPlot = 5

while phiToPlot < 180

phiNumGEANT = ((phiToPlot+5)/10)
phiNumEXPR = phiNumGEANT;

whichToPlot = 2;
curve = "";
if whichToPlot == 1
    curve = 'Compton Integral'
end
if whichToPlot == 2
    curve = 'FEP'
end
figure('units','normalized','position',[.09 .09 .8 .8])

curveToPlotGEANT =
GEANTCount_Compton_FEP_MatchEXPR_Conv2(whichToPlot,:,:phiNumGEANT);
normGEANT =
sum(GEANTCount_Compton_FEP_MatchEXPR_Conv2(whichToPlot,:,:phiNumGEANT));

```

```

curveToPlotGEANT_norm = curveToPlotGEANT/normGEANT;
%curveToPlotGEANT_ERR = 1.645*(1./sqrt(curveToPlotGEANT))*(1/normGEANT);
for point = 1:72
    curveToPlotGEANT_ERR(point) = 1.645*sqrt((curveToPlotGEANT(point)/normGEANT)*(1-
(curveToPlotGEANT(point)/normGEANT))/normGEANT)
end

curveToPlotEXPR = EXPRCount_Compton_FEP(whichToPlot,:,phiNumEXPR);
normEXPR = sum(EXPRCount_Compton_FEP(whichToPlot,:,phiNumEXPR));
curveToPlotEXPR_norm = curveToPlotEXPR/normEXPR;
%curveToPlotEXPR_ERR = 1.645*(1./sqrt(curveToPlotEXPR))*(1/normEXPR);
for point = 1:72
    curveToPlotEXPR_ERR(point) = 1.645*sqrt((curveToPlotEXPR(point)/normEXPR)*(1-
(curveToPlotEXPR(point)/normEXPR))/normEXPR)
end

%normToMin =
min(EXPRCount_Compton_FEP(whichToPlot,:,phiNumEXPR))/min(GEANTCount_Compton
_FEP_MatchEXPR_Conv(whichToPlot,:,phiNumGEANT))
%plot(angles(EXPRCount_Compton_FEP(whichToPlot,:,phiNumEXPR)/normEXPR,
'LineWidth',2)
%plot(angles(EXPRCount_Compton_FEP(whichToPlot,:,phiNumEXPR), 'LineWidth',2)
%hold on
%plot(angles,GEANTCount_Compton_FEP_MatchEXPR_Conv(whichToPlot,:,phiNumGEANT
)/normGEANT, 'LineWidth',2)
%plot(angles,GEANTCount_Compton_FEP_MatchEXPR_Conv(whichToPlot,:,phiNumGEANT
)*normToMin, 'LineWidth',2)
% title([curve ' Count \phi=' num2str(phiToPlot) '\circ Detector Response Curve']);
% xlabel('Mask Rotation Angle', 'fontsize',16)
% ylabel('Normalized Count', 'fontsize',16)
% set(gca,'FontSize',16)
% legend('Experiment','GEANT')
% ylim([0,16000])
% xlim([0,360])

errorbar(angles,curveToPlotGEANT_norm,curveToPlotGEANT_ERR,'LineWidth',3)
hold on
errorbar(angles,curveToPlotEXPR_norm,curveToPlotEXPR_ERR,'LineWidth',3)

title([curve ' Normalized Count \phi=' num2str(phiToPlot) '\circ Detector Response Curve']);
xlabel('Mask Rotation Angle', 'fontsize',16)
ylabel('Normalized Count', 'fontsize',16)
set(gca,'FontSize',16)
legend('GEANT 90% Confidence Interval','Experiment 90% Confidence Interval')
ylim([0,.03])
xlim([0,360])

saveas(gcf,['FEPcurvesPhi' num2str(phiToPlot) '.png'])

```

```

phiToPlot = phiToPlot + 10

end

% store to put into a csv
EXPR_CI = zeros(72,36);
for phi = 1:18
    EXPR_CI(:,phi) =
EXPRCount_Compton_FEP(1,:,phi)/sum(EXPRCount_Compton_FEP(1,:,phi));
end

EXPR_FEP = zeros(72,36);
for phi = 1:18
    EXPR_FEP(:,phi) =
EXPRCount_Compton_FEP(2,:,phi)/sum(EXPRCount_Compton_FEP(2,:,phi));
end

GEANT_CI = zeros(72,18);
for phi = 1:18
    GEANT_CI(:,phi) =
GEANTCount_Compton_FEP_MatchEXPR_Conv(1,:,phi)/sum(GEANTCount_Compton_FEP
_MatchEXPR_Conv(1,:,phi));
end

GEANT_FEP = zeros(72,18);
for phi = 1:18
    GEANT_FEP(:,phi) =
GEANTCount_Compton_FEP_MatchEXPR_Conv2(2,:,phi)/sum(GEANTCount_Compton_FE
P_MatchEXPR_Conv2(2,:,phi));
end

%%%%%%% AN ASIDE ON PLOTTING STUFF
%%%%%%

% PLOT ALL OF THE FEP
for phiInt = 1:18
    phi = phiInt*10^-5
    plot(angles,GEANTCount_Compton_FEP_MatchEXPR(2,:,phiInt), 'LineWidth',2)
    hold on
    title({'GEANT \phi=5-155\circ Detector Response Curve, FEP'}, 'fontsize',18);
    xlabel('Mask Rotation Angle', 'fontsize',16)
    ylabel('Count (500,000 source particles per)', 'fontsize',16)
    set(gca,'FontSize',16)
end

legend('5phi','15phi','25phi','35phi','45phi','55phi','65phi','75phi','85phi','95phi','105phi','115phi',
'125phi','135phi','145phi','155phi','165phi','175phi')
% PLOT ALL OF THE COMPTON INTEGRALS
for phiInt = 1:16
    phi = phiInt*10^-5

```

```

plot(angles,GEANTCount_Compton_FEP_MatchEXPR(1,:,phiInt), 'LineWidth',2)
hold on
title({'['GEANT \phi=5-155\circ Detector Response Curve, Compton Integral']}, 'fontsize',18);
xlabel('Mask Rotation Angle', 'fontsize',16)
ylabel('Count (500,000 source particles per)', 'fontsize',16)
set(gca,'FontSize',16)
end

legend('15phi','25phi','35phi','45phi','55phi','65phi','75phi','85phi','95phi','105phi','115phi','125ph
i','135phi','145phi','155phi','165phi')
% PLOT ALL OF THE FEP / COMPTON INTEGRALS
for phiInt = 1:16
    phi = phiInt*10-5

plot(angles,GEANTCount_Compton_FEP_MatchEXPR(2,:,phiInt)./GEANTCount_Compton_F
EP_MatchEXPR(1,:,phiInt), 'LineWidth',2)
    hold on
    title({'['GEANT \phi=5-155\circ Detector Response Curve, FEP/Compton Integral']}, 
'fontsize',18);
    xlabel('Mask Rotation Angle', 'fontsize',16)
    ylabel('Count (500,000 source particles per)', 'fontsize',16)
    set(gca,'FontSize',16)
end

legend('15phi','25phi','35phi','45phi','55phi','65phi','75phi','85phi','95phi','105phi','115phi','125ph
i','135phi','145phi','155phi','165phi')
% PLOT ALL OF THE COMPTON INTEGRALS/FEP
for phiInt = 1:16
    phi = phiInt*10-5

plot(angles,GEANTCount_Compton_FEP_MatchEXPR(1,:,phiInt)./GEANTCount_Compton_F
EP_MatchEXPR(2,:,phiInt), 'LineWidth',2)
    hold on
    title({'['GEANT \phi=5-155\circ Detector Response Curve, Compton Integral/FEP']}, 
'fontsize',18);
    xlabel('Mask Rotation Angle', 'fontsize',16)
    ylabel('Count (500,000 source particles per)', 'fontsize',16)
    set(gca,'FontSize',16)
end

legend('15phi','25phi','35phi','45phi','55phi','65phi','75phi','85phi','95phi','105phi','115phi','125ph
i','135phi','145phi','165phi')
% Plot just 1 comparison of FEP and Compton Integral / FEP (normalized to
% area underneath the curve
phiInt = 10
phi = phiInt*10-5
curveToPlot = GEANTCount_Compton_FEP_MatchEXPR(2,:,phiInt)
normalizeCurve = sum(curveToPlot)
ratioToPlot =
GEANTCount_Compton_FEP_MatchEXPR(1,:,phiInt)./GEANTCount_Compton_FEP_Match
EXPR(2,:,phiInt)

```

```

normalizeRatio = sum(ratioToPlot)
plot(angles, curveToPlot/normalizeCurve)
hold on
plot(angles, ratioToPlot/normalizeRatio, 'LineWidth',2)

title({'GEANT \phi=' int2str(phi) 'circ Detector Response Curve (FEP vs CI/FEP)'}, 'fontsize',18);
legend('FEP','CI/FEP')
xlabel('Mask Rotation Angle', 'fontsize',16)
ylabel('Normalized Count', 'fontsize',16)
set(gca,'FontSize',16)
hold off

%%%%%%%%%%%% - %%%%%%

```

Imaging Algorithm

```

totTheta = 72
totPhi = 18
DRC = 72

thetas = zeros(72,1)
for i = 1:72
    thetas(i,1) = (i-1)*5;
end
phis = zeros(18,1)
for i = 1:18
    phis(i,1) = (i-1)*10+5;
end

% GEANT library and experimental values based on FEP

% EXPRCount_Compton_FEP
% GEANTCount_Compton_FEP_MatchEXPR_Conv

% row = shift int
% column = phi
% value = DRC (72 long)
GEANT_library = zeros(totTheta, totPhi, DRC);
Experimental_Curves = zeros(totTheta, totPhi, DRC);

for phi = 1:18
    for shift = 1:72 % this is the theta
        GEANT_library(shift,phi,:) =
        circshift(GEANTCount_Compton_FEP_MatchEXPR_Conv2(2,:,:phi),[0,shift]);
        GEANT_library(shift,phi,:) =
        GEANT_library(shift,phi,:)/sum(GEANT_library(shift,phi,:));
    end
end

```

```

for phi = 1:18
    for shift = 1:72 % this is the theta
        Experimental_Curves(shift,phi,:) = circshift(EXPRCount_Compton_FEP(2,:,:,phi),[0,shift]);
        Experimental_Curves(shift,phi,:) =
    Experimental_Curves(shift,phi,:)/sum(Experimental_Curves(shift,phi,:));
    end
end

figure
phiInt = 6
for i = 1:10
    plot(squeeze(GEANT_library(i,phiInt,:)))
    hold on
end

% You have an array of errors for each experimental curve for each theta, phi position
% trueExpr trueExpr errWithSim errWithSim
errors = zeros(totTheta, totPhi, totTheta, totPhi);

for phiExpr = 1:totPhi
    for thetaExpr = 1:totTheta
        errMatrix = zeros(totTheta,totPhi); % with each one in the library
        for errPhi=1:totPhi
            for errTheta = 1:totTheta
                for DRCindex = 1:72
                    errMatrix(errTheta,errPhi) = errMatrix(errTheta,errPhi) +
                    (Experimental_Curves(thetaExpr,phiExpr,DRCindex) -
                    GEANT_library(errTheta,errPhi,DRCindex))^2;
                end
            end
        end
        % for that experimental position
        errors(thetaExpr,phiExpr,:,:)= errMatrix/72;
    end
    phiExpr
end

predictErrorTheta_FINAL = zeros(72,18);
predictErrorPhi_FINAL = zeros(72,18);
%predictErrorThetaAvg = zeros(72,18);
%predictErrorPhiAvg = zeros(72,18);
predictTheta = zeros(72,18);
predictPhi = zeros(72,18);

for truePhiExpr = [5:10:175]
    for trueThetaExpr = [5:5:360]

```

```

trueThetaIntExpr = trueThetaExpr/5;
truePhiIntExpr = (truePhiExpr+5)/10;

errSurfToPlot = squeeze(errors(trueThetaIntExpr,truePhiIntExpr,:,:));

[thetaSimPredInt1,phiSimPredInt1] = find(errSurfToPlot == min(errSurfToPlot(:)),1);
%errSurfToPlot(thetaSimPredInt1,phiSimPredInt1) = 10^7;
[%[thetaSimPredInt2,phiSimPredInt2] = find(errSurfToPlot == min(errSurfToPlot(:)),1);
%errSurfToPlot(thetaSimPredInt2,phiSimPredInt2) = 10^7;
%[thetaSimPredInt3,phiSimPredInt3] = find(errSurfToPlot == min(errSurfToPlot(:)),1);

%thetaSimPredIntAvg = (thetaSimPredInt1 + thetaSimPredInt2 + thetaSimPredInt3)/3;
%phiSimPredIntAvg = (phiSimPredInt1 + phiSimPredInt2 + phiSimPredInt3)/3;

predThetaSim = (thetaSimPredInt1*5);
predPhiSim = (phiSimPredInt1*10)-5;

%predThetaSimAvg = (thetaSimPredIntAvg*5);
%predPhiSimAvg = (phiSimPredIntAvg*10)-5;

errTheta = abs(trueThetaExpr - predThetaSim);
errTheta = min([abs(errTheta),abs(360-errTheta)]);
%errThetaAvg = trueThetaExpr - predThetaSimAvg;
%errThetaAvg = min([abs(errThetaAvg),abs(360-errThetaAvg),abs(errThetaAvg-360)])]

predictTheta(trueThetaIntExpr,truePhiIntExpr) = predThetaSim;
predictErrorTheta_FINAL(trueThetaIntExpr,truePhiIntExpr) = errTheta;
%predictErrorThetaAvg(trueThetaIntExpr,truePhiIntExpr) = errThetaAvg;

errPhi = abs(truePhiExpr - predPhiSim)
errPhi = min([abs(errPhi),abs(360-errPhi)])
%errPhiAvg = truePhiExpr - predPhiSimAvg;
%errPhiAvg = min([abs(errPhiAvg),abs(360-errPhiAvg),abs(errPhiAvg-360)])]

predictPhi(trueThetaIntExpr,truePhiIntExpr) = predPhiSim;
predictErrorPhi_FINAL(trueThetaIntExpr,truePhiIntExpr) = errPhi;
%predictErrorPhiAvg(trueThetaIntExpr,truePhiIntExpr) = errPhiAvg;

end

```

end

end

```

trueThetaExpr = 125
truePhiExpr = 75

```

```

trueThetaIntExpr = trueThetaExpr/5;
truePhiIntExpr = (truePhiExpr+5)/10;
start = 1.2*10^(-6)

```

```

i = 5*10^(-6)
%levels = [(start-
i),start,(start+i),(start+2*i),(start+3*i),(start+4*i),(start+5*i),(start+6*i),(start+7*i),(start+8*i),
(start+9*i),(start+10*i)]

% Visualize a representative surface plot
errSurfToPlot = squeeze(errors(trueThetaIntExpr,truePhiIntExpr,:,:));
surf(phis,thetas,errSurfToPlot);
%contour(phis,thetas,errSurfToPlot,40, 'LineWidth',3)

title(['Mean Squared Error Surface for Experimental FEP Detector Response Curve
(\theta=125\circ, \phi=75\circ)', 'fontsize',20])
xlabel('Phi', 'fontsize',16)
ylabel('Theta', 'fontsize',16)
zlabel('Mean Squared Error', 'fontsize',16)
set(gca,'FontSize',18)
xlim([0,180])
ylim([0,360])
view([90 90]);
colorbar
saveas(gcf,'errorSurf.png')

saveas(gcf,['FEPcurvesPhi' num2str(phiToPlot) '.png'])

avgErrorTheta = mean2(predictErrorTheta_FINAL(:,[1:11,13:18]))
avgErrorPhi = mean2(predictErrorPhi_FINAL(:,[1:11,13:18]))

```

Appendix G

This appendix contains representative R code that is used to run the statistical tests that were employed to compare the GEANT and MCNP data as well as the GEANT and experimental data.

Compare Energy Spectra

```
##### COMPARING GEANT AND EXPR SPECTRA

# Goes 5 Phi to 180 Phi (inc 5) - GROSS COUNT (converted so that theta 0 to 355)
GEANT_EXPR_Spectra =
read.csv("/Users/jvl2xv/Documents/MATLAB/Thesis/ScriptsAndWorkbooks/GEANT_EXPR_Spectra/EnergySpectra_GEANT_EXPR.csv", sep=",", header=T)

### AD AND KS TEST

install.packages("kSamples")
install.packages("stats")
install.packages("ADGofTest")
library(stats)
library(kSamples)

GEANT_EXPR_Spectra$pval_AD = c(10,10,10,10)
GEANT_EXPR_Spectra$pval_KS = c(10,10,10,10)

#(45,45)
GEANT_EXPR_Spectra$pval_AD[1] =
ad.test(GEANT_EXPR_Spectra$X45_45.GEANT[200:1000],GEANT_EXPR_Spectra$X45_45EXPR[200:1000])$ad[1,3]
GEANT_EXPR_Spectra$pval_KS[1] =
ks.test(GEANT_EXPR_Spectra$X45_45.GEANT[200:1000],GEANT_EXPR_Spectra$X45_45EXPR[200:1000])$p.value
#(90,45)
GEANT_EXPR_Spectra$pval_AD[2] =
ad.test(GEANT_EXPR_Spectra$X90_45.GEANT[200:1000],GEANT_EXPR_Spectra$X90_45EXPR[200:1000])$ad[1,3]
GEANT_EXPR_Spectra$pval_KS[2] =
```

```

ks.test(GEANT_EXPR_Spectra$X90_45.GEANT[200:1000],GEANT_EXPR_Spectra$X90_45.
EXPR[200:1000])$p.value
#(45,95)
  GEANT_EXPR_Spectra_pval_AD[3] =
ad.test(GEANT_EXPR_Spectra$X45_95.GEANT[200:1000],GEANT_EXPR_Spectra$X45_95.
EXPR[200:1000])$ad[1,3]
  GEANT_EXPR_Spectra_pval_KS[3] =
ks.test(GEANT_EXPR_Spectra$X45_95.GEANT[200:1000],GEANT_EXPR_Spectra$X45_95.
EXPR[200:1000])$p.value
#(90,95)
  GEANT_EXPR_Spectra_pval_AD[4] =
ad.test(GEANT_EXPR_Spectra$X90_95.GEANT[200:1000],GEANT_EXPR_Spectra$X90_95.
EXPR[200:1000])$ad[1,3]
  GEANT_EXPR_Spectra_pval_KS[4] =
ks.test(GEANT_EXPR_Spectra$X90_95.GEANT[200:1000],GEANT_EXPR_Spectra$X90_95.
EXPR[200:1000])$p.value

```

Compare Detector Response Curves

```

##### COMPARING GEANT AND EXPR DETECTOR RESPONSE CURVES

# Goes 5 Phi to 180 Phi (inc 5) - GROSS COUNT (converted so that theta 0 to 355)
EXPR_CI =
read.csv("/Users/jvl2xv/Documents/MATLAB/Thesis/ScriptsAndWorkbooks/GEANT_EXPR_
DRC/EXPR_CI.csv", sep=",", header=T)
EXPR_FEP =
read.csv("/Users/jvl2xv/Documents/MATLAB/Thesis/ScriptsAndWorkbooks/GEANT_EXPR_
DRC/EXPR_FEP.csv", sep=",", header=T)
# Goes 5 Phi to 175 Phi (inc 10) - GROSS COUNT (theta 0 to 355)
GEANT_CI =
read.csv("/Users/jvl2xv/Documents/MATLAB/Thesis/ScriptsAndWorkbooks/GEANT_EXPR_
DRC/GEANT_CI.csv", sep=",", header=T)
GEANT_CI =
read.csv("/Users/jvl2xv/Documents/MATLAB/Thesis/ScriptsAndWorkbooks/GEANT_EXPR_
DRC/GEANT_CI_Conv.csv", sep=",", header=T)
GEANT_FEP =
read.csv("/Users/jvl2xv/Documents/MATLAB/Thesis/ScriptsAndWorkbooks/GEANT_EXPR_
DRC/GEANT_FEP.csv", sep=",", header=T)
GEANT_FEP =
read.csv("/Users/jvl2xv/Documents/MATLAB/Thesis/ScriptsAndWorkbooks/GEANT_EXPR_
DRC/GEANT_FEP_Conv.csv", sep=",", header=T)

```

```

### AD AND KS TEST

```

```

install.packages("kSamples")
install.packages("stats")
install.packages("ADGofTest")
library(stats)
library(kSamples)

```

```

p_val_AD_FEP = rep(10, times = 18)
p_val_AD_CI = rep(10, times = 18)
p_val_KS_FEP = rep(10, times = 18)
p_val_KS_CI = rep(10, times = 18)

phi = 5
while (phi < 180) {
  phiNumGEANT = ((phi+5)/10);
  phiNumEXPR = phiNumGEANT;

  print(cat("EXPR", phiNumEXPR));
  print(cat("GEANT",phiNumGEANT));

  dataGEANT_FEP = GEANT_FEP[[phiNumGEANT+1]];
  dataEXPR_FEP = EXPR_FEP[[phiNumEXPR+1]];

  dataGEANT_CI = GEANT_CI[[phiNumGEANT+1]];
  dataEXPR_CI = EXPR_CI[[phiNumEXPR+1]];

  p_val_AD_FEP[phiNumGEANT] = ad.test(dataGEANT_FEP,dataEXPR_FEP)$ad[1,3]
  p_val_AD_CI[phiNumGEANT] = ad.test(dataGEANT_CI,dataEXPR_CI)$ad[1,3]

  p_val_KS_FEP[phiNumGEANT] = ks.test(dataGEANT_FEP,dataEXPR_FEP)$p.value
  p_val_KS_CI[phiNumGEANT] = ks.test(dataGEANT_CI,dataEXPR_CI)$p.value

  phi = phi + 10
}

```

Appendix H

A type 76B76/3M-E1-X-NEG SCIONIX HOLLAND 3" x 3" NaI(Tl) detector (serial number SFQ770) was utilized as the detector in this experiment. A CAEN Model NIM8304 crate held the ORTEC 556 High Voltage Power Supply, NIMBox NDA8 DAC, ORTEC 460 Delay Line Amplifier, and the ORTEC 926 ADCAM MCB. An ORTEC Pre-Amplifier was placed between the NaI(Tl) detector and the linear amplifier. The configuration is seen in Figure 11. Experimental settings are found below.

ORTEC 460 Delay Line Amplifier:

Controls

Fine gain: X.65
Course gain: X20
Total gain: X13
Integration time constant (shaping filter): .04 μ s
Input polarity: negative

Performance

Integral nonlinearity: $\leq \pm 0.05\%$
Noise: $\leq 60 \mu V rms$
Delay line shaping: 1 μ s (both lines)
Temperature instability: Gain ($\leq \pm 0.01\%/\text{ }^{\circ}\text{C}$) DC Level ($\leq \pm 0.1 mV/\text{ }^{\circ}\text{C}$)
Count rate stability: Pulsar peak at 85% of analyzer range shifts $\leq 0.2\%$ for 0 to 10^5 cps of 662 keV gamma with peak at 75% of analyzer range

556 High Voltage Power Supply:

Controls

Output level: 500 V

Reference source for output voltage: Internal reference source

Performance

Regulation: $\leq \pm 0.0025\%$ variation in output voltage for combined line and load variations at constant temperature

Temperature instability: $\leq \pm 50 \text{ ppm}/^\circ\text{C}$ after 30 min warmup

Long-term drift: $\leq 0.1\%/\text{hour}$ and $\leq 0.3\% / 24 \text{ hour}$ at constant temperature

Bibliography

- [1] Hutcheson, A. L., Phlips, B. F., Wulf, E. A., Mitchell, L. J., Johnson, W. N., & Leas, B. E. (2013). Maritime detection of radiological/nuclear threats with hybrid imaging system. 2013 IEEE International Conference on Technologies for Homeland Security (HST). doi:10.1109/ths.2013.6699030
- [2] Kowash, B.R. (2008). A Rotating Modulation Imager for the Orphan Source Search Problem (Doctoral dissertation).
- [3] Ferguson, C.D., Kazi, T., Perera, J. "Commercial Radioactive Sources: Surveying the Security Risks". Monterey Institute for International Studies: Center for Nonproliferation Studies. Occasional Paper #11. Jan. 2003.
- [4] Sharma, A.C. et al. "Design and Development of a High-Energy Gamma Camera for Use with NSECT- Imaging: Feasibility for Breast Imaging". IEEE Trans Nucl Sci. Vol 54, #5. Oct 2007. p 1498-1507.
- [5] Wurtz, R., Ziock, K., Fabris, L., & Graham, R. (2005). Comparing Imaging and Non-Imaging Techniques for Reducing Background Clutter and Resolving Distant Point Sources. IEEE Nuclear Science Symposium Conference Record, 2005, 1, 338-342. doi:10.1109/nssmic.2005.1596266
- [6] Vetter, K., Mihailescu, L., Nelson, K., Valentine, J., & Wright, D. (2006). Gamma-ray Imaging Methods. doi:10.2172/1036848
- [7] Dicke, R.H., Scatter-hole cameras for x-ray and gamma rays. *Astrophys. J.* 153, L101-06 (1968).
- [8] Ziock, K., Collins, J., Fabris, L., Gallagher, S., Horn, B., Lanza, R., & Madden, N. (2006). Source-search sensitivity of a large-area, coded-aperture, gamma-ray imager. *IEEE Transactions on Nuclear Science*, 53(3), 1614-1621. doi:10.1109/tns.2006.875285
- [9] Kilner, J. R., & Nakano, G. H. (1989). EUV, X-Ray, and Gamma-Ray Instrumentation for Astronomy and Atomic Physics. doi:10.1117/12.962562
- [10] Schönfelder, V., Hirner, A., & Schneider, K. (1973). A telescope for soft gamma ray astronomy. *Nuclear Instruments and Methods*, 107(2), 385-394. doi:10.1016/0029-554x(73)90257-7
- [11] Bernabeu, J., Clinthorne, N., Dewaraja, Y., Lacasta, C., Llosá, G., Mikuž, M., . . . Žontar, D.

(2004). Development of a high efficiency and high resolution Compton probe for prostate imaging. Nuclear Instruments and Methods in Physics Research Section A: Accelerators, Spectrometers, Detectors and Associated Equipment, 527(1-2), 58-61.
doi:10.1016/j.nima.2004.03.038

[12] H. Inc., Specifications of polaris-h gamma-ray imaging spectrometer 2014 [Online]. Available: h3dgamma.com

[13] P. Co., “Gegi gamma-ray imaging detector,” 2014 [Online]. Available: phdsc.com

[14] Fitzgerald, J. G. (2015). A Rotating Scatter Mask for Inexpensive Gamma-Ray Imaging in Orphan Source Search: Simulation Results. IEEE Transactions on Nuclear Science, 62(1), 340-348. doi:10.1109/tns.2014.2379332

[15] Boyce, N.O. (2010). Thermal Neutron Point Source Imaging Using a Porating Modulation Collimator (RMC) (Master’s thesis).

[16] Lawson, R. S. (2013). Gamma Camera SPECT. Practical SPECT/CT in Nuclear Medicine, 47-75. doi:10.1007/978-1-4471-4703-9_4

[17] Calderon, Y. (2014). Design, Development, and Modeling of a Compton Camera Tomographer Based on Room Temperature Solid State Pixel Detector (Doctoral dissertation).

[18] Chapter 4. Geant4 User Support. (n.d.). Retrieved January 04, 2017, from http://geant4.web.cern.ch/geant4/workAreaUserDocKA/Backup/Docbook_UsersGuides_beta/IntroductionToGeant4/html/ch04.html

[19] Knoll, G. F. (1979). Radiation detection and measurement. New York: Wiley.

[20] Lewis, E. E., & Miller, W. F. (1984). Computational methods of neutron transport. New York: Wiley.

[21] XCOM: Photon Cross Sections Database. (2016, October 04). Retrieved January 05, 2017, from <https://www.nist.gov/pml/xcom-photon-cross-sections-database>

[22] Thompson, A. et al. (2009). X-ray Data Booklet (3rd ed.). Lawrence Berkeley National Laboratory: Center for X-ray Optics and Advanced Light Source.

[23] Decay Schemes. (n.d.). Retrieved January 05, 2017, from http://www.nucleonica.net/wiki/index.php?title=Decay_Schemes

[24] Helmer, R., & Checkev, V. (2006). Table de Radionucleides. Retrieved January 5, 2017, from http://www.nucleide.org/DDEP_WG/Nuclides/Cs-137_tables.pdf

[25] Engmann S, Cousineau D. Comparing distributions: the two-sample Anderson-Darling test

as an alter-native to the Kolmogorov-Smirnoff test. Journal of Applied Quantitative Methods. 2011; 6(3):1–17.

[26] Bityukov, S., Maksimushkina, A., & Smirnova, V. (2016). Comparison of histograms in physical research. Nuclear Energy and Technology, 2(2), 108-113.

doi:10.1016/j.nucet.2016.05.007

[27] Wright, D. (2012, April 19). A Short Guide to Choosing a Physics List. Retrieved January 5, 2017, from <http://geant4.slac.stanford.edu/MSFC2012/ChoosePhys.pdf>

[28] Spherical coordinate system. (n.d.). Retrieved January 05, 2017, from https://en.wikipedia.org/wiki/Spherical_coordinate_system

[29] Barrett, H. H., & Swindell, W. (1981). Radiological imaging: the theory of image formation, detection, and processing. New York: Academic Press.

[30] Gardner, R. P., & Sood, A. (2004). A Monte Carlo simulation approach for generating NaI detector response functions (DRFs) that accounts for non-linearity and variable flat continua. Nuclear Instruments and Methods in Physics Research Section B: Beam Interactions with Materials and Atoms, 213, 87-99. doi:10.1016/s0168-583x(03)01539-8

[31] Matlab R2016a. The MathWorks. 2016.

[32] H. (2017, January 15). Modal Assurance Criterion (MAC). Retrieved February 03, 2017, from <https://community.plm.automation.siemens.com/t5/Testing-Knowledge-Base/Modal-Assurance-Criterion-MAC/ta-p/368008>

[33] Prekeges, J. (2013). Nuclear medicine instrumentation. Burlington, MA: Jones & Bartlett Learning.

REPORT DOCUMENTATION PAGE

Form Approved
OMB No. 0704-0188

The public reporting burden for this collection of information is estimated to average 1 hour per response, including the time for reviewing instructions, searching existing data sources, gathering and maintaining the data needed, and completing and reviewing the collection of information. Send comments regarding this burden estimate or any other aspect of this collection of information, including suggestions for reducing the burden, to Department of Defense, Washington Headquarters Services, Directorate for Information Operations and Reports (0704-0188), 1215 Jefferson Davis Highway, Suite 1204, Arlington, VA 22202-4302. Respondents should be aware that notwithstanding any other provision of law, no person shall be subject to any penalty for failing to comply with a collection of information if it does not display a currently valid OMB control number.

PLEASE DO NOT RETURN YOUR FORM TO THE ABOVE ADDRESS.

1. REPORT DATE (DD-MM-YYYY) 23-02-2017			2. REPORT TYPE Master's Thesis	3. DATES COVERED (From - To) Sept 2015 - March 2017	
4. TITLE AND SUBTITLE Rotating Scatter Mask for Gamma Source Imaging			5a. CONTRACT NUMBER		
			5b. GRANT NUMBER		
			5c. PROGRAM ELEMENT NUMBER		
6. AUTHOR(S) Logan, Julie V, GS-09 Air Force Material Command			5d. PROJECT NUMBER		
			5e. TASK NUMBER		
			5f. WORK UNIT NUMBER		
7. PERFORMING ORGANIZATION NAME(S) AND ADDRESS(ES) Air Force Institute of Technology Graduate School of Engineering and Management (AFIT/EN) 2950 Hobson Way Wright-Patterson AFB OH 45433-7765			8. PERFORMING ORGANIZATION REPORT NUMBER AFIT-ENP-13-M-07		
9. SPONSORING/MONITORING AGENCY NAME(S) AND ADDRESS(ES) Defense Threat Reduction Agency 8725 John J Kingman Rd #6201 Fort Belvoir, VA 22060			10. SPONSOR/MONITOR'S ACRONYM(S) DTRA		
			11. SPONSOR/MONITOR'S REPORT NUMBER(S)		
12. DISTRIBUTION/AVAILABILITY STATEMENT Distribution Statement A. Approved for Public Release; Distribution Unlimited.					
13. SUPPLEMENTARY NOTES This work is declared a work of the U.S. Government and is not subject to copyright protection in the United States.					
14. ABSTRACT Current gamma imaging systems are limited in utility due to their cost, size, narrow field of view, and low image formation efficiency. This effort constitutes a critical step in the development of an imaging system that is limited by none of these factors. This gamma imaging system consists of a routine NaI(Tl) scintillation detector coupled with a rotating scatter mask, the geometry of which is specifically chosen such that the detected signal obtained from one complete mask rotation provides sufficient information to uniquely determine the source direction. This mask encases the detector and can be completely encapsulated within a 0.045 m ³ cube (side length of 35.56 cm). A GEANT4 simulation was developed to model the functionality of this system and obtain a library of detector response curves. This simulation was validated via statistical comparisons with experimental and MCNP data. Using the results of the simulation, an algorithm was developed that was shown to predict experimental source direction over a nearly 4π field of view with average errors that were smaller than the resolution in the library of curves employed to image, with an average error in both the azimuthal angle and polar angle of less than 5°.					
15. SUBJECT TERMS nuclear detection; nuclear imaging; gamma source; nuclear engineering; GEANT					
16. SECURITY CLASSIFICATION OF: a. REPORT U		17. LIMITATION OF ABSTRACT UU	18. NUMBER OF PAGES 260	19a. NAME OF RESPONSIBLE PERSON Lt Col Buckley E O'Day, AFIT/ENP 19b. TELEPHONE NUMBER (Include area code) 937-255-3636 Ext 4609 buckley.o'day@afit.edu	